State Preparation and Conditional Dynamics of Quantum Systems

Anne Ersbak Bang Nielsen

Lundbeck Foundation Theoretical Center for Quantum System Research,
Department of Physics and Astronomy, Aarhus University, Denmark

PhD Thesis
April 2010

This thesis has been submitted to the Faculty of Science at Aarhus University, Denmark, in partial fulfilment of the requirements for obtaining the PhD degree in Physics. The studies have been carried out under supervision of Professor Klaus Mølmer in the Lundbeck Foundation Theoretical Center for Quantum System Research at the Department of Physics and Astronomy, Aarhus University, Denmark, from August 2006 to April 2010 and in Professor Hideo Mabuchi's group at the Edward L. Ginzton Laboratory, Stanford University, California, USA, from January 2009 to June 2009.

Lundbeck Foundation Theoretical Center for Quantum System Research
Department of Physics and Astronomy
Aarhus University
Ny Munkegade 120
DK-8000 Århus C
Denmark
Email: annebn@phys.au.dk
Printed by SUN-TRYK, Aarhus University

Acknowledgments

First of all, I would like to thank my supervisor Klaus Mølmer for his support. I am grateful to Klaus Mølmer for giving me a lot of freedom to work on my own and do whatever I want while at the same time being extremely helpful, both with new inspiring ideas and useful advices. I would also like to thank Hideo Mabuchi for giving me the opportunity to visit Mabuchilab at Stanford University for half a year and for being extremely helpful. It has been very interesting and instructive to work at a foreign university, and I would like to thank all members of Mabuchilab for giving me a good reception and for being very kind people. I would also like to acknowledge several interesting discussions with people I have met during my visit, in particular Hideo Mabuchi, Joseph Kerckhoff, Hendra Nurdin, Ramon van Handel, Anthony Miller, Gopal Sarma, Michael Armen, and Kendrick Kwon.

During my PhD studies I have had the pleasure to visit a number of groups for shorter periods of time, and in this respect I would like to thank QUANTOP for a very instructive visit to the Niels Bohr Institute. In particular, I would like to acknowledge discussions with Jonas Neergaard-Nielsen, Bo Melholt Nielsen, Eugene Polzik, and Anders Sørensen. I would also like to thank Ignacio Cirac's group, in particular Christine Muschik, for a couple of very interesting visits to the Max Planck Institute of Quantum Optics. I would like to thank Christine Muschik, Géza Giedke, and Karl Vollbrecht for collaboration and Christine Muschik for numerous discussions and good company. Additionally, I would like to thank Luis Orozco and David Norris for an interesting visit to the University of Maryland.

I would like to thank all current and former members of the Lundbeck Foundation Theoretical Center for Quantum System Research for providing a very nice atmosphere at the university. In addition, I would like to thank Christian Madsen, Christian Martiny, and Henriette Leth for good company and Uffe Poulsen, Antonio Negretti, and Asa Hopkins for collaboration. I would also like to thank my fellow students during the first years, in particular Helle Svendsen, Heine Thomsen, Thomas Kjærgaard, Lasse Straasø, Lise Jensen, and Niels Villumsen, for the many great times we have spent together. Almost last, but certainly not least, thanks to my family.

Support from an Elite Research Scholarship from the Danish Ministry of Science, Technology, and Innovation is gratefully acknowledged.

Anne Ersbak Bang Nielsen,

Århus, April 2010.

List of publications

[I] Anne E. B. Nielsen and Klaus Mølmer, *Single-photon-state generation from a continuous-wave nondegenerate optical parametric oscillator*, Phys. Rev. A **75**, 023806 (2007); arXiv:quant-ph/0611268.

[II] Anne E. B. Nielsen and Klaus Mølmer, *Photon number states generated from a continuous-wave light source*, Phys. Rev. A **75**, 043801 (2007); arXiv:quant-ph/0612129.

[III] Anne E. B. Nielsen and Klaus Mølmer, *Conditional generation of path-entangled optical* $|N,0\rangle+|0,N\rangle$ *states*, Phys. Rev. A **75**, 063803 (2007); arXiv:0704.0397.

[IV] Anne E. B. Nielsen and Klaus Mølmer, *Multimode analysis of the light emitted from a pulsed optical parametric oscillator*, Phys. Rev. A **76**, 033832 (2007); arXiv:0706.4159.

[V] Anne E. B. Nielsen and Klaus Mølmer, *Transforming squeezed light into a large-amplitude coherent-state superposition*, Phys. Rev. A **76**, 043840 (2007); arXiv:0708.1956.

[VI] Anne E. B. Nielsen and Klaus Mølmer, *Stochastic master equation for a probed system in a cavity*, Phys. Rev. A **77**, 052111 (2008); arXiv:0802.1225.

[VII] Anne E. B. Nielsen and Klaus Mølmer, *Atomic spin squeezing in an optical cavity*, Phys. Rev. A **77**, 063811 (2008); arXiv:0805.0482.

[VIII] Anne E. B. Nielsen, Uffe V. Poulsen, Antonio Negretti, and Klaus Mølmer, *Atomic quantum superposition state generation via optical probing*, Phys. Rev. A **79**, 023841 (2009); arXiv:0812.4048.

[IX] Anne E. B. Nielsen, Asa S. Hopkins, and Hideo Mabuchi, *Quantum filter reduction for measurement-feedback control via unsupervised manifold learning*, New J. Phys. **11**, 105043 (2009); arXiv:0905.1139.

[X] Anne E. B. Nielsen, *Fighting decoherence in a continuous two-qubit odd- or even-parity measurement with a closed-loop setup*, Phys. Rev. A. **81**, 012307 (2010); arXiv:0908.0817.

[XI] Anne E. B. Nielsen and Klaus Mølmer, *Deterministic multimode photonic device for quantum-information processing*, Phys. Rev. A **81**, 043822 (2010); arXiv:1001.1429.

[XII] Anne E. B. Nielsen, Christine A. Muschik, Geza Giedke, and K. G. H. Vollbrecht, *Quantum state engineering, purification, and number-resolved photon detection with high-finesse optical cavities*, Phys. Rev. A **81**, 043832 (2010); arXiv:1002.0127.

Contents

Chapter 1

Introduction

Motivation

Within the last decades it has become possible to investigate the properties of quantum mechanical systems in extremely clean experiments, for instance to study the interactions of a single atom with single quanta of a light field. Such experiments allow us to test quantum mechanics at a fundamental level and to achieve a thorough understanding of how quantum mechanical systems behave. The consequences of the laws of quantum mechanics also pave the way for a large number of technological applications, some of which may themselves be valuable scientific tools.

One example is the quantum computer [1][1]. In one type of quantum computer proposals, information is encoded in quantum mechanical two-level systems, which are referred to as qubits. The two levels could, for instance, be two internal levels of an atom or ion, two different collective states of an ensemble of atoms, two harmonic oscillator states of an ion in an ion trap, two orthogonal polarizations of a photon, two levels of a defect, or two states of a superconducting circuit. The main strength of the quantum computer compared to a classical computer is the fact that a qubit is not necessarily in one of the two states $|0\rangle$ or $|1\rangle$ but may be in a superposition $a|0\rangle + b|1\rangle$ of the two states. This property allows the quantum computer to carry out computations on a superposition of several input states in parallel on a single register, and a significant speedup compared to classical computing can be gained. It is, however, not straightforward to read out the results, which imposes limitations, but solutions have been found in certain cases. Early examples are the Deutsch-Jozsa algorithm [2] to determine whether a function is constant or balanced, Shor's algorithm [3] to factorize large numbers, and Grover's algorithm [4] to search for an element in an unsorted list. More recently, an algorithm [5] has been proposed to estimate expectation

---

[1] Arabic numerals in square brackets refer to the bibliography, Roman numerals in square brackets refer to the list of publications, and numbers in brackets like (1.1) refer to equations.

values of the form $x^T Mx$, where M is a matrix, x is the solution to a set of linear equations, and T denotes the transpose, which is a problem that often appears in science. Another interesting potential of quantum computing is the quantum simulator [6], which uses well-known controllable interactions to simulate the dynamics of another quantum system. This is interesting because the number of variables describing the state of a quantum system very easily becomes so large that it is impossible to simulate the dynamics of the system on a classical computer. Large scale quantum computing has not been realized so far, but single gates and computations on systems with a few qubits have been demonstrated, see e.g. [7, 8, 9].

Quantum mechanics also provides new possibilities within cryptography. An example is quantum key distribution [10] in which two distant parties Alice and Bob would like to create a string of random bits (the key) that is known to both Alice and Bob but not to anyone else. In a typical scheme, Alice sends a random sequence of quantum states to Bob, e.g. encoded in single photons or groups of single photons, and Bob then applies some kind of measurements to the states he receives. By subsequent communication over a classical channel, e.g. a phone line, it is possible both to construct the key and to use the laws of quantum mechanics to check whether someone has tried to tap the quantum channel. If this is not the case, the key can be used for encrypting a secret message. Small scale quantum cryptographic systems have already been implemented and are commercially available [11]. A related possibility is to use the outcome of quantum mechanical measurements to generate random numbers, which is very useful, for instance, in computer simulations.

A lot of effort has been put into designing methods to send quantum information over long distances, both to facilitate quantum key distribution and to create quantum correlations between systems held by distant parties. Such links allow Alice to use teleportation [12] to send the state of a quantum system to Bob without sending the system itself. To do so, Alice performs a joint measurement on the system and her part of the link, and Bob then applies an operation to his part of the link, which depends on the measurement outcome. Teleportation has been demonstrated in more experiments, see for instance [13] for a teleportation between light and matter over a distance of half a meter.

The possibility to generate quantum states with an extremely small uncertainty in a given observable can be used for improving the precision of ultra precise measurements. This is, for instance, relevant in magnetometry, atomic clocks, and gravitational wave detection. An example is a recent experiment [14], in which measurements are used to decrease the variance of one component of the collective (pseudo-)spin vector of an atomic ensemble by creating quantum correlations between the atoms, and this decrease is utilized to improve the precision of an atomic clock.

In order to exploit all the useful properties of quantum systems, it is important to be able to understand and control their dynamics. To build a quantum computer, e.g., one should be able to drive the computer into a well-defined initial quantum state and subsequently apply various gate operations to the qubits (or at least to manipulate the state of the computer in such a way that the readout of some measurements applied to the system provides the result of the computation). Various quantum computer proposals, precision measurements, fundamental tests of quantum mechanics, and quantum cryptography require a number of different input states as a resource, and it is important to find easy ways to produce these states.

In the present thesis, we investigate how the state of a quantum system evolves when the system is subjected to measurements, and we show how measurements and other techniques can be used for preparing quantum systems in various quantum states. If we would like to control the dynamics of a quantum system, we could try to engineer a Hamiltonian, which does precisely what we are interested in. In practice, however, we are limited by the physically available interactions. Measurements provide a way to enlarge the toolbox of easily applicable transformations, and it has turned out that measurements are extremely useful for transforming, in particular, states of light. As an example, it is generally difficult to achieve nonlinear interactions between photons via unitary dynamics, but single-photon sources, linear optics, and photon number resolving detectors suffice for quantum computing [15, 16].

In many introductory quantum mechanics textbooks, observables are introduced as Hermitian operators on the Hilbert space of the considered quantum system, and a measurement of an observable is assumed to instantaneously project the state of the system onto an eigenstate of the observable. The measurement outcome is the corresponding eigenvalue and the probability to obtain a particular eigenvalue is the overlap between the initial state of the system and the eigenstate. Here, we are concerned with a more general type of measurements, where we divide the system into subsystems and only perform a measurement on some of the subsystems, or we allow the system to interact with a probe, which is subsequently detected. Furthermore, the detection process may occur continuously in time, and the measurements may not provide complete information about the detected state. As we are interested in what can be done experimentally, we shall generally start from a setup composed of a number of experimentally available devices and then analyze the time evolution of the state of the involved quantum systems.

The outcome of a quantum mechanical measurement is, in general, random, and the time evolution of the state of the measured system depends on the measurement result. A specific transformation can, however, be obtained by conditioning on a specific measurement outcome, i.e., by repeating the experiment until the desired measurement outcome is observed. We shall consider several examples of such conditional measurements in the thesis.

A further possibility is to apply feedback to the system. One can, for instance, allow the parameters in the Hamiltonian to depend on the outcome of measurements applied to the system, or one can use an output from the system as an input to the system (e.g., allow the system to interact repeatedly with a probe rather than detecting the probe). Feedback is a very useful technique to force a quantum system into a specific state and stabilize it in that state even if noise is present. We shall not engineer feedback schemes as such in the thesis, except for a single straightforward example, but we address the problem of using the outcome of a continuous measurement to estimate the current state of the system in a feedback loop and provide an example of the dynamics of a system subjected to feedback.

In addition to the measurement based state preparation schemes, we shall also investigate the possibility to produce states of light by use of the Rydberg blockade mechanism between neutral atoms.

Outline of the thesis

To keep the length of the thesis within reasonable limits (and specifically within the maximum allowed size of 200 pages), I have chosen not to present all the projects I have worked on during my PhD studies, but instead concentrate on some of the results obtained in publications [I-II], [IV-VII], and [IX-XII] together with a few unpublished results. Rather than making a collection of publications, I have rewritten the papers into one joint story in order to make the thesis more readable and to select the most important parts of the papers. Some parts of the publications have been rewritten entirely and new results have been added, while other parts have been included with only a few changes to avoid writing the same story a second time. The only exception is publication [XI], which I have included in full in Chap. 7. I have chosen to do so because this paper is both recent and sufficiently brief that it has not been necessary to shorten it. An ongoing project on topological states and another ongoing project on optical switches will not be discussed.

The thesis is divided into two main parts. The first part, which consists of Chaps. 2-7, treats of generation of various quantum mechanical states of light, either by use of conditional measurements or by use of the Rydberg blockade mechanism. Chapter 2 is an introduction to the theoretical techniques used throughout the thesis to describe various experimental setups. We introduce field operators and modes, explain how the quantum mechanical state of a continuous beam of light is specified, and consider how the state is changed when the beam interacts with different optical components. In Chap. 3, we provide a model of the optical parametric oscillator (OPO), which is the light source used in the experimental setups discussed in the following chapters. A special feature of the model is the fact that it allows an almost arbitrary time variation of the laser field used to pump the

OPO. In Chap. 4, we analyze a setup to generate photon number states by subjecting the light emitted from an OPO to a conditional measurement. The generated light field is a continuous beam, and our main concern is to determine which mode of the beam one should select in order to obtain the best photon number states. The states are generated at random times, which is often undesirable, and in Chap. 5 we investigate the possibility to modify the conditioning procedure to generate quantum states at specific times, but with a probability smaller than unity. In Chap. 6, we propose a protocol to generate Schrödinger cat states of light, which also relies on conditional measurements. In Chap. 7, we suggest to use an ensemble of atoms to generate a rich variety of quantum mechanical states of light deterministically. The basic idea is to use the possibility of strong interactions between atoms in Rydberg states to prepare the ensemble in a given quantum mechanical state and then transfer the state to light via cooperative spontaneous emission.

The second part of the thesis, which consists of Chaps. 8-12, deals with cavity quantum electrodynamics (QED). In Chap. 8, we spend a few pages on showing how we can use the techniques from Chap. 2 to derive a general equation for the time evolution of the state of a system, which is placed in an optical cavity and probed with a continuous beam of light. We also provide an example of the dynamics that can emerge from the equation. In Chap. 9, we propose a method to improve an earlier proposal to measure whether two atoms, placed in different cavities and each with two ground state levels, are in the same ground state level or in different ground state levels without revealing the state of the individual atoms. In Chap. 10, we turn things around and use measurements applied to single atoms in cavities to probe the state of a light field. We propose a scheme to generate states of light with interesting quantum mechanical properties, and we suggest a method to build a detector, which counts the number of photons in a pulse of light without destroying it. The subject of Chap. 11 is state estimation in measurement based feedback control of quantum systems. To apply state dependent feedback, one needs to compute the state of the system in real time, which is typically not possible because the dynamics is too complicated. We present a general method to obtain a simplified description of the dynamics of a quantum system, and we investigate the utility of the method for the specific case of controlling the state of a probed two-level atom in a cavity. In Chap. 12, we move on to probing of ensembles of atoms in cavities. Treating each atom as a spin-1/2 system, one can use measurements to reduce the variance of one component of the total spin vector of the atoms, and we compare the performance of such measurements when a cavity is included in the setup to the performance when a cavity is not included. Chapter 13 concludes the thesis with a discussion of the obtained results. After the conclusion, we provide a summary and a list of the abbreviations introduced in the thesis.

Chapter 2

Multimode description of continuous beams of light

During the thesis we shall investigate various experimental setups involving beams of light and different optical components, and we start with a brief introduction to the theoretical framework we use to describe such systems. In Sec. 2.1, we establish the connection between field operators and the electromagnetic fields, and we introduce the notion of modes and mode functions. In Sec. 2.2, we briefly describe different ways to represent quantum mechanical states of light, and in Sec. 2.3, we consider the action of a few basic optical components, which we use as building blocks throughout the thesis. Finally, we discuss various detector models in Sec. 2.4. The chapter is based mainly on textbook material and does not contain any new results.

2.1 Field operators and modes

Maxwell's equations

The dynamics of electromagnetic fields in free space is determined by the source free Maxwell equations [17]

$$\nabla \cdot \mathbf{E}(\mathbf{r},t) = 0, \qquad \nabla \times \mathbf{E}(\mathbf{r},t) = -\frac{\partial \mathbf{B}(\mathbf{r},t)}{\partial t}, \tag{2.1}$$

$$\nabla \cdot \mathbf{B}(\mathbf{r},t) = 0, \qquad \nabla \times \mathbf{B}(\mathbf{r},t) = \frac{1}{c^2}\frac{\partial \mathbf{E}(\mathbf{r},t)}{\partial t}, \tag{2.2}$$

where $\mathbf{E}(\mathbf{r},t)$ and $\mathbf{B}(\mathbf{r},t)$ are the electric field and the magnetic field at position $\mathbf{r} = (x,y,z)$ and at time t, respectively, and c is the speed of light in vacuum. The fields may be expressed in terms of the vector potential $\mathbf{A}(\mathbf{r},t)$ and the scalar potential $\phi(\mathbf{r},t)$,

$$\mathbf{E}(\mathbf{r},t) = -\frac{\partial \mathbf{A}(\mathbf{r},t)}{\partial t} - \nabla\phi(\mathbf{r},t), \qquad \mathbf{B}(\mathbf{r},t) = \nabla \times \mathbf{A}(\mathbf{r},t), \tag{2.3}$$

and in Coulomb gauge, $\nabla \cdot \mathbf{A} = 0$, the source free Maxwell equations take the form

$$\nabla^2 \phi(\mathbf{r}, t) = 0, \qquad \nabla^2 \mathbf{A}(\mathbf{r}, t) = \frac{1}{c^2}\frac{\partial^2 \mathbf{A}(\mathbf{r}, t)}{\partial t^2} + \frac{1}{c^2}\frac{\partial}{\partial t}\nabla\phi(\mathbf{r}, t). \tag{2.4}$$

Since there are no charges, the scalar potential is constant and does not contribute to the fields. The vector potential then fulfils the wave equation and may be written on the form [18]

$$\mathbf{A}(\mathbf{r}, t) = \sum_{\lambda}\sum_{\mathbf{k}} \left(\alpha_{\mathbf{k},\lambda}\mathbf{f}_{\mathbf{k},\lambda}(\mathbf{r})e^{-i\omega_{\mathbf{k}}t} + \alpha^*_{\mathbf{k},\lambda}\mathbf{f}^*_{\mathbf{k},\lambda}(\mathbf{r})e^{i\omega_{\mathbf{k}}t}\right), \tag{2.5}$$

where $\alpha_{\mathbf{k},\lambda}$ are expansion coefficients, $\mathbf{f}_{\mathbf{k},\lambda}(\mathbf{r})$ are orthonormal vector functions fulfilling

$$(\nabla^2 + k^2)\mathbf{f}_{\mathbf{k},\lambda}(\mathbf{r}) = 0, \tag{2.6a}$$

$$\nabla \cdot \mathbf{f}_{\mathbf{k},\lambda}(\mathbf{r}) = 0, \tag{2.6b}$$

$$\int_V \mathbf{f}^*_{\mathbf{k},\lambda}(\mathbf{r}) \cdot \mathbf{f}_{\mathbf{k}',\lambda'}(\mathbf{r}) d^3r = \delta^3_{\mathbf{k}\mathbf{k}'}\delta_{\lambda\lambda'}, \tag{2.6c}$$

and the relevant boundary conditions, k is the length of the wave vector $\mathbf{k} = (k_x, k_y, k_z)$, V is the volume of the region of space in which we would like to determine the fields, $\delta_{\lambda\lambda'}$ is the Kronecker delta, $\delta^3_{\mathbf{k}\mathbf{k}'} = \delta_{k_x k'_x}\delta_{k_y k'_y}\delta_{k_z k'_z}$, and $\omega_{\mathbf{k}} = kc$. The λ-index may take two different values and is included to take into account that two different polarizations are allowed for each wave vector $\mathbf{k}$. Each term in the double sum on the right hand side of (2.5) is the contribution to $\mathbf{A}(\mathbf{r}, t)$ from one mode of the field, and $\mathbf{f}_{\mathbf{k},\lambda}(\mathbf{r})$ is the corresponding (vector-valued) mode function.

Quantization

In a quantum mechanical treatment, the vector potential and the electric and magnetic fields are operators. To find out how these operators should be chosen, we need to identify the Hamiltonian and the set of conjugate generalized position and momentum coordinates, which reproduce Maxwell's equations. The position and momentum coordinates are then replaced by noncommuting operators. As this is explained in several textbooks (see e.g. [18]), we shall not go through the details here, but simply state the result: the expansion coefficients should be regarded as operators

$$\alpha_{\mathbf{k},\lambda} = -i\sqrt{\frac{\hbar}{2\epsilon_0\omega_{\mathbf{k}}}}\hat{a}_{\mathbf{k},\lambda}, \tag{2.7}$$

where $\hbar$ is Planck's constant divided by 2π, ϵ_0 is the vacuum permittivity, and the properties of the field annihilation operators $\hat{a}_{\mathbf{k},\lambda}$ are characterized by the commutator relations

$$[\hat{a}_{\mathbf{k},\lambda}, \hat{a}_{\mathbf{k}',\lambda'}] = 0, \qquad [\hat{a}_{\mathbf{k},\lambda}, \hat{a}^\dagger_{\mathbf{k}',\lambda'}] = \delta^3_{\mathbf{k},\mathbf{k}'}\delta_{\lambda,\lambda'}. \tag{2.8}$$

Beams of light

We would like to specialize to the case of a light beam propagating in the positive z-direction and with a slowly varying transverse profile, which is broad compared to the wavelength of the light. The beam is then approximately a plane wave. Assuming periodic boundary conditions for the z-coordinate, $\mathbf{f}_{\mathbf{k},\lambda}(x, y, z + L_z) = \mathbf{f}_{\mathbf{k},\lambda}(x, y, z)$, the relevant solutions to (2.6) take the form

$$\mathbf{f}_{\mathbf{k},\lambda}(x, y, z) = \frac{1}{\sqrt{L_z}} h(x, y) e^{ik_z z} \mathbf{e}_\lambda, \tag{2.9}$$

where the transverse mode function $h(x, y)$ is a slowly varying function of x and y normalized such that $\iint |h(x, y)|^2 dxdy = 1$, k_z may take any of the values $k_z = 2\pi n_z/L_z$, where n_z is a positive integer (to ensure propagation in the positive z-direction), and $\mathbf{e}_\lambda$ is one of two orthogonal unit vectors in the xy-plane. We assume throughout the thesis that only one transverse mode is populated.

In the limit $L_z \to \infty$, we can replace the sum over k_z in (2.5) by an integral. To obtain the required $\Delta k_z = 2\pi/L_z$ on the right hand side of (2.5), we define a new mode function, which is $(\Delta k_z)^{-1/2} = (L_z/(2\pi))^{1/2}$ times the old mode function, and a new continuous field annihilation operator $\hat{a}_\lambda(k_z) = \hat{a}_{\mathbf{k},\lambda}(\Delta k_z)^{-1/2}$. This amounts to replacing the Kronecker delta $\delta_{k_z k'_z}$ in (2.6c) and (2.8) by the Dirac delta function $\delta(k_z - k'_z)$. Converting the integral over k_z to an integral over angular frequency $\omega = \omega_{\mathbf{k}} = k_z c$, we finally obtain [19]

$$\begin{aligned} \boldsymbol{A}(\mathbf{r}, t) = \sum_\lambda \int_0^\infty \sqrt{\frac{\hbar}{4\pi\epsilon_0 c\omega}} \Big(&- ih(x, y)\hat{a}_\lambda(\omega)\boldsymbol{e}_\lambda e^{-i\omega(t - z/c)} \\ &+ ih^*(x, y)\hat{a}^\dagger_\lambda(\omega)\boldsymbol{e}^*_\lambda e^{i\omega(t-z/c)}\Big) d\omega, \end{aligned} \tag{2.10}$$

where $[\hat{a}_\lambda(\omega), \hat{a}^\dagger_{\lambda'}(\omega')] = \delta_{\lambda\lambda'}\delta(\omega - \omega')$.

In the rest of the thesis, we shall use $\hat{a}_\lambda(\omega)$ to describe beams of light rather than the vector potential or the electric and magnetic fields. We shall also find it convenient to introduce the continuous field operators in time domain as the Fourier transform of $\hat{a}_\lambda(\omega)$,

$$\hat{a}_\lambda(t) = \frac{1}{\sqrt{2\pi}} \int_{-\infty}^\infty \hat{a}_\lambda(\omega) e^{-i\omega t} d\omega, \quad \hat{a}_\lambda(\omega) = \frac{1}{\sqrt{2\pi}} \int_{-\infty}^\infty \hat{a}_\lambda(t) e^{i\omega t} dt. \tag{2.11}$$

It follows from the commutator relation above that $[\hat{a}_\lambda(t), \hat{a}^\dagger_{\lambda'}(t')] = \delta_{\lambda\lambda'}\delta(t - t')$. For laser light within the optical region of the electromagnetic spectrum, we note that the lower limit of integration over frequency in Eq. (2.10) can be extended to minus infinity because the central frequency of the light (for instance, 5×10^{14} Hz) is very large compared to the bandwidth (i.e., the width of the frequency distribution) of the light (for instance, 1 MHz [20]). (In other words, the expectation value of, for instance, $\hat{a}_\lambda(\omega)$ is zero for all states of interest unless ω lies within some narrow interval around the central frequency.) If we furthermore assume that the coefficient $(\hbar/(4\pi\epsilon_0 c\omega))^{1/2}$ is practically constant within the relevant frequency interval, we observe that $\mathbf{A}(x, y, 0, t) \propto \sum_\lambda(-ih(x, y)\hat{a}_\lambda(t)\mathbf{e}_\lambda + h.c.)$, where *h.c.* is the Hermitian conjugate. A similar approximation leads to $\mathbf{E}(x, y, 0, t) \propto \sum_\lambda(h(x, y)\hat{a}_\lambda(t)\mathbf{e}_\lambda + h.c.)$, which illustrates the close relationship between the electric field and $\hat{a}_\lambda(t)$.

Discrete mode field operators

As an alternative to the continuous field operators $\hat{a}_\lambda(\omega)$ and $\hat{a}_\lambda(t)$, we can choose a complete set of orthonormal mode functions $f_j(t)$,

$$\sum_j f_j^*(t) f_j(t') = \delta(t - t'), \qquad \int f_i(t) f_j^*(t) dt = \delta_{ij}, \tag{2.12}$$

and describe the light beams in terms of the single-mode operators

$$\hat{a}_{\lambda,j} = \int f_j^*(t)\hat{a}_\lambda(t)dt = \int f_j^*(\omega)\hat{a}_\lambda(\omega)d\omega, \tag{2.13}$$

where $f_j(\omega)$ is the inverse Fourier transform of $f_j(t)$ and $[\hat{a}_{\lambda,i}, \hat{a}^\dagger_{\lambda',j}] = \delta_{\lambda\lambda'}\delta_{ij}$ as detailed in [19]. In particular, we shall often use the time-localized mode functions

$$f_j(t) = \begin{cases} 1/\sqrt{\Delta t} & \text{if } t_j - \Delta t/2 < t \leq t_j + \Delta t/2 \\ 0 & \text{otherwise} \end{cases}, \tag{2.14}$$

where $t_j = j\Delta t$, $j = 0, \pm 1, \pm 2, \ldots$, and Δt is sufficiently small to be regarded as infinitesimal such that $\hat{a}_{\lambda,j} = \hat{a}_\lambda(t_j)\sqrt{\Delta t}$ (in practice, we move into a frame rotating with the optical frequency of the light and choose Δt to be long compared to the wavelength of the light but small compared to all other relevant timescales). Note that, from this point of view, the time argument is simply a label, which keeps track of the different modes. In the following, we suppress the λ-index unless we are explicitly considering modes with different polarization.

2.2 Representations of quantum states of light

The density operator

To calculate expectation values of the field operators, we need to specify the quantum mechanical state of the light field, which is done in terms of the modes introduced in (2.13). As basis states we use direct products of the eigenstates $|n_j\rangle$ of the hermitian operators $\hat{a}_j^\dagger \hat{a}_j$. It follows from the commutator relation that n_j is a nonnegative integer, $\hat{a}_j|n_j\rangle = \sqrt{n_j}|n_j - 1\rangle$, and $\hat{a}_j^\dagger|n_j\rangle = \sqrt{n_j+1}|n_j+1\rangle$, and the physical interpretation is that $\hat{a}_j^\dagger \hat{a}_j$ is the operator representing the number of photons in the jth mode, $\hat{a}_j$ annihilates a photon in the jth mode, and $\hat{a}_j^\dagger$ creates a photon in the jth mode [21]. A general state vector representing the quantum mechanical state of N modes may thus be written as

$$|\psi\rangle = \sum_{n_1=0}^{\infty} \sum_{n_2=0}^{\infty} \cdots \sum_{n_N=0}^{\infty} c_{n_1 n_2 \ldots n_N} |n_1\rangle \otimes |n_2\rangle \otimes \ldots \otimes |n_N\rangle. \tag{2.15}$$

We may not know the precise quantum mechanical state of the system under consideration, however, and it is then relevant to include a classical uncertainty in the representation of our knowledge of the state of the system. This is done by introducing the density operator ρ. For the state in (2.15), $\rho = |\psi\rangle\langle\psi|$, but more generally $\rho = \sum_\alpha p_\alpha |\psi_\alpha\rangle\langle\psi_\alpha|$, where p_α is the probability that the system is in the state $|\psi_\alpha\rangle$. If it is possible to write $\rho = |\psi\rangle\langle\psi|$ for some choice of $|\psi\rangle$, the state is said to be pure, but otherwise it is mixed. When the state is represented by a density operator, the expectation value $\langle\hat{O}\rangle$ of an operator $\hat{O}$ is the classical average of the quantum expectation values, and thus

$$\langle\hat{O}\rangle = \sum_\alpha p_\alpha \langle\psi_\alpha|\hat{O}|\psi_\alpha\rangle = \sum_q \langle q|\hat{O} \sum_\alpha p_\alpha |\psi_\alpha\rangle\langle\psi_\alpha|q\rangle = \mathrm{Tr}(\hat{O}\rho), \tag{2.16}$$

where $|q\rangle$ is a complete set of orthonormal states and Tr denotes the trace. The purity of a state is defined as $\mathrm{Tr}(\rho^2)$, which is unity for pure states and smaller than unity for mixed states. If the system consists of two subsystems A and B, we say that the subsystems are entangled if it is impossible to write the density operator of the system on the form $\rho = \sum_\alpha p_\alpha \rho_\alpha^{(A)} \otimes \rho_\alpha^{(B)}$, where $\rho_\alpha^{(A)}$ and $\rho_\alpha^{(B)}$ are density operators on A and B, respectively [18]. For pure states, the subsystems are entangled if the state vector of the system can not be written as a product $|\psi\rangle = |\psi\rangle_A \otimes |\psi\rangle_B$ of state vectors on A and B.

The density operator may be represented in a different basis than the one specified by the state vectors $|\psi_\alpha\rangle$, and in the photon number state basis, the density operator representing the collective state of N modes of a light field can be written on the form

$$\rho = \sum_{n_1=0}^{\infty} \sum_{n_2=0}^{\infty} \cdots \sum_{n_N=0}^{\infty} \sum_{m_1=0}^{\infty} \sum_{m_2=0}^{\infty} \cdots \sum_{m_N=0}^{\infty} \rho_{n_1,n_2,\ldots,n_N,m_1,m_2,\ldots,m_N}$$
$$\times |n_1\rangle \otimes |n_2\rangle \otimes \ldots \otimes |n_N\rangle\langle m_1| \otimes \langle m_2| \otimes \ldots \otimes \langle m_N|. \tag{2.17}$$

In order to be a valid density operator, ρ must be Hermitian ($\rho = \rho^\dagger$), normalized ($\mathrm{Tr}(\rho) = 1$), and positive semidefinite (i.e., all eigenvalues of the density operator are nonnegative). For brevity we shall often omit the $\otimes$ symbols and sometimes write the numbers n_1, n_2, …, n_N within the same ket. Further details on density operators may be found in [18].

A particularly important example of a state of light is the coherent state. The single-mode coherent state [22]

$$|\alpha_j\rangle = e^{\alpha_j \hat{a}_j^\dagger - \alpha_j^* \hat{a}_j}|0\rangle = e^{-\frac{1}{2}|\alpha_j|^2} \sum_{n_j=0}^{\infty} \frac{\alpha_j^{n_j}}{\sqrt{n_j!}}|n_j\rangle \tag{2.18}$$

with amplitude α_j is an eigenstate of $\hat{a}_j$ with eigenvalue α_j. The vacuum (i.e., zero-photon) state $|0\rangle$ is a special case with $\alpha_j = 0$, and all other coherent states are obtained by application of the displacement operator $D_{\hat{a}_j}(\alpha_j) = e^{\alpha_j \hat{a}_j^\dagger - \alpha_j^* \hat{a}_j}$. We shall also need continuous (or multimode) coherent states [19]

$$|\{\alpha(t)\}\rangle = e^{\int \left(\alpha(t)\hat{a}^\dagger(t) - \alpha^*(t)\hat{a}(t)\right)dt}|0\rangle = e^{\sum_j \left(\alpha_j \hat{a}_j^\dagger - \alpha_j^* \hat{a}_j\right)}|0\rangle = \prod_j |\alpha_j\rangle. \tag{2.19}$$

Here, $|0\rangle$ is shorthand notation for the state with zero photons in all modes, $\alpha_j = \int f_j^*(t)\alpha(t)dt$, and $|\{\alpha(t)\}\rangle$ is seen to be the direct product of single-mode coherent states independent of the choice of the mode functions $f_j(t)$. $|\{\alpha(t)\}\rangle$ is an eigenstate of $\hat{a}_j$ with eigenvalue α_j and an eigenstate of $\hat{a}(t)$ with eigenvalue $\alpha(t)$. We shall also use the word amplitude for $\alpha(t)$. We finally note that the inner product $\langle\beta_j|\alpha_j\rangle = \exp(-|\alpha_j|^2/2 - |\beta_j|^2/2 + \alpha_j\beta_j^*)$ between two different coherent states of the same mode is nonzero because $\hat{a}_j$ is not a hermitian operator. Coherent states can be produced by lasers, and we shall often take these states as our starting point.

The Wigner function

An alternative way to specify the state of light is to use Wigner functions. Wigner functions are analogues to classical phase space distributions, but since it is impossible to specify both position and momentum with infinite precision in quantum mechanics, the Wigner function may take negative values in limited regions of phase space. It is hence classified as a pseudo phase space distribution. If negative values occur, it signifies that the state is nonclassical. In the context of Wigner functions, the position and momentum of a light field mode are to be understood through the equivalence between the annihilation operator $\hat{a}_j$ and the step down operator of the one-dimensional quantum mechanical harmonic oscillator [23]. The (dimensionless) position and momentum operators of the jth light mode are thus defined as $\hat{x}_j = (\hat{a}_j + \hat{a}_j^\dagger)/\sqrt{2}$ and $\hat{p}_j = -i(\hat{a}_j - \hat{a}_j^\dagger)/\sqrt{2}$, respectively. The N-mode Wigner function may be calculated from the N-mode density operator

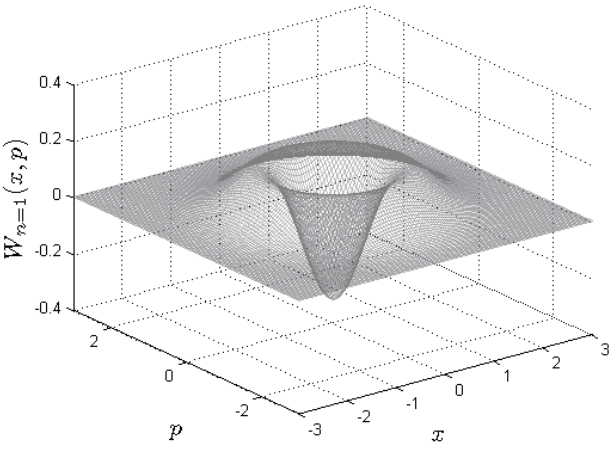

Figure 2.1: Wigner function of a single-photon state.

in (2.17) as [22]

$$W(x_1,p_1,x_2,p_2,\ldots,x_N,p_N) = \\ \left(\frac{1}{2\pi^2}\right)^N \int_{-\infty}^{\infty}\int_{-\infty}^{\infty}\cdots\int_{-\infty}^{\infty}\left(\prod_{j=1}^{N} e^{-i\sqrt{2}\eta_{i,j}x_j+i\sqrt{2}\eta_{r,j}p_j}\right) \\ \times \operatorname{Tr}\left(\left(\prod_{j=1}^{N} e^{i\sqrt{2}\eta_{i,j}\hat{x}_j-i\sqrt{2}\eta_{r,j}\hat{p}_j}\right)\rho\right)\prod_{j=1}^{N}\left(d\eta_{r,j}d\eta_{i,j}\right), \quad (2.20)$$

where x_j and p_j are the position and momentum quadrature variables of the jth mode, respectively. As an example, the Wigner function

$$W_{n=1}(x,p) = \pi^{-1}\left(2x^2+2p^2-1\right)e^{-x^2-p^2} \quad (2.21)$$

of a single-mode single-photon state $|\psi\rangle = |1\rangle$ is plotted in Fig. 2.1. Note that $W_{n=1}(0,0) = -\pi^{-1} < 0$.

A special class of states is the Gaussian states, which are represented by Gaussian Wigner functions

$$W(x_1,p_1,\ldots,x_N,p_N) = \frac{1}{\pi^N\sqrt{\det(V)}}\exp\left(-(y-\langle\hat{y}\rangle)^T V^{-1}(y-\langle\hat{y}\rangle)\right), \quad (2.22)$$

where $y = (x_1,p_1,\ldots,x_N,p_N)^T$ is a column vector of the quadrature variables, $\hat{y} = (\hat{x}_1,\hat{p}_1,\ldots,\hat{x}_N,\hat{p}_N)^T$ is a column vector of position and momentum operators of the light modes, and V is the $2N\times 2N$ covariance matrix, which is defined as $V = \langle(\hat{y}-\langle\hat{y}\rangle)(\hat{y}-\langle\hat{y}\rangle)^T\rangle + \langle(\hat{y}-\langle\hat{y}\rangle)(\hat{y}-\langle\hat{y}\rangle)^T\rangle^T$. It follows from (2.20) that the multimode coherent state (2.19) is a Gaussian state with $V = I$ and $\langle \hat{y} \rangle = \sqrt{2}(\mathrm{Re}(\alpha_1), \mathrm{Im}(\alpha_1), \ldots, \mathrm{Re}(\alpha_N), \mathrm{Im}(\alpha_N))^T$, where I is the $2N \times 2N$ identity matrix and N is the number of modes. Gaussian states are important because they are very common and because they are particularly easy to work with since they are defined in terms of a small number of variables.

2.3 Optical components

We next include optical components into our description. Optical components are devices, which are inserted into the pathways of the beams to accomplish specific operations. In this section, we describe the phase shifter, the wave plate, the beam splitter, and the polarizing beam splitter. Nonlinear crystals will be considered in Chap. 3, and we shall see later how these five basic components can be used to build a large number of more complex devices. Detectors will be discussed in Sec. 2.4.

We shall not be concerned with the precise properties of the fields inside the optical components, but only with the fields outside the components. We thus use an input-output formalism, where we only consider the relation between the fields before and after the interaction with a given component. We assume throughout that the bandwidth of the light fields is sufficiently narrow to ensure that the transformation can be regarded as being independent of frequency. It is then convenient to use the time-localized mode functions in (2.14) and regard a beam of light as a train of modes moving along with the speed of light. When one of the modes hits an optical component, we apply certain transformations either to the field operators of that mode, if we choose to work in the Heisenberg picture, or to the density operator or the Wigner function, if we choose to work in the Schrödinger picture.

The phase shifter

A phase shifter (PS), Fig. 2.2(a), changes the phase of a light field, and the interaction with the jth mode is associated with the unitary operator

$$U_{\mathrm{PS}}^{\hat{a}_j}(\phi) = e^{-i\phi \hat{a}_j^\dagger \hat{a}_j}. \tag{2.23}$$

In the Schrödinger picture, the phase shifter applies the transformation $\rho \to U_{\mathrm{PS}}^{\hat{a}_j}(\phi)\rho(U_{\mathrm{PS}}^{\hat{a}_j}(\phi))^\dagger$, and in the Heisenberg picture the field operator $\hat{a}'_j$ after the interaction is related to the field operator $\hat{a}_j$ before the interaction through the transformation

$$\hat{a}_j \to \hat{a}'_j = (U_{\mathrm{PS}}^{\hat{a}_j}(\phi))^\dagger \hat{a}_j U_{\mathrm{PS}}^{\hat{a}_j}(\phi) = \hat{a}_j e^{-i\phi}, \tag{2.24}$$

where we have used the Baker-Hausdorff lemma [23] in the last step. As the transformation of the field operator simply amounts to a basis transfor-

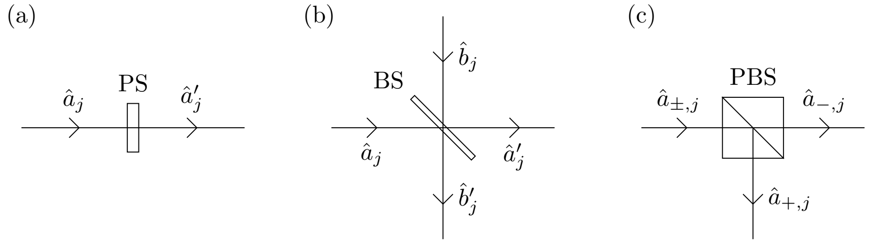

Figure 2.2: Input and output fields of (a) a phase shifter (PS), (b) a beam splitter (BS), and (c) a polarizing beam splitter (PBS).

mation, the phase shifter transforms Gaussian states into Gaussian states following the transformation

$$\langle \hat{y} \rangle \to S \langle \hat{y} \rangle, \quad V \to SVS^T, \tag{2.25}$$

where S is a block diagonal matrix consisting of the blocks S_1, S_2, …, S_N, where S_i is the 2×2 identity matrix if $i \neq j$ and

$$S_j = \begin{bmatrix} \cos(\phi) & \sin(\phi) \\ -\sin(\phi) & \cos(\phi) \end{bmatrix}. \tag{2.26}$$

A phase shifter may consist of a piece of material with a different refractive index than air or vacuum, but, in practice, the same effect can be obtained by adjusting the length of the path followed by the light beam by a fraction of a wavelength.

The wave plate

A wave plate (WP) is a piece of anisotropic material, for which the refractive index depends on the orientation of the wave plate and the polarization and propagation directions of the light field. Wave plates can be used for changing the relative phase of two spatially overlapping modes with different polarizations and for transforming between, for instance, linearly and circularly polarized light. The half wave plate (HWP) is a special case, which changes the phase of one polarization component by π relative to the phase of the other polarization component.

The beam splitter

A beam splitter (BS), Fig. 2.2(b), is a partially transmitting mirror, which acts on two modes at a time. The transformation that can occur within an ideal beam splitter is transfer of one photon from one of the input modes $\hat{a}_j$ or $\hat{b}_j$ to the other, and, in the Schrödinger picture, the transformation takes the form $\rho \to U_{\mathrm{BS}}^{\hat{a}_j\hat{b}_j}(t_{\mathrm{BS}}^2)\rho(U_{\mathrm{BS}}^{\hat{a}_j\hat{b}_j}(t_{\mathrm{BS}}^2))^\dagger$, where [24]

$$U_{\mathrm{BS}}^{\hat{a}_j\hat{b}_j}(t_{\mathrm{BS}}^2) = \exp\left(i\tan^{-1}\left(\sqrt{(1-t_{\mathrm{BS}}^2)/t_{\mathrm{BS}}^2}\right)\left(\hat{a}_j^\dagger\hat{b}_j + \hat{a}_j\hat{b}_j^\dagger\right)\right). \tag{2.27}$$

The coefficient in the exponent is expressed in terms of the transmissivity t_{BS}^2 of the beam splitter, which is apparent if the transformation is written in the Heisenberg picture

$$\hat{a}_j \to \hat{a}_j' = (U_{\mathrm{BS}}^{\hat{a}_j\hat{b}_j}(t_{\mathrm{BS}}^2))^\dagger\hat{a}_j U_{\mathrm{BS}}^{\hat{a}_j\hat{b}_j}(t_{\mathrm{BS}}^2) = t_{\mathrm{BS}}\hat{a}_j + ir_{\mathrm{BS}}\hat{b}_j, \tag{2.28a}$$

$$\hat{b}_j \to \hat{b}_j' = (U_{\mathrm{BS}}^{\hat{a}_j\hat{b}_j}(t_{\mathrm{BS}}^2))^\dagger\hat{b}_j U_{\mathrm{BS}}^{\hat{a}_j\hat{b}_j}(t_{\mathrm{BS}}^2) = t_{\mathrm{BS}}\hat{b}_j + ir_{\mathrm{BS}}\hat{a}_j, \tag{2.28b}$$

where $r_{\mathrm{BS}}^2 = 1 - t_{\mathrm{BS}}^2$ is the reflectivity of the beam splitter. We shall always take r_{BS} and t_{BS} to be nonnegative real numbers. We note that (2.28) involves a specific choice of phases (see [25] for the general case), but this is of little practical importance as additional phase factors can be absorbed into a small change of the path lengths as explained above. The modes $\hat{a}_j$ and $\hat{b}_j$ need not be time-localized modes, but the mode functions must be identical when we use discrete modes. We shall use the term 50:50 beam splitter for a beam splitter with $r_{\mathrm{BS}}^2 = t_{\mathrm{BS}}^2 = 1/2$.

Beam splitters transform Gaussian states into Gaussian states following (2.25) with the nontrivial part of S given by

$$S_j = \begin{bmatrix} t_{\mathrm{BS}} & 0 & 0 & -r_{\mathrm{BS}} \\ 0 & t_{\mathrm{BS}} & r_{\mathrm{BS}} & 0 \\ 0 & -r_{\mathrm{BS}} & t_{\mathrm{BS}} & 0 \\ r_{\mathrm{BS}} & 0 & 0 & t_{\mathrm{BS}} \end{bmatrix}. \tag{2.29}$$

Coherent states are particularly easy to handle since two independent single-mode coherent states with amplitudes α and β transform into two independent single-mode coherent states with amplitudes $t_{\mathrm{BS}}\alpha + ir_{\mathrm{BS}}\beta$ and $t_{\mathrm{BS}}\beta + ir_{\mathrm{BS}}\alpha$.

The polarizing beam splitter

A polarizing beam splitter (PBS), Fig. 2.2(c), transmits one polarization component (denoted '−' in the figure) of the incident beam and reflects the other (denoted '+' in the figure). This allows us to spatially separate and combine light beams with orthogonal polarizations such that we have the opportunity to apply a given transformation simultaneously to both polarization components or only one of them as we like.

2.4 Measurements and loss

Measurements are important in order to extract information about the outcome of an experiment and as a tool to manipulate the state of quantum systems. Here we consider the avalanche photodiode (APD) and the balanced homodyne detector.

Avalanche photodiodes

Avalanche photodiodes are designed to detect single photons. When a light field enters into an APD, it travels through a medium, which is able to absorb photons. As above, we assume that the bandwidth of the field is sufficiently narrow to ensure that the absorption efficiency is practically the same for all relevant frequencies. Photon absorption is accompanied by excitation of an electron from a bound state to a free state or a conduction band state. This signal is amplified, and the resulting photocurrent is measured.

There are a number of models describing the action of an APD in the literature, which apply under different circumstances. In the click detector model [26], the interaction between the light field and the detector is treated in time-dependent perturbation theory. For this to be valid, the intensity of the detected beam must be low, but the detection efficiency may be high if the absorbing medium is thick. Assuming unit detection efficiency, the probability to observe a click in the infinitesimal time interval from $t_j - \Delta t/2$ to $t_j + \Delta t/2$ is $\mathrm{Tr}(\hat{a}(t_j)\rho\hat{a}^\dagger(t_j))\Delta t$. If the detector clicks, the density operator is transformed according to

$$\rho \to \frac{\hat{a}(t_j)\rho\hat{a}^\dagger(t_j)}{\mathrm{Tr}(\hat{a}(t_j)\rho\hat{a}^\dagger(t_j))}, \qquad \text{(click detector)} \tag{2.30}$$

and if it does not click, the observed mode is projected onto the vacuum state, $\rho \to \langle 0_j|\rho|0_j\rangle \otimes |0_j\rangle\langle 0_j| / \mathrm{Tr}(\langle 0_j|\rho|0_j\rangle \otimes |0_j\rangle\langle 0_j|)$. Since $\hat{a}_j = \hat{a}(t_j)\sqrt{\Delta t}$ is practically equivalent to the operator $|0_j\rangle\langle 1_j|$ for weak fields, the final state of the observed mode is the vacuum state in both cases, and we can omit this mode in writing the state.

If the detection efficiency η is not unity, we may as well say that part of the light is observed with perfect efficiency, while the remaining part is not observed at all. A general way to account for linear photon losses is to insert a fictitious beam splitter into the relevant beam or in front of the relevant component, which is then assumed to be lossless [27]. The reflectivity of the beam splitter is set to $1 - \eta$ (which is the number of lost photons per incident photon), and the second input to the beam splitter is a vacuum state. The reflected field leaves the setup, and we anticipate that it will never return and interfere coherently with the remaining light fields. When this is the case, we can reduce the loss to a classical uncertainty by applying the trace operation to the lost field. For a Gaussian state, this is done simply by erasing the corresponding rows and columns of V and the corresponding elements of $\langle\hat{y}\rangle$, and for a general state we integrate the Wigner function over the position and momentum quadratures of the mode. It is sometimes useful to imagine that the lost field is subjected to a projective measurement in an arbitrary basis, but with an unknown measurement result, which is mathematically equivalent. Loss is often accompanied by a suppression of quantum interferences, and we shall refer to this phenomenon as decoherence.

The (unit efficiency) on/off detector model [27] is often used when considering detection of a single-mode field (i.e., all modes of the detected beam except one are in the vacuum state). It is assumed that the detector precisely absorbs photons with the spectral properties of the incoming mode, but if the amplification process (the avalanche) has already been initiated by one photon, the detector will not respond to further photons in the incoming mode. Consequently, there are only two possible detection outcomes: the 'off' detection, where no photons are observed, $\rho \rightarrow \langle 0_j|\rho|0_j\rangle / \operatorname{Tr}(\langle 0_j|\rho|0_j\rangle)$, and the 'on' detection, where at least one photon is detected,

$$\rho \rightarrow \frac{\sum_{n_j=1}^{\infty}\langle n_j|\rho|n_j\rangle}{\operatorname{Tr}(\sum_{n_j=1}^{\infty}\langle n_j|\rho|n_j\rangle)}. \qquad \text{(on/off detector)} \qquad (2.31)$$

The sum over n_j is an average over all states that are compatible with an 'on' detection event, and we have traced out the detected mode, since all photons in this mode are absorbed or lost in the detection process. The probability to get an 'off' detection is $\operatorname{Tr}(\langle 0_j|\rho|0_j\rangle)$.

For many applications it is preferable to have a photon number state resolving detector. Such a detector counts the number of photons in the observed mode and transforms the density operator as

$$\rho \rightarrow \frac{\langle n_j|\rho|n_j\rangle}{\operatorname{Tr}(\langle n_j|\rho|n_j\rangle)}, \qquad \text{(photon number state detector)} \qquad (2.32)$$

where n_j is the number of detected photons and $\operatorname{Tr}(\langle n_j|\rho|n_j\rangle)$ is the probability to observe n_j photons. One proposal for building a photon number state resolving detector is to divide the detected beam into several beams and observe each of these with an APD (see, for instance, [28] for an implementation). Even though progress is being made, perfect photon number state resolving detection is very difficult to achieve in practice because it requires lossless conditions. (The efficiency is, e.g., about 33 % in [28].)

Balanced homodyne detection

Another important detector type is the balanced homodyne detector [29]. The detector consists of a 50:50 beam splitter and two photodetectors as shown in Fig. 2.3(a). The beam splitter mixes the input beam with a local oscillator, which is a light beam in a coherent state with large amplitude and a fixed phase relative to the detected field. Each photodetector produces a photocurrent, which is proportional to the number of photons hitting the detector, and the component labeled with a minus sign in the figure

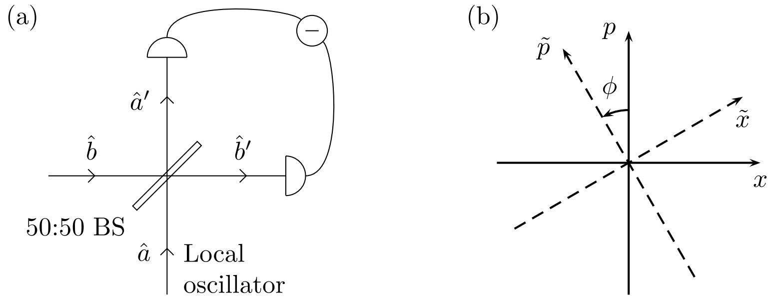

Figure 2.3: (a) Balanced homodyne detector and (b) coordinate transformation in phase space.

computes the difference between the two photocurrents. For simplicity, we consider detection of a single-mode field. Using the notation in the figure, the measured operator is proportional to

$$|\alpha|^{-1}(\hat{b}'^{\dagger}\hat{b}' - \hat{a}'^{\dagger}\hat{a}') = i|\alpha|^{-1}(\hat{a}\hat{b}^{\dagger} - \hat{a}^{\dagger}\hat{b}), \tag{2.33}$$

where α is the amplitude of the local oscillator. When $|\alpha| \to \infty$, the local oscillator can be treated classically $\hat{a} \to \alpha = |\alpha|e^{i\phi}$, and (2.33) reduces to

$$ie^{i\phi}\hat{b}^{\dagger} - ie^{-i\phi}\hat{b} = -\sqrt{2}\sin(\phi)\hat{x} + \sqrt{2}\cos(\phi)\hat{p} \equiv \sqrt{2}\hat{\tilde{p}}. \tag{2.34}$$

If we define a new set of quadrature variables, Fig. 2.3(b), as

$$\tilde{x} = \cos(\phi)x + \sin(\phi)p, \tag{2.35a}$$

$$\tilde{p} = -\sin(\phi)x + \cos(\phi)p, \tag{2.35b}$$

it can be shown [18] that the probability density $P(\tilde{p})$ to measure a given eigenvalue of $\hat{\tilde{p}}$ is the integral of the Wigner function in the direction perpendicular to the $\tilde{p}$-axis

$$P(\tilde{p}) = \int_{-\infty}^{\infty} W(\tilde{x}\cos(\phi) - \tilde{p}\sin(\phi), \tilde{p}\cos(\phi) + \tilde{x}\sin(\phi))d\tilde{x}. \tag{2.36}$$

If the experiment is repeated several times with the input mode prepared in the same state each time, it is thus possible to measure $P(\tilde{p})$, and if this is done for several values of ϕ, the Wigner function of the state of the input mode can be reconstructed from the data [29]. One important application of homodyne detection is to experimentally verify the expected output of a state preparation protocol. If a continuous beam is measured with a local oscillator in a continuous coherent state, we instead obtain a time series of quadrature values from which the measured quadrature value of an arbitrarily shaped mode can also be extracted as the integral of the product of the measured date and the complex conjugate of the mode function [30]. The efficiency of the photodetectors can be close to unity (e.g., 0.98 in [31]).

Chapter 3

The optical parametric oscillator

The optical parametric oscillator is a light source that consists of a nonlinear crystal inside an optical cavity. When a laser beam pumps the crystal, pairs of photons are generated in a process called parametric down conversion (PDC), and these photons make up the OPO output field. The purpose of the cavity is to enhance the PDC process by sending the generated photons through the crystal several times. The light generated by an OPO is very interesting by itself, and the OPO has been studied in several papers and textbooks (see e.g. [26, 32, 33, 34]) with the primary aim of investigating the possibilities to generate light with a reduced variance of one of the quadrature operators relative to the variance of the quadrature operators of the vacuum state (i.e., squeezed light). Our aim is to go a step further and study how measurements can be used for transforming the OPO output, which is Gaussian, into various non-Gaussian states of light.

Before doing so, however, we need to develop a suitable model of the OPO as the treatments in the above references are not sufficiently general for our purposes. The primary problem is that the pump field is assumed to be monochromatic. An investigation of the case of a periodically varying pump field has been put forward in [35], but we would like to allow an arbitrary temporal shape of the pump field such that we can consider pulsed pump fields and investigate the significance of changing the duration of the pulses. A second significant difference is that we do not restrict our analysis to one or two cavity modes, but include all longitudinal modes of the cavity. This is relevant since we would like to consider pump pulses that are not necessarily long compared to the length of the cavity. In addition, it leads to the interesting property that we can remove the cavity in a continuous way, and the model is thus suitable to investigate the transition between an OPO and single-pass PDC. We shall, however, mostly consider the OPO limit in the following chapters and make approximations appropriate for the OPOs used in the experiments in [30, 31, 36]. Multimode analyses of single-pass PDC with pulsed pump fields are available in [37, 38] (see also [39] for a multimode analysis of the squeezing properties of solitons in optical fibers).

We start with a brief description of the PDC process in Sec. 3.1. Based on [IV][1], we then present our OPO model in Sec. 3.2. Finally, in Sec. 3.3, we specialize to the case of a monochromatic pump field in order to get a first idea of the properties of the OPO output field and to show how our findings reduce to those of the above references in the appropriate limit.

3.1 Parametric down conversion

The core element of an OPO is a nonlinear crystal, which is able to convert a single photon with angular frequency ω into two photons with angular frequencies ω_1 and ω_2, respectively, where $\omega = \omega_1 + \omega_2$ due to energy conservation. This process is represented by the operator $\hat{a}^\dagger(\omega_1)\hat{a}^\dagger(\omega_2)\hat{a}(\omega_1+\omega_2)$. Due to the large difference in frequency, the pump field providing the initial photons is completely distinguishable from the down converted field. We can assume that the pump field is sufficiently strong to be treated classically, $\hat{a}(\omega_1+\omega_2) \to g(\omega_1+\omega_2)$, where $g(\omega)$ is the amplitude of the pump field in frequency domain, and neglect pump depletion (for the OPO in [30], for instance, the ratio between the flux of pump photons and the flux of down converted photons is roughly of order 10^7). The unitary operator describing the transformation that occurs when the whole beam passes through the crystal then takes the form (excluding phase shifts, which can be absorbed into the effective path length as usually, and loss, which will be taken into account separately)

$$U_{\mathrm{sq,I}} = \exp\left(-\frac{i}{2}\left(\iint \chi_0 g(\omega_1+\omega_2)\hat{a}^\dagger(\omega_1)\hat{a}^\dagger(\omega_2)d\omega_1 d\omega_2 + h.c.\right)\right). \quad (3.1)$$

The parameter χ_0 describes the strength of the process and depends on the second order susceptibility of the crystal, the length of the crystal, and the phase matching conditions (see [21] for details). The subscript 'I' refers to type I PDC, which means that both photons in the generated pairs have the same polarization.

In [30], the bandwidth of the down converted photons is of order 10^{12} Hz, but the resonance properties of the OPO cavity and external filters select a narrow range of frequencies, and only frequencies within a bandwidth of about 9 MHz (full width at half maximum (FWHM)) are actually used in the experiment. It thus seems reasonable to assume that the down conversion efficiency is approximately the same for all frequencies that are not filtered away or suppressed. This allows us to move χ_0 outside the integrals, and

---

[1] Copyright (2007) by the American Physical Society.

after conversion to the time domain, we obtain

$$U_{\mathrm{sq,I}} = \exp\left(-\frac{i}{2}\left(\int \chi(t)\hat{a}^\dagger(t)\hat{a}^\dagger(t)dt + \int \chi^*(t)\hat{a}(t)\hat{a}(t)dt\right)\right), \tag{3.2}$$

where $\chi(t) \equiv \sqrt{2\pi}\chi_0 g(t)$ and $g(t)$ is the Fourier transform of $g(\omega)$. If we rewrite the time integrals into sums over time-localized modes, $U_{\mathrm{sq,I}}$ factorizes into a product of operators

$$U_{\mathrm{sq,I}}^{\hat{a}_j} = \exp\left(-\frac{i}{2}\left(\chi(t_j)(\hat{a}_j^\dagger)^2 + \chi^*(t_j)\hat{a}_j^2\right)\right) \tag{3.3}$$

acting on a single mode. When mode j passes through the crystal,

$$\hat{a}_j \to (U_{\mathrm{sq,I}}^{\hat{a}_j})^\dagger \hat{a}_j U_{\mathrm{sq,I}}^{\hat{a}_j} = \cosh(|\chi(t_j)|)\hat{a}_j - ie^{i\phi(t_j)}\sinh(|\chi(t_j)|)\hat{a}_j^\dagger \tag{3.4}$$

in the Heisenberg picture, where $\chi(t_j) \equiv |\chi(t_j)|e^{i\phi(t_j)}$. The transformation is linear in the field operators, and it follows from (2.20) that the crystal transforms Gaussian states into Gaussian states following (2.25) with

$$S_j = \begin{bmatrix} \cosh(|\chi_j|) + \sinh(|\chi_j|)\sin(\phi_j) & -\sinh(|\chi_j|)\cos(\phi_j) \\ -\sinh(|\chi_j|)\cos(\phi_j) & \cosh(|\chi_j|) - \sinh(|\chi_j|)\sin(\phi_j) \end{bmatrix}, \tag{3.5}$$

where $\chi_j \equiv \chi(t_j)$ and $\phi_j \equiv \phi(t_j)$.

To establish the connection between PDC and squeezing, we note that the covariance matrix of a mode, which is initially in the vacuum state, is transformed from the 2×2 identity matrix into a diagonal matrix with diagonal $(e^{-2|\chi_j|}, e^{2|\chi_j|})^T$ when $\phi_j = -\pi/2$, i.e., the variance of the quadrature operator $\hat{x}$ is reduced below the vacuum level, while the variance of the conjugate quadrature operator $\hat{p}$ is increased above the vacuum level in order to avoid violation of Heisenberg's uncertainty relation $\mathrm{var}(\hat{x})\,\mathrm{var}(\hat{p}) \geq 1/4$. The resulting state is a single-mode squeezed vacuum state.

3.2 Correlation functions of the optical parametric oscillator

We next consider the OPO in its entirety as illustrated in Fig. 3.1. For simplicity, we assume that the cavity mirrors are completely transmitting at the frequencies of the pump field. Light field losses inside the cavity are taken into account as in Sec. 2.4. Losses may occur at different positions, but we assume that all losses occur at a point on the path from the crystal to BS_1, which is the worst case situation.

Our aim is to express the output field operator $\hat{b}(t)$ in terms of the input field operator $\hat{a}(t)$ in the Heisenberg picture. Referring to Eqs. (2.28) and

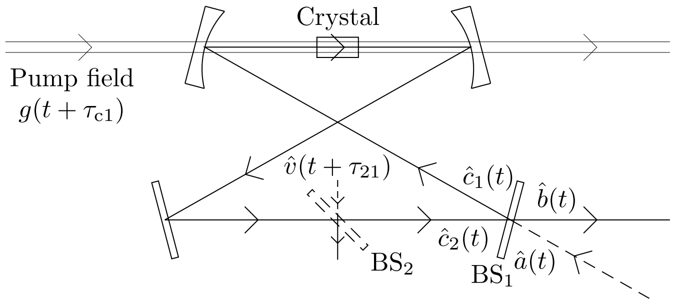

Figure 3.1: Model of an optical parametric oscillator. The classical field $g(t+\tau_{c1})$, which is assumed to pass unhindered through the cavity mirrors, pumps the nonlinear crystal, and the generated photons circulate in the cavity until they are eventually transmitted through the beam splitter BS$_1$. The input field $\hat{a}(t)$ is in the vacuum state. The fictitious beam splitter BS$_2$ and the field $\hat{v}(t+\tau_{21})$, which is also in the vacuum state, are included to account for intracavity losses. τ_{c1} is the light traveling time from the crystal to BS$_1$, and τ_{21} is the light traveling time from BS$_2$ to BS$_1$.

(3.4) and the notation in Fig. 3.1, we find

$$\hat{b}(t) = t_1\hat{c}_2(t) + ir_1\hat{a}(t), \quad \hat{c}_1(t) = t_1\hat{a}(t) + ir_1\hat{c}_2(t), \tag{3.6a}$$

$$\hat{c}_2(t) = -it_2\Big(\cosh(|\chi(t)|)\hat{c}_1(t-\tau) + ie^{i\phi(t)}\sinh(|\chi(t)|)\hat{c}_1^\dagger(t-\tau)\Big) + ir_2\hat{v}(t), \tag{3.6b}$$

where $t_i^2 = 1 - r_i^2$ is the transmissivity of BS$_i$, τ is the round trip time of light in the cavity, and we have included a phase factor of i for each mirror because a mirror can be regarded as a beam splitter with zero transmissivity. To simplify the notation, we have chosen the time arguments of g and $\hat{v}$ such that $g(t)$ is the amplitude of the pump field at the position of the crystal at time $t-\tau_{c1}$ and $\hat{v}(t)$ is the field annihilation operator of the field that hits BS$_2$ at time $t-\tau_{21}$.

We would like the squeezing operations at times separated by τ to add up in phase, which amounts to the requirement $\phi(t) = \phi(t-\tau)$ for all t. When this is fulfilled, it is always the same quadrature that is squeezed at times t, $t\pm\tau$, $t\pm 2\tau$, …, and the solution of (3.6) takes the form

$$\begin{aligned}
\hat{b}(t) = ir_1\hat{a}(t) - it_1^2\sum_{n=0}^{\infty} r_1^n t_2^{n+1}\Bigg(&\cosh\left(\sum_{k=0}^{n}|\chi(t-k\tau)|\right)\hat{a}(t-(n+1)\tau) \\
&+ ie^{i\phi(t)}\sinh\left(\sum_{k=0}^{n}|\chi(t-k\tau)|\right)\hat{a}^\dagger(t-(n+1)\tau)\Bigg) + it_1r_2\hat{v}(t) \\
&+ it_1r_2\sum_{n=0}^{\infty}(r_1t_2)^{n+1}\Bigg(\cosh\left(\sum_{k=0}^{n}|\chi(t-k\tau)|\right)\hat{v}(t-(n+1)\tau)
\end{aligned}$$

$$+ ie^{i\phi(t)} \sinh\left(\sum_{k=0}^{n} |\chi(t-k\tau)|\right) \hat{v}^\dagger(t-(n+1)\tau)\Bigg). \quad (3.7)$$

The first term represents the part of the input field that is reflected directly into the output beam, and the second term is a sum over terms representing the field that enters into the cavity at time $t-(n+1)\tau$ and travels $n+1$ rounds in the cavity before it leaves through BS_1 at time t. Similarly, the third term represents the part of the field entering at BS_2, which is transmitted out of the cavity the first time it hits BS_1, and the fourth term is a sum over terms representing the part of the field entering at BS_2, which is reflected $n+1$ times at BS_1 before it is transmitted.

The output field from the OPO is Gaussian since all the above transformations preserve the Gaussian nature of the input fields. To specify the state of the output field completely, it is thus sufficient to specify $\langle\hat{b}(t)\rangle$ (or $\langle\hat{b}_j\rangle$) and the two-time correlation functions $\langle\hat{b}^\dagger(t)\hat{b}(t')\rangle$ and $\langle\hat{b}(t)\hat{b}(t')\rangle$ (or $\langle\hat{b}_j^\dagger\hat{b}_k\rangle$ and $\langle\hat{b}_j\hat{b}_k\rangle$), which can be calculated straightforwardly from (3.7) (note that the expectation values are calculated with respect to the vacuum input states since we are using the Heisenberg picture). $\langle\hat{b}(t)\rangle = 0$,

$$\begin{aligned}\langle\hat{b}^\dagger(t)\hat{b}(t')\rangle = t_1^2t_2^2(1-r_1^2t_2^2)\Bigg(&\sum_{q=1}^{\infty}\sum_{m=0}^{\infty}(r_1t_2)^{q+2m}\sinh\left(\sum_{k=0}^{m}|\chi(t-k\tau)|\right)\\ &\times\sinh\left(\sum_{k=0}^{q+m}|\chi(t'-k\tau)|\right)\delta(t-t'+q\tau)+\sum_{q=0}^{\infty}\sum_{m=0}^{\infty}(r_1t_2)^{q+2m}\\ &\times\sinh\left(\sum_{k=0}^{q+m}|\chi(t-k\tau)|\right)\sinh\left(\sum_{k=0}^{m}|\chi(t'-k\tau)|\right)\delta(t-t'-q\tau)\Bigg) \quad (3.8)\end{aligned}$$

and

$$\begin{aligned}&\langle\hat{b}(t)\hat{b}(t')\rangle =\\ &-ie^{i\phi(t)}t_1^2t_2^2(1-r_1^2t_2^2)\Bigg(\sum_{q=1}^{\infty}\sum_{m=0}^{\infty}(r_1t_2)^{q+2m}\sinh\left(\sum_{k=0}^{m}|\chi(t-k\tau)|\right)\\ &\times\cosh\left(\sum_{k=0}^{q+m}|\chi(t'-k\tau)|\right)\delta(t-t'+q\tau)+\sum_{q=0}^{\infty}\sum_{m=0}^{\infty}(r_1t_2)^{q+2m}\\ &\times\cosh\left(\sum_{k=0}^{q+m}|\chi(t-k\tau)|\right)\sinh\left(\sum_{k=0}^{m}|\chi(t'-k\tau)|\right)\delta(t-t'-q\tau)\Bigg). \quad (3.9)\end{aligned}$$

We shall investigate the implications of these equations in Chap. 5, but for now we specialize to the case of a monochromatic pump field, which is on resonance with the cavity, to gain some intuition about the operation of the OPO in a simpler setting.

3.3 Monochromatic pump field

For a monochromatic pump field on resonance with the cavity, we have $\chi(t) = |\chi|e^{-2i\omega_0 t + i\phi_0}$, where $|\chi|$ is time-independent and $2\omega_0 = 2\pi N/\tau$ for some positive integer N. This expression fulfils $\phi(t) = \phi(t-\tau)$. In order to ensure convergence of the sums in (3.8) and (3.9), we require $r_1 t_2 e^{|\chi|} < 1$, which is the below threshold condition and the relevant regime for our purposes. Above threshold, a semiclassical analysis shows that the steady state solution with a vanishing expectation value of the field operators of the cavity field is no longer stable, and instead solutions with nonzero cavity field amplitudes appear [40, 41].

To explore the properties of the output field from the OPO, we compute the Fourier transform of (3.7)

$$\begin{aligned}\hat{b}(\omega) = {}& i\left(r_1 - t_1^2 t_2 G_+(\omega)/2\right)\hat{a}(\omega) + e^{i\phi_0} t_1^2 t_2 G_-(\omega)\hat{a}^\dagger(2\omega_0 - \omega)/2 \\ &+ i t_1 r_2 \left(1 + r_1 t_2 G_+(\omega)/2\right)\hat{v}(\omega) - e^{i\phi_0} t_1 r_1 t_2 r_2 G_-(\omega)\hat{v}^\dagger(2\omega_0 - \omega)/2, \quad (3.10)\end{aligned}$$

where

$$G_\pm(\omega) \equiv \frac{e^{|\chi| + i\omega\tau}}{1 - r_1 t_2 e^{|\chi| + i\omega\tau}} \pm \frac{e^{-|\chi| + i\omega\tau}}{1 - r_1 t_2 e^{-|\chi| + i\omega\tau}}, \qquad (3.11)$$

and obtain

$$\begin{aligned}\langle \hat{b}^\dagger(\omega)\hat{b}(\omega')\rangle = {}& t_1^2 t_2^2 (1 - r_1^2 t_2^2)\sinh^2(|\chi|)\delta(\omega - \omega')/\big(1 + 4r_1^2 t_2^2\cosh^2(|\chi|) \\ &+ r_1^4 t_2^4 + 2 r_1 t_2\left(r_1 t_2 \cos(2\omega\tau) - 2(1 + r_1^2 t_2^2)\cosh(|\chi|)\cos(\omega\tau)\right)\big) \\ &\equiv S_{\mathrm{OPO}}(\omega)\delta(\omega - \omega'). \quad (3.12)\end{aligned}$$

From this we observe that the spectrum $S_{\mathrm{OPO}}(\omega)$ of the output field is a periodic function of ω with maxima at the cavity resonance frequencies $\omega = n2\pi/\tau$, where n is any positive integer. The free spectral range (FSR) $2\pi/\tau$ of the cavity is inversely proportional to the length of the cavity, and the distance between the maxima is thus large, if the cavity is small. In addition, the ratio $(1+r_1 t_2 e^{|\chi|})^2(1+r_1 t_2 e^{-|\chi|})^2/((1-r_1 t_2 e^{|\chi|})^2(1-r_1 t_2 e^{-|\chi|})^2)$ between the maximum and minimum values of $S_{\mathrm{OPO}}(\omega)$ is large if we choose a value of $r_1 t_2$ close to unity and a value of $|\chi|$ close to zero (without violating $r_1 t_2 e^{|\chi|} < 1$). In this limit, $S_{\mathrm{OPO}}(\omega)$ consists of well-separated peaks as shown in Fig. 3.2 (the dotted line), where we assume N to be even such that ω_0 is a resonance frequency of the cavity. Since the pump field is monochromatic, we know that a photon with frequency $\omega_0 + \delta\omega$ has also been created if we detect a photon with frequency $\omega_0 - \delta\omega$ in the output. In particular, we may have $\delta\omega = m\Delta\omega$, where m is an integer and $\Delta\omega$ is the FSR of the OPO cavity, in which case the two photons belong to the peaks separated by $\pm m$ FSRs from the peak at ω_0. If we use a frequency filter with a bandwidth, which is broad compared to the width of the peaks, but narrow compared to the FSR, we can thus operate the OPO in two

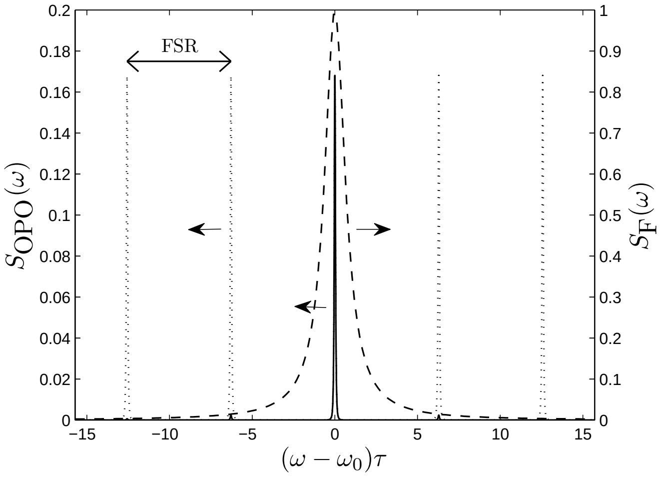

Figure 3.2: The spectrum $S_{\mathrm{OPO}}(\omega)$ of the output from the OPO (defined in Eq. (3.12)) is shown as a dotted line and the free spectral range is indicated. The dashed line is the spectral shape $S_{\mathrm{F}}(\omega)$ of the filter in Eq. (3.17) with $\omega_0' = \omega_0$, and the solid line is the spectrum of the output after filtering, i.e., the product of $S_{\mathrm{OPO}}(\omega)$ and $S_{\mathrm{F}}(\omega)$. The parameters are $|\chi| = 0.014$, $\tau = 2.7$ ns, $t_1^2 = 0.127$, and $r_2^2 = 0.004$ for the OPO and $\kappa_F = 2\pi \times 45$ MHz for the filter (i.e., the same parameters as in Chap. 5).

different ways. We can either select the peak at ω_0, which is referred to as a degenerate OPO, or we can select the peaks at $\omega_0 \pm m\Delta\omega$, $m \neq 0$, which is referred to as a nondegenerate OPO.

The degenerate OPO

From a theoretical point of view, we can remove all the modes that are filtered away by taking the limit, where the FSR goes to infinity, $2\pi/\tau \to \infty$, while the contributions $\kappa_1 \equiv t_1^2/\tau$ and $\kappa_2 \equiv r_2^2/\tau$ to the cavity decay rate $\kappa_1 + \kappa_2$ and the squeezing parameter $\epsilon \equiv |\chi|/\tau$ stay fixed. For the case of a degenerate OPO, we can thus obtain simplified two-time correlation functions if we Taylor expand $\langle \hat{b}^\dagger(\omega)\hat{b}(\omega')\rangle$ and $\langle \hat{b}(\omega)\hat{b}(\omega')\rangle$ to lowest order in τ around ω_0 and Fourier transform, which leads to

$$\langle \hat{b}^\dagger(t)\hat{b}(t')\rangle = \frac{\kappa_1}{\kappa_1+\kappa_2}\frac{\lambda^2-\mu^2}{4}\left(\frac{e^{-\mu|t-t'|}}{2\mu} - \frac{e^{-\lambda|t-t'|}}{2\lambda}\right)e^{i\omega_0(t-t')}, \tag{3.13a}$$

$$\langle \hat{b}(t)\hat{b}(t')\rangle = \frac{\kappa_1}{\kappa_1+\kappa_2}\frac{\lambda^2-\mu^2}{4}\left(\frac{e^{-\mu|t-t'|}}{2\mu} + \frac{e^{-\lambda|t-t'|}}{2\lambda}\right)e^{-i\omega_0(t+t')}, \tag{3.13b}$$

where $\lambda \equiv (\kappa_1+\kappa_2)/2+\epsilon$, $\mu \equiv (\kappa_1+\kappa_2)/2-\epsilon$, and we have chosen $\phi_0 = \pi/2$. This result is precisely the correlation functions derived in [26] for a single mode cavity. The below threshold condition requires $\epsilon/(\kappa_1+\kappa_2) < 1/2$.

The nondegenerate OPO

For the nondegenerate OPO, we define two operators $\hat{b}_\pm(\omega)$, which are the Taylor expansions of (3.10) around $\omega_0 \pm m\Delta\omega$. In this way, $\hat{b}_\pm(\omega)$ represents the field belonging to the peak at $\omega_0 \pm m\Delta\omega$. As the overlap between these peaks is considered to be zero, $\hat{b}_+(\omega)$ and $\hat{b}_-(\omega)$ are effectively independent fields with $[\hat{b}_+(\omega), \hat{b}_-^\dagger(\omega')] = 0$. Defining $\hat{b}_\pm(t)$ as the Fourier transform of $\hat{b}_\pm(\omega)$, we find $\langle \hat{b}_\pm(t)\rangle = 0$ and

$$\langle \hat{b}_\pm^\dagger(t)\hat{b}_\mp(t')\rangle = \langle \hat{b}_\pm(t)\hat{b}_\pm(t')\rangle = 0, \tag{3.14a}$$

$$\langle \hat{b}_\pm^\dagger(t)\hat{b}_\pm(t')\rangle = \frac{\kappa_1}{\kappa_1+\kappa_2}\frac{\lambda^2-\mu^2}{4}\left(\frac{e^{-\mu|t-t'|}}{2\mu} - \frac{e^{-\lambda|t-t'|}}{2\lambda}\right)e^{i(\omega_0 \pm m\Delta\omega)(t-t')}, \tag{3.14b}$$

$$\langle \hat{b}_\pm(t)\hat{b}_\mp(t')\rangle = \frac{\kappa_1}{\kappa_1+\kappa_2}\frac{\lambda^2-\mu^2}{4}\left(\frac{e^{-\mu|t-t'|}}{2\mu} + \frac{e^{-\lambda|t-t'|}}{2\lambda}\right) \times e^{-i(\omega_0 \pm m\Delta\omega)t}e^{-i(\omega_0 \mp m\Delta\omega)t'}, \tag{3.14c}$$

for the nondegenerate OPO.

In fact, there is also a third mode of operation, where the two photons in a pair are generated with opposite polarizations, which is referred to as type II PDC. In this case, the unitary operator (3.3) is replaced by

$$U_{\mathrm{sq,II}}^{\hat{a}_{\pm,j}} = \exp\left(-i\left(\chi^*(t_j)\hat{a}_{+,j}\hat{a}_{-,j} + \chi(t_j)\hat{a}_{+,j}^\dagger\hat{a}_{-,j}^\dagger\right)\right), \tag{3.15}$$

where '+' and '−' denote the two polarizations. Following the same steps as above, it turns out that the one- and two-time correlation functions of the output fields $\hat{b}_\pm(t)$ are the same as for the type I nondegenerate OPO (with $\epsilon \equiv |\chi|/\tau$ as before), except that $m = 0$ when we Taylor expand around ω_0 for both fields. For a discussion of the possibilities to fulfil the resonance conditions for type I and type II PDC in a cavity when differences in phase matching conditions are taken into account and an experimental investigation of the output fields for the former case see [42].

Filtering

A more accurate alternative to the above procedure is to explicitly include a frequency filter in the modeling. A frequency filter may consist of an empty cavity as in Fig. 3.3. The filter transmits frequencies that are close to one of the cavity resonances, whereas frequencies far from resonances are reflected at the input mirror. The round trip time τ_{F} of light in the filter cavity is chosen to be smaller than τ to obtain a larger FSR of the filter than of the OPO. As far as possible, it should also be avoided that an integer multiples of FSRs of the filter approximately coincides with an integer multiples of

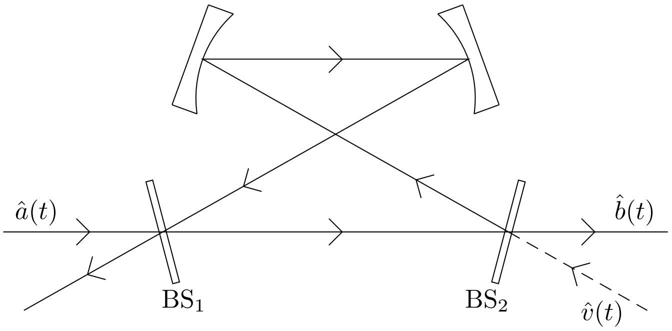

Figure 3.3: A filter cavity with input field $\hat{a}(t)$ and output field $\hat{b}(t)$. The field operator $\hat{v}(t)$ represents a field in the vacuum state.

FSRs of the OPO. To ensure this in an experiment, one can use more filter cavities one after the other with different FSRs as in [30]. Theoretically, however, this does not solve the problem, since we have assumed an infinite bandwidth of the down conversion process. To remove the peaks far from resonance, we instead use the same trick as above and take the limit where τ_F goes to zero with $\kappa_1 = t_1^2/\tau_\mathrm{F}$ and $\kappa_2 = t_2^2/\tau_\mathrm{F}$ kept fixed, where t_i^2 is the transmissivity of BS$_i$. We shall take $\kappa_1 = \kappa_2 = \kappa_\mathrm{F}$ in the following, since the filter is then perfectly transmitting at resonance. Taylor expanding around a filter cavity resonance ω_0' gives the output field

$$\hat{b}(\omega) = i\left(1 - \frac{\kappa_\mathrm{F}}{\kappa_\mathrm{F} - i(\omega - \omega_0')}\right)\hat{v}(\omega) + \frac{\kappa_\mathrm{F}}{\kappa_\mathrm{F} - i(\omega - \omega_0')}\hat{a}(\omega) \tag{3.16}$$

from which we compute

$$\langle \hat{b}^\dagger(\omega)\hat{b}(\omega)\rangle = \frac{\kappa_\mathrm{F}^2}{\kappa_\mathrm{F}^2 + (\omega - \omega_0')^2}\langle \hat{a}^\dagger(\omega)\hat{a}(\omega)\rangle \equiv S_\mathrm{F}(\omega)\langle \hat{a}^\dagger(\omega)\hat{a}(\omega)\rangle. \tag{3.17}$$

The shape $S_\mathrm{F}(\omega)$ of the filter in frequency domain is thus a Lorentzian with full width at half maximum of $2\kappa_\mathrm{F}$ as shown in Fig. 3.2.

3.4 Conclusion

In summary, we have derived the one- and two-time correlation functions for the output field from an OPO, and we have discussed some properties of the output field for the special case of a monochromatic pump field. For pulsed pump fields, we also expect the parametric down conversion process to be most efficient at the resonance frequencies of the OPO cavity, and selection of specific peaks of the output field as in the monochromatic case is meaningful at least as long as the bandwidth of the pulses is small compared to the free spectral range of the OPO cavity.

Chapter 4

Photon number states from a continuous wave source

The basic idea of the photon number state generation protocol discussed in the present chapter is to utilize the fact that photons are always generated in pairs in a nondegenerate OPO. Since the photons in a pair are distinguishable, we can divide the output into two beams (the trigger and the signal), and detection of n photons in the trigger beam heralds the presence of n photons of the signal type. In this chapter, we consider the case of a monochromatic pump field (i.e., a continuous wave OPO), and as we shall see in more detail below, the trigger photons must be detected within a short time interval to ensure that the n signal photons belong to approximately the same mode. The relevant setup is depicted in Fig. 4.1 for the case of a type II OPO, but we can equally well use a type I nondegenerate OPO if we replace the PBS with a filter cavity (Fig. 3.3). The resonance frequency of the filter is chosen as $\omega_0' = \omega_0 + m\Delta\omega$, $m \in \mathbb{Z} \setminus \{0\}$, and the trigger beam is the transmitted field (the field labeled $\hat{b}(t)$ in Fig. 3.3), while the signal beam is the reflected field (the field to the lower left in Fig. 3.3 that is not labeled). The reflected field contains all the peaks of the OPO output except the one at $\omega_0 + m\Delta\omega$, but we can use a second frequency filter to select the peak at $\omega_0 - m\Delta\omega$ if required. (Filtering is essential in the trigger channel because the APD is sensitive to photons in a broad frequency range.) We note that the theoretical analysis given below is, in fact, independent of whether we use a type II or a type I nondegenerate OPO, since the one- and two-time correlation functions derived in Sec. 3.3 for the two cases are identical (except that we may have $m = 0$ for type II).

Photon number states are valuable resource states in, for instance, state preparation schemes [43] and quantum computing [15], and single-photon states are particularly useful for quantum key distribution purposes [10] because they are indivisible light units. n-photon states can also be used for boosting the rate of n-photon absorption processes without increasing

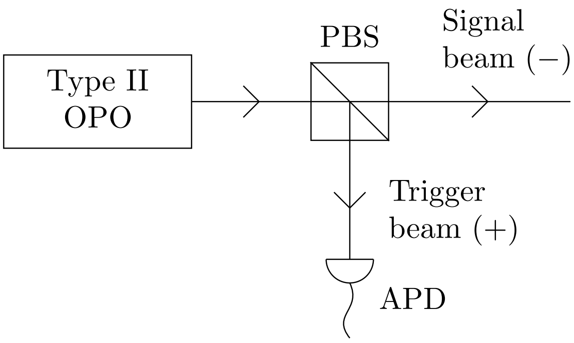

Figure 4.1: n-photon state generation illustrated for the case of a type II OPO. The OPO produces pairs of photons with different polarizations (denoted '+' and '−'), and the PBS splits the output into a signal beam consisting of the '−' polarized photons and a trigger beam consisting of the '+' polarized photons. The trigger beam is observed with an APD, and for a sufficiently weak OPO pump field, n detection events within a short time interval approximately projects a particular mode of the signal beam onto an n-photon state. (The efficiency of real APDs is close to zero in a small time interval (the dead time) after a detection event (e.g., about 40 ns for the Si-APD used in [36]). To circumvent this problem, one can divide the trigger beam into n beams and observe each of these beams with a detector. It turns out, however, that the conditional state of the signal beam is the same for the two cases when we use the click detector model, and we thus ignore such complications here. Furthermore, we do not include filters explicitly because we use Eqs. (3.14) to describe the output field from the OPO.)

the light intensity [44], and single-photon sources can be used for building random number generators. The importance of, especially, single-photon states is emphasized by the large number of single-photon sources that have been developed, including, for instance, attenuated laser light, quantum dots [45], a single ion in a cavity [46], a single atom in a cavity [47], and atomic ensembles [48, 49] (see [50] for a review).

An advantage of the measurement based protocol considered here is the fact that a detection event in the APD reveals the presence of a photon in a well-defined temporal mode of the signal beam, and this is an efficient way to suppress the zero-photon state component of the generated states. As a consequence, the fidelity, i.e., the overlap between the state actually generated and the desired single-photon state, can be large, and negative values of the Wigner function, occurring for true single-photon states, have been demonstrated experimentally for these states [31, 51]. The zero-photon state component of the states prepared using the alternative single-photon sources mentioned above is generally large due to imperfections. The generation procedure may fail or the photon may not be emitted into the correct output mode, and there is no direct way to check when it succeeds except for a (destructive) photon counting measurement of the output. In [47], for instance, a photon is only generated in 9 % of the trials. On the other hand, the two-photon and higher photon number state components are almost absent for the sources based on a single atom, ion, or quantum dot, and this is important for applications within quantum cryptography.

Another issue is timing. Timing is often important in practical applications, where the photon source is a part of a larger setup. A typical example is the interference of light states at a beam splitter, in which case the arrival times of the two inputs need to be synchronized. For atoms and quantum dots the photon emission is triggered, for instance, by a light pulse, and the emission time is thus controllable. For the continuous wave OPO, on the other hand, the photons are generated at random times. We shall investigate the possibility to circumvent this problem via time gating in the next chapter. Finally, we note that the OPO setup is significantly simpler than the experiments involving cooling and trapping of atoms. In fact, the difficulty in trapping a single atom inside a micro cavity limits the number of photons that can be emitted from the source in [47] to about 3×10^5 before the atom escapes.

Conditional measurements applied to the output field from an OPO may also be regarded as a way to transform a Gaussian state of light into a non-Gaussian state. Non-Gaussian operations are of great interest because they are required for universal quantum computing over continuous variables [52, 53]. Another proposal for generating non-Gaussian states is to use a cross-Kerr nonlinearity, homodyne detection, and feedback or feedforward [54, 55]. A major challenge in this direction is to realize sufficiently large cross-Kerr nonlinearities experimentally, but progress is being made [56].

Several experiments have already demonstrated preparation of photon number states and other quantum states of light by application of conditional measurements to the output from either a continuously pumped OPO or pulsed single-pass PDC. Detection of one or two trigger beam photons have led to preparation of single-photon states [31, 51, 57, 58, 59, 60] and two-photon states [61], and related experiments [30, 36, 60, 62, 63] have demonstrated preparation of so-called photon subtracted squeezed states as we shall discuss further in the next two chapters. The typical way to verify the output in such experiments is to measure a particular mode of the signal beam with a homodyne detector as described in Sec. 2.4 and then reconstruct the Wigner function of that mode. Our contribution to the theoretical investigation of photon number state generation from a continuous wave OPO is to determine, which mode of the signal beam one should optimally choose to obtain the largest possible overlap with the desired single-mode n-photon state. Experiments of the above type involving a single on/off trigger beam detection event have been analyzed in [64], where an expansion in a complete set of prolate spheroidal wave functions is used to describe the multimode output field and the outcome of homodyne detection, assuming a box-shaped spectral profile of the OPO output and a box-shaped temporal profile of the detected signal mode. Here, we follow the alternative approach outlined in [65], which allows us to only consider the trigger and signal modes that are actually observed and freedom to choose any shapes of the mode functions without significantly complicating the analysis. As we consider the case of a monochromatic pump field, we use Eqs. (3.14) as input to our description. Since the trivial time-dependent phase factors in (3.14) are canceled by corresponding trivial phase factors on the mode functions, we drop these factors in the following for simplicity.

In the following, we first analyze the case of single-photon state generation in Sec. 4.1. We compute the optimal choice of signal mode function numerically, compare with experimental results, and discuss different models of the detection of the trigger beam. This part of the project has been motivated by a partial collaboration with Eugene Polzik's group, which was working on the experiment described in [31] at that time. We then turn to generation of general photon number states. In Sec. 4.2, we provide a simple expression for the conditional state of the signal beam in the limit of a weak pump field, and in Sec. 4.3, we use this expression to optimize the signal mode function analytically for n-photon state preparation. The chapter is based on [I][1] and [II][2].

4.1 Single photodetection event

Conditional output state

To determine the optimal choice of signal beam mode function, we first compute the state generated in a given but arbitrary mode $f_{\mathrm{s}}(t)$ of the signal beam when conditioning on a single photodetection event in the trigger beam at time t_{c}. The timescale for significant variations in the output from the OPO is given by the mean lifetime $(\kappa_1+\kappa_2)^{-1}$ of a photon in the OPO cavity. For a detector resolution (≤ 1 ns in [36]), which is small compared to $(\kappa_1+\kappa_2)^{-1}$ ($= 20$ ns in [31]), we can thus regard the detection process as instantaneous and assume that the detection event takes place in the time-localized trigger mode function in (2.14), which is centered at time t_{c}, and we denote this mode function by $f_{\mathrm{t}}(t)$ in the following. In practice, the trigger detector is turned on at all times, and each detection event heralds the presence of an approximate single-photon state in a particular mode of the signal beam. For now we assume that all detection events are accepted as successful independent of the measurement records for the surrounding time-localized trigger modes. In this case, we effectively average over all

---

[1] Copyright (2007) by the American Physical Society.

[2] Copyright (2007) by the American Physical Society.

possible measurement results for these modes, which, in turn, is equivalent to not measuring these modes at all. We thus trace out all modes of the trigger beam except the mode with mode function $f_{\mathrm{t}}(t)$.

Losses are taken into account as in Sec. 2.4, and the single-mode operators of the observed modes are thus

$$\hat{b}_{\mathrm{t}} = \int f_{\mathrm{t}}^*(t') \Big(\sqrt{\eta_{\mathrm{t}}} \hat{b}_+(t') + i\sqrt{1-\eta_{\mathrm{t}}} \hat{b}_{+,\mathrm{vac}}(t') \Big) \mathrm{d}t', \tag{4.1a}$$

$$\hat{b}_{\mathrm{s}} = \int f_{\mathrm{s}}^*(t') \Big(\sqrt{\eta_{\mathrm{s}}} \hat{b}_-(t') + i\sqrt{1-\eta_{\mathrm{s}}} \hat{b}_{-,\mathrm{vac}}(t') \Big) \mathrm{d}t', \tag{4.1b}$$

where the operators $\hat{b}_\pm(t)$ represent the output field from the OPO as in the previous chapter, $\hat{b}_{\pm,\mathrm{vac}}(t)$ are field operators representing beams in the vacuum state, and $1-\eta_{\mathrm{t}}$ $(1-\eta_{\mathrm{s}})$ is the loss in the trigger (signal) channel, including propagation losses and detector efficiencies below unity. As noted in [65], we can now use (4.1), $\hat{b}_{\pm,\mathrm{vac}}(t)|0\rangle = 0$, $\langle \hat{b}_\pm(t)\rangle = 0$, (3.14), and the definition of V and $\hat{y}$ below (2.22) to explicitly write down the Gaussian Wigner function $W(x_{\mathrm{t}}, p_{\mathrm{t}}, x_{\mathrm{s}}, p_{\mathrm{s}})$ of these two modes. In this way, we automatically trace out all the irrelevant modes, and the multimode problem is reduced to a two-mode problem.

The next step is to take the measurement of the trigger mode into account [65]. As we consider detection of an infinitesimal temporal mode of a continuous beam of light of low intensity, we use the click detector model from Sec. 2.4. The transformation $\rho \to \hat{b}_{\mathrm{t}} \rho \hat{b}_{\mathrm{t}}^\dagger / P$ of the density operator, where $P = \mathrm{Tr}(\hat{b}_{\mathrm{t}} \rho \hat{b}_{\mathrm{t}}^\dagger)$, translates into a certain transformation of the Wigner function [26]. After tracing out the observed trigger mode, this leads to the following expression for the Wigner function of the conditional state of the considered signal mode [I]

$$W_{\mathrm{c}}(x_{\mathrm{s}}, p_{\mathrm{s}}) = \frac{1}{2P} \iint \left(x_{\mathrm{t}}^2 + p_{\mathrm{t}}^2 - 1 \right) W(x_{\mathrm{t}}, p_{\mathrm{t}}, x_{\mathrm{s}}, p_{\mathrm{s}}) dx_{\mathrm{t}} dp_{\mathrm{t}} \tag{4.2}$$

$$= \frac{1}{\pi} \left(\frac{1}{V_{33}} + \frac{V_{13}^2 + V_{14}^2}{V_{33}^3 (V_{11} - 1)} \left(x_{\mathrm{s}}^2 + p_{\mathrm{s}}^2 - V_{33} \right) \right) e^{-\left(x_{\mathrm{s}}^2 + p_{\mathrm{s}}^2\right)/V_{33}}, \tag{4.3}$$

where V_{ij} are the elements of the covariance matrix of the unconditional state described by $W(x_{\mathrm{t}}, p_{\mathrm{t}}, x_{\mathrm{s}}, p_{\mathrm{s}})$ and we have utilized the fact that $V_{11} = V_{22}$, $V_{33} = V_{44}$, $V_{13} = -V_{24}$, $V_{14} = V_{23}$, $V_{12} = V_{34} = 0$, and $V_{ij} = V_{ji}$ in the last step.

We note that $W_{\mathrm{c}}(x_{\mathrm{s}}, p_{\mathrm{s}})$ depends on $f_{\mathrm{s}}(t)$, ϵ, κ_1, κ_2, and η_{s} through V, but it does not depend on η_{t}, because V_{13}^2, V_{14}^2, and $V_{11} - 1$ are all proportional to η_{t}, while V_{33} is independent of η_{t}. Due to the conditioning procedure, a trigger channel efficiency below unity only reduces the number of observed detection events per unit detection time. Moreover, it turns out that $W_{\mathrm{c}}(x_{\mathrm{s}}, p_{\mathrm{s}})$ only depends on κ_1, κ_2, and η_{s} through $\kappa \equiv \kappa_1 + \kappa_2$ and $\eta_{\mathrm{s}}' \equiv \eta_s \kappa_1 / \kappa$, while the probability P to actually detect a photon in the time interval $]t_\mathrm{c} - \Delta t/2, t_\mathrm{c} + \Delta t/2]$ only depends on Δt, κ, ϵ, and $\eta_\mathrm{t}' \equiv \eta_\mathrm{t}\kappa_1/\kappa$. A nonzero value of κ_2 (i.e., a cavity loss) is thus equivalent to an increase in the cavity decay rate by κ_2 and a reduction of both the trigger and the signal channel efficiencies by the factor $\kappa_1/(\kappa_1 + \kappa_2)$. This is not surprising as $1 - \kappa_1/(\kappa_1 + \kappa_2)$ is the fraction of the photons generated inside the cavity that escape from the cavity without being emitted into the output beams.

Optimal signal mode function

Having computed the conditional state of the signal mode, we can also compute the resulting single-photon state fidelity $F_1(f_\mathrm{s}(t)) \equiv \langle 1|\rho_\mathrm{c}|1\rangle$, where ρ_c is the density operator corresponding to $W_\mathrm{c}(x_\mathrm{s}, p_\mathrm{s})$. According to Sec. 4.3.2 of [18], we can reexpress $\langle 1|\rho_\mathrm{c}|1\rangle$ as 2π times the integral of the product of $W_\mathrm{c}(x_\mathrm{s}, p_\mathrm{s})$ and the Wigner function $W_{n=1}(x_\mathrm{s}, p_\mathrm{s})$ of a single-photon state given in (2.21). We hence obtain

$$F_1(f_\mathrm{s}(t)) = 2\pi \iint W_{n=1}(x_\mathrm{s}, p_\mathrm{s}) W_\mathrm{c}(x_\mathrm{s}, p_\mathrm{s}) dx_\mathrm{s} dp_\mathrm{s} \tag{4.4}$$

$$= \frac{2(V_{11} - 1)(V_{33}^2 - 1) + 2(3 - V_{33})(V_{13}^2 + V_{14}^2)}{(V_{11} - 1)(1 + V_{33})^3}. \tag{4.5}$$

The task is now to find the optimal mode function $f_\mathrm{op}(t)$, which maximizes $F_1(f_\mathrm{s}(t))$. We do this numerically by choosing a random (but normalized) initial mode function defined on a grid in a window around the detection time t_c. In each step of the iteration, we choose a random grid point and change either the phase or the norm of the value of the mode function at that point by a random amount. We then normalize the resulting mode function (if required) and check whether the fidelity $F_1(f_\mathrm{s}(t))$ has increased. The change is only kept in the next iteration if it has. Using this method, it turns out that phase of the optimal mode function is constant except for sudden jumps of π, and an analytical calculation [I] confirms that the variation of $F_1(f_\mathrm{s}(t))$ indeed vanishes if this is the case. Changing the phase of the mode function by a constant amount corresponds to a rotation of $W_\mathrm{c}(x_\mathrm{s}, p_\mathrm{s})$ in phase space, and as $W_{n=1}(x_\mathrm{s}, p_\mathrm{s})$ is rotationally invariant, this will not change $F_1(f_\mathrm{s}(t))$. We can thus choose $f_\mathrm{s}(t)$ to be real.

Rerunning the above algorithm for a real mode function, we obtain the results shown in Fig. 4.2, where we have also plotted the average number of detection events per unit time in the trigger beam

$$r = \frac{P}{\Delta t} = \eta_\mathrm{t}\langle \hat{b}_+^\dagger(t_\mathrm{c})\hat{b}_+(t_\mathrm{c})\rangle = \frac{2\eta_\mathrm{t}'\kappa(\epsilon/\kappa)^2}{1 - 4(\epsilon/\kappa)^2} \tag{4.6}$$

for $\eta_\mathrm{t}' = 1$. We note that r/η_t' is the average number of photon pairs generated per unit time in the OPO. Since the photons decay out of the cavity at the rate κ, it follows that the photons are, on average, well-separated

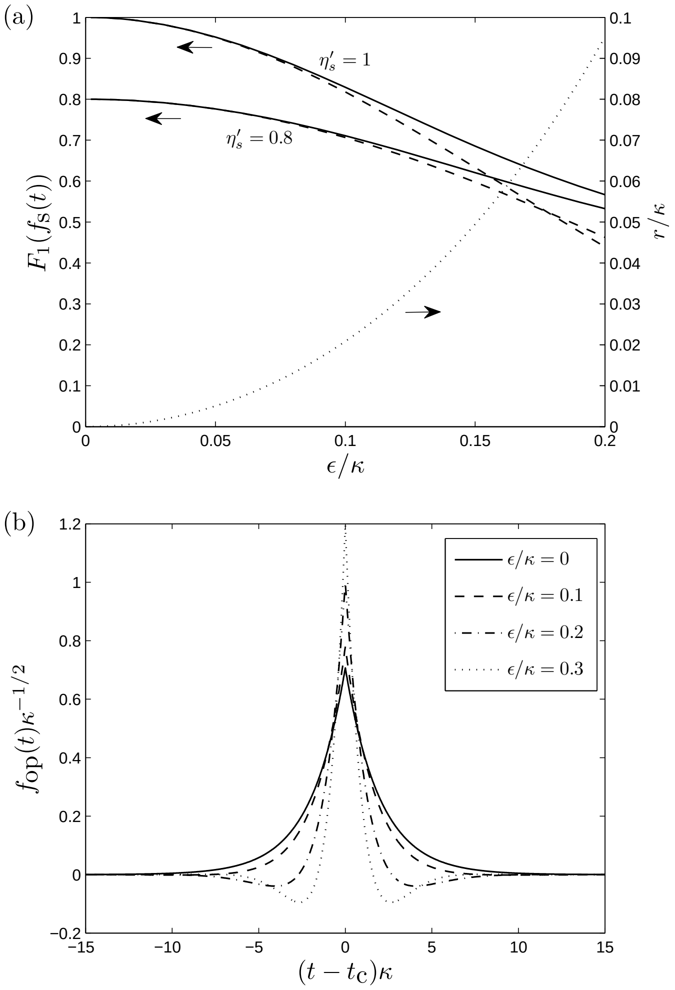

Figure 4.2: (a) Single-photon state fidelity for $f_\mathrm{s}(t) = f_\mathrm{op}(t)$ (solid lines) and for $f_\mathrm{s}(t) = \sqrt{\kappa/2}\exp(-\kappa|t - t_\mathrm{c}|/2)$ (dashed lines) as a function of ϵ/κ for $\eta_\mathrm{s}' = 1$ (upper curves) and $\eta_\mathrm{s}' = 0.8$ (lower curves). The dotted line is the rate r of trigger detection events for $\eta_\mathrm{t}' = 1$ (note that $r \propto \eta_\mathrm{t}'$). (b) Optimal signal mode functions for single-photon state generation, when we condition on a detection event at time t_c. $\eta_\mathrm{s}' = 1$, and the values of ϵ/κ are stated in the legend.

in the OPO output beams if $r/(\eta_{\mathrm{t}}'\kappa) \ll 1$. When the photons are well-separated, the two-photon and higher-photon number state components of the generated state are very small, and this explains why we obtain a large single-photon state fidelity for small ϵ/κ. In fact, it follows from (4.5) that $F_1(f_{\mathrm{op}}(t)) \to \eta_{\mathrm{s}}'$ for $\epsilon/\kappa \to 0$. In an experiment, it is, however, not feasible to choose ϵ/κ arbitrarily small because r vanishes for $\epsilon/\kappa \to 0$, and it would take infinitely long time to obtain enough data points for the reconstruction of the output state (in [31], e.g., the data set consists of 180000 measurements). It is also important that the number of trigger detection events per unit time is significantly larger than the rate of dark counts of the APD (i.e., the rate of false clicks, which is about 100 s^{-1} in [31]). There is thus a trade off between fidelity and the rate of trigger detection events, and a reasonable approach is to determine the lowest acceptable value of r for the considered experiment and then use equation (4.6) to compute the corresponding value of ϵ, from which we can predict the expected fidelity.

Considering Fig. 4.2(b), it turns out that the square of the norm of the optimal mode function in the limit $\epsilon/\kappa \to 0$ coincides with the probability distribution (4.7) obtained from the following classical model. Imagine that two distinguishable objects S and T are created at time t_0 and both decay at the rate κ. The probability density that T (S) decays at time $t \geq t_0$ is then $\kappa \exp(-\kappa(t-t_0))$. If t_0 is, in fact, unknown, but we observe that T decays at time t_{c}, we know that the creation took place within the infinitesimal time interval $]t_0 - \Delta t_0, t_0]$, $t_0 \leq t_{\mathrm{c}}$, with probability $\kappa \exp(-\kappa(t_{\mathrm{c}} - t_0))\Delta t_0$. The probability density that S decays at time t given that T decays at time t_{c} is hence given by

$$\int_{-\infty}^{\min(t,t_{\mathrm{c}})} \kappa e^{-\kappa(t-t_0)} \kappa e^{-\kappa(t_{\mathrm{c}}-t_0)} dt_0 = \frac{\kappa}{2} e^{-\kappa|t-t_{\mathrm{c}}|}. \tag{4.7}$$

The basic structure of the mode function in the limit of a weak pump field can thus be explained from the fact that the photons spend different amounts of time in the cavity, and the signal photon generated at the same time as the observed trigger photon may appear earlier or later than the trigger photon in the output. When ϵ/κ is nonzero, the photon pairs are no longer completely separated, and the shape of the optimal mode function changes in order to reduce the overlap with the additional photons generated, while maintaining a large overlap with the photon in the signal beam created at the same time as the observed trigger photon.

One can also maximize the fidelity analytically, which leads to the following integral equation for the optimal mode function [I]

$$\xi f_{\mathrm{op}}(t) = c_1[f_{\mathrm{op}}(t)] \frac{\lambda^2 - \mu^2}{4} \int f_{\mathrm{op}}(t') \left(\frac{e^{-\mu|t-t'|}}{2\mu} - \frac{e^{-\lambda|t-t'|}}{2\lambda} \right) dt'$$

$$+ c_2[f_{\mathrm{op}}(t)]\frac{\lambda^2-\mu^2}{4}\left(\frac{e^{-\mu|t-t_{\mathrm{c}}|}}{2\mu}+\frac{e^{-\lambda|t-t_{\mathrm{c}}|}}{2\lambda}\right), \quad (4.8)$$

where ξ is a Lagrange multiplier introduced to keep $f_{\mathrm{op}}(t)$ normalized, $c_1[f_{\mathrm{op}}(t)]$ and $c_2[f_{\mathrm{op}}(t)]$ are time-independent functionals of $f_{\mathrm{op}}(t)$, and $f_{\mathrm{op}}(t)$ is assumed to be real. When ϵ is sufficiently small, the first term on the right hand side is of order ϵ^2, while the second term is of order ϵ^0, and for $\epsilon/\kappa \to 0$, the equation reduces to $f_{\mathrm{op}}(t) = \sqrt{\kappa/2}\exp(-\kappa|t-t_{\mathrm{c}}|/2)$, which precisely matches the solid line in Fig. 4.2(b). It is now tempting to use this expression as a starting point to solve (4.8) iteratively to higher and higher orders in ϵ. It turns out, however, that the validity of this method is very limited because sufficiently small ϵ means $\epsilon/\kappa \ll 1$ and $\epsilon|t-t_{\mathrm{c}}| \ll 1$, and even though a typical value of $|t-t_{\mathrm{c}}|$ is κ^{-1}, the mode function is significantly different from zero in a time interval, which is broader than 10 κ^{-1}. In the end, the mode function obtained to second order in ϵ turns out not to be more accurate than the zeroth order mode function for values of ϵ/κ around 0.1. On the other hand, we observe from Fig. 4.2(a) that the zeroth order approximation to the optimal mode function actually provides fidelities that are close to the optimal value for all ϵ/κ for which the fidelity is high.

Comparison with experimental results

The theoretical method described above has been utilized in [31] to analyze the experimental results on single-photon state generation from a continuous wave type I nondegenerate OPO obtained in the same paper, and we briefly discuss the outcome. The experimental parameters are $\epsilon/\kappa = 0.045$, $\kappa = 2\pi \times 8$ MHz, $\eta_{\mathrm{t}}' = 0.06$, and $\eta_{\mathrm{s}}' = 0.75$. From these values we expect the number of trigger detection events per unit detection time to be $r = 1.23 \times 10^4$ s^{-1}, which is close to, but slightly lower than, the observed value of 1.28×10^4 s^{-1}. For perfect signal channel efficiency, $\eta_{\mathrm{s}}' = 1$, it should be possible to reach a fidelity of $F_1(f_{\mathrm{op}}(t)) = 0.96$, while $F_1(f_{\mathrm{op}}(t)) = 0.74$ for the actual value of η_{s}'. The observed single-photon state fidelity is 0.61. In [31], it is suggested that this discrepancy could be due to inefficient filtering of the trigger beam plus the approximately 100 dark counts per second, which is consistent with the fact that the experimental value of r is larger than the theoretical value. A trigger detection caused by a photon from one of the wrong peaks of the OPO output or a dark count effectively means that the observed signal mode is in the unconditional state, and since the unconditional state is almost vacuum, the effect is similar to an additional loss in the signal beam. Laser noise and beginning diode saturation are also mentioned as possible sources of the deviation from the expected fidelity. As the zeroth order mode function is very close to optimal for $\epsilon/\kappa = 0.045$, this mode function has been used in the analysis.

Continuous trigger detection

We have seen that the single-photon state fidelity decreases if the photons are not well-separated in the output. This suggest that we could indeed improve the fidelity if we use a more complicated conditioning procedure, where we condition on a detection event surrounded by an interval of no detection events, which is broader than the temporal width of the optimized mode functions in Fig. 4.2(b). This can be done by dividing the interval into a large number of time-localized trigger modes and computing the Gaussian Wigner function of these modes and a single signal mode. All the included trigger modes except $f_{\mathrm{t}}(t)$ are then projected onto the vacuum state and traced out before we condition on the trigger detection event as above. The computation is significantly simplified by the fact that the vacuum state is Gaussian.

The result of such a calculation (see [I] for details) shows that we can, in principle, produce single-photon states with unit fidelity for nonzero ϵ/κ if $\eta_{\mathrm{t}}' = \eta_{\mathrm{s}}' = 1$. This appears because we know from the measurement results that no other photon pairs have been created close to the observed trigger photon. In this case, the optimal signal mode function reduces to the zeroth order mode function. In present day experiments, however, η_{t}' is generally low (e.g., $\eta_t' = 0.06$ as above). When η_{t}' is close to zero, we learn almost nothing from a no click event because this is the most likely outcome even if a photon is transmitted into the trigger channel, and for $\eta_{\mathrm{t}}' \to 0$, we reobtain the results from the more simple conditioning scheme considered above.

4.2 Conditional output state for n photodetection events in the weak pump limit

To produce higher photon number states, we condition on more detection events in the trigger channel. This is done by including the appropriate number of time-localized trigger modes in the description and applying the transformation (4.2) once for each trigger mode (in any order). A significant difference compared to the single-photon case, however, is the fact that the n-photon state fidelity is now also a function of the temporal distances between the conditioning detection events, and to simplify matters and focus on this new aspect, we assume the limit $\epsilon/\kappa \to 0$ and $\eta_{\mathrm{s}}' = 1$ in the following. Referring to the results in Fig. 4.2, we expect that the mode functions obtained in this limit are close to optimal also for the experimentally interesting values of ϵ/κ, which is indeed confirmed for $n = 2$ in [II].

Conditional output state in the weak pump limit

We first show that the state produced in the signal beam when conditioning on detection events at times $t_{\mathrm{c}i}$, $i = 1, 2, \ldots, n$, is

$$|\psi_n\rangle = N_n \left(\prod_{i=1}^{n} \int g_i(t_i) \hat{b}_-^\dagger(t_i) dt_i \right) |0\rangle, \tag{4.9}$$

where N_n is a normalization constant and

$$g_i(t) \equiv \sqrt{\frac{\kappa}{2}} \exp\left(-\frac{\kappa}{2} |t - t_{\mathrm{c}i}| \right). \tag{4.10}$$

This is a reasonable result because we have seen in Sec. 4.1 that detection of a trigger photon at time t_c effectively creates a photon in the signal beam mode $\sqrt{\kappa/2}\exp(-\kappa|t - t_\mathrm{c}|/2)$, and for $\epsilon/\kappa \to 0$, there will be no additional photons in the signal beam.

To prove it, we show that (4.9) gives the correct expectation value for all normally ordered products of signal beam annihilation and creation operators, i.e.,

$$\begin{aligned}
&\lim_{\epsilon/\kappa \to 0} \frac{\left\langle \left(\prod_{i=1}^{n} \hat{b}_+^\dagger(t_{\mathrm{c}i}) \right) \left(\prod_{j=1}^{m} \hat{b}_-^\dagger(t'_j) \right) \left(\prod_{k=1}^{p} \hat{b}_-(t''_k) \right) \left(\prod_{q=1}^{n} \hat{b}_+(t_{\mathrm{c}q}) \right) \right\rangle}{\left\langle \left(\prod_{i=1}^{n} \hat{b}_+^\dagger(t_{\mathrm{c}i}) \right) \left(\prod_{q=1}^{n} \hat{b}_+(t_{\mathrm{c}q}) \right) \right\rangle} \\
&= \iint \cdots \int \left(\prod_{i=1}^{n} g_i(t_i) \right) \left(\prod_{q=1}^{n} g_q(t_{n+q}) \right) \langle 0| \left(\prod_{i=1}^{n} \hat{b}_-(t_i) \right) \left(\prod_{j=1}^{m} \hat{b}_-^\dagger(t'_j) \right) \\
&\times \left(\prod_{k=1}^{p} \hat{b}_-(t''_k) \right) \left(\prod_{q=1}^{n} \hat{b}_-^\dagger(t_{n+q}) \right) |0\rangle \left(\prod_{i=1}^{2n} dt_i \right) \Big/ \iint \cdots \int \left(\prod_{i=1}^{n} g_i(t_i) \right) \\
&\times \left(\prod_{q=1}^{n} g_q(t_{n+q}) \right) \langle 0| \left(\prod_{i=1}^{n} \hat{b}_-(t_i) \right) \left(\prod_{q=1}^{n} \hat{b}_-^\dagger(t_{n+q}) \right) |0\rangle \left(\prod_{i=1}^{2n} dt_i \right).
\end{aligned} \tag{4.11}$$

Here, the left hand side (LHS) is the expectation value of a normally ordered product of m signal beam creation operators and p signal beam annihilation operators computed using the state obtained after annihilating n photons in the trigger beam at times $t_{\mathrm{c}i}$, $i = 1, 2, \ldots, n$, from the actual output from the OPO, and the right hand side (RHS) is the expectation value of the same product of signal beam operators obtained for the state (4.9).

The left hand side

The LHS is evaluated using Wick's theorem for Gaussian states with zero mean values (i.e., $\langle \hat{b}_\pm(t) \rangle = 0$ for our case) [66], which states that

$$\begin{aligned}
\langle \hat{B}_1 \hat{B}_2 \ldots \hat{B}_{2k} \rangle = \langle \hat{B}_1 \hat{B}_2 \rangle \langle \hat{B}_3 \hat{B}_4 \hat{B}_5 \ldots \hat{B}_{2k} \rangle + \langle \hat{B}_1 \hat{B}_3 \rangle \langle \hat{B}_2 \hat{B}_4 \hat{B}_5 \ldots \hat{B}_{2k} \rangle \\
+ \ldots + \langle \hat{B}_1 \hat{B}_{2k} \rangle \langle \hat{B}_2 \hat{B}_3 \hat{B}_4 \ldots \hat{B}_{2k-1} \rangle
\end{aligned} \tag{4.12}$$

and $\langle \hat{B}_1 \hat{B}_2 \dots \hat{B}_{2k+1} \rangle = 0$, where $\hat{B}_i$ is either an annihilation or a creation operator and k is a positive integer. The LHS of (4.11) may thus be expressed in terms of the two-time correlation functions in (3.14). For small ϵ/κ, we note that

$$\langle \hat{b}_\pm^\dagger(t) \hat{b}_\pm(t') \rangle \approx \frac{2\epsilon^2}{\kappa} \left(1 + \frac{\kappa}{2}|t-t'|\right) \mathrm{e}^{-\frac{\kappa}{2}|t-t'|}, \tag{4.13a}$$

$$\langle \hat{b}_\pm(t) \hat{b}_\mp(t') \rangle \approx \sqrt{\frac{2\epsilon^2}{\kappa}} \sqrt{\frac{\kappa}{2}} \mathrm{e}^{-\frac{\kappa}{2}|t-t'|}, \tag{4.13b}$$

while $\langle \hat{b}_\pm^\dagger(t) \hat{b}_\mp(t') \rangle = \langle \hat{b}_\pm(t) \hat{b}_\pm(t') \rangle = 0$. It follows that the LHS of (4.11) is zero if $m \neq p$ since all the terms obtained by applying Wick's theorem to the numerator when $m+p$ is even contain at least one of the expectation values $\langle \hat{b}_\pm^\dagger(t) \hat{b}_\mp(t') \rangle$ or $\langle \hat{b}_\pm(t) \hat{b}_\pm(t') \rangle$. It also follows that the denominator on the LHS of (4.11) is proportional to ϵ^{2n}. In the numerator the lowest order terms in ϵ are those that contain as many expectation values of the type $\langle \hat{b}_\pm(t) \hat{b}_\mp(t) \rangle$ (or $\langle \hat{b}_\pm^\dagger(t) \hat{b}_\mp^\dagger(t) \rangle$) as possible. These terms are proportional to $\epsilon^{\max(2n,2m)}$ for $m = p$. To obtain a nonzero LHS in the limit $\epsilon/\kappa \to 0$, it is thus necessary to require that $m = p \leq n$.

Assuming $m = p \leq n$ and keeping only the lowest order terms in ϵ, it follows from Wick's theorem and (4.13) that the LHS of (4.11) is

$$\begin{aligned} \text{LHS} = \frac{1}{(n-m)!} \sum_{P_i} \sum_{P_j} & g_{i_1}(t_1') \dots g_{i_m}(t_m') g_{j_1}(t_1'') \dots g_{j_m}(t_m'') \\ & \times I_{i_{m+1} j_{m+1}} \dots I_{i_n j_n} \Big/ \sum_{P_j} I_{1 j_1} \dots I_{n j_n}, \end{aligned} \tag{4.14}$$

where

$$I_{ij} \equiv \int g_i(t) g_j(t) dt = \left(1 + \frac{\kappa}{2}|t_{ci} - t_{cj}|\right) \exp\left(-\frac{\kappa}{2}|t_{ci} - t_{cj}|\right) \tag{4.15}$$

and the summations are over all permutations of the n i-indices and all permutations of the n j-indices, respectively.

The right hand side

By counting the number of photons created and annihilated in the numerator, it is immediately apparent that the RHS of (4.11) is zero if $m = p \leq n$ is not fulfilled. For $m = p \leq n$, we use the relation

$$\hat{b}_-(t_k'') \left(\prod_{i=1}^{n} \hat{b}_-^\dagger(t_i) \right) |0\rangle = \sum_{j=1}^{n} \delta(t_k'' - t_j) \left(\prod_{\substack{i=1 \\ i \neq j}}^{n} \hat{b}_-^\dagger(t_i) \right) |0\rangle \tag{4.16}$$

repeatedly to obtain

$$\langle 0|\prod_{i=1}^{n}\hat{b}_-(t_i)\prod_{j=1}^{m}\hat{b}_-^\dagger(t'_j)\prod_{k=1}^{m}\hat{b}_-(t''_k)\prod_{q=1}^{n}\hat{b}_-^\dagger(t_{n+q})|0\rangle =$$
$$\frac{1}{(n-m)!}\sum_{P_i}\sum_{P_j}\delta(t'_1-t_{i_1})\dots\delta(t'_m-t_{i_m})\delta(t''_1-t_{n+j_1})\dots$$
$$\times\,\delta(t''_m-t_{n+j_m})\delta(t_{i_{m+1}}-t_{n+j_{m+1}})\dots\delta(t_{i_n}-t_{n+j_n}). \quad (4.17)$$

Inserting (4.17) into the RHS of (4.11) we immediately obtain the result (4.14), which means that LHS = RHS as postulated.

4.3 Optimal mode function for n-photon state generation in the weak pump limit

The state $|\psi_n\rangle$ is a multimode state, and the detection events in the trigger channel must be close in order to produce an n-photon state rather than n single-photon states. In this section, we calculate the signal mode function $f_\mathrm{s}(t)$, which maximizes the overlap between $|\psi_n\rangle$ and the single-mode n-photon state

$$|n\rangle = \frac{1}{\sqrt{n!}}\left(\hat{b}_\mathrm{s}^\dagger\right)^n|0\rangle = \frac{1}{\sqrt{n!}}\left(\int f_\mathrm{s}(t)\hat{b}_-^\dagger(t)dt\right)^n|0\rangle. \quad (4.18)$$

The overlap evaluates to

$$F_n(f_\mathrm{s}(t)) = |\langle\psi_n|n\rangle|^2 = n!|N_n|^2\prod_{i=1}^{n}\left|\int f_\mathrm{s}(t_i)g_i(t_i)dt_i\right|^2, \quad (4.19)$$

and since $g_i(t_i)$ is real and positive, it follows that it is optimal to choose the phase of $f_\mathrm{s}(t)$ to be time-independent. We can thus assume $f_\mathrm{s}(t)$ to be real. Variational optimization of $\prod_{i=1}^{n}\int f_\mathrm{s}(t_i)g_i(t_i)dt_i$ under the constraint $\int f_\mathrm{s}(t)^2dt = 1$ leads to

$$\xi f_\mathrm{op}(t) = \sum_{i=1}^{n}g_i(t)\prod_{j\neq i}\int f_\mathrm{op}(t_j)g_j(t_j)dt_j, \quad (4.20)$$

where ξ is a Lagrange multiplier and $f_\mathrm{op}(t)$ is the optimal choice of $f_\mathrm{s}(t)$ as above. The optimal mode function is thus

$$f_\mathrm{op}(t) = \sum_{i=1}^{n}c_ig_i(t), \quad (4.21)$$

where the coefficients c_i are determined from the relations

$$\xi c_i = \prod_{j\neq i}\left(\sum_{k=1}^{n}c_kI_{kj}\right), \qquad \sum_{i=1}^{n}\sum_{j=1}^{n}c_ic_jI_{ij} = 1, \quad (4.22)$$

and I_{ij} is defined in (4.15).

Examples

Let us consider a few examples. For $n = 1$, we find $f_{\mathrm{op}}(t) = g_1(t)$ and $F_1(f_{\mathrm{op}}(t)) = 1$ as expected. For $n = 2$, $f_{\mathrm{op}}(t) = (g_1(t) + g_2(t))/\sqrt{2(1 + I_{12})}$ and $F_2(f_{\mathrm{op}}(t)) = (1 + I_{12})^2/(2(1 + I_{12}^2))$. In fact, it follows from (4.9) that the conditional state of the signal beam is the two-mode state

$$|\psi_2\rangle = \frac{1 + I_{12}}{\sqrt{2(1 + I_{12}^2)}}|2\rangle|0\rangle - \frac{1 - I_{12}}{\sqrt{2(1 + I_{12}^2)}}|0\rangle|2\rangle, \tag{4.23}$$

where the mode function of the first (last) mode is $g_+(t)$ ($g_-(t)$) defined by

$$g_\pm(t) = \frac{1}{\sqrt{2(1 \pm I_{12})}}(g_1(t) \pm g_2(t)). \tag{4.24}$$

The squares of the norms of the coefficients in (4.23) are plotted as a function of the separation between the detection events in Fig. 4.3(a). The optimal two-photon state fidelity is seen to decrease from unity at zero separation to one half at infinite separation, which happens because the state changes from a perfect two-photon state into two separated single-photon states occupying the modes with mode functions $g_1(t)$ and $g_2(t)$. It is interesting to note that $F_2(f_{\mathrm{op}}(t)) \approx 1 - (\kappa|t_{\mathrm{c}2} - t_{\mathrm{c}1}|/4)^4$ for $\kappa|t_{\mathrm{c}2} - t_{\mathrm{c}1}| \ll 1$, and in this region the two-photon fidelity thus decreases extremely slowly with separation of the detection events. Even for $\kappa|t_{\mathrm{c}2} - t_{\mathrm{c}1}| = 2$, the optimized fidelity is still as large as $F_2(f_{\mathrm{op}}(t)) = 0.977$. This is an important result because it allows us to use less restrictive conditioning requirements with a resulting increase in the success rate.

The optimal mode function is more complicated for $n = 3$, and we consider two special cases. For $t_{\mathrm{c}2} - t_{\mathrm{c}1} = t_{\mathrm{c}3} - t_{\mathrm{c}2}$ we obtain

$$c_1 = c_3 = \sqrt{\frac{I_{12}^2 - 2(1 + I_{13}) + I_{12}\sqrt{I_{12}^2 + 4(1 + I_{13})}}{6(2I_{12}^2 - (1 + I_{13}))(1 + I_{13})}}, \tag{4.25a}$$

$$c_2 = -2c_1 I_{12} + \sqrt{1 + 2c_1^2(2I_{12}^2 - (1 + I_{13}))}, \tag{4.25b}$$

and for $t_{\mathrm{c}2} = t_{\mathrm{c}1}$ we obtain

$$c_1 = c_2 = \sqrt{\frac{(4 - I_{13}^2) - \sqrt{(4 - I_{13}^2)^2 - 16(1 - I_{13}^2)}}{24(1 - I_{13}^2)}}, \tag{4.26a}$$

$$c_3 = \frac{1 - 6c_1^2}{3c_1 I_{13}}. \tag{4.26b}$$

The three-photon state fidelity is plotted in Fig. 4.3(b), and also in this case it decreases extremely slowly in the region where $\kappa|t_{\mathrm{c}3} - t_{\mathrm{c}1}| \ll 1$. In fact, $F_3(f_{\mathrm{op}}(t)) \approx 1 - (\kappa|t_{\mathrm{c}3} - t_{\mathrm{c}1}|/2)^4/48$ for $t_{\mathrm{c}2} - t_{\mathrm{c}1} = t_{\mathrm{c}3} - t_{\mathrm{c}2}$, and $F_3(f_{\mathrm{op}}(t)) \approx 1 - (\kappa|t_{\mathrm{c}3} - t_{\mathrm{c}1}|/2)^4/27$ for $t_{\mathrm{c}2} = t_{\mathrm{c}1}$. In the opposite limit, $\kappa|t_{\mathrm{c}3} - t_{\mathrm{c}1}| \to \infty$,

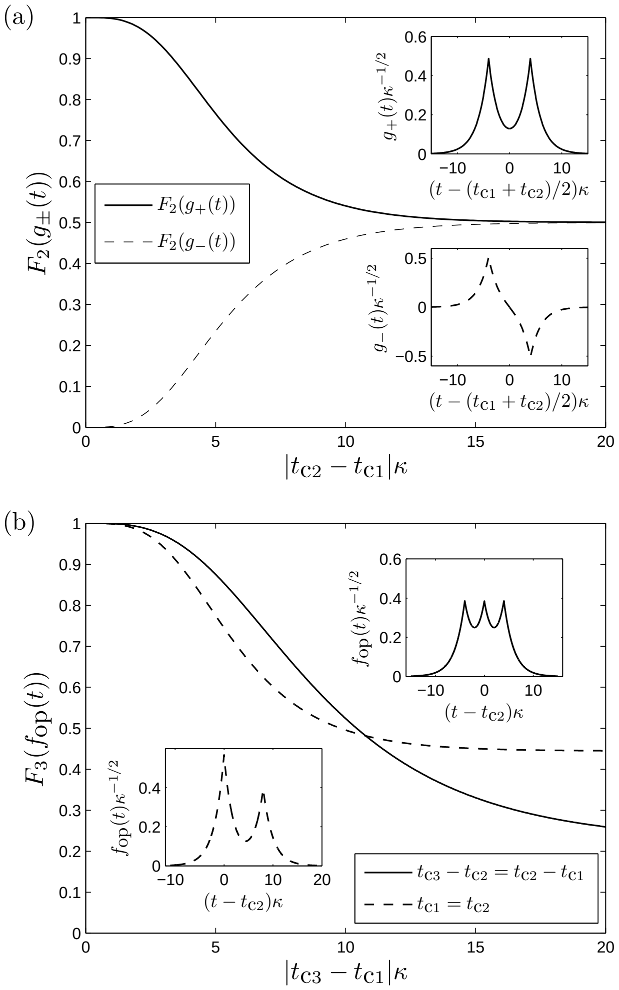

Figure 4.3: (a) Two-photon state fidelity for the modes with mode functions $g_\pm(t)$ for $n = 2$ as a function of the separation between the trigger detection events in the limit $\epsilon/\kappa \to 0$ and $\eta'_{\mathrm{s}} = 1$. The mode functions are shown for $\kappa(t_{c2} - t_{c1}) = 8$ in the insets. Note that $f_{\mathrm{op}}(t) = g_+(t)$ and $F_2(g_+(t)) + F_2(g_-(t)) = 1$. (b) Optimal three-photon state fidelity as a function of the separation between the detection events for $n = 3$ and $t_{c3} - t_{c2} = t_{c2} - t_{c1}$ (solid) or $t_{c1} = t_{c2}$ (dashed) in the limit $\epsilon/\kappa \to 0$ and $\eta'_{\mathrm{s}} = 1$. The upper right (lower left) inset is the optimal mode function for the former (latter) case and $\kappa(t_{c3} - t_{c1}) = 8$.

we have $F_3(f_{\text{op}}(t)) \to 2/9$ for $t_{\text{c}2} - t_{\text{c}1} = t_{\text{c}3} - t_{\text{c}2}$. More generally, when all detection events are well-separated, we have $c_1 = c_2 = \ldots = c_n = n^{-1/2}$, and the single-mode operators $\hat{b}_i \equiv \int g_i(t)\hat{b}_-(t)dt$ become independent such that $[\hat{b}_i, \hat{b}_j^\dagger] = \delta_{ij}$ and $|\psi_n\rangle = \hat{b}_1^\dagger \hat{b}_2^\dagger \ldots \hat{b}_n^\dagger |0\rangle$. In this limit,

$$F_n(f_{\text{op}}(t)) \to |\langle 0|\hat{b}_1\hat{b}_2\ldots\hat{b}_n \frac{1}{\sqrt{n!}}\left(\frac{1}{\sqrt{n}}\left(\hat{b}_1^\dagger + \hat{b}_2^\dagger + \ldots + \hat{b}_n^\dagger\right)\right)^n |0\rangle|^2 = \frac{n!}{n^n}. \tag{4.27}$$

For $t_{\text{c}2} = t_{\text{c}1}$, we have $F_3(f_{\text{op}}(t)) \to 4/9$, which can also be obtained from a simple calculation similar to the one above.

4.4 Conclusion

We have considered preparation of single- and higher-photon number states occupying a single mode of the signal beam from a continuous wave OPO conditioned on a specific outcome of a measurement applied to the trigger beam. For single-photon state preparation, we have provided an expression for the conditional state of an arbitrary mode of the signal beam conditioned on a single photodetection event in the trigger beam, and we have used this expression to calculate the single-photon state fidelity, from which we could optimize the choice of signal mode function numerically. It has turned out that the mode function $\sqrt{\kappa/2}\exp(-\kappa|t-t_{\text{c}}|/2)$, which is optimal in the limit of zero pump intensity, is, in fact, close to optimal for all values of ϵ/κ that lead to a high fidelity. In addition, a comparison with experimental results have shown that the model predicts the correct rate of trigger detection events, but the calculated fidelity is too high, which can be due to inefficient filtering in the experiment.

Since the weak pump limit provides useful results for single-photon state generation, we have considered preparation of general photon number states in that limit. We have shown that each detection event in the trigger beam effectively creates a single photon in the signal beam mode with mode function $\sqrt{\kappa/2}\exp(-\kappa|t - t_{\text{c}i}|/2)$, where $t_{\text{c}i}$ is the detection time, and we have found that the optimal choice of signal mode function is a weighted sum of these functions. We have provided the explicit weight factors for a few special cases and found that the optimized n-photon state fidelity is close to unity even if the n trigger detection events are not exactly simultaneous.

Chapter 5

Absolute timing and pulsed light sources

The experiments demonstrating heralded generation of quantum states of light by application of PDC and conditional measurements cited in the last chapter use either a continuous wave (CW) OPO as light source or pulsed single-pass (SP) PDC in free space. For sources based on a CW OPO, the cavity enhances the down conversion efficiency and limits the bandwidth of the down converted field to the bandwidth of the cavity (which is typically some megahertz). As a consequence, it is possible to obtain a high spectral brightness (number of photons produced per unit time per unit bandwidth) compared to the sources based on SP PDC (for instance, a factor of 10^4 higher [67]). The narrow bandwidth is particularly important in experiments involving interactions between the generated light states and atoms since the linewidth of atomic transitions is on the megahertz scale. The cavity also ensures that the down converted field is emitted into a well-defined spatial mode in contrast to the case of SP PDC, where spatial filtering is used to define the modes. For the pulsed setup, the generated states are naturally confined to particular parts of the signal beam because photon pairs are only generated during the periods where a pump pulse passes through the crystal. It is thus possible to generate, e.g., a single-photon state at a predefined time with a certain success probability. In the CW case, on the other hand, photon pairs may be generated at any time.

In this chapter, we are particularly concerned with the possibility to generate quantum states of light, which can subsequently be stored in atomic ensembles. For this purpose, it is desirable to have a source with a narrow bandwidth and at the same time be able to generate the quantum state at a predefined time because the mapping of the state of a particular mode of the signal beam onto atomic degrees of freedom can be accomplished by use of a strong storage pulse [68], which should, of course, be synchronized with the state preparation. If we insist on using a CW OPO, we could, in principle, wait until the state preparation protocol is successful and then generate the strong pulse at the right time relative to the arrival time of the state, but this approach is undesirable in practise because it would be necessary to delay the quantum state, for instance, by sending it through a very long optical fiber, which would introduce additional losses and hence degrade the mapping fidelity. Alternatively, we could initiate the generation of the strong pulse and then condition on a trigger detection event at the right time relative to the arrival time of the strong pulse, but since the success probability vanishes in the limit, where the detection event is required to take place at a precise time, we are led to consider whether it is practical to condition on a detection event occurring at any time within a predefined interval of finite duration T. We address this question below, where we also investigate the possibility to combine the benefits of the CW OPO and pulsed SP PDC by using an OPO pumped with pulses that are longer than the length of the OPO cavity. To do so, we need the full multimode theory developed in Sec. 3.2. This project has also been motivated by an ongoing experiment in Eugene Polzik's group, which has now been published in [67].

In Sec. 5.1, we present our model and explain how we compute the conditional state of the signal beam numerically. We then discuss the performance of the protocol in Sec. 5.2, where we also briefly consider SP PDC. In Sec. 5.3, we provide examples of optimized mode functions and observe how they differ from the optimal mode functions in Chap. 4. We also derive a simple expression, which approximates the optimal mode function for pulsed pump fields and large T. The chapter is based on [IV][1].

5.1 Model and parameters

In this chapter, we consider a slightly different conditional state preparation protocol, which is illustrated in Fig. 5.1. The OPO is of type I, and we use a beam splitter to divide the output field into a signal beam and a trigger beam. The filter in the trigger channel selects the degenerate peak of the OPO output. When the reflectivity of the beam splitter is low, it is unlikely to reflect more than one photon into the trigger beam at a time, and the conditional state is thus a photon subtracted squeezed vacuum state. In the lossless case, such a state is a superposition of only odd photon number states, and for low pump intensities it reduces to a single-photon state. Here, we would like to produce nonclassical states with negative values of the Wigner function, and we thus optimize the signal mode function in order to obtain the most negative value of the conditional Wigner function at the origin of phase space $W_{\mathrm{c}}(0,0)$ (the position where the Wigner function of a single-photon state attains its most negative value (Eq. (2.21) and Fig. 2.1)). Since $W(0,0) = \sum_{n=0}^{\infty}(\rho_{2n,2n} - \rho_{2n+1,2n+1})/\pi$ for a single-mode state with

---

[1] Copyright (2007) by the American Physical Society.

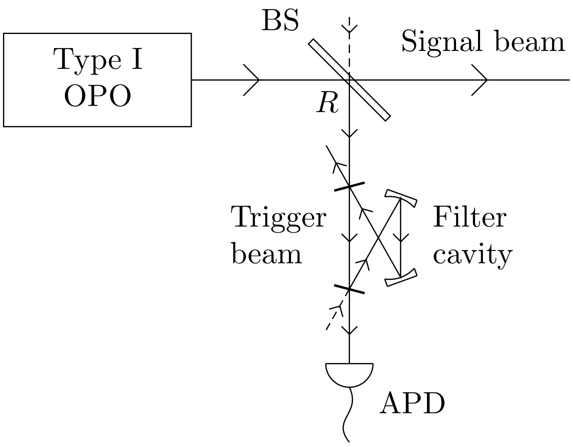

Figure 5.1: Setup to conditionally prepare a photon subtracted squeezed vacuum state. The output field from the OPO is divided into a trigger beam and a signal beam at the beam splitter BS with reflectivity $R \ll 1$ (the second input is a vacuum state). The field reflected into the trigger channel is filtered and observed with an APD, and the state preparation is conditioned on a trigger detection event within a predefined time interval of duration T. The resonance frequency of the filter is chosen as half of the carrier frequency of the OPO pump field.

density operator $\rho = \sum_{n=0}^{\infty}\sum_{m=0}^{\infty}\rho_{nm}|n\rangle\langle m|$ in the photon number state basis [18], this is equivalent to maximizing the odd photon number state contents.

When we compute the conditional state of the signal beam, we need to average over all possible detection records, which are accepted as successful. Trigger modes outside the acceptance interval of duration T can be traced out as usually, and the interval itself is divided into $m = T/\Delta t$ time-localized modes of (infinitesimal) width Δt. For low trigger beam intensity and/or low trigger channel efficiency, which are the relevant conditions for the parameters considered below, we can neglect the possibility to detect two or more photons within the interval. The Wigner function of the state produced in a single mode of the signal beam is then $W_{\mathrm{c}}(x_{\mathrm{s}}, p_{\mathrm{s}}) = \sum_{i=1}^{m} P_i W_{\mathrm{c}i}(x_{\mathrm{s}}, p_{\mathrm{s}}) / \sum_{j=1}^{m} P_j$, where $W_{\mathrm{c}i}(x_{\mathrm{s}}, p_{\mathrm{s}})$ is the Wigner function of the signal mode obtained when we condition on a detection event in the ith trigger mode, P_i is the probability to observe a detection event in that mode, and $P = \sum_{i=1}^{m} P_i$ is the success probability of the protocol. Note that $P_i = \langle \hat{b}_{\mathrm{t}i}^{\dagger}\hat{b}_{\mathrm{t}i}\rangle$, where $\hat{b}_{\mathrm{t}i}$ is the field annihilation operator of the ith trigger mode. We can compute $W_{\mathrm{c}i}(x_{\mathrm{s}}, p_{\mathrm{s}})$ and P_i by following the same steps as in Sec. 4.1, i.e., we express $\hat{b}_{\mathrm{t}i}$ and the annihilation operator $\hat{b}_{\mathrm{s}}$ of the signal mode in terms of the annihilation operators of the OPO output field (using (2.28) and the Fourier transform of (3.16)), we compute V and

Quantity	Symbol	Value
OPO round trip time	τ	2.7 ns
Loss in OPO cavity	r_2^2	0.004
Transmission of OPO output mirror	t_1^2	0.127
Beam splitter reflectivity	R	0.05
Filter bandwidth (FWHM)	$2\kappa_{\mathrm{F}}$	$2\pi \times 90$ MHz
Trigger channel efficiency	η_{t}	0.07
Signal channel efficiency	η_{s}	0.70

Table 5.1: Parameters used in the numerical calculations. The values are chosen in accordance with Refs. [30, 31, 36]. ($\tau = 2.7$ ns corresponds to a length of the OPO cavity of 81 cm.)

$\langle\hat{y}\rangle$ (by use of (3.8) and (3.9)) and write down the Gaussian Wigner function of the two modes, and finally we apply the transformation in (4.2). Alternatively, we can calculate the Gaussian Wigner function of the signal and the trigger modes before conditioning in the Schrödinger picture, i.e., we start with the Gaussian Wigner function for a multimode vacuum state and apply the appropriate beam splitter and squeezing transformations to the covariance matrix. We use the former method for CW pump fields, and the latter for pulsed pump fields. In both cases we optimize the signal mode function over all real functions.

The parameters used in this chapter are summarized in table 5.1. Note that the filter bandwidth $2\pi \times 90$ MHz is broad compared to the bandwidth of the peaks of the spectrum of the output from a CW OPO ($\approx (t_1^2 + r_2^2)/\tau = 2\pi \times 7.7$ MHz), but narrow compared to the distance $2\pi/\tau = 2\pi \times 370$ MHz between two peaks as shown in Fig. 3.2. For the case of a CW pump field, we choose values of $|\chi|$ (see Eqs. (3.3) and (3.4)), for which the total flux of photons in the degenerate peak of the OPO output field is of order 2×10^6 s^{-1} as in Ref. [30]. This corresponds to a success probability of $P = 2\times10^6\ \mathrm{s}^{-1} \times R\eta_{\mathrm{t}}T = 1.9 \times 10^{-4}$ for $T/\tau = 10$. For the case of pulsed pump fields we assume that the pump pulse has a Gaussian envelope such that

$$|\chi(t)| = \frac{2s\tau^{1/2}}{\pi^{1/4}T_{\mathrm{p}}^{1/2}} \exp\left(-\frac{t^2}{2T_{\mathrm{p}}^2}\right), \tag{5.1}$$

where s and T_{p} quantify the strength and the duration of the pulse, respectively. Note that (5.1) is defined in a rotating frame as in the previous chapter. Outside the rotating frame there is an extra factor of $e^{-2i\omega_0 t}$ on the right hand side. The value of s is chosen to obtain similar success probabilities as for the CW case. The temporal position of the trigger acceptance interval is arbitrary for CW pump fields, but for pulsed pump fields we choose the position to maximize the success probability. Finally, we require that T is at least as large as the temporal resolution of the APD detector (≈ 1 ns [36] or 0.4 τ).

5.2 Success probability and $W_{\mathrm{c}}(0,0)$

Several examples of numerical results for P and $W_{\mathrm{c}}(0,0)$ are provided in Fig. 5.2. Considering Fig. 5.2(a), we observe that the success probability increases with $|\chi|$ for the CW case and with s for fixed T_{p} for the pulsed case as expected. It also increases with T because the number of terms in the sum $\sum_{i=1}^{m} P_i$ increases. For CW fields, all P_i are equal and the increase is linear, but for pulsed pump fields, the curves approach a constant value as T exceeds the temporal width of the trigger beam intensity distribution, which is roughly of order the width of the intensity distribution of the pump field ($\approx 2T_{\mathrm{p}}$) plus the standard deviation of the lifetime of a photon in the OPO cavity ($\approx \kappa^{-1} \equiv \tau/(t_1^2 + r_2^2) = 7.6\ \tau$) plus the standard deviation of the lifetime of a photon in the filter cavity ($(2\kappa_{\mathrm{F}})^{-1} = 0.7\ \tau$).

Figure 5.2(b) shows that it is, indeed, possible to obtain negative values of $W_{\mathrm{c}}(0,0)$ for noninfinitesimal values of T and realistic experimental parameters. It is also apparent that more negative values of $W_{\mathrm{c}}(0,0)$ are realized for short pulses than for CW fields with similar success probabilities, and this difference is particularly pronounced for large T. We note that it is preferable to have a low signal beam intensity because we optimize the odd photon number state contents of the produced state, and an odd photon number state with more than one photon transforms into a state with almost equal odd and even photon number state contributions if it is subjected to a loss of $1-(1-R)\eta_{\mathrm{s}} t_1^2/(t_1^2+r_2^2) = 36\ \%$, while a single-photon state is transformed into a state with a single-photon state fidelity of 0.64 and a zero-photon state fidelity of 0.36. When T is short compared to the temporal width of the trigger beam intensity distribution after the filter, we find that the number of photons in the optimal signal mode function is smaller for pulses than for CW fields with similar success probabilities. This appears because the requirement of equal success probabilities for small T forces the maximal flux of photons in the trigger beam in the pulsed case to be equal to the constant flux of photons in the trigger beam in the CW case. We thus expect a more negative value of $W_{\mathrm{c}}(0,0)$ for pulses as observed in the figure.

For noninfinitesimal values of T, the optimal signal mode function is a compromise between the optimal signal mode functions obtained by conditioning on a detection event at a precise time within T, and we expect that $W_{\mathrm{c}}(0,0)$ is less negative if these mode functions are very different. For CW fields the compromise is between a set of mode functions similar to those in Fig. 4.2(b), but positioned with equal spacings along the acceptance interval, and as T increases the overlap between the first and the last mode function decreases, which explains the observed increase in $W_{\mathrm{c}}(0,0)$ with T. Referring to Eq. (4.15), we expect this effect to set in, when $\kappa T/2$ is of order unity, i.e., when $T \sim 2/\kappa = 15\ \tau$ (or $T \sim 2/\kappa + 1/\kappa_{\mathrm{F}} = 17\ \tau$ if we take the filter cavity into account), which agrees with the figure (the origin of the

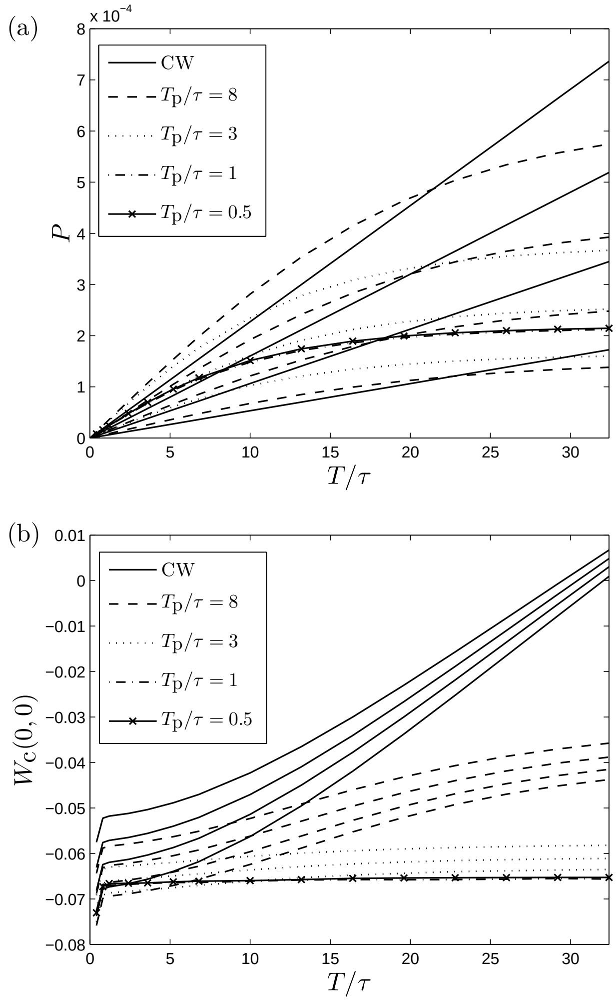

Figure 5.2: (a) Success probability P and (b) value of the conditional Wigner function at the origin $W_\mathrm{c}(0,0)$ as a function of the duration T of the trigger acceptance interval. Solid lines: CW pump field with $|\chi| = 0.010$, 0.014, 0.017, and 0.020; dashed lines: pulsed pump field with $T_\mathrm{p}/\tau = 8$ and $s = 0.030$, 0.040, 0.050, and 0.060; dotted lines: pulsed pump field with $T_\mathrm{p}/\tau = 3$ and $s = 0.040$, 0.050, and 0.060; dash-dotted line: pulsed pump field with $T_\mathrm{p}/\tau = 1$ and $s = 0.070$; solid line with crosses: pulsed pump field with $T_\mathrm{p}/\tau = 0.5$ and $s = 0.097$. Within each series a smaller s or $|\chi|$ corresponds to a more negative value of $W_\mathrm{c}(0,0)$ and a smaller success probability. The dash-dotted line and the solid line with crosses almost coincide in the figure.

steep rise to the very left will be explained in the next section).

For pulses, on the other hand, the optimal signal mode function obtained by conditioning on a detection event at a precise time is determined both by the detection time and the shape of the pump pulse, and modes corresponding to detection events in the outer parts of the acceptance interval are not important if T is large compared to the temporal width of the trigger beam intensity distribution after the filter because the probability to detect a photon in these outer regions is small. For large T the square of the norm of the optimal mode function approximately follows the intensity distribution in the signal beam, and $W_{\mathrm{c}}(0,0)$ approaches a constant value. If the temporal width of $|\chi(t)|$ ($\approx 2\sqrt{2}\ T_{\mathrm{p}}$) is short compared to $2/\kappa + 1/\kappa_{\mathrm{F}}$, we do not observe a significant increase in $W_{\mathrm{c}}(0,0)$ with T before the constant value is reached because the broadening of the optimal mode function due to the presence of the OPO cavity and the filter is large compared to the time interval in which the pump field is turned on, i.e., if we condition on a detection event at a precise time, we obtain almost the same optimal mode function independent of the actual detection time in the trigger beam. In other words, the detection time provides very little information about the time at which the photon is created in the crystal because the standard deviation of the lifetime of a photon in the OPO cavity plus the standard deviation of the lifetime of a photon in the filter cavity is large compared to the duration of the time interval in which photon pairs are created. In the figure, we indeed observe a significant increase in $W_{\mathrm{c}}(0,0)$ with T for the curves with $T_{\mathrm{p}}/\tau = 8$, while there is almost no increase for the curves with $T_{\mathrm{p}}/\tau = 3$, 1, and 0.5 in the region $T > \tau$, and the curves become more and more constant as T_{p} decreases.

It is undesirable to choose pump pulses that are shorter than the length of the OPO cavity. The enhancement effect of the cavity disappears in this limit because the pump pulse is already gone when the down converted field returns to the crystal after one round trip. Each of the time-localized cavity modes is thus at most subjected to a single squeezing operation. This effect is also apparent in the figure as we need to increase s when we decrease T_{p} to avoid a reduction in success probability. We expect the increase in s to eventually lead to an increase in $W_{\mathrm{c}}(0,0)$ as demonstrated below for SP PDC. Furthermore, if the pulses are short compared to the length of the OPO cavity, the frequency bandwidth of the down converted field exceeds the free spectral range of the cavity, which is better avoided if the light is to interact with a collection of atoms.

Single-pass parametric down conversion

Before proceeding we briefly discuss SP PDC. We note that the purpose of the present subsection is to clarify the role of the OPO cavity in the results obtained above. It is not meant as a model of the experiments in, for instance, Philippe Grangier's group, which would require several adjustments. We should, for instance, decrease the length of the pulses to femtosecond pulses and consider the transverse structure of the fields more carefully. A detailed model of these experiments is provided in [69]. SP PDC combined with conditional measurements is also discussed in [64, 70].

We found above that negative values of $W_{\mathrm{c}}(0,0)$ can be achieved for large T if the optimal mode functions obtained by conditioning on a detection event at a precise time within the acceptance interval does not depend very much on the chosen detection time. To achieve this, it is important that the actual detection time of a photon in the trigger beam does not allow us to say precisely when the second photon from the same pair leaves the source. When the cavity is absent, it is only the delay in the filter cavity in the trigger channel, which can separate the two photons temporally. We thus only expect negative values of $W_{\mathrm{c}}(0,0)$ if $\min(T, 2T_{\mathrm{p}})$ is small compared to the standard deviation $(2\kappa_{\mathrm{F}})^{-1}$ of the lifetime of a photon in the filter cavity.

In Fig. 5.3, we have plotted $W_{\mathrm{c}}(0,0)$ as a function of half of the bandwidth of the filter cavity for $T_{\mathrm{p}} = 2.7$ ns and T much larger than the temporal width of the trigger beam intensity distribution after the filter. These results are obtained exactly as above except that $t_1^2 = 0$. As expected we observe negative values for small $\kappa_{\mathrm{F}} T_{\mathrm{p}}$, but $W_{\mathrm{c}}(0,0)$ does not continue to decrease with decreasing $\kappa_{\mathrm{F}} T_{\mathrm{p}}$. To understand this effect, we have also plotted the values of s required to keep the success probability at 2×10^{-4} and the expectation value of the number of photons in the optimized signal mode. When we decrease the bandwidth of the filter, fewer photons are allowed to pass, and we need to increase s to keep the success probability constant. At the same time, the increase in s also increases the expectation value of the number of photons in the generated pulse in the signal beam, which in turn leads to less negative values of $W_{\mathrm{c}}(0,0)$ due to losses as explained above. Finally, we note that the required values of s are significantly higher for SP PDC due to lack of the enhancement effect of the cavity. The inset in Fig. 5.3 illustrates the reduction of the bandwidth of the square of the norm of the optimal signal mode function in frequency space when the OPO cavity is included in the setup.

5.3 Optimal mode function

CW pump fields

A few examples of optimal mode functions for the case of a CW pump field are shown in Fig. 5.4. The main plot is the optimized mode function for $|\chi| = 0.017$ and $T/\tau = 0.4$. Also for this setup, we expect the optimal mode function to take the form $\sqrt{\kappa/2}\exp(-\kappa|t - t_{\mathrm{c}}|/2)$ in the limit of low pump intensity, no loss, and $R \to 0$ when T is infinitesimal and we use the

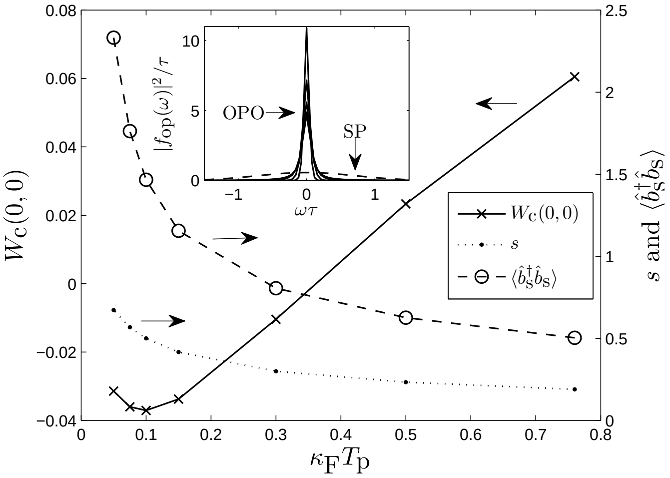

Figure 5.3: $W_{\mathrm{c}}(0,0)$ (solid line with crosses), s (dotted line with dots), and expectation value (after loss) of the number of photons in the optimal signal mode (dashed line with rings) as a function of half of the filter bandwidth for single-pass parametric down conversion with a pulsed pump field with $T_{\mathrm{p}} = 2.7$ ns. T is long compared to the trigger beam intensity distribution after the filter, and s is chosen to keep the success probability at $P = 2 \times 10^{-4}$. The rightmost point corresponds to the filter bandwidth used in Fig. 5.2. The inset shows examples of $|f_{\mathrm{op}}(\omega)|^2$, where ω is measured with respect to ω_0. The dashed line is for the same parameters as the point at $\kappa_{\mathrm{F}} T_{\mathrm{p}} = 0.1$ in the main plot. In order of increasing width, the solid lines are for $T/\tau = 32.4$ and a CW OPO with $|\chi| = 0.014$, a pulsed OPO with $s = 0.040$ and $T_{\mathrm{p}}/\tau = 8$, a pulsed OPO with $s = 0.050$ and $T_{\mathrm{p}}/\tau = 3$, a pulsed OPO with $s = 0.070$ and $T_{\mathrm{p}}/\tau = 1$, and a pulsed OPO with $s = 0.097$ and $T_{\mathrm{p}}/\tau = 0.5$.

two-time correlation functions in Eqs. (3.13) for the OPO output. When we do not take the limit $\tau \to 0$, however, we observe some additional features. In particular, there is a fast variation of period τ. To understand this, we note that a given time-localized mode inside the OPO cavity only hits the output beam splitter at times separated by τ. Two photons generated at the same time inside the crystal hence leave the cavity at times separated by an integer number of τs, and without filtering, the optimal mode function would consist of a series of spikes separated by τ. If the filter cavity is present, the trigger photon is delayed by an unknown amount, but since the standard deviation of the lifetime of a photon in the filter cavity is only about 0.7 τ, the detection time still provides partial information about the time of generation of the photon pair, and the optimal mode function exhibits a periodic variation. The optimal mode function is also shifted slightly to the left due to the extra delay of the trigger photon compared to the signal photons.

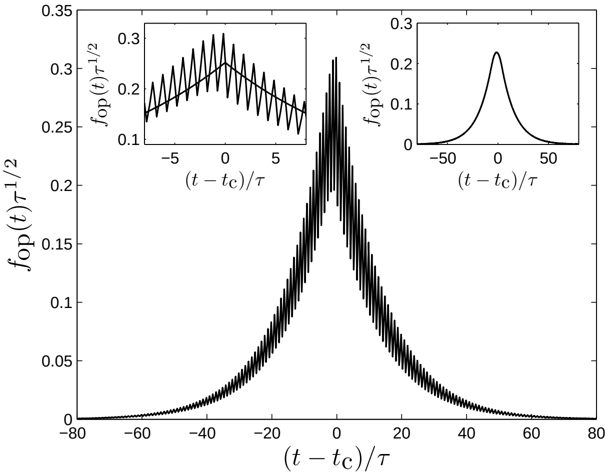

Figure 5.4: Optimal signal mode function for $T/\tau = 0.4$ and a CW pump field with $|\chi| = 0.017$. Here, t_{c} denotes the midpoint of the acceptance interval. The left inset shows an enlarged view of the mode function and the function $\sqrt{\kappa/2}\exp(-\kappa|t-t_{\text{c}}|/2)$ with $\kappa = (t_1^2 + r_2^2)/\tau = 2\pi \times 7.7$ MHz, and the right inset is the optimal mode function for $T/\tau = 10$. The lack of perfect symmetry around $t = t_{\text{c}}$ is a consequence of the filtering.

If T is increased, we need to make a compromise between the mode functions obtained for infinitesimal T, but since these mode functions have local maxima at different positions, the overlap is not perfect. This explains the rapid increase in $W_{\text{c}}(0,0)$ to the very left in Fig. 5.2(b). When T exceeds τ, the fast variation is smoothed out, and the increase in $W_{\text{c}}(0,0)$ with T is slower because the optimal mode function for a detection event at time t_{c} has local maxima at the same positions as the optimal mode function for a detection event at time $t_{\text{c}} + \tau$.

Pulsed pump fields

For pulsed pump fields, we also observe a fast variation of period τ for small T, which is smoothed out when T exceeds τ. The optimal mode function for $T/\tau = 32.4$, $T_{\text{p}}/\tau = 3$, and $s = 0.05$ is shown in Fig. 5.5, where we have also plotted $|\chi(t)|$. As expected, the generated output field is broadened and delayed compared to the pump field because the generated photons spend an unknown amount of time in the OPO cavity. Since $W_{\text{c}}(0,0)$ and P are both independent of T for large T, and since we must choose the same mode function independent of the actual trigger detection time, the optimal mode function is determined solely from the generated output field when T is large. In this limit, it seems reasonable that the optimal mode function just follows the square root of the intensity distribution in the signal beam.

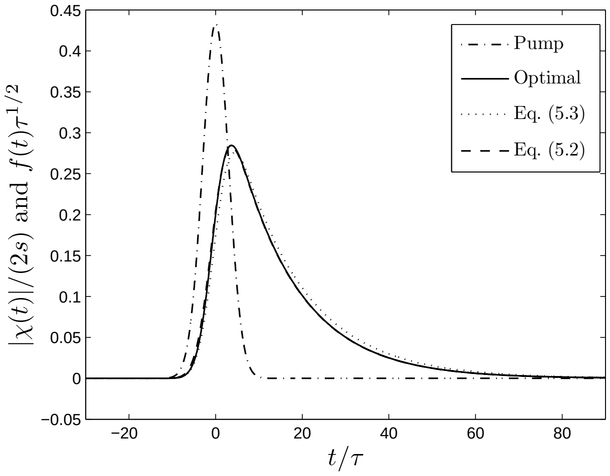

Figure 5.5: Pump pulse (dash-dotted) and optimal mode function (solid) for $T_\mathrm{p}/\tau = 3$, $s = 0.05$, and $T/\tau = 32.4$. The dotted line is the function in Eq. (5.3), and the dashed line, which is almost indistinguishable from the optimal mode function in the figure, is the function in Eq. (5.2). $W_\mathrm{c}(0,0) = -0.0591$ for the dotted line, -0.0610 for the dashed line, and -0.0611 for the solid line.

Calculating the intensity distribution from Eq. (3.8), this argument leads to

$$f_\mathrm{op}(t) \propto \sqrt{\sum_{n=0}^{\infty} (r_1 t_2)^{2n} \sinh^2\left(\sum_{k=0}^{n} |\chi(t-k\tau)|\right)}. \tag{5.2}$$

Without the above theory at hand, a first guess for the optimal mode function for large T would be the convolution

$$f_\mathrm{op}(t) \propto \int_{-\infty}^{t} |\chi(t')| \exp\left(-\frac{\kappa}{2}(t-t')\right) dt', \tag{5.3}$$

which is the transformation one would get by filtering $|\chi(t)|$ with an empty and infinitely small cavity with decay rate $\kappa = (t_1^2 + r_2^2)/\tau$. In Fig. 5.5, we see that both functions are indeed quite close to optimal, but (5.2) provides a better estimate than (5.3).

5.4 Conclusion

In conclusion, we have found that it is possible to prepare states with a negative value of the Wigner function at the origin of phase space for realistic experimental parameters if we condition on a detection event at any time within an interval of finite duration T. To achieve negative values, the optimal mode functions obtained by conditioning on a precise detection time within T should not depend too much on the choice of detection time. In particular, it is important that the detection time of a trigger photon does not provide precise information on the time at which the second photon from the same pair leaves the source. The two photons are always generated at the same time inside the crystal, but the OPO cavity and the filter cavity broaden the temporal profiles and lead to the required uncertainty in the temporal separation between the two. In general, we need to require that either T or the temporal width of the pump pulses is short compared to the sum of the inverse of the decay rates of the two cavities. On the other hand, the duration of the pump pulses should be longer than the round trip time of light in the OPO cavity in order to benefit from the enhancement effect of the down conversion process in a cavity and in order to limit the bandwidth of the down converted field. We have also provided a simple analytical approximation to the optimal mode function in the limit, where T is much longer than the temporal width of the trigger beam intensity distribution after the filter, and we have presented a theoretical model, which allows us to calculate the optimal mode function and the Wigner function of the prepared state in general.

The prediction of negative values of the Wigner function at the origin for finite T has been verified experimentally in [67]. We can, however, not directly compare the results obtained here with the experimental values because the experimental setup involves a nondegenerate OPO rather than a degenerate OPO and the shape of the pump pulses is close to rectangular and not Gaussian. In the experiment, pulses are obtained from a CW beam by use of a pulse shaping element, which should also be included in the modeling, in particular because the element does not completely extinguish the field between the pulses. Nevertheless, the experimentally measured value of $W_{\mathrm{c}}(0,0)$ for a pulse of duration 49 ns and an acceptance window of $T = 40$ ns $= 15\ \tau$ is -0.061, which is approximately the same as our results for a pump pulse with $2T_{\mathrm{p}} = 16\ \tau = 43$ ns. For a pump pulse of duration 20 ns, on the other hand, the measured value of $W_{\mathrm{c}}(0,0)$ is 0.027, even though we would expect a more negative value for the shorter pulse. In [67], it is suggested that the high value is due to a decrease in the signal to noise ratio.

Chapter 6

Large amplitude Schrödinger cat states

Conditional measurements constitute a versatile tool to transform quantum states of light, and there are several more possibilities than those we have already investigated. In the present chapter, we propose a scheme to conditionally generate large amplitude Schrödinger cat states [V][1], and in [III], we have suggested a protocol to prepare $N00N$ states.

A Schrödinger cat state is a quantum superposition of macroscopically distinguishable states, and it is of fundamental interest because it demonstrates quantum mechanical behavior on a macroscopic scale. Such superpositions are very fragile because a measurement performed on just a tiny bit of the state is sufficient to project the state onto one of the states in the superposition, and it is thus completely essential to avoid losses during and after preparation, which is difficult to achieve in experiments. In quantum optics the term Schrödinger cat state is traditionally used for a superposition of two coherent states such as the even (+) and odd (−) cat states

$$|\psi_{\mathrm{cat}}^{\pm}\rangle = \frac{1}{\sqrt{2(1 \pm \exp(-2|\alpha|^2))}} \left(|\alpha\rangle \pm |-\alpha\rangle\right). \tag{6.1}$$

We shall refer to the parameter α as the amplitude of the cat state, and $|\alpha|^2$, which is proportional to the distance in phase space between the maxima of the (Gaussian) Wigner functions corresponding to $|\alpha\rangle$ and $|-\alpha\rangle$, quantifies the size of the cat. We note that the two components of the cat state are only truly distinguishable for large $|\alpha|^2$ since $|\langle -\alpha|\alpha\rangle|^2 = \exp(-4|\alpha|^2)$. Schrödinger cat states are one of the main ingredients in coherent state quantum computing with linear optics and photon counting detectors as proposed in [71, 72]. In [71], cat states with $|\alpha| \geq \sqrt{6} \approx 2.45$ are requested, and we thus use $|\alpha| = \sqrt{6}$ as a reference value in the following even though

---

[1] Copyright (2007) by the American Physical Society.

it has now been shown [72] that states with $|\alpha| > 1.2$ suffice for quantum computing.

$N00N$ states are two-mode states of the form $|\psi_{N00N}\rangle = 2^{-1/2}(|N\rangle|0\rangle + e^{i\phi}|0\rangle|N\rangle)$, where $e^{i\phi}$ is an arbitrary phase factor and $|N\rangle$ is a photon number state. They have attracted much attention due to the fact that the relative phase of the two terms changes by $N\zeta$ if one of the modes is subjected to a single-photon phase shift of ζ. This property can be utilized to improve the precision of interferometric measurements [73] and to enhance the spatial resolution in quantum lithography [44]. A common strategy to investigate properties of $N00N$ states experimentally is to construct detection procedures, which are able to select the $N00N$ state component of quantum states delivered by the source in the experiment [74]. On the contrary, our proposal [III] is constructed to actually generate high fidelity $N00N$ states by use of an experimentally realistic setup. (In fact, the required setup is the same as the one used recently to analyze a photonic six-qubit singlet state in [75].) The analysis provided in [III] shows that the formalism used in Chaps. 4 and 5 for CW fields also provides a useful tool to obtain analytical results for measurements applied to single and few-mode Gaussian fields. We shall, however, not discuss the protocol further here.

In the following, we would like to focus on the quantum state engineering aspect rather than the multimode character of the fields, and we thus simplify to a single-mode description. In particular, we assume that our resource states are single-mode squeezed vacuum states

$$|\psi_{\mathrm{SMSS}}\rangle = e^{\frac{|\chi|}{2}((\hat{b}^\dagger)^2-\hat{b}^2)}|0\rangle = (1-\lambda^2)^{1/4}\sum_{n=0}^{\infty}\sqrt{\frac{(2n)!}{2^{2n}n!^2}}\lambda^n|2n\rangle, \tag{6.2}$$

where $\lambda \equiv \tanh(|\chi|)$, $\hat{b}$ is the annihilation operator of the mode, and we have chosen the phase convention $\chi = i|\chi|$ in Eq. (3.3). Such states are often used as an approximation to the outcome of SP PDC with short pulses. For an OPO, the above state is approximately obtained in the limit of a very small round trip time of light in the OPO cavity and a pump pulse duration much shorter than the inverse of the OPO cavity decay rate. Furthermore, we use either the on/off detector model or the photon number state resolving detector model from Sec. 2.4. Multimode results for $N00N$ state generation by use of CW OPO sources are provided in [III].

In Sec. 6.1, we discuss different methods to generate Schrödinger cat states of light before we present the details of our proposal in Sec. 6.2. The optimal cat state fidelity of the generated states is computed in Sec. 6.3, and in Sec. 6.4 we discuss the success probability of our protocol.

6.1 Methods to generate Schrödinger cat states

In [76], it has been realized that states obtained by mixing a vacuum state and a single-mode squeezed vacuum state on a beam splitter and conditioning on measuring an m-photon state in one of the output modes is very similar to an odd (even) Schrödinger cat state for m odd (even). Accurate photon number state resolving detection is not yet feasible in practice, but a successful strategy has been to suppress the high-photon number state components in the observed mode by choosing a beam splitter with low reflectivity. The measurement back action of a single photodetection event in the trigger channel is then very similar to projecting the trigger mode on a single-photon state. It thus turns out that the photon subtracted squeezed vacuum states considered in the previous chapter have a high odd cat state fidelity, but only for small amplitude cat states ($|\alpha| \lesssim 1.2$). Such states have been realized experimentally for both pulsed fields [62, 63] and CW fields [30, 36], and the applicability of photon subtracted squeezed vacuum states for teleportation of coherent state superpositions and fundamental tests of quantum mechanics has been investigated in [77] and [78], respectively.

The high fidelity between photon subtracted squeezed states and odd cat states of small amplitude appears because both states are superpositions of odd photon number states and for small $|\alpha|$ and a suitable choice of squeezing parameter the coefficients of the superpositions are similar. For higher values of $|\alpha|$, however, this is no longer the case, and alternative methods are required. One such method is to mix two small cat states with amplitude α on a beam splitter to produce a cat state with amplitude $\sqrt{2}\alpha$ in one of the output ports conditioned on a specific measurement outcome for a measurement applied to the light emerging from the other output port [79]. In principle, it is possible to produce arbitrarily large cat states by this method, but the success probability decreases exponentially with the number of amplification steps.

Cat states with $|\alpha|^2 = 2.6$ squeezed by 3.5 dB have been prepared experimentally in [80]. To achieve this, a two-photon state is first prepared via conditional detection. The state is then mixed with vacuum on a beam splitter and one of the output modes is subjected to homodyne detection. As mentioned in the previous chapter, the Wigner function is $+1/\pi$ at the origin for all even photon number states, but $-1/\pi$ for all odd photon number states, and it turns out to be possible to ensure that the trigger mode contains an even number of photons by conditioning on a measurement result for the detected quadrature, which is sufficiently close to zero. The remaining state in the other output port is then a superposition of $|0\rangle$ and $|2\rangle$, which has a large fidelity with a squeezed even cat state. In principle, this state can then be unsqueezed to obtain the cat state.

The results in [76] show that larger cat states can be obtained, albeit with a smaller success probability, by conditional subtraction of more than one photon as demonstrated experimentally in [81]. In our proposal, we show how a combination of photon subtractions and displacement operations can be used to incorporate free parameters into the expression for the produced state, which can then be optimized to boost the cat state fidelity obtained for a fixed number of photon subtractions. As a side benefit, the required amount of squeezing of the input state is reduced. For the proposed setup, a quantum interference ensures that the subtracted number of photons is always either even or odd, such that the output state is either an even or an odd cat state. A related proposal [82] uses two conditional photodetections and a single displacement operation to synthesize general superpositions of coherent states.

6.2 Ideal transformation and experimental implementation

Let us first consider photon subtraction from a general single-mode input state $\rho_{\mathrm{in},1}$ with annihilation operator $\hat{b}$. The relevant experimental setup is depicted in the leftmost dotted box in Fig. 6.1. The input state is mixed with a vacuum state with annihilation operator $\hat{v}_1$ at a beam splitter BS_1 with reflectivity $R_1 = 1 - T_1$, and the reflected field is observed with a detector. Assuming the on/off detector model and conditioning on an 'on' detection event, we obtain the conditional output state

$$\rho_{\mathrm{out},1} = P_1^{-1} \sum_{n=1}^{\infty} \langle n | U_{\mathrm{BS}_1}^{\hat{v}_1 \hat{b}}(T_1) | 0 \rangle \rho_{\mathrm{in},1} \langle 0 | \left(U_{\mathrm{BS}_1}^{\hat{v}_1 \hat{b}}(T_1) \right)^{\dagger} | n \rangle, \tag{6.3}$$

where P_1, which is determined from the normalization, is the probability of success and the beam splitter operation $U_{\mathrm{BS}_1}^{\hat{v}_1 \hat{b}}(T_1)$ is defined in Eq. (2.27). For T_1 close to unity, we may Taylor expand $P_1 \rho_{\mathrm{in},1}$ to first order in R_1 to obtain $\rho_{\mathrm{out},1} \approx P_1^{-1} R_1 \hat{b} \rho_{\mathrm{in},1} \hat{b}^{\dagger}$. In this limit, the setup thus implements the application of the annihilation operator to the input state.

As noted above, $\hat{b}|\psi_{\mathrm{SMSS}}\rangle$ is a superposition of odd photon number states, while $|\psi_{\mathrm{SMSS}}\rangle$ is a superposition of even photon number states. Our proposal is to apply operators of the form $\hat{O}_k \equiv \prod_{i=1}^{k} (\hat{b}^2 - \beta_i^2)$ to these states, where β_i are arbitrary complex numbers. In this way, $\hat{O}_k \hat{b} |\psi_{\mathrm{SMSS}}\rangle$ ($\hat{O}_k |\psi_{\mathrm{SMSS}}\rangle$) is again a superposition of odd (even) photon number states, but we now have k free complex parameters, which we can choose to maximize the cat state fidelity.

We suggest to implement the operator $\hat{b}^2 - \beta^2$ as in the rightmost dotted box in Fig. 6.1. As shown in [24], the transformation occurring at BS_4 displaces the input field by $i\sqrt{R_4}\phi_4$ in the limit $R_4 \to 0$ for fixed $\sqrt{R_4}\phi_4$ (the field leaving BS_4, which is traveling to the right in the figure, is traced out). The complete conditional transformation occurring when a mode initially in

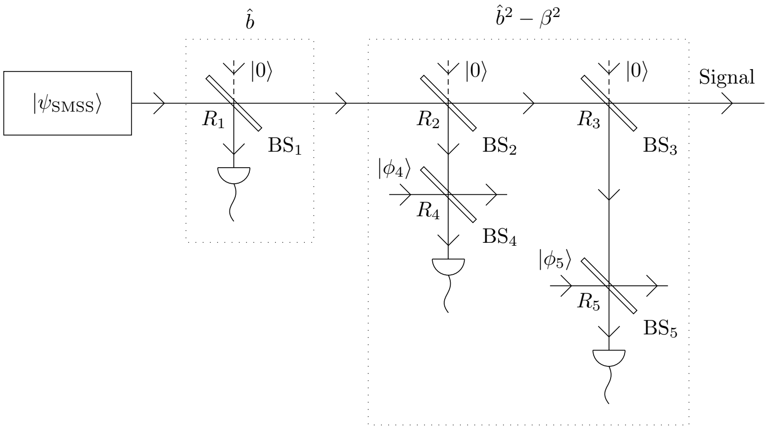

Figure 6.1: Proposed setup to generate large amplitude Schrödinger cat states with high fidelity conditioned on detection events in all the detectors. The source produces a single-mode squeezed vacuum state, $R_i = 1-T_i \ll 1$ is the reflectivity of beam splitter BS_i, $r_i = \sqrt{R_i}$, $t_i = \sqrt{T_i}$, and $|\phi_4\rangle$ and $|\phi_5\rangle$ are coherent states with amplitudes $\phi_4 = r_2\beta/r_4$ and $\phi_5 = -r_3\beta/r_5$, respectively. When all the components are included, the setup produces the state $(\hat{b}^2-\beta^2)\hat{b}|\psi_{\mathrm{SMSS}}\rangle$. To generate the state $(\hat{b}^2-\beta^2)|\psi_{\mathrm{SMSS}}\rangle$, we omit the part inside the leftmost dotted box, to generate the state $\hat{b}|\psi_{\mathrm{SMSS}}\rangle$, we omit the part inside the rightmost dotted box, and to generate the state $|\psi_{\mathrm{SMSS}}\rangle$, we omit the parts inside both of the dotted boxes.

the state $\rho_{\mathrm{in},2}$ passes BS_2 from left to right and an 'on' detection is observed in the detector below BS_4 is hence

$$\rho_{\mathrm{out},2} = P_2^{-1}\sum_{n=1}^{\infty}\langle n|D_{\hat{v}_2}(i\sqrt{R_4}\phi_4)U_{\mathrm{BS}_2}^{\hat{v}_2\hat{b}}(T_2)|0\rangle\rho_{\mathrm{in},2} \otimes \langle 0|(U_{\mathrm{BS}_2}^{\hat{v}_2\hat{b}}(T_2))^{\dagger}(D_{\hat{v}_2}(i\sqrt{R_4}\phi_4))^{\dagger}|n\rangle, \quad (6.4)$$

where P_2 is the success probability, $\hat{v}_2$ is the annihilation operator of the vacuum state entering at the second input port of BS_2, and the displacement operator $D_{\hat{a}}(\alpha) = \exp(\alpha\hat{a}^{\dagger} - \alpha^*\hat{a})$ is defined in Sec. 2.2. To lowest order in R_2, this simplifies to $\rho_{\mathrm{out},2} = P_2^{-1}R_2(\hat{b}+\beta)\rho_{\mathrm{in},2}(\hat{b}^{\dagger}+\beta^*)$. Similarly, if the input state to BS_3 coming from the left is $\rho_{\mathrm{in},3}$, the conditional output state after BS_3 takes the form $\rho_{\mathrm{out},3} = P_3^{-1}R_3(\hat{b}-\beta)\rho_{\mathrm{in},3}(\hat{b}^{\dagger}-\beta^*)$ to lowest order in R_3, where P_3 is the probability to obtain the required 'on' detection event. Combining these two transformations, we see that the setup within the rightmost dotted box in Fig. 6.1 conditionally applies the operator $\hat{b}^2-\beta^2$ to the input state. In other words, by choosing an appropriate value of the ratio between the coherent state amplitudes ϕ_4 and ϕ_5, we ensure that the two subtracted photons both originate either from the input mode or from the two ancilla modes. To implement $\hat{O}_k$, we concatenate k of these elements.

6.3 Cat state fidelity

Since the success probability decreases rapidly with the number of photon subtractions, we concentrate on the states $|\psi_{\mathrm{SMSS}}\rangle$, $\hat{b}|\psi_{\mathrm{SMSS}}\rangle$, $(\hat{b}^2 - \beta^2)|\psi_{\mathrm{SMSS}}\rangle$, and $(\hat{b}^2 - \beta^2)\hat{b}|\psi_{\mathrm{SMSS}}\rangle$ in the following. The setups required to produce these states are shown in Fig. 6.1.

The even cat state fidelity of $|\psi_{\mathrm{SMSS}}\rangle$ evaluates to

$$F_{\mathrm{cat}}^{(0)} = |\langle\psi_{\mathrm{cat}}^{+}|\psi_{\mathrm{SMSS}}\rangle|^2 = \frac{(1-\lambda^2)^{1/2}e^{\lambda\,\mathrm{Re}(\alpha^2)}}{\cosh(|\alpha|^2)}. \tag{6.5}$$

The Wigner functions corresponding to $|\psi_{\mathrm{cat}}^{\pm}\rangle$ are not invariant under rotations around the origin of phase space, and since we have chosen λ to be real in Eq. (6.2), we obtain the largest cat state fidelity for a given cat size $|\alpha|^2$ if $\alpha = \alpha^*$. For $\alpha = \alpha^*$, the fidelity is maximized for

$$\lambda = \lambda^{(0)} \equiv \frac{\sqrt{1+4\alpha^2}-1}{2\alpha^2} \tag{6.6}$$

The odd cat state fidelity of the state $\hat{b}|\psi_{\mathrm{SMSS}}\rangle$ is

$$F_{\mathrm{cat}}^{(1)} = \frac{|\langle\psi_{\mathrm{cat}}^{-}|\hat{b}|\psi_{\mathrm{SMSS}}\rangle|^2}{\langle\psi_{\mathrm{SMSS}}|\hat{b}^\dagger\hat{b}|\psi_{\mathrm{SMSS}}\rangle} = \frac{(1-\lambda^2)^{3/2}|\alpha|^2e^{\lambda\,\mathrm{Re}(\alpha^2)}}{\sinh(|\alpha|^2)}, \tag{6.7}$$

which is maximized for $\alpha = \alpha^*$ and

$$\lambda = \lambda^{(1)} \equiv \frac{\sqrt{9+4\alpha^4}-3}{2\alpha^2}. \tag{6.8}$$

For $(\hat{b}^2 - \beta^2)|\psi_{\mathrm{SMSS}}\rangle$, we obtain the even cat state fidelity

$$F_{\mathrm{cat}}^{(2)} = \frac{|\langle\psi_{\mathrm{cat}}^{+}|(\hat{b}^2-\beta^2)|\psi_{\mathrm{SMSS}}\rangle|^2}{\langle\psi_{\mathrm{SMSS}}|((\hat{b}^\dagger)^2-(\beta^*)^2)(\hat{b}^2-\beta^2)|\psi_{\mathrm{SMSS}}\rangle} \tag{6.9}$$

$$= \frac{(1-\lambda^2)^{1/2}e^{\lambda\,\mathrm{Re}(\alpha^2)}}{\cosh(|\alpha|^2)}\frac{(\lambda+\lambda^2(\alpha^*)^2-\beta^2)(\lambda+\lambda^2\alpha^2-(\beta^*)^2)}{|\beta|^4-(\beta^2+(\beta^*)^2)\frac{\lambda}{1-\lambda^2}+\frac{\lambda^2(1+2\lambda^2)}{(1-\lambda^2)^2}}, \tag{6.10}$$

which is maximized for $\alpha = \alpha^*$,

$$\lambda = \lambda^{(2)} \equiv \frac{\sqrt{(3+\sqrt{6})^2+4\alpha^4}-(3+\sqrt{6})}{2\alpha^2}, \tag{6.11}$$

and

$$\beta^2 = (\beta^{(2)})^2 \equiv \frac{1}{5+2\sqrt{6}}\alpha^2. \tag{6.12}$$

Finally, the odd cat state fidelity of the state $(\hat{b}^2 - \beta^2)\hat{b}|\psi_{\mathrm{SMSS}}\rangle$ is

$$
\begin{aligned}
F_{\mathrm{cat}}^{(3)} &= \frac{|\langle\psi_{\mathrm{cat}}^{-}|(\hat{b}^2 - \beta^2)\hat{b}|\psi_{\mathrm{SMSS}}\rangle|^2}{\langle\psi_{\mathrm{SMSS}}|\hat{b}^\dagger((\hat{b}^\dagger)^2 - (\beta^*)^2)(\hat{b}^2 - \beta^2)\hat{b}|\psi_{\mathrm{SMSS}}\rangle} \\
&= \frac{(1-\lambda^2)^{3/2}|\alpha|^2 e^{\lambda\,\mathrm{Re}(\alpha^2)}}{\sinh(|\alpha|^2)} \frac{(3\lambda + \lambda^2(\alpha^*)^2 - \beta^2)(3\lambda + \lambda^2\alpha^2 - (\beta^*)^2)}{|\beta|^4 - 3(\beta^2 + (\beta^*)^2)\frac{\lambda}{1-\lambda^2} + \frac{9\lambda^2}{1-\lambda^2} + \frac{15\lambda^4}{(1-\lambda^2)^2}},
\end{aligned}
\tag{6.13}
$$

which is maximized for $\alpha = \alpha^*$,

$$
\lambda = \lambda^{(3)} \equiv \frac{\sqrt{\left(5+\sqrt{10}\right)^2 + 4\alpha^4} - \left(5+\sqrt{10}\right)}{2\alpha^2}, \tag{6.14}
$$

and

$$
\beta^2 = (\beta^{(3)})^2 \equiv \frac{3}{7+2\sqrt{10}}\alpha^2. \tag{6.15}
$$

These results are plotted in Fig. 6.2, where we also show the optimal choice of lambda and the maximized cat state fidelity for ordinary subtraction of two and three photons, corresponding to $\beta = 0$, for reference. It is seen that the maximal cat state fidelity increases when we subtract more photons, and a significant improvement can be gained by introducing and optimizing the parameter β. At the same time, the required squeezing to obtain the maximal fidelity is decreased, which is an experimental advantage. For $\alpha = \sqrt{6}$, for instance, $F_{\mathrm{cat}}^{(1)} = 0.786$ for $\lambda = 0.781$, while $F_{\mathrm{cat}}^{(3)} = 0.976$ for $\beta = 1.16$ and $\lambda = 0.529$. The degree of squeezing is often expressed as the factor by which the variance of the squeezed quadrature is reduced compared to the vacuum level, i.e., as $10\log_{10}((1-\lambda)/(1+\lambda))$ dB. Optimally, we should thus use -9.1 dB and -5.9 dB of squeezing for the two cases, respectively. In the cat state generation experiment reported in [63], a squeezing of -2.5 dB obtained via SP PDC has been used, and the more recent cat state generation experiment reported in [81] has used a squeezing of -6.8 dB, also obtained via SP PDC. For CW OPOs, more experiments have now achieved squeezing levels in the range of -6 dB to -10 dB [83].

6.4 Success probability

In practise, we can not choose the reflectivities of BS$_1$, BS$_2$, and BS$_3$ in Fig. 6.1 to be zero because the success probability vanishes in that limit. On the other hand, if the reflectivities are nonzero, the beam splitters effectively induce a loss from the signal beam into the trigger beams, which degrades the fidelity when we use on/off detectors. Let us first consider generation of the state $(\hat{b}^2 - \beta^2)|\psi_{\mathrm{SMSS}}\rangle$ for the parameters $\alpha = 2$, $\lambda = 0.529$, and $\beta = 0.636$, giving an optimal even cat state fidelity of 0.971. If we assume that BS$_2$

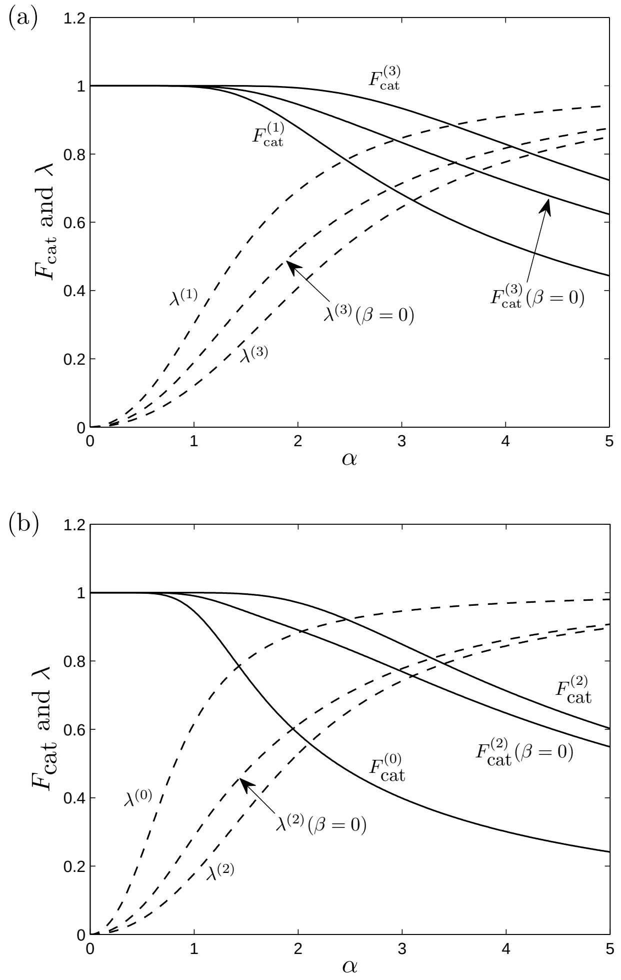

Figure 6.2: (a) Optimal value of λ and odd cat state fidelity $F_{\rm cat}$ as a function of α for the states $\hat{b}|\psi_{\rm SMSS}\rangle$ ($\lambda^{(1)}$ and $F_{\rm cat}^{(1)}$), $(\hat{b}^2 - \beta^2)\hat{b}|\psi_{\rm SMSS}\rangle$ ($\lambda^{(3)}$ and $F_{\rm cat}^{(3)}$), and $\hat{b}^3|\psi_{\rm SMSS}\rangle$ ($\lambda^{(3)}(\beta = 0)$ and $F_{\rm cat}^{(3)}(\beta = 0)$). (b) Optimal value of λ and even cat state fidelity $F_{\rm cat}$ as a function of α for the states $|\psi_{\rm SMSS}\rangle$ ($\lambda^{(0)}$ and $F_{\rm cat}^{(0)}$), $(\hat{b}^2 - \beta^2)|\psi_{\rm SMSS}\rangle$ ($\lambda^{(2)}$ and $F_{\rm cat}^{(2)}$), and $\hat{b}^2|\psi_{\rm SMSS}\rangle$ ($\lambda^{(2)}(\beta = 0)$ and $F_{\rm cat}^{(2)}(\beta = 0)$).

and BS_3 both have a reflectivity of 0.01, the success probability to generate the state is approximately $R_2R_3\langle\psi_{\mathrm{SMSS}}|((\hat{b}^\dagger)^2-(\beta^*)^2)(\hat{b}^2-\beta^2)|\psi_{\mathrm{SMSS}}\rangle = 4\times10^{-5}$. With a repetition rate of order 10^6 s^{-1} as in [61, 62], we can then generate about 41 states per second. A rough idea of the corresponding fidelity decrease can be obtained by subjecting a perfect even cat state with $\alpha=2$ to a loss of $1-(1-0.01)^2$. After the loss the fidelity with an even cat state with $\alpha=2$ is reduced to 0.93, which is still high compared to the fidelity of 1/2 between a coherent state $|\alpha\rangle$ and the cat state (6.1) in the limit of large α. For generation of the state $(\hat{b}^2-\beta^2)\hat{b}|\psi_{\mathrm{SMSS}}\rangle$, we find a success probability of approximately $R_1R_2R_3\langle\psi_{\mathrm{SMSS}}|\hat{b}^\dagger((\hat{b}^\dagger)^2-(\beta^*)^2)(\hat{b}^2-\beta^2)\hat{b}|\psi_{\mathrm{SMSS}}\rangle = 6.4\times10^{-7}$ when $R_1=R_2=R_3=0.01$, $\alpha=\sqrt{6}$, $\lambda=0.529$, and $\beta=1.16$. If we subject a perfect odd cat state with $\alpha=\sqrt{6}$ to a loss of $1-(1-0.01)^3$, the cat state fidelity decreases from 1 to 0.85. We note that cat state generation by ordinary subtraction of three photons has recently been achieved experimentally, although with a lower fidelity [81].

The above results show that Schrödinger cat states of moderate amplitude can be generated with good fidelity by use of on/off detectors, which do not need to have near unit efficiency, but they also illustrate the point that lossless conditions are absolutely essential in order to produce large amplitude cat states with high fidelity. If losses, including detection inefficiency, can be avoided, however, it is also possible to construct photon number resolving detectors, and with such detectors at hand we can indeed obtain cat states with fidelities that are practically identical to those in Fig. 6.2, but with a considerable success probability as we now demonstrate for the case of generation of the state $(\hat{b}^2-\beta^2)\hat{b}|\psi_{\mathrm{SMSS}}\rangle$.

When we assume photon number resolving detectors and nonzero values of R_1, R_2, and R_3, we obtain the output state

$$\begin{aligned}&\frac{-i}{\sqrt{P}}\frac{r_1r_2r_3}{t_1t_2^2t_3^3}e^{\frac{1}{2}(r_2^2+r_3^2)|\beta|^2}e^{(r_2^2/t_2-r_3^2)\beta^*\hat{b}/t_3}\\&\qquad\times(\hat{b}^2-t_2t_3^2\beta^2+(t_2-1)t_3\beta\hat{b})\hat{b}(t_3t_2t_1)^{\hat{b}^\dagger\hat{b}}|\psi_{\mathrm{SMSS}}\rangle\end{aligned}\tag{6.16}$$

conditioned on three single-photon state detections in the trigger beams (P is the success probability as usually). The operator acting on the input state $|\psi_{\mathrm{SMSS}}\rangle$ now also includes terms, which annihilate an even number of photons if $\beta\neq0$. We can, however, reduce the significance of these terms if we choose $r_2^2/t_2=r_3^2$ to cancel the exponential factor and avoid too large values of R_2.

For $r_2^2/t_2=r_3^2$, the odd cat state fidelity of (6.16) evaluates to

$$\begin{aligned}\tilde{F}_{\mathrm{cat}}^{(3)}=&\frac{(1-\tilde{\lambda}^2)^{3/2}|\alpha|^2e^{\tilde{\lambda}\,\mathrm{Re}(\alpha^2)}}{\sinh(|\alpha|^2)}\\&\times\frac{(3\tilde{\lambda}+\tilde{\lambda}^2(\alpha^*)^2-\tilde{\beta}^2)(3\tilde{\lambda}+\tilde{\lambda}^2\alpha^2-(\tilde{\beta}^*)^2)}{|\tilde{\beta}|^4-(\tilde{\beta}^2+(\tilde{\beta}^*)^2)\frac{3\tilde{\lambda}}{1-\tilde{\lambda}^2}+\frac{(t_2-1)^2}{t_2}|\tilde{\beta}|^2\frac{1+2\tilde{\lambda}^2}{1-\tilde{\lambda}^2}+\frac{9\tilde{\lambda}^2}{1-\tilde{\lambda}^2}+\frac{15\tilde{\lambda}^4}{(1-\tilde{\lambda}^2)^2}},\end{aligned}\tag{6.17}$$

where $\tilde{\lambda} \equiv t_1^2 t_2^2 t_3^2 \lambda$ and $\tilde{\beta}^2 \equiv t_2 t_3^2 \beta^2$. Except for an extra term in the denominator and the new definitions of λ and β^2, this expression is the same as Eq. (6.13). The extra term is small when T_2 is close to unity, and we thus expect it to be nearly optimal to choose $\tilde{\lambda} = \lambda^{(3)}$ and $\tilde{\beta}^2 = (\beta^{(3)})^2$. We can then choose t_2 in such a way that the extra term is, e.g., a factor of 10^{-3} smaller than the sum of the other terms in the denominator, in which case the fidelity is only reduced by 0.1 % relative to the values in Fig. 6.2. Finally, we can choose T_1 to maximize the success probability

$$P = \frac{r_1^2 r_2^2 r_3^2}{t_1^2 t_2^4 t_3^6} e^{(r_2^2 + r_3^2)|\beta|^2} \sqrt{\frac{1-\lambda^2}{1-\tilde{\lambda}^2}} \Bigg(|\tilde{\beta}|^4 \frac{\tilde{\lambda}^2}{1-\tilde{\lambda}^2} + \frac{(t_2-1)^2}{t_2} |\tilde{\beta}|^2 \frac{\tilde{\lambda}^2(1+2\tilde{\lambda}^2)}{(1-\tilde{\lambda}^2)^2} \\ - 2\,\mathrm{Re}(\tilde{\beta}^2) \frac{3\tilde{\lambda}^3}{(1-\tilde{\lambda}^2)^2} + \frac{3\tilde{\lambda}^4(3+2\tilde{\lambda}^2)}{(1-\tilde{\lambda}^2)^3} \Bigg), \quad (6.18)$$

which is achieved for $T_1 = ((\tilde{\lambda}^4 + 8T_2^2 T_3^2 \tilde{\lambda}^2)^{1/2} - \tilde{\lambda}^2)/(2T_2^2 T_3^2)$ (provided this expression leads to valid values of T_1 and λ). In this way, we obtain $\tilde{F}_{\mathrm{cat}}^{(3)} = 0.975$ and $P = 6 \times 10^{-4}$ for $\alpha = \sqrt{6}$, $T_1 = 0.671$, $T_2 = 0.954$, $T_3 = 0.953$, $\beta^2 = 1.45$, and $\lambda = 0.868$ (corresponding to -11.5 dB).

It is thus theoretically possible to achieve large cat states with high fidelity and a reasonable success rate for sufficiently favorable experimental conditions. At present, the experimentally achievable fidelities are, however, significantly lower. In [63], for instance, cat states with $|\alpha|^2 = 0.79$ are obtained with a fidelity of 0.70, whereas cat states with $|\alpha|^2 = 1.7$ are obtained with a fidelity of 0.53 in [30] (both experiments rely on subtraction of one photon).

6.5 Conclusion

In conclusion, we have proposed a protocol to generate large amplitude Schrödinger cat states, which relies on displacement operations and conditional photon subtractions. We have analyzed the performance of the protocol for the case of subtraction of two and three photons compared to ordinary subtraction of zero, one, two, or three photons, and we have found that the addition of displacement operations can increase the theoretically achievable fidelity for a given cat size significantly. A combination of the CW results obtained in Sec. 4.3 for the mode structure of states conditioned on two detection events adapted to the case of a degenerate OPO and the idea presented in the present chapter of introducing ancilla modes to improve the fidelity has now been used in an experimentally realized proposal to generate even cat states by ancilla assisted photon subtraction [84, 85, 86]. In brief, it has been demonstrated that conditional photon subtractions at times t_{c1} and t_{c2} from the output of a degenerate CW OPO prepares the signal mode $g_+(t)$ defined in Eq. (4.24) in an even cat state with high fidelity if $\kappa|t_{c2} - t_{c1}| \lesssim 4$.

It is possible to translate the procedure into a setup, where two photons are subtracted from the mode $g_+(t)$ or from the mode $g_-(t)$ without the possibility to subtract one photon from each mode (see [86]), and the temporal separation between the photon subtractions is an adjustable parameter. In this way, $g_-(t)$ acts as an ancilla, just as the coherent states $|\phi_4\rangle$ and $|\phi_5\rangle$ in our proposal. The experimental advantage of using $g_-(t)$ rather than $|\phi_4\rangle$ and $|\phi_5\rangle$ as ancilla is the fact that the modes $g_\pm(t)$ are automatically phase locked to each other. The drawback is the fact that the modes $g_\pm(t)$ are not completely uncorrelated after the measurement, which slightly reduces the purity of the produced states. The experimentally achieved fidelities are 0.76 for cat states with $|\alpha|^2 = 1.2$ and 0.60 for cat states with $|\alpha|^2 = 2.0$, which is a significant improvement compared to the experiments relying on subtraction of one photon cited above. The setup accomplishing the transformation $\rho_{\text{in},2} \to P_2^{-1} R_2(\hat{b}+\beta)\rho_{\text{in},2}(\hat{b}^\dagger+\beta^*)$ has recently been demonstrated experimentally in [87], and the recent demonstration of ordinary subtraction of three photons from a squeezed vacuum state in [81] is also a significant step towards realizing our protocol for subtraction of three photons.

Chapter 7

Deterministic preparation of states of light with Rydberg blockade in atomic ensembles

We next turn to a very different approach to generate quantum states of light. The basic idea is to prepare the desired state in an ensemble of atoms and then transfer the state to light via cooperative spontaneous emission. Manipulation of the state of the atomic ensemble can be achieved by use of classical laser pulses and the Rydberg blockade mechanism [88]. To explain the Rydberg blockade mechanism, let us first consider two atoms each with a ground state level $|g\rangle$ and a Rydberg state $|r\rangle$ with large principal quantum number (e.g., around 70). If the atoms are within a distance of about 10 μm from each other, the energy required to excite both atoms to the Rydberg state is significantly different from twice the energy required to excite one isolated atom to the Rydberg state for appropriate choices of the state $|r\rangle$. We refer to this energy difference as the blockade shift. A large blockade shift can arise if the state $|r\rangle|r\rangle$ couples to another state $|r'\rangle|r''\rangle$ of nearly the same energy (a Förster resonance [88]), where $|r'\rangle$ is a second Rydberg state of the first atom and $|r''\rangle$ is a second Rydberg state of the second atom. As a consequence, a laser resonant with the transition from $|g\rangle$ to $|r\rangle$ will not excite both atoms to the state $|r\rangle$ at the same time if the Rabi frequency is small compared to the blockade shift. Instead, there is a Rabi oscillation between the states $|g\rangle|g\rangle$ and $(|g\rangle|r\rangle + |r\rangle|g\rangle)/\sqrt{2}$ (assuming an appropriate choice of phases) with a Rabi frequency, which is a factor of $\sqrt{2}$ larger than the Rabi frequency for one atom. Illuminating K atoms that are within a distance of about 10 μm from each other, we similarly obtain a Rabi oscillation between the state with all atoms in the ground state and the state consisting of a superposition of terms with one atom in the Rydberg state with a Rabi frequency, which is a factor of $\sqrt{K}$ larger than the single-atom Rabi frequency.

If the atoms have more than one ground state level, we can use the blockade to move one atom at a time to different ground state levels as illustrated in Fig. 7.1(b). Here, all atoms are initially prepared in the ground state level $|0\rangle$, which can be done by optical pumping. A π pulse[1] ([20] Chap. 8) transfers one atom to the Rydberg state $|r\rangle$, and a second π pulse moves this atom to the ground state level $|j\rangle$.[2] We do not know which atom is transferred, so the final state is a superposition of all terms with one atom in $|j\rangle$ with phase factors determined by the wave vector of the laser field and the position of the transferred atom. If the first pulse is replaced by, e.g., a $\pi/2$ pulse, we obtain a superposition between the state with all atoms in the ground state and the state with one atom in $|j\rangle$. We can also make the transition of one atom from $|0\rangle$ to $|j\rangle$ dependent on the presence or absence of an atom in a single-atom state $|j'\rangle$ as shown in Fig. 7.1(c). If an atom is present in $|j'\rangle$, the first π pulse transfers this atom to the Rydberg state $|r'\rangle$, and the transfer of one atom from $|0\rangle$ to $|j\rangle$ via $|r\rangle$ by the second and third π pulses is prevented by the blockade shift. The fourth π pulse then transfers the atom in $|r'\rangle$ back to $|j'\rangle$. If no atom is present in $|j'\rangle$, π pulses 1 and 4 do not have any effect, and an atom is transferred from $|0\rangle$ to $|j\rangle$. Finally, we note that a conditional phase shift can be obtained by applying a π pulse between $|j'\rangle$ and $|r'\rangle$, a 2π pulse between $|j\rangle$ and $|r\rangle$, and a π pulse between $|j'\rangle$ and $|r'\rangle$. This set of pulses changes the phase of the state by π unless $|j\rangle$ and $|j'\rangle$ are both unoccupied.

We can select N single-atom ground state levels $|1\rangle$, $|2\rangle$, …, $|N\rangle$ in addition to the reservoir state $|0\rangle$ and regard these levels as qubits, which are in the logical state zero if the level is unoccupied and in the logical state one if the level is occupied by one atom as proposed in [89] and further developed in [90]. Universality of the operations that can be achieved with laser pulses and the Rydberg blockade mechanism ensures that any N qubit state can be prepared. The occupation numbers of the single-atom levels can be converted into a sequence of light pulses containing one or zero photons as illustrated in Fig. 7.1(a). To transfer the population in $|j\rangle$ to light, we use a π pulse to transfer the population in $|j\rangle$ to an excited state $|e\rangle$, which decays by spontaneous emission. If $|e\rangle$ is occupied, the collective state of the atoms is a superposition of all possible terms with one atom in the excited state. As a consequence, if the atoms are fixed in space, the emission

---

[1] Note that the pulse area depends on the total number of atoms in the two levels coupled by the laser due to the collective enhancement of the Rabi frequency. To avoid ambiguities, we assume throughout that the number of atoms in $|0\rangle$ is large compared to the total number of atoms in other single-atom states such that the number of atoms in $|0\rangle$ is practically constant. Furthermore, we shall only consider collective states for which the occupation of all single-atom levels different from $|0\rangle$ is zero or one. Operations involving levels, which may be occupied by, e.g., zero, one, or two atoms, can, however, be accomplished by using more complicated pulse sequences.

[2] Selectivity can be achieved by utilizing selection rules and by splitting the energy of different Zeeman levels with a homogeneous magnetic field during the transitions.

leads to an interference pattern, which ensures that the photon is emitted in a particular direction determined by the wave vectors of the pulses used to prepare the atomic state, and the excited atom is transferred to the reservoir state. This cooperative emission process has been investigated in detail in [49, 91, 92], and it has been found [49] that an ensemble of about 1000 atoms is sufficiently large to obtain directional emission of the photon (the probability to emit the photon within an angle of 0.3 rad from the main emission direction is 95 %) and sufficiently small to facilitate efficient Rydberg blocking. We note that further processing of the state of the atoms may occur between the emission events, and, in particular, the number of emitted pulses is not restricted to N.

Experiments demonstrating single photon emission from an atomic ensemble, which do not use the Rydberg blockade mechanism, have been described in [48, 93]. Instead, the state with one atom in $|j\rangle$ and all other atoms in $|0\rangle$ is generated by coupling $|0\rangle$ to an excited state $|e\rangle$ with a nonresonant laser and conditioning on detection of a photon emitted spontaneously in a Raman transition from $|0\rangle$ and $|j\rangle$ (i.e., one photon is absorbed from the laser light and a photon with different properties is emitted into the detector while the state of one of the atoms changes from $|0\rangle$ to $|j\rangle$). The choice of a nonresonant laser ensures that the transfer is sufficiently inefficient to mostly eliminate cases, where more than one atom is transferred to $|j\rangle$. The single-photon state is then generated by transferring the population from $|j\rangle$ to $|e\rangle$ with a π pulse as above. It is desirable to use the Rydberg blockade mechanism in the preparation step in order to improve the efficiency and avoid transfer of more than one atom to $|j\rangle$. So far blockade within volumes of a collection of atoms has been observed experimentally [94]. The Rydberg blockade mechanism has also been used very recently to achieve a controlled NOT gate [1] between two individually addressable atoms with a fidelity of 0.58 after correction for atom loss [95] and generation of entanglement between two atoms with a fidelity of 0.75 after correction for atom loss [96]. Theoretical investigations show that gate errors on the order of 10^{-3} should be achievable [88].

The idea of using the Rydberg blockade shift to obtain gate operations between atoms has been proposed in [97], and this idea has been extended to state manipulation of atomic ensembles in [98]. Specifically, [98] proposes a method to generate an arbitrary superposition of different numbers of atoms in a single single-atom state and mentions the enhanced coupling of this state to light. In [99], it has been proposed to use two single-atom levels to generate an entangled state of light, which occupies two different polarization modes. Below, we extend this idea to generation of multimode states of light, where the emitted light may still be entangled with the atomic ensemble, and the ensemble may undergo several processing and light emission steps. The proposal is extremely flexible and facilitates generation of a large number of different states. As specific examples, we provide protocols to generate Greenberger-Horne-Zeilinger (GHZ) states, one of the four Bell states, and cluster states. GHZ states are Scrödinger cat like states, the Bell state is used in a recent proposal for quantum key distribution [100], and cluster states are important for measurement based quantum computing [101]. In addition to the flexibility, another clear advantage of the proposal presented below compared to the protocols for state preparation by conditional measurements considered in the previous chapters is the fact that it is deterministic. Further experimental advance is required to realize the proposal, but the low errors predicted theoretically are very promising. As a consequence, we consider only the ideal case of perfect operation of the applied gates. A copy[3] of [XI] follows below.

Deterministic multimode photonic device for quantum-information processing

Anne E. B. Nielsen and Klaus Mølmer
Lundbeck Foundation Theoretical Center for Quantum System Research,
Department of Physics and Astronomy, Aarhus University,
DK-8000 Århus C, Denmark

We propose the implementation of a light source that can deterministically generate a rich variety of multimode quantum states. The desired states are encoded in the collective population of different ground hyperfine states of an atomic ensemble and converted to multimode photonic states by excitation to optically excited levels followed by cooperative spontaneous emission. Among our examples of applications, we demonstrate how two-photon-entangled states can be prepared and implemented in a protocol for a reference-frame-free quantum key distribution and how one-dimensional as well as higher-dimensional cluster states can be produced.

PACS numbers: 42.50.Dv, 32.80.Ee, 42.50.Ex, 42.50.Nn

7.1 Introduction

Quantum states of light are efficient carriers of quantum information with applications in quantum computing, quantum cryptography, and quantum networks. Their most serious drawback is the absence of suitable nonlinear interactions which can produce and transform the desired states. Measurement back action presents one means to accommodate the required nonlinearities and paves the way for universal quantum computing with the tools of linear optics, but certain resource states such as single-photon states [15] or superpositions of coherent states [71] are required, while even more involved

---

[3] Copyright (2010) by the American Physical Society.

states, such as cluster states [102], are needed to perform successfully with high probability. An efficient method to prepare general quantum states of light deterministically would constitute a significant step forward for optical quantum-information processing.

There are a number of different strategies to produce nonclassical states of light. Squeezed states and multimode states with quantum correlated amplitudes can be produced directly by optical parametric oscillators and beam splitters, while these states can be further transformed into states with non-Gaussian amplitude distributions by conditional measurements [31, 36, 80]. The probabilistic nature of the schemes, however, limits the variety of states that can be produced by this method. Another successful approach uses laser excitation of an atomic ensemble with all atoms in the same single-atom state and detection of a spontaneously emitted photon to conditionally prepare a superposition state with different atoms populating the final state of the spontaneous emission process. The atomic state is generated at a random instant, and the ensemble is then ready to deterministically emit a single photon at the moment when the experimentalist couples the singly occupied state to an optically excited state [48, 103, 104].

In the present paper, we propose a source that is capable of producing a large variety of quantum states of light. We focus on coding of quantum bits for quantum computing and communication, and we use multiple spatial and temporal modes to provide multibit registers with different entangled states. The basic idea is to prepare the equivalent state in an ensemble of cold atoms and, in a stepwise process, convert the atomic state to a quantum state of light [Fig. 7.1(a)], as proposed for two-mode states in Ref. [99]. To avoid the requirement of individual addressing of the atoms and to facilitate the efficient conversion to light, we encode the quantum state in the collective populations of different internal states of the atoms as proposed in Ref. [89]. The transfer of precisely one atom in the ensemble to an initially unoccupied internal state is carried out via intermediate excitation of a Rydberg-excited state and makes use of the so-called Rydberg blockade mechanism [97, 98]. It is thus possible to initialize the ensemble with all atoms populating a definite internal reservoir state, denoted $|0\rangle$ in the following, and to subsequently encode, in principle, any quantum superposition states of an N-bit register based on N different internal states, labeled $|1\rangle, |2\rangle, \ldots, |N\rangle$, with each qubit value set to zero if the state is unpopulated and to unity if the corresponding state is populated by precisely one atom. This is ensured by the universality of the collective quantum computing proposal with Rydberg blockade [89]. Here, however, we also have the freedom to process the state of the atomic ensemble between light-emission events. We can thus reuse the atomic levels and generate entangled light states with more than N qubits. Our current task with the Rydberg-blocked ensemble is a more dedicated one than quantum computing, and rather than appeal to universality, we will describe explicit schemes which in a few efficient steps use the Rydberg

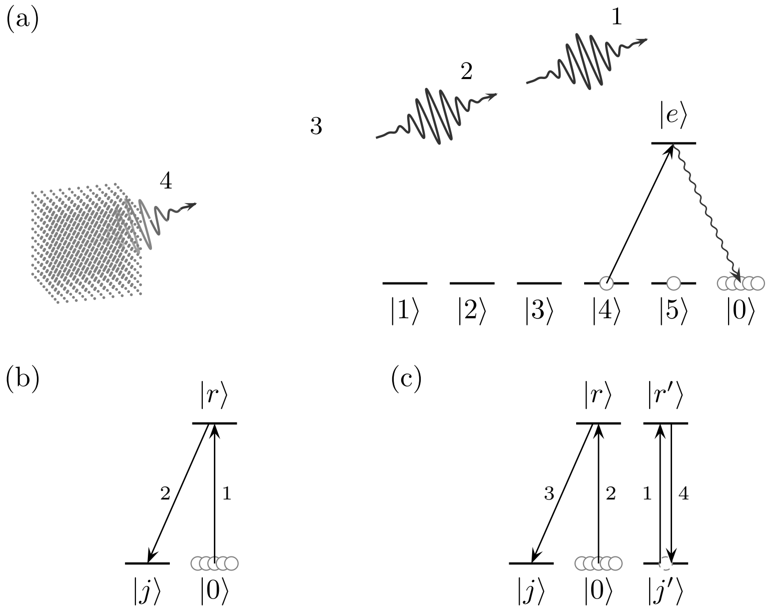

Figure 7.1: (Color online) (a) Stepwise transfer of a quantum state encoded in a cold atomic ensemble to light. The initial state of the ensemble is an arbitrary superposition of states with zero or one atom in the single-atom levels $|1\rangle$ to $|5\rangle$, and during the conversion process, occupation by one atom translates into a single photon in a corresponding spatiotemporal light mode. For the case illustrated, the states $|1\rangle$, $|2\rangle$, $|4\rangle$, and $|5\rangle$ are occupied initially. (b) Preparation of the atomic state. The excitation from $|0\rangle$ to a Rydberg state $|r\rangle$ is off-resonant if more than a single atom is excited, and a collectively distributed single excitation can be subsequently transferred to a unit atomic population of the single-atom ground-state level $|j\rangle$. (c) The feeding of state $|j\rangle$ by the attempted transfer $|0\rangle \rightarrow |r\rangle \rightarrow |j\rangle$ can also be made conditional on the population of another state $|j'\rangle$ if that state is excited to a Rydberg state $|r'\rangle$ interacting with $|r\rangle$.

interaction, the physical properties of the internal atomic level structure, and the collective emission properties of the ensemble to provide the optical states of interest.

7.2 State preparation and emission

The Rydberg blockade mechanism [97] utilizes the large dipole-dipole interaction between atoms in certain Rydberg states that are not separated by more than about 10 μm. Due to this interaction, states with two or more atoms in Rydberg-excited states have energies that are significantly different from the sum of the single-atom excitation energies, and therefore resonant excitation of a few micrometer-sized ensemble from the reservoir ground atomic state will coherently drive the system toward the state with a single coherently distributed Rydberg excitation in the ensemble. The Rabi frequency for this transition is collectively enhanced by the factor $\sqrt{K}$, where K is the number of atoms. This enhancement and the blocking of further excitation have been seen for a pair of atoms ($K = 2$) [105, 106], and blocking and enhanced coupling have also been observed in larger samples of atoms [94]. After a π pulse on the coherent transition, there is a single ensemble Rydberg excitation, and one can subsequently drive this collectively shared population into a low-lying state [Fig. 7.1(b)]. To provide the coupling in a fully selective manner between the desired internal states, we suggest using polarization selection rules and the optical frequency resolution of different Zeeman ground states of the atoms in a homogeneous magnetic field switched on during state selective processes.

In the following, the ket $|n_1 n_2 \cdots n_N\rangle$ denotes a state with $n_j \in \{0, 1\}$ atoms in the single-atom state $|j\rangle$, $j = 1, 2, \ldots, N$, and the remaining atoms in the reservoir state $|0\rangle$. In writing this state, phase factors arising from the different positions of the atoms within the laser-traveling wave fields are taken into account. The state $|10 \cdots 0\rangle$, for instance, with one atom in $|1\rangle$ and zero atoms in $|2\rangle$ to $|N\rangle$ is

$$|10 \cdots 0\rangle = \frac{1}{\sqrt{K}} \sum_{j=1}^{K} e^{i\mathbf{k}_0 \cdot \mathbf{r}_j} |0\rangle_1 |0\rangle_2 \cdots |1\rangle_j \cdots |0\rangle_K, \tag{7.1}$$

where $K \gg N$ is the number of atoms in the ensemble, $|j\rangle_k$ means that the kth atom is in the internal state $|j\rangle$, $\mathbf{r}_j$ is the position of the jth atom, and $\mathbf{k}_0$ is the resulting wave vector of the light pulses used to bring the ensemble to the above state (i.e., $\mathbf{k}_0 = \sum_i \delta n_i \mathbf{k}_i$, where $\mathbf{k}_i$ is the wave vector of the ith laser pulse and δn_i is 1 if a photon is absorbed and -1 if a photon is emitted during the ith pulse).

If we apply a π pulse with wave vector $\mathbf{k}_e$ to transfer the atom in the state $|1\rangle$ to the optically excited state $|e\rangle$, the amplitude for emission of a photon with wave vector $\mathbf{k}$ and polarization $\mathbf{e}_{\mathbf{k}}$ when the atom decays to the state $|0\rangle$ is proportional to $K^{-1/2} \sum_{j=1}^{K} \langle 0|\mathbf{e}_{\mathbf{k}} \cdot \mathbf{d}|e\rangle e^{i(\mathbf{k}'_0 - \mathbf{k}) \cdot \mathbf{r}_j}$, where $\mathbf{d}$ is the dipole operator and $\mathbf{k}'_0 = \mathbf{k}_0 + \mathbf{k}_e$. The transition probability $P(\mathbf{k})$ is thus proportional to

$$P(\mathbf{k}) \propto \frac{1}{K} \left| \sum_{j=1}^{K} e^{i(\mathbf{k}'_0 - \mathbf{k}) \cdot \mathbf{r}_j} \right|^2 . \tag{7.2}$$

The factor $1/K$ suppresses emission in all directions except $\mathbf{k} \approx \mathbf{k}'_0$, for which the sum is approximately K and $P(\mathbf{k}) \propto K$. The value of $c|\mathbf{k}|$ must also equal the atomic excitation frequency. The factor $1/K$ is replaced by $1/K^2$ if the atom decays to a different hyperfine level, and such transitions are thus also suppressed. With an ensemble of about 1000 atoms, it is possible to satisfy the requirement of all atoms being at most 10 μm apart, while the ensemble is still large enough to ensure directional emission of the photon [49, 91]. A detailed analysis of light emission from various arrangements of atoms can be found in Refs. [92, 99]. To map a general superposition of the states $|n_1 n_2 \cdots n_N\rangle$ to N temporally distinct light pulses, we simply transfer one internal state population after the other to the optically excited state, as illustrated schematically for $N = 5$ in Fig. 7.1(a), and we can even renew the populations of the atomic states during the conversion process if desired.

7.3 Greenberger-Horne-Zeilinger and Bell states

We now turn to a description of explicit schemes to generate particular quantum states of light. We start with the M-mode Greenberger-Horne-Zeilinger (GHZ) state $(|+\rangle_1|+\rangle_2 \ldots |+\rangle_M + |-\rangle_1|-\rangle_2 \ldots |-\rangle_M)/\sqrt{2}$, where $|+(-)\rangle_m$ denotes a single-(zero-)photon state in the mth mode. To prepare this state, we first apply a $\pi/2$ pulse between $|0\rangle$ and a Rydberg level $|r'\rangle$ followed by a π pulse between $|r'\rangle$ and the ground-state level $|j'\rangle$, which leads to a superposition of having zero and one atom in $|j'\rangle$. A train of entangled pulses, all containing either zero or one photon, can then be emitted by conditional feeding of the state $|j\rangle$, as shown in Fig. 7.1(c). After $M - 1$ emissions, we apply a π pulse between $|j'\rangle$ and $|r'\rangle$, a π pulse between $|r'\rangle$ and $|0\rangle$, and a π pulse between $|j'\rangle$ and $|r'\rangle$, which coherently changes the population in $|j'\rangle$ between zero and one. The last mode is then released by transferring the population in $|j'\rangle$ to an excited state.

The maximally entangled two-mode Bell state $|\Psi_-\rangle = (|R\rangle_1|L\rangle_2 - |L\rangle_1 |R\rangle_2)/\sqrt{2}$, where R and L denote right and left polarized photons, respectively, can be prepared, if we first prepare the atoms in the collective state $|\Psi_-^{\text{at}}\rangle = (|1010\rangle - |0101\rangle)/\sqrt{2}$, making use of the five hyperfine states in Fig. 7.2. This is done as follows: (i) Transfer one atom from $|0\rangle$ to $|2\rangle$ via a Rydberg level. (ii) Use a Raman transition between $|2\rangle$ and $|3\rangle$ to obtain the transformation $|0100\rangle \rightarrow (|0010\rangle - |0100\rangle)/\sqrt{2}$. (iii) Move an atom from $|0\rangle$ to $|4\rangle$ if and only if $|3\rangle$ is unoccupied, and an atom from $|0\rangle$ to $|1\rangle$ if and only if $|2\rangle$ is unoccupied using the conditional method in Fig. 7.1(c). The optical release of the state $|\Psi_-^{\text{at}}\rangle$ is then achieved as explained in Fig. 7.2. If the light pulses are released by spontaneous Raman transitions in the atoms, the temporal shape of the emitted photon pulse can be controlled by the coupling laser amplitude. Conversely, incident light pulses with a known temporal shape can be transferred via Raman processes to a collective atomic population in different states. By subsequent application of Rydberg quantum gates, the state can be processed and analyzed, and the ensemble can thus, for example, be used to distinguish among all four polarization or photon-number-encoded Bell states.

As a specific application of the two-mode optical Bell state, we implement

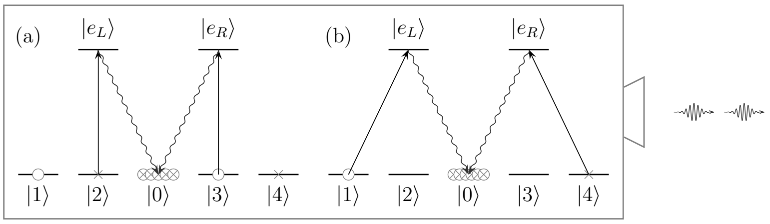

Figure 7.2: (Color online) Generation of the photonic Bell state $(|R\rangle_1|L\rangle_2 - |L\rangle_1|R\rangle_2)/\sqrt{2}$ from the collective atomic state $(|1010\rangle - |0101\rangle)/\sqrt{2}$ (where the first term is indicated with circles, and the second with crosses). (a) A light pulse transfers the populations in $|2\rangle$ and $|3\rangle$ to the excited states $|e_L\rangle$ and $|e_R\rangle$, respectively, and the subsequent atomic decay to the state $|0\rangle$ leads to emission of the first photon, which is L polarized if $|e_L\rangle$ is populated and R polarized if $|e_R\rangle$ is populated. (b) The second photon is similarly obtained via spontaneous emission after transfer of the populations in the states $|1\rangle$ and $|4\rangle$ to the excited states.

the double trine scheme for a quantum key distribution, proposed recently by Tabia and Englert [100]. This scheme has the appealing features that the users of the communication channel, Alice and Bob, do not need to share a common reference frame, and it is possible to extract 0.573 key bits per trine state, which is close the the theoretical maximum. The scheme applies a sequence of groups of three photons with orthogonal polarizations R and L. The groups are chosen at random among three mixed quantum states ρ_i, $i = 1, 2, 3$, each being a direct product of a completely mixed state $(|R\rangle\langle R| + |L\rangle\langle L|)/2$ of the ith photon and a pure Bell state $(|R\rangle|L\rangle - |L\rangle|R\rangle)/\sqrt{2}$ of the other two photons. To produce such a state, we prepare the atomic state $|\Psi_-^{\mathrm{at}}\rangle$ and interweave its conversion to light with the emission of a mixed polarization state of a single photon. The mixed state $(|R\rangle\langle R| + |L\rangle\langle L|)/2$ can be generated by using a classical random decision to determine whether an atom is moved from $|0\rangle$ to $|e_L\rangle$ or from $|0\rangle$ to $|e_R\rangle$ via a Rydberg level. The subsequent decay back to $|0\rangle$ then produces the photon with the apparent random polarization. Note that the emission of the randomly polarized photon may occur independently of the state of the levels $|1\rangle$, $|2\rangle$, $|3\rangle$, and $|4\rangle$, and the three photons can thus be emitted in any order, which allows Alice to prepare any of the states ρ_i. The detection by Bob consists simply in measuring the polarization of the individual photons in any basis and does not require any further complicated processing of the states.

7.4 Cluster states

Recently, Lindner and Rudolph proposed using a quantum dot to prepare one-dimensional cluster states of photons [107] (also see Note added). Fol-

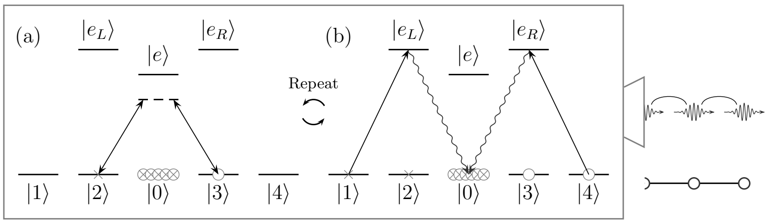

Figure 7.3: (Color online) Generation of a one-dimensional cluster state. Initially, one atom is moved to $|3\rangle$. (a) In each iteration step, a $\pi/2$ pulse is applied to the (Raman) transition between $|2\rangle$ and $|3\rangle$. An atom is then moved from $|0\rangle$ to $|1\rangle$ if and only if $|3\rangle$ is unoccupied, and an atom is moved from $|0\rangle$ to $|4\rangle$ if and only if $|2\rangle$ is unoccupied. (Note that the sum of the populations in $|2\rangle$ and $|3\rangle$ is always one atom.) (b) The populations in $|1\rangle$ and $|4\rangle$ are transferred to $|e_L\rangle$ and $|e_R\rangle$, respectively, which leads to emission of a photon, and the process is repeated. The bonds between the emitted photons illustrate the cluster state entanglement, and the graph representing the state is shown below the photons.

lowing their approach, such cluster states can be produced as shown in Fig. 7.3. Starting with all atoms in $|0\rangle$, the initialization consists of moving one atom to the state $|3\rangle$ via a Rydberg level. We then use a Raman transition to apply a $\pi/2$ pulse between $|2\rangle$ and $|3\rangle$. Using the controlled feeding of atomic states shown in Fig. 7.1(c), we can apply the transformations $|0100\rangle \rightarrow |1100\rangle$ and $|0010\rangle \rightarrow |0011\rangle$ and subsequently transfer the populations in $|1\rangle$ and $|4\rangle$ to $|e_L\rangle$ and $|e_R\rangle$, respectively. After emission of a photon thus entangled with the atomic population remaining in states $|2\rangle$ and $|3\rangle$, one applies again a $\pi/2$ pulse between $|2\rangle$ and $|3\rangle$ followed by a new Rydberg-controlled feeding of the populations in $|1\rangle$ and $|4\rangle$ and emission of the next photon. This procedure is iterated, and one gradually builds up a one-dimensional cluster state of light pulses. After the desired number of iterations, the cluster is decoupled from the atomic state by measuring the state of the last emitted photon in the basis $\{|L\rangle, |R\rangle\}$.

The behavior of one-dimensional cluster states can be efficiently simulated on a classical computer, and they are hence not useful resource states for cluster state quantum computing [101]. Our method can, however, be generalized to higher-dimensional cluster states by involving more internal levels of the atoms. To generate, for instance, the two-dimensional cluster state shown in Fig. 7.4(c), we can use eight hyperfine states to prepare two one-dimensional cluster states in parallel and then add a controlled phase gate in each iteration step to obtain the bonds between them. The details of the processing of the state of the ensemble between each emission of photons are shown in Fig. 7.4(a), and the emission follows the same procedure as for the one-dimensional cluster state. The cluster state is decoupled from the atomic ensemble by measuring the state of the last two emitted pho-

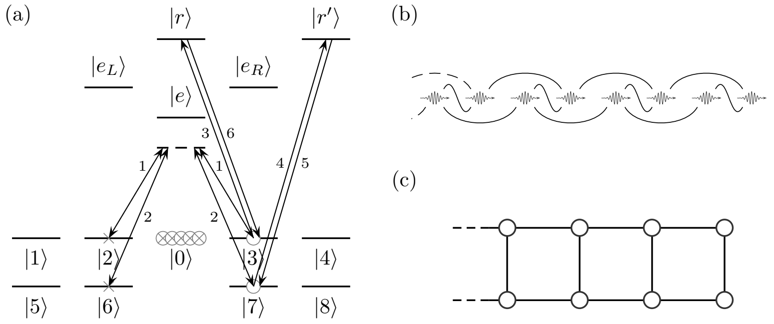

Figure 7.4: (Color online) Generation of a two-dimensional cluster state. Initially, one atom is moved to $|3\rangle$, and one atom is moved to $|7\rangle$. (a) In each iteration step, a $\pi/2$ pulse is applied to the transition between $|2\rangle$ and $|3\rangle$ (pulse 1) and to the transition between $|6\rangle$ and $|7\rangle$ (pulse 2). The π pulses 3-6 then change the phase of the state by π unless $|3\rangle$ and $|7\rangle$ are both unoccupied. Atoms are moved from $|0\rangle$ to $|1\rangle$, $|4\rangle$, $|5\rangle$, and $|8\rangle$ conditioned on $|3\rangle$, $|2\rangle$, $|7\rangle$, and $|6\rangle$ being unoccupied, respectively, and photons are emitted by transferring first the populations in $|1\rangle$ and $|4\rangle$ and subsequently the populations in $|5\rangle$ and $|8\rangle$ to $|e_L\rangle$ and $|e_R\rangle$. (b) The first eight emitted photons and (c) the corresponding graph.

tons. Larger two-dimensional cluster states can be obtained by weaving more one-dimensional cluster states together, and one can also form tubes and three-dimensional structures. In reality, the finite number of internal states of the atoms restricts the possibilities, and to comply with this, we suggest emitting the light pulses from a one- or two-dimensional array of individually addressable ensembles with separations that are small enough to allow long-distance Rydberg phase gates [108] between nearest-neighbor ensembles.

7.5 Conclusion

In conclusion, we have proposed a multipurpose, multimode photonic source and constructed explicit schemes to prepare GHZ states, double trine states, and cluster states. We have only considered states with at most one photon per mode, but we anticipate that the same mechanism allows emission of more photons into the same mode [99]. The collective encoding generalizes naturally to this case by allowing atomic-state populations exceeding one. Experiments on Rydberg-state-mediated one- and two-bit operations are still in their infancy, but according to theoretical estimates, their fidelities may be high enough that entangled photonic states with tens of modes may be prepared. A Rydberg-state-mediated quantum gate may typically be accomplished in about 10^{-6} s, and recent experimental results with pulsed laser fields even demonstrate Rabi oscillations to Rydberg states taking place on a time scale of about 1 ns [109]. The time required to emit a single photon can be as short as 10^{-7} s [49]. These time scales are much faster than Rydberg-state lifetimes on the order of milliseconds. The shape of the laser pulses used to excite the atoms leaves some freedom to tailor the shape and duration of the emitted pulses, and the emission direction is controllable and may vary from mode to mode. The number of photons that can be emitted by a single ensemble is limited in practice, because the interactions with the ensemble are not perfectly symmetric. The collective state of the ensemble may, however, be brought back to the symmetric state by optical pumping of all atoms into the reservoir state or by a transfer of the atomic internal state populations via the Rydberg gate mechanism to a new ensemble from which the photon emission can proceed.

Note added. Recently, a related quantum-dot proposal to produce photonic two-dimensional cluster states has been derived by Economou *et al.* [110].

Acknowledgments

This work was supported by ARO-IARPA.

Chapter 8

Conditional dynamics of a probed system in a cavity

In the following chapters, we shall investigate how measurements can be utilized to manipulate the state of atoms. Specifically, we shall consider measurements, where the atoms interact with a CW light field, which is subsequently detected. As in Chap. 3, we enclose the atoms in a cavity to enhance the effective light-atom interaction strength. The interaction changes the state of the light field in a way, which depends on the state of the atoms, and each detected segment of the light field thus provides a bit of information about the state of the atoms. A strong motivation for considering such probing strategies is the several recent experimental achievements within the field. It has, for instance, been demonstrated that it is possible to transport single atoms into and out of a cavity in a controlled manner and to place an atom at a specific position within a cavity [111, 112]. Other experiments have measured the spectrum of a Bose-Einstein condensate coupled to a cavity [113, 114] and investigated the correlations and counting statistics of an atom laser [115]. Efforts are also directed towards building small scale networks for processing of quantum information, and experiments with cavities connected to optical fibers on a chip have been reported [114, 116, 117].

The rigorous framework of quantum stochastic calculus is very useful for deriving equations for the time evolution of continuously monitored quantum systems [118], and systematic methods to obtain descriptions of quantum networks constructed by concatenating smaller quantum systems have also been developed [119]. We shall, however, avoid to introduce the formalism here as we shall only need it in connection with adiabatic elimination [120, 121] of excited atomic states. Instead, as an introduction to the following chapters, we briefly show in Sec. 8.1 how we can use the methods of Chaps. 2-6 to derive a stochastic differential equation, which describes the conditional time evolution of a probed system in a cavity when the light field leaking out of the cavity is subjected to homodyne detection. The treatment of the homodyne detection is inspired by [122]. In [122], it is investigated how the state of the field inside an empty cavity evolves under homodyne detection of the field leaking out of the cavity. Here, we are interested in probing, and we hence include intracavity dynamics and an input probe beam, which leads to additional terms in the final equation. The main differences between the derivation presented below and the derivation in [122] are that we use the Schrödinger picture throughout and describe the homodyne detection in terms of projections onto photon number states rather than using quantum trajectories with annihilations of single photons and that we represent the state of the system by density operators rather than state vectors. In Sec. 8.2, we consider absorptive bistability of a probed two-level atom in a cavity as an example of an application of the derived equation. We introduce this example, even though it is well-known, because we shall need the obtained results in Chap. 11, where we use the system as a test system. The presentation is based on [VI][1] and [IX][2].

8.1 Stochastic master equation

The relevant setup is depicted in Fig. 8.1. We describe the light beams in terms of time-localized modes (2.14) of width dt. We note that the state of the probe beam and the state of the LO beam are both a direct product of single mode coherent states according to (2.19). The time evolution of the modes that have not yet reached $\mathrm{BS_C}$ or $\mathrm{BS_H}$ is hence independent of the dynamics inside the cavity and of the homodyne detection, and we only need to consider the modes that are currently transformed at the beam splitters. As indicated in the figure, we denote the amplitude of the relevant probe beam mode at time t by $\zeta(t)\sqrt{dt}$ and the amplitude of the relevant LO mode by α (where α may depend on time). Since the LO is strong, we assume $|\alpha|^2 \gg 1$. We also assume that the detector is placed just outside the cavity, and the problem then reduces to keeping track of the time evolution of the probed system and the intracavity field. When the angular frequency of the input field is close to a resonance angular frequency ω_C of the cavity, the dynamics in a frame rotating with ω_C typically takes place on a timescale, which is long compared to the round trip time τ of light in the cavity (for the experiments under consideration, a typical cavity length is in the neighborhood of 100 μm such that τ is of order 10^{-12} s, while decay rates and coupling strengths typically are in the MHz range). This allows us to regard τ as infinitesimal, and we hence choose $dt = \tau$ in the following. The light field inside the cavity is then a single-mode field with annihilation operator $\hat{a}$, and we use $\rho(t)$ to denote the density operator of the state of the system

---

[1] Copyright (2008) by the American Physical Society.

[2] Copyright (2009) by IOP Publishing Ltd and Deutsche Physikalische Gesellschaft.

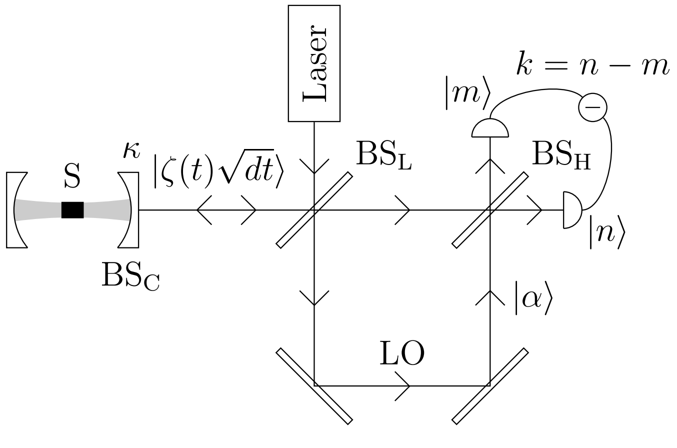

Figure 8.1: Probing of a system in a cavity. The cavity is shown to the left, and the black box labeled S represents the system. The left cavity mirror is perfectly reflecting, while the right cavity mirror labeled $\mathrm{BS_C}$ is partially transmitting with transmissivity $t_{\mathrm{C}}^2 = \kappa\tau$, where κ is the cavity decay rate and τ is the round trip time of light in the cavity. The laser produces a light beam in a continuous coherent state, and the beam splitter $\mathrm{BS_L}$ divides this beam into a probe beam traveling to the cavity and a local oscillator (LO). The transmissivity of BS_L is assumed to be very close to unity, and practically all the light emitted from the cavity travels directly to the 50:50 beam splitter BS_H, where it is mixed with the local oscillator and detected. In each time step, the two detectors record n and m photons, respectively, and the measurement outcome is $k \equiv n - m$.

and the cavity mode.

Considering all the transformations that occur between t and $t + dt$, we can express $\rho(t + dt)$ in terms of $\rho(t)$ as follows

$$\rho(t+dt) = \frac{1}{P_k}\sum_m \langle m+k|\langle m|U_{\mathrm{BS_H}}U_{\mathrm{BS_C}}|\alpha\rangle|\zeta(t)\sqrt{dt}\rangle(\rho(t) + \mathcal{L}\rho(t)dt) \\ \otimes \langle\zeta(t)\sqrt{dt}|\langle\alpha|U^\dagger_{\mathrm{BS_C}}U^\dagger_{\mathrm{BS_H}}|m\rangle|m+k\rangle. \quad (8.1)$$

Starting from the middle, the term $\mathcal{L}\rho(t)dt$ accounts for the internal dynamics of the system and the interaction between the system and the cavity field in the time interval from t to $t + dt$. The beam splitter operator

$$U_{\mathrm{BS_C}} = \exp\left(\tan^{-1}\left(\frac{t_{\mathrm{C}}}{r_{\mathrm{C}}}\right)\left(\hat{a}^\dagger\hat{b} - \hat{a}\hat{b}^\dagger\right)\right), \quad r_{\mathrm{C}} \equiv \sqrt{1 - t_{\mathrm{C}}^2}, \quad (8.2)$$

acts on the cavity mode and on the input beam mode in the state $|\zeta(t)\sqrt{dt}\rangle$ with annihilation operator $\hat{b}$. With this definition, $U^\dagger_{\mathrm{BS_C}}\hat{a}U_{\mathrm{BS_C}} = r_{\mathrm{C}}\hat{a} + t_{\mathrm{C}}\hat{b}$ and $U^\dagger_{\mathrm{BS_C}}\hat{b}U_{\mathrm{BS_C}} = r_{\mathrm{C}}\hat{b} - t_{\mathrm{C}}\hat{a}$, which ensures that the mode with annihilation operator $\hat{a}$ is also the cavity mode after the interaction. Furthermore, $\hat{a}$ is not multiplied by a phase factor, and we do hence not need to include additional phase shifts inside the cavity to ensure that the probe field is on resonance if $\zeta(t)$ is time-independent in the rotating frame. The remaining parts of (8.1) account for the homodyne detection of the output field from the cavity. The beam splitter $\mathrm{BS_H}$ is represented by the operator $U_{\mathrm{BS_H}} = \exp(i\pi(\hat{b}^\dagger\hat{c} + \hat{b}\hat{c}^\dagger)/4)$, where $\hat{c}$ is the annihilation operator of the LO mode, which is initially in the state $|\alpha\rangle$. The detectors project the mode with annihilation operator $\hat{c}$ on an m-photon state, and the mode with annihilation operator $\hat{b}$ on an $(m+k)$-photon state, but since it is only the difference k in the number of detected photons that is actually recorded, we sum over all possible values of m. Finally, we include a normalization constant P_k^{-1}, where P_k is the probability to obtain the measurement outcome k in the considered time interval.

When we expand $U_{\mathrm{BS_C}}$ and $|\zeta(t)\sqrt{dt}\rangle$ to first order in dt, we obtain

$$\begin{aligned}
\rho(t+dt) = \frac{1}{P_k}\Big(&u_{00}(1-|\zeta(t)|^2dt)\rho(t) + u_{11}|\zeta(t)|^2\rho(t)dt \\
&+ 2^{-1/2}u_{20}\zeta(t)^2\rho(t)dt + 2^{-1/2}u_{02}(\zeta(t)^*)^2\rho(t)dt + u_{00}\mathcal{L}\rho(t)dt \\
&+ u_{10}(\zeta(t)-\sqrt{\kappa}\hat{a})\rho(t)\sqrt{dt} + u_{01}\rho(t)(\zeta(t)^*-\sqrt{\kappa}\hat{a}^\dagger)\sqrt{dt} \\
&+ u_{00}\sqrt{\kappa}\zeta(t)\hat{a}^\dagger\rho(t)dt + u_{00}\sqrt{\kappa}\zeta(t)^*\rho(t)\hat{a}dt - u_{11}\sqrt{\kappa}\zeta(t)^*\hat{a}\rho(t)dt \\
&- u_{11}\sqrt{\kappa}\zeta(t)\rho(t)\hat{a}^\dagger dt - u_{20}\sqrt{2\kappa}\zeta(t)\hat{a}\rho(t)dt - u_{02}\sqrt{2\kappa}\zeta(t)^*\rho(t)\hat{a}^\dagger dt \\
&+ \frac{\kappa}{2}\big(2u_{11}\hat{a}\rho(t)\hat{a}^\dagger - u_{00}\hat{a}^\dagger\hat{a}\rho(t) - u_{00}\rho(t)\hat{a}^\dagger\hat{a} \\
&+ \sqrt{2}u_{20}\hat{a}^2\rho(t) + \sqrt{2}u_{02}\rho(t)(\hat{a}^\dagger)^2\big)dt\Big),
\end{aligned} \tag{8.3}$$

where

$$u_{pq} \equiv \sum_m \langle m+k|\langle m|U_{\mathrm{BS_H}}|\alpha\rangle|p\rangle\langle q|\langle\alpha|U_{\mathrm{BS_H}}^\dagger|m\rangle|m+k\rangle \tag{8.4}$$

and $|p\rangle$ and $|q\rangle$ are photon number states. To evaluate u_{pq}, we compute

$$\langle n|\langle m|U_{\mathrm{BS_H}}|\alpha\rangle|q\rangle = \left(\frac{\alpha}{\sqrt{2}}\right)^{n+m}\frac{(-i)^n e^{-|\alpha|^2/2}}{\sqrt{n!m!q!}}\frac{i^q}{\alpha^q}\frac{d^q}{dx^q}(x^n(2+x)^m)\Big|_{x=-1}. \tag{8.5}$$

The squared norm of the q-independent factor $(\alpha/\sqrt{2})^{n+m}e^{-|\alpha|^2/2}/\sqrt{n!m!}$ is a product of two Poisson distributions $(n!)^{-1}\mu^n e^{-\mu}$ with mean value $\mu = |\alpha|^2/2$ and variance $\mu = |\alpha|^2/2$. $n-\mu$ is thus typically of order $\sqrt{\mu}$, and expanding $\ln((n!)^{-1}\mu^n e^{-\mu})$ to order $(1/\sqrt{\mu})^0$, we find

$$\frac{1}{n!}\mu^n e^{-\mu} \approx \frac{1}{\sqrt{2\pi\mu}}\exp\left(-\frac{(n-\mu)^2}{2\mu}\right). \tag{8.6}$$

Converting the sum in (8.4) into an integral, we then obtain

$$u_{00} = \frac{1}{\sqrt{2\pi}|\alpha|}\exp\left(-\frac{k^2}{2|\alpha|^2}\right), \qquad u_{10} = -ie^{-i\phi}\frac{k}{|\alpha|}u_{00}, \tag{8.7}$$

$$u_{20} = -2^{-1/2}e^{-2i\phi}\left(\frac{k^2}{|\alpha|^2}-1\right)u_{00}, \qquad u_{11} = \frac{k^2}{|\alpha|^2}u_{00}. \tag{8.8}$$

The normalization condition $\mathrm{Tr}(\rho(t+dt)) = 1$ leads to

$$\begin{aligned} P_k = u_{00}\bigg(1 + \frac{k}{|\alpha|}\langle \hat{A}+\hat{A}^\dagger\rangle\sqrt{dt} + \left(\frac{k^2}{|\alpha|^2}-1\right)\Big(|\zeta(t)|^2 - \frac{1}{2}\zeta(t)^2e^{-2i\phi} \\ - \frac{1}{2}(\zeta(t)^*)^2e^{2i\phi} + \kappa\langle\hat{a}^\dagger\hat{a}\rangle - \frac{\kappa}{2}e^{-2i\phi}\langle\hat{a}^2\rangle - \frac{\kappa}{2}e^{2i\phi}\langle(\hat{a}^\dagger)^2\rangle \\ - \sqrt{\kappa}(\zeta(t)-\zeta(t)^*e^{2i\phi})\langle\hat{a}^\dagger\rangle - \sqrt{\kappa}(\zeta(t)^*-\zeta(t)e^{-2i\phi})\langle\hat{a}\rangle\Big)dt\bigg), \end{aligned} \tag{8.9}$$

where $\hat{A} \equiv -ie^{-i\phi}(\zeta(t) - \sqrt{\kappa}\hat{a})$ and ϕ is the phase of the local oscillator, i.e., $\alpha = |\alpha|e^{i\phi}$. Comparing this result to

$$\frac{1}{\sqrt{2\pi(|\alpha|^2+\epsilon)}}\exp\left(-\frac{(k-\delta)^2}{2(|\alpha|^2+\epsilon)}\right) \approx u_{00}\left(1 + \frac{k\delta}{|\alpha|^2} + \left(\frac{k^2}{|\alpha|^2}-1\right)\frac{\epsilon+\delta^2}{2|\alpha|^2}\right) \tag{8.10}$$

for $\delta^2 \ll |\alpha|^2$ and $\epsilon \ll |\alpha|^2$, it follows that P_k is a Gaussian function of k with mean value $\delta = |\alpha|\langle\hat{A}+\hat{A}^\dagger\rangle\sqrt{dt}$ and variance $|\alpha|^2(1+\epsilon/|\alpha|^2)$, where $\epsilon/|\alpha|^2 \propto dt$. To order $\sqrt{dt}$, we may thus replace $k/|\alpha|$ by the stochastic variable

$$\frac{k}{|\alpha|} = \langle\hat{A}+\hat{A}^\dagger\rangle\sqrt{dt} + \frac{dW_\mathrm{s}}{\sqrt{dt}}, \tag{8.11}$$

where dW_s is a stochastic variable with a Gaussian probability distribution with mean value zero and variance dt. This expression provides a convenient way to simulate realistic sequences of measurement outcomes.

dW_s is a Wiener increment, and as shown in [123], the proper way to Taylor expand an expression containing a dW_s is to expand it to second order in dW_s and apply the rules $(dW_\mathrm{s})^2 = dt$ and $dW_\mathrm{s}dt = 0$. Remembering this, we use (8.9) and (8.11) to rewrite (8.3) into the final result $\rho(t+dt) = \rho(t) + d\rho(t)$,

$$\begin{aligned} d\rho(t) = \mathcal{L}\rho(t)dt + \sqrt{\kappa}[\hat{a}^\dagger,\rho(t)]\zeta(t)dt - \sqrt{\kappa}[\hat{a},\rho(t)]\zeta^*(t)dt + \Big(\hat{A}\rho(t) + \rho(t)\hat{A}^\dagger \\ - \langle\hat{A}+\hat{A}^\dagger\rangle\rho(t)\Big)dW_\mathrm{s} + \frac{\kappa}{2}\left(2\hat{a}\rho(t)\hat{a}^\dagger - \hat{a}^\dagger\hat{a}\rho(t) - \rho(t)\hat{a}^\dagger\hat{a}\right)dt, \end{aligned} \tag{8.12}$$

which is the stochastic master equation (SME) describing the time evolution of the state of the system and the cavity mode conditioned on the measurement outcome (8.11). The second and third terms on the right hand side of (8.12) describe the input of probe light into the cavity through $\mathrm{BS_C}$, the fourth term represents the knowledge obtained due to the homodyne detection, and the fifth term originates from the decay of the cavity field due to transmission through $\mathrm{BS_C}$. We remind the reader that (8.12) is written in a frame rotating with the cavity resonance angular frequency ω_C. If the probe beam and the LO beam are both monochromatic fields with angular frequency ω_L, the time dependence of $\zeta(t)$ and of $e^{i\phi}$ is given as $e^{-i(\omega_\mathrm{L}-\omega_\mathrm{C})t}$. (Alternatively, we can transform into a frame rotating with angular frequency ω_L in which case an extra term, $-i(\omega_\mathrm{C}-\omega_\mathrm{L})[\hat{a}^\dagger\hat{a},\rho(t)]dt$, appears on the right hand side of (8.12).) We note that the x-quadrature of the output field is measured if $e^{i\phi}/e^{-i(\omega_\mathrm{L}-\omega_\mathrm{C})t}=e^{-i\pi/2}$ and the p-quadrature is measured if $e^{i\phi}/e^{-i(\omega_\mathrm{L}-\omega_\mathrm{C})t}=1$ (cf. Fig. 2.3(b)).

If the efficiency of the photodetectors is η_d rather than unity, Eqs. (8.11) and (8.12) are still valid provided we replace $|\alpha|$ by $\sqrt{\eta_\mathrm{d}}|\alpha|$ and define $\hat{A}$ as $\hat{A}=-ie^{-i\phi}\sqrt{\eta_\mathrm{d}}(\zeta-\sqrt{\kappa}\hat{a})$. Cavity loss adds the term $(\kappa_\mathrm{L}/2)(2\hat{a}\rho(t)\hat{a}^\dagger-\hat{a}^\dagger\hat{a}\rho(t)-\rho(t)\hat{a}^\dagger\hat{a})dt$ to the right hand side of (8.12), where κ_L is the contribution to the cavity decay rate from loss.

Itô and Stratonovich form

Equation (8.12) is an Itô equation with the property that $\rho(t)$ and dW_s are statistically independent. There is also an alternative formulation, Stratonovich calculus, in which $(dW_\mathrm{s})^2=0$, but $\rho(t)$ and dW_s are not statistically independent [18]. We shall generally write Itô equations as $dx=a(x,t)dt+b(x,t)dW_\mathrm{s}$ and Stratonovich equations as $dx=\underline{a}(x,t)dt+\underline{b}(x,t)\circ dW_\mathrm{s}$. For real vectors x with elements x_i, the conversion rule is $\underline{a}_i(x,t)=a_i(x,t)-\frac{1}{2}\sum_j b_j(x,t)\frac{\partial}{\partial x_j}b_i(x,t)$ and $\underline{b}_i(x,t)=b_i(x,t)$ [124] (complex equations may be treated as twice as many real equations).

The linear stochastic master equation

Equation (8.12) is nonlinear in $\rho(t)$ because $\langle\hat{A}\rangle$ depends on $\rho(t)$. If $\mathcal{L}\rho(t)$ is linear in $\rho(t)$, we note, however, that we can obtain a linear equation if we avoid to normalize $\rho(t+dt)$ and avoid to introduce the expression (8.11) for k. Removing the factor $1/P_k$, we need to divide the right hand side of (8.3) by u_{00} to ensure that $\rho(t+dt)\to\rho(t)$ for $dt\to 0$. Changing variables from k to $dy_\mathrm{s}\equiv k\sqrt{dt}/|\alpha|$, (8.3) then takes the linear form

$$\begin{aligned}\rho(t+dt)&=\rho(t)+\mathcal{L}\rho(t)dt+\sqrt{\kappa}\left[\hat{a}^\dagger,\rho(t)\right]\zeta(t)dt-\sqrt{\kappa}\left[\hat{a},\rho(t)\right]\zeta^*(t)dt\\&\quad+(\hat{A}\rho(t)+\rho(t)\hat{A}^\dagger)dy_\mathrm{s}+\frac{\kappa}{2}(2\hat{a}\rho(t)\hat{a}^\dagger-\hat{a}^\dagger\hat{a}\rho(t)-\rho(t)\hat{a}^\dagger\hat{a})dt.\end{aligned}\tag{8.13}$$

$P_k=u_{00}\,\mathrm{Tr}(\rho(t+dt))$, and the probability density for dy_s is hence

$$P_{dy_\mathrm{s}}=\frac{P_k|\alpha|}{\sqrt{dt}}=\frac{1}{\sqrt{2\pi dt}}\exp\left(-\frac{(dy_\mathrm{s})^2}{2dt}\right)\mathrm{Tr}(\rho(t+dt)).\tag{8.14}$$

For $\eta_\mathrm{d} \neq 1$, the same equations hold, but dy_s is defined according to $dy_\mathrm{s} \equiv k\sqrt{dt}/(\sqrt{\eta_\mathrm{d}}|\alpha|)$, and $\hat{A} = -ie^{-i\phi}\sqrt{\eta_\mathrm{d}}(\zeta - \sqrt{\kappa}\hat{a})$.

Iterating (8.13) conditioned on the measurement sequence $dy_\mathrm{s}(t_1)$, $dy_\mathrm{s}(t_2)$, ..., $dy_\mathrm{s}(t_N)$ with $t_1 = t$ and $t_{i+1} = t_i + dt$, the conditional state after N steps is $\rho(t+Ndt)/\mathrm{Tr}(\rho(t+Ndt))$, and the probability to observe the specified sequence is

$$\mathrm{Tr}(\rho(t+Ndt))\prod_{i=1}^{N}\left(\frac{1}{\sqrt{2\pi dt}}\exp\left(-\frac{(dy_\mathrm{s}(t_i))^2}{2dt}\right)\right). \tag{8.15}$$

We shall refer to $y_\mathrm{s} = \sum_i dy_\mathrm{s}(t_i) = \int dy_\mathrm{s}$ as the integral of the photocurrent.

8.2 Bistable dynamics of a single atom in a cavity

As an example of an application of the SME, we consider probing of a two-level atom in a cavity. Such a system exhibits a variety of interesting dynamics [125], including scenarios where trajectories of the atom-cavity state tend to localize transiently but jump between multiple regions of state space on longer timescales. We loosely refer to such behavior as bistability, and we use the term semistable region to refer to the local regions of state space, where the system spends most of its time. The phase bistable regime, for which there are two semistable regions with different values of the phase of the cavity field, has been investigated in several papers [126, 127, 128], and it has been demonstrated that quantum jumps between the two regions can be observed via homodyne detection [127]. Below we shall concentrate on the absorptive bistable regime, for which the two semistable regions have different values of the amplitude of the cavity field [129]. Bistable systems are interesting both due to the nontrivial dynamics and because they have potential applications as memory units and switches. Examples of experimental investigations of bistability in cavity QED systems are provided in [130, 131, 132].

Model

In the following, we denote the ground state of the atom by $|g\rangle$ and the excited state by $|e\rangle$. The cavity field couples the two levels, and the excited state decays at a rate γ to the ground state via spontaneous emission. The photons are emitted in random directions, and it is not experimentally feasible to detect all of them with high efficiency. We thus assume that these photons are simply lost. In the dipole and rotating wave approximations, we then have [18]

$$\mathcal{L}\rho(t) = -\frac{i}{\hbar}[H,\rho(t)] + \frac{\gamma}{2}(2\hat{\sigma}\rho(t)\hat{\sigma}^\dagger - \hat{\sigma}^\dagger\hat{\sigma}\rho(t) - \rho(t)\hat{\sigma}^\dagger\hat{\sigma}) \tag{8.16}$$

with Hamiltonian

$$H = \hbar\Delta\hat{\sigma}^\dagger\hat{\sigma} + \hbar(g^*\hat{a}^\dagger\hat{\sigma} + g\hat{a}\hat{\sigma}^\dagger). \tag{8.17}$$

Here, $\hat{\sigma} = |g\rangle\langle e|$ is the atomic lowering operator, Δ is the atomic transition angular frequency in the rotating frame, $\hbar g = -\mathbf{d}_{ge}\cdot\mathbf{f}(\mathbf{r})\sqrt{\hbar\omega_\mathrm{C}/(2\epsilon_0)}$, $\mathbf{r}$ is the position of the atom, $\mathbf{f}(\mathbf{r})$ is the mode function of the cavity mode (including polarization), $\mathbf{d}_{ge} = \langle g|\mathbf{d}|e\rangle$ is the dipole matrix element for the atomic transition with $\mathbf{d} = -e\mathbf{r}_\mathrm{e}$ if we assume that the field interacts primarily with one electron in the atom, e is the absolute value of the charge of an electron, and $\mathbf{r}_\mathrm{e}$ is the position operator of the electron. For a standing wave cavity, as the one depicted in Fig. 8.1, the norm of g changes with a period of half of the wavelength of the cavity field when moving along the cavity axis, and the transverse profile of the cavity mode is often a Gaussian, whose width depends on the position along the cavity axis. For simplicity, we assume that the atom is trapped at a fixed position inside the cavity, such that the coupling strength g is constant.

We assume that the probe field and the LO are both monochromatic fields with angular frequency ω_L, and we remove the explicit time dependence from the SME by working in a frame rotating with the angular frequency ω_L. We can then use the second order derivative-free predictor-corrector integration method provided in [124] to integrate the SME numerically. This method is basically a more accurate version of the Itô-Euler integration method. While the latter replaces the infinitesimal numbers dt and dW_s by finite but small numbers, the former involves additional correction terms and evaluations of the factors multiplying dt and dW_s for different inputs. We choose a set of parameters for which the dynamics of the system is known to be absorptive bistable [133]: $\omega_\mathrm{C} = \omega_\mathrm{L}$, $\Delta/\gamma_\perp = 0$, $\kappa/(2\gamma_\perp) = 0.1$, $g/\gamma_\perp = -i\sqrt{2}$, and $\sqrt{\kappa}\zeta/\gamma_\perp = 0.56$, where $\gamma_\perp = \gamma/2$ is the transverse atomic decay rate and we have replaced $\zeta(t)$ by ζ. For these parameters, the expectation value of the number of photons in the cavity is typically below approximately 22, and we can truncate the basis of the Hilbert space of the cavity field at 59 photons without significant errors, which leads to a density matrix of dimension 120 × 120. As initial state, we choose the state with zero photons in the cavity and the atom in the ground state.

Dynamics

Results of the integration for a given realization of the measurement noise dW_s are shown in Fig. 8.2, where we have plotted the time evolution of the expectation values of the field quadrature operators $\hat{x}$ and $\hat{p}$ and the expectation values of the atomic Pauli operators $\hat{\sigma}_x = \hat{\sigma} + \hat{\sigma}^\dagger$, $\hat{\sigma}_y = i(\hat{\sigma} - \hat{\sigma}^\dagger)$, and $\hat{\sigma}_z = [\hat{\sigma}^\dagger, \hat{\sigma}]$. As claimed, the system is seen to jump between two semistable regions with different expectation values of the operators. One

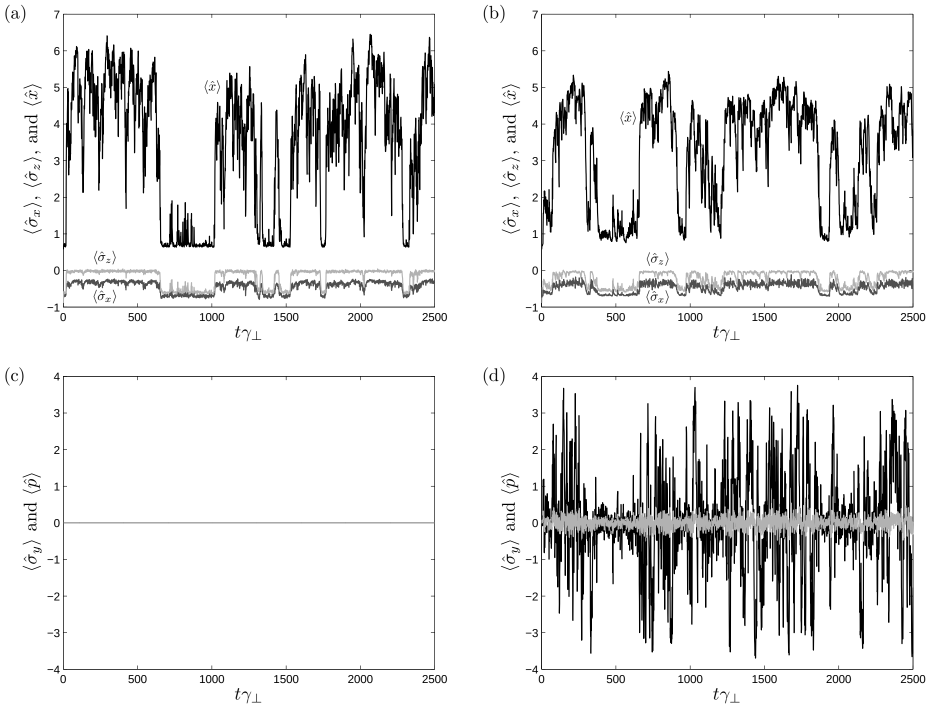

Figure 8.2: Stochastic time evolution of $\langle\hat{x}\rangle$ (black), $\langle\hat{\sigma}_z\rangle$ (light gray), and $\langle\hat{\sigma}_x\rangle$ (gray) (upper plots) and of $\langle\hat{p}\rangle$ (black) and $\langle\hat{\sigma}_y\rangle$ (light gray) (lower plots) for homodyne detection of the x-quadrature (left plots) and for homodyne detection of the p-quadrature (right plots).

region (henceforth denoted the lower semistable region (LSR)) is characterized by a rather low cavity field amplitude and a value of $\langle\hat{\sigma}_z\rangle$ closer to -1 than 1, and the other region (henceforth denoted the upper semistable region (USR)) has a higher field amplitude and a value of $\langle\hat{\sigma}_z\rangle$ close to zero. In order to be a semistable region, the net rate at which photons are injected into the cavity due to the coupling to the probe field must balance the rate of spontaneous emission events. To get a rough idea of the physics involved, we ignore the measurements for a moment and assume that the cavity field is in a coherent state with amplitude ξ. If the cavity was empty, it follows from (8.12) with $\mathcal{L}\rho(t)dt = 0$ and $\rho(t) = |\xi\rangle\langle\xi|$ that $d\xi/dt = \sqrt{\kappa}\zeta - (\kappa/2)\xi$. For a given (real) value of ξ, the net rate of photon injection is $d\langle\hat{a}^\dagger\hat{a}\rangle/dt = d\xi^2/dt = \xi(2\zeta/\sqrt{\kappa} - \xi)\kappa$. The injection process is hence most efficient midway between $\xi = 0$ and the steady state field amplitude $\xi = 2\zeta/\sqrt{\kappa}$ for an empty cavity. The average rate of spontaneous emission events is γ times the probability that the atom is in the excited state, and this quantity increases from zero to $\gamma/2$ when ξ increases from zero to infinity. The LSR corresponds to a relatively low photon injection rate due to a low value of ξ, and the atom can emit the injected photons

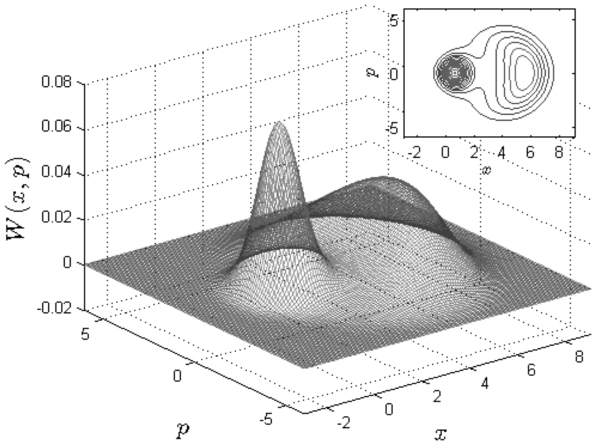

Figure 8.3: Wigner function of the steady state cavity field obtained when the output field from the cavity is not detected (i.e., the steady state solution of (8.12) without the stochastic term traced over the state of the atom). The inset is a contour plot of the Wigner function with level curves at $W(x,p) = 0.005, 0.010, \ldots, 0.075$.

without being saturated. From Fig. 8.2(a), we find $\xi \approx \langle\hat{x}\rangle/\sqrt{2} \approx 0.5$ and $\langle\hat{\sigma}_z\rangle \approx -0.5$. These numbers lead to an estimated photon injection rate of $0.5\ \gamma_\perp$ and an estimated rate of spontaneous emission events of $0.5\ \gamma_\perp$. For the USR, the atomic transition is saturated, and the rate of spontaneous emission events is nearly $\gamma_\perp$. To balance this rate, the cavity field amplitude assumes a value sufficiently close to $2\zeta/\kappa$. The value obtained from Fig. 8.2(a) is $\xi \approx 3.7$, which leads to an estimated photon injection rate of approximately $1.4\ \gamma_\perp$.

The value of $\langle\hat{x}\rangle$ tends to fluctuate more in the USR than it does in the LSR, which indicates that the USR is comprised of a larger number of states. For an x-quadrature measurement, $\langle\hat{p}\rangle$ and $\langle\hat{\sigma}_y\rangle$ are both zero at all times for the chosen initial state due to symmetry (for $\phi = -\pi/2$, $\omega_{\mathrm{L}} = \omega_{\mathrm{C}}$, $\Delta = 0$, $\zeta^* = \zeta$, and $g^* = -g$, the SME is invariant under the anti-unitary transformation $\hat{T}$ given by $\hat{T}\hat{a}\hat{T}^{-1} = \hat{a}$, $\hat{T}\hat{\sigma}\hat{T}^{-1} = \hat{\sigma}$, and $\hat{T}i\hat{T}^{-1} = -i$, which changes the sign of $\hat{p}$ and $\hat{\sigma}_y$ but not of $\hat{x}$, $\hat{\sigma}_x$, and $\hat{\sigma}_z$). For a p-quadrature measurement, $\langle\hat{p}\rangle$ and $\langle\hat{\sigma}_y\rangle$ are noisy, but the noise is seen to be significantly reduced in the LSR compared to in the USR. We note that for an x-quadrature measurement, the two semistable regions correspond to different mean values of the photocurrent. For a p-quadrature measurement, on the other hand, the mean photocurrent is the same for the two semistable regions, and the distinguishability relies on the differences in the precise dynamics within the two regions (for instance, the width of the fluctuations of $\langle\hat{p}\rangle$). We also note that the time evolution of the density

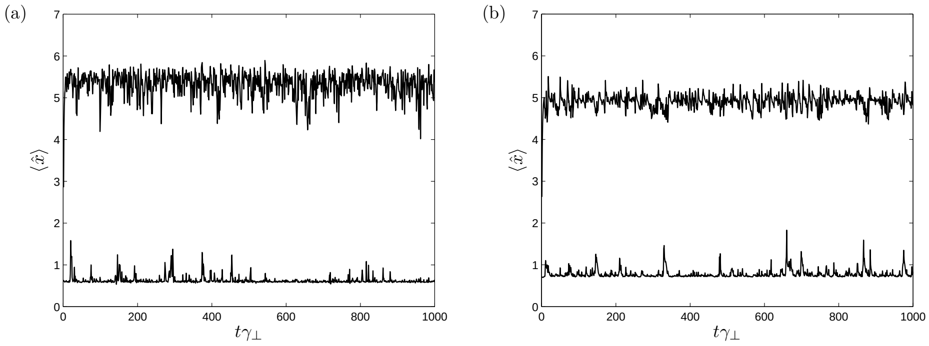

Figure 8.4: Stochastic time evolution of $\langle\hat{x}\rangle$ when we add the feedback term (8.18) to the SME. (a) Homodyne detection of the x-quadrature. $x_0 = 5.37$ and $s_\mathrm{p} = 0.53$ for the upper curve, and $x_0 = 0.57$ and $s_\mathrm{p} = 0.71$ for the lower curve. (b) Homodyne detection of the p-quadrature. $x_0 = 4.95$ and $s_\mathrm{p} = 0.53$ for the upper curve, and $x_0 = 0.71$ and $s_\mathrm{p} = 0.71$ for the lower curve.

operator is influenced by the fact that we retrieve information about the state of the system via homodyne detection. If we average over all possible measurement outcomes by turning off the detector, the density operator decays to a steady state with a bimodal structure as apparent in Fig. 8.3, where we have traced out the atomic state and plotted the Wigner function of the cavity field. Note that the LSR looks more like a coherent state than the USR does, and it is to be expected that the above crude model provides less accurate results for the USR.

Feedback control

As a final remark, we note that feedback control can be used for controlling the dynamics. If, for instance, we add the (proportional) feedback term

$$d\rho_\mathrm{fb}(t) = s_\mathrm{p} e(t)[\hat{a} - \hat{a}^\dagger, \rho(t)]\gamma_\perp dt, \quad e(t) \equiv \langle\hat{x}\rangle - x_0, \tag{8.18}$$

to the SME, where s_p and x_0 are constants, we obtain the time evolution of $\langle\hat{x}\rangle$ shown for a given noise realization in Fig. 8.4. The feedback term increases the drive field amplitude whenever $\langle\hat{x}\rangle < x_0$ and decreases the drive field amplitude whenever $\langle\hat{x}\rangle > x_0$. As a result, it is possible to keep the system within the USR or within the LSR for appropriate choices of x_0. The fluctuations of $\langle\hat{x}\rangle$ can be decreased by increasing the feedback strength s_p, but we have chosen the stated values for later comparison with the results obtained in Chap. 11.

8.3 Conclusion

In conclusion, we have introduced several concepts and equations that are important in the following chapters. We have demonstrated how the well-known stochastic master equation for a probed system in a cavity can be derived from the basic physical processes involved by use of the methods of Chaps. 2-6. We have only considered the limit of an infinitesimal round trip time τ of light in the cavity, but an advantage of the presented method is the fact that it is straightforward to generalize it to finite τ, including the possibility of significant changes of the state of the light field within one round trip, which is relevant for optically thick atomic ensembles. We have also investigated absorptive bistability of a single probed two-level atom in a cavity. Further examples of applications are provided in [VI].

Chapter 9

Continuous two-qubit parity measurement

When we probe a quantum mechanical system, the interaction between the system and the probe and the knowledge we obtain by measuring the probe both disturb the state of the system. Under certain circumstances, it is, however, possible to construct measurements, which act to slowly project the state of the system onto an eigenstate of an observable of the system without otherwise disturbing the time evolution of the observable. A very interesting perspective of such measurements is the possibility to prepare systems in an eigenstate of an observable. An example is given in [134], where atoms are used to probe the number of photons in a microwave cavity, which leads to generation of photon number states. To achieve such quantum nondemolition (QND) measurements, one should avoid first that the probe-system interaction affects the time evolution of the measured observable in the Heisenberg picture and second that the inevitable increase in uncertainty of observables not commuting with the measured observable changes the time evolution of the measured observable [135]. An example, where the latter condition is not fulfilled, is if we make a precise measurement of the position of a free particle, which is initially in a state with small momentum uncertainty. The measurement leads to a broadening of the momentum distribution, which in turn affects the time evolution of the position of the particle. Precise conditions for determining when a measurement is of the QND type are discussed in [136], but here we only consider systems for which the Hamiltonian describing the internal dynamics of the system in absence of the probe is zero. In the lossless case, it is then sufficient to require that the measured observable commutes with the Hamiltonian describing the interaction between the system and the probe.

A particularly interesting case arises when the measured observable has degenerate eigenvalues. One may then obtain partial information about the state of the system, while leaving specific subspaces unaffected. This possibility paves one way to conditionally prepare a collection of atoms in a Schrödinger cat state via probing [137] and to protect quantum information. An example of the latter is the three-qubit bit-flip quantum error correction code [1], which works as follows. Each qubit of information is encoded in the states $|{\downarrow\downarrow\downarrow}\rangle$ and $|{\uparrow\uparrow\uparrow}\rangle$ (the code space) of three physical qubits, where $|{\downarrow}\rangle$ and $|{\uparrow}\rangle$ denote the two levels of one physical qubit. A single bit-flip error can then be detected by measuring the parity of qubits 1 and 2 and the parity of qubits 2 and 3 (the parity is even if the qubits are in the same state and odd if they are in different states). If an error has occurred, we know from the measurement results, which qubit has flipped, and the error can hence be corrected without affecting the stored information. Parity measurements are also interesting in their own right, for instance as a tool to prepare two initially uncorrelated qubits in an entangled state. Below, we shall refer to the subspace spanned by $\{|{\downarrow\downarrow}\rangle, |{\uparrow\uparrow}\rangle\}$ as the even (parity) subspace and the subspace spanned by $\{|{\downarrow\uparrow}\rangle, |{\uparrow\downarrow}\rangle\}$ as the odd (parity) subspace.

A method to perform a parity measurement on two qubits has been proposed in [138]. In this work, each qubit consists of a single atom in a cavity, and the states $|{\downarrow}\rangle$ and $|{\uparrow}\rangle$ are two hyperfine states of the ground state manifold of the atom. The measurement proceeds by allowing a probe field, which is on resonance with the cavity and initially in a continuous coherent state $|\{\alpha(t)\}\rangle$ (see (2.19)), to interact sequentially with the two qubits, and the probe field is then detected with a homodyne detector. It is assumed that the probe field couples the state $|{\uparrow}\rangle$ resonantly to an excited state $|e\rangle$, while no light-atom interaction takes place if the considered atom is in the state $|{\downarrow}\rangle$. If the intensity of the probe field is not too high and the light-atom coupling strength is large compared to the rate of spontaneous emission and the cavity decay rate, the probe field is reflected at the input mirror of the cavity if the atom is in the state $|{\uparrow}\rangle$ because the light-atom interaction prevents the cavity field from building up. On the contrary, if the atom is in the state $|{\downarrow}\rangle$, the cavity field does build up because the probe field is on resonance with the cavity and does not see the atom. As we shall see in detail below, this means that the interaction between the probe light and one qubit changes the phase of the probe field by π if the atom is in the state $|{\downarrow}\rangle$ and does not change the phase of the probe field if the atom is in the state $|{\uparrow}\rangle$ (for an appropriate choice of phase convention). This type of interaction has been proposed in [139]. The parity of the two qubits is hence odd if the phase of the probe field has changed by π after interaction with both qubits and even if the phase of the probe field has changed by 0 or 2π. Note that the measurement takes a finite amount of time because there is a significant overlap between the Wigner functions corresponding to the single-mode coherent states $|\alpha(t)\sqrt{dt}\rangle$ and $|-\alpha(t)\sqrt{dt}\rangle$, i.e., we need to detect several of the time-localized modes of the probe beam to see the difference. The decrease in intensity of the cavity field when the atom is in the state $|{\uparrow}\rangle$ compared to the intensity when the atom is in the state $|{\downarrow}\rangle$ has been used in a recent experiment [117] to readout the state of a single atom in a cavity with a fidelity exceeding 0.9992 in a readout time of 100 μs.

Quantum error correction is often thought of as a discrete process, in which practically instantaneous measurements at certain times during a quantum computation project the state of the system on a subspace, which is either the code space or a state in which an error has occurred. In the latter case, the error may be corrected before the computation proceeds or it may be recorded and corrected later. An alternative approach is continuous quantum error correction [140, 141] in which errors are corrected continuously in time by application of feedback. This is, for instance, useful if one would like to increase the lifetime of a quantum memory. The continuous probing of qubits described above is suitable for such constructions, and, in fact, it has been used in a proposal to implement a continuous version of the three-qubit bit-flip code [142] with the modification that the probe fields are not detected but rather used directly to control the applied feedback by use of optical switches. In this way, the setup automatically corrects errors without the need for any external actions, and the state of the qubits remains close to the code space at all times.

Independent of whether the probe field is detected or used directly in a feedback loop, it is important to minimize decoherence within the even and the odd parity subspaces due to the interaction with the probe. The scheme in [138] is sensitive to light field losses between and within the two cavities as well as to spontaneous emission from the excited state of each atom, arising because the field is not completely expelled from the cavity when the atom is in the state $|\uparrow\rangle$. The purpose of the present chapter is to show that a slight modification of the setup can decrease the rate of decoherence in the odd parity subspace or in the even parity subspace significantly. The basic idea of our proposal is to allow the probe field to interact several times with the two qubits by reflecting some of the light emerging from the second cavity back onto the input mirror of the first cavity. Exploiting constructive and destructive interference between light fields having traveled a different number of round trips in the resulting loop, it is possible to reduce the intensity of the cavity fields and the field between the two cavities for one of the parity subspaces without reducing the sensitivity of the parity measurement. The decrease in light intensity reduces the average number of photons lost per unit time, which in turn reduces the rate of decoherence within that subspace. We also consider an alternative parity measurement in which the probe field is not on resonance with the atomic transition, and we compare the performance of the two approaches.

In Sec. 9.1, we study the interaction between the probe field and a single qubit in more detail, both for a resonant and a nonresonant light-atom interaction. We identify an appropriate parameter regime and provide analytical results for the cavity field and the transformation of the probe field. These results are used in Sec. 9.2 to explain the details of our proposal. In

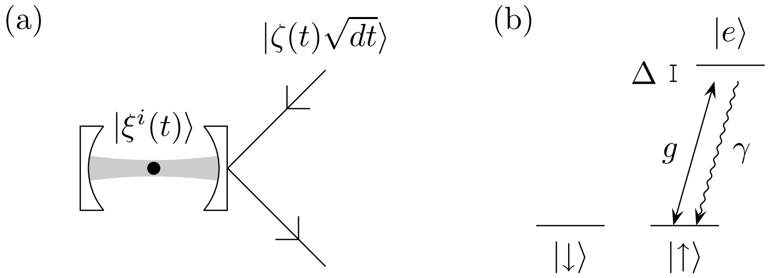

Figure 9.1: (a) Interaction of a probe field with a single atom in a cavity and (b) the relevant level structure of the atom.

Sec. 9.3, we derive an equation for the final purity after the measurement of a state restricted to either the odd or the even parity subspace and identify the parameters, which characterize the performance of the proposal. These parameters are evaluated for a nonresonant light-atom interaction in Sec. 9.4 and for a resonant light-atom interaction in Sec. 9.5, where we also compare the two approaches. The chapter is based on [X][1].

9.1 Single atom in a cavity

Before considering the complete parity measurement, we describe the relevant interaction between a probe field and a cavity containing a single atom as illustrated in Fig. 9.1(a)[2], and we show how we can simplify the description in the parameter regime of interest.

Light-atom interaction

The relevant level structure of the atom is shown in Fig. 9.1(b). The cavity field couples the state $|\uparrow\rangle$ to the excited state $|e\rangle$ with coupling strength g and detuning Δ, and the state $|e\rangle$ decays at a rate γ by spontaneous emission to the state $|\uparrow\rangle$. Decay from $|e\rangle$ to $|\downarrow\rangle$ is assumed to be forbidden by selection rules. The part of the SME describing the interaction between the atom and the cavity field is then given by Eqs. (8.16) and (8.17) with $\hat{\sigma} = |\uparrow\rangle\langle e|$. In the following, we assume $g = g^* \geq 0$ and choose to work in a frame rotating with the angular frequency ω_{L} of the probe field.

We are only interested in the parameter regime for which the probability to populate the excited level is small because we would like to avoid leakage of information to the surroundings due to spontaneous emission. We

---

[1] Copyright (2010) by the American Physical Society.

[2] The input and output fields of a standing wave cavity can be separated by use of a circulator as drawn in Fig. 1 of [142]. For convenience, we draw the beams as if they make an angle with the cavity axis as in [138] instead of explicitly showing the circulator.

thus assume that either the atomic decay rate or the absolute value of the light-atom detuning is large compared to the effective driving of the atomic transition, which amounts to the condition

$$\frac{g^2|\langle\hat{a}\rangle_\uparrow|^2}{\gamma^2/4+\Delta^2} \sim \epsilon, \tag{9.1}$$

where $\langle\hat{a}\rangle_\uparrow$ is the expectation value of the cavity field operator conditioned on the atom being in the state $|\uparrow\rangle$ and $\epsilon \ll 1$ is a small number. We also assume the weak probe condition $\sqrt{\kappa}|\zeta(t)|/g \sim \epsilon^{1/2}$. Under these assumptions, we can simplify the description by eliminating the excited state adiabatically, and we may ignore the coupling between the cavity mode and the light modes outside the cavity while doing so.

Formally, we write down the quantum stochastic differential equation [118], which describes the interaction between the atom and the cavity field and the interaction between the cavity field and the probe beam, and we assume that all terms proportional to γ or Δ scale as ϵ^{-1}, while all terms proportional to g scale as $\epsilon^{-1/2}$, and all other terms scale as ϵ^0. Following the procedure in [120, 121], we then take the limit $\epsilon \to 0$. Only terms arising from the interaction between the atom and the cavity field are affected, and the final result amounts to the replacement of the interaction between the atom and the cavity field by the effective interaction

$$\begin{aligned}\mathcal{L}\rho(t) = {}& \frac{i\Delta g^2}{(\gamma/2)^2+\Delta^2}\left[\hat{a}^\dagger\hat{a}|\uparrow\rangle\langle\uparrow|,\rho(t)\right] + \frac{\gamma}{2}\frac{g^2}{(\gamma/2)^2+\Delta^2} \\ & \times\left(2\hat{a}|\uparrow\rangle\langle\uparrow|\rho(t)|\uparrow\rangle\langle\uparrow|\hat{a}^\dagger - \hat{a}^\dagger\hat{a}|\uparrow\rangle\langle\uparrow|\rho(t) - \rho(t)|\uparrow\rangle\langle\uparrow|\hat{a}^\dagger\hat{a}\right),\end{aligned} \tag{9.2}$$

where the Hilbert space of the atom is now restricted to the subspace spanned by $\{|\downarrow\rangle,|\uparrow\rangle\}$. The first term changes the phase of the cavity field by $\Delta g^2/((\gamma/2)^2+\Delta^2)$ per photon per unit time conditioned on the atom being in the state $|\uparrow\rangle$, and the second term is a conditional photon loss corresponding to an additional contribution to the cavity decay rate of $\gamma g^2/((\gamma/2)^2+\Delta^2)$ if the atom is in the state $|\uparrow\rangle$. Note that there is no coupling between the states $|\downarrow\rangle$ and $|\uparrow\rangle$ in (9.2).

Conditional steady state field amplitudes

An important point to note is the fact that if the state of the atom is $|\downarrow\rangle$ or $|\uparrow\rangle$, then the interaction in (9.2) corresponds to a combination of optical components, which transform coherent states into coherent states. As a consequence, the solution of $d\rho(t)/dt = \mathcal{L}\rho(t)$, which fulfils the relevant initial conditions, takes the form $\rho(t) = \sum_i\sum_j c_{ij}(t)|\xi^i(t)\rangle\langle\xi^j(t)| \otimes |i\rangle\langle j|$, where $i,j \in \{\downarrow,\uparrow\}$ and $|\xi^i(t)\rangle$ is a single-mode coherent state of the cavity mode. Inserting this solution into $d\rho(t)/dt = \mathcal{L}\rho(t)$ and assuming the limit of an infinitesimal round trip time $\tau = dt$ of light in the cavity, we find that the conditional cavity field amplitudes $\xi^i(t)$ change by

$$(d\xi^i(t))_{\mathcal{L}} = -\left(\frac{\gamma}{2} - i\Delta\right) \frac{g^2 \delta_{i\uparrow}}{(\gamma/2)^2 + \Delta^2} \xi^i(t) dt \tag{9.3}$$

within one round trip time, and the coefficients $c_{ij}(t)$ change by

$$(dc_{ij}(t))_{\mathcal{L}} = \frac{\gamma}{2} \frac{g^2}{(\gamma/2)^2 + \Delta^2} \left(2\xi^i(\xi^j)^* \delta_{i\uparrow}\delta_{j\uparrow} - |\xi^i|^2 \delta_{i\uparrow} - |\xi^j|^2 \delta_{j\uparrow}\right) c_{ij}(t) dt, \tag{9.4}$$

where δ_{ij} is the Kronecker delta. The latter equation expresses the decay of $c_{\downarrow\uparrow}(t)$ and $c_{\uparrow\downarrow}(t)$ due to the loss term (note that $(dc_{\downarrow\downarrow}(t))_{\mathcal{L}} = (dc_{\uparrow\uparrow}(t))_{\mathcal{L}} = 0$).

The detuning $\delta = \omega_{\mathrm{C}} - \omega_{\mathrm{L}}$ between the angular frequency ω_{C} of the cavity resonance and the angular frequency ω_{L} of the probe field leads to a further change of ξ^i by $e^{-i\delta dt}\xi^i(t) - \xi^i(t) = -i\delta\xi^i(t)dt$, and the interaction between the cavity field and the mode of the probe beam hitting the cavity input mirror in the interval from t to $t + dt$ transforms $|\xi^i(t) + (d\xi^i(t))_{\mathcal{L}} - i\delta\xi^i(t)dt\rangle|\zeta(t)\sqrt{dt}\rangle$ into

$$\begin{aligned} U_{\mathrm{BS_C}}|\xi^i(t) + (d\xi^i(t))_{\mathcal{L}} - i\delta\xi^i(t)dt\rangle|\zeta(t)\sqrt{dt}\rangle &= |\xi^i(t) - (\kappa/2)\xi^i(t)dt \\ + (d\xi^i(t))_{\mathcal{L}} - i\delta\xi^i(t)dt + \sqrt{\kappa}\zeta(t)dt\rangle &\otimes |(\zeta(t) - \sqrt{\kappa}\xi^i(t))\sqrt{dt}\rangle, \end{aligned} \tag{9.5}$$

where the beam splitter transformation $U_{\mathrm{BS_C}}$ for the input mirror is defined in Eq. (8.2) and $t_{\mathrm{C}}^2 = \kappa dt$ is assumed to be small. Altogether, $\xi^i(t)$ thus fulfils the differential equation

$$\frac{d\xi^i(t)}{dt} = -\frac{\kappa}{2}\xi^i(t) - \left(\frac{\gamma}{2} - i\Delta\right) \frac{g^2\delta_{i\uparrow}}{(\gamma/2)^2 + \Delta^2}\xi^i(t) - i\delta\xi^i(t) + \sqrt{\kappa}\zeta(t). \tag{9.6}$$

If $\zeta(t)$ is time-independent ($\zeta(t) = \zeta$), it follows that $\xi^i(t)$ decays at a rate $(\kappa/2)(1 + 2C\delta_{i\uparrow}/(1 + D^2))$, where $C \equiv 2g^2/(\kappa\gamma)$ is the (single atom) cooperativity parameter and $D \equiv 2\Delta/\gamma$, towards the steady state value

$$\xi^i = \frac{2\zeta}{\sqrt{\kappa}} \frac{1 + D^2}{1 + D^2 + 2C\delta_{i\uparrow} - 2iCD(\delta_{i\uparrow} - \delta(1 + D^2)/(\kappa CD))}. \tag{9.7}$$

Note that this time evolution is independent of what may happen to the output field from the cavity. If we denote the conditional, steady state output field amplitude $\zeta - \sqrt{\kappa}\xi^i$ (see (9.5)) by $F^i\zeta$, we find

$$F^i = -\frac{1 + D^2 - 2C\delta_{i\uparrow} + 2iCD(\delta_{i\uparrow} - \delta(1 + D^2)/(\kappa CD))}{1 + D^2 + 2C\delta_{i\uparrow} - 2iCD(\delta_{i\uparrow} - \delta(1 + D^2)/(\kappa CD))}. \tag{9.8}$$

Due to energy conservation, we have $|F^i| \leq 1$.

Let us first consider the resonant case $D = 0$ with $\delta = 0$. The conditional steady state cavity field amplitudes then evaluate to $\xi^{\downarrow} = 2\zeta/\sqrt{\kappa}$ and $\xi^{\uparrow} =$

$2\zeta/\sqrt{\kappa}/(1+2C)$, respectively, and $F^{\downarrow} = -1$, while $F^{\uparrow} = -(1-2C)/(1+2C)$. As postulated above, the conditional output field amplitudes $F^{\downarrow}\zeta$ and $F^{\uparrow}\zeta$ thus differ by a sign in the single atom strong coupling limit $C \gg 1$, which allows us to distinguish between the atomic states $|\downarrow\rangle$ and $|\uparrow\rangle$ via homodyne detection of the output field (if ζ is real, we measure the x-quadrature). Furthermore, the cavity field amplitude is close to zero if the atom is in the state $|\uparrow\rangle$.

For the nonresonant case $D \sim C \gg 1$, we may neglect the terms 1 and $\mp 2C\delta_{i\uparrow}$ in the numerator and in the denominator of (9.8) to lowest order in $1/C$, and if we choose $\delta = (\kappa/2)DC/(1+D^2)$, which we shall do in the remainder of this chapter, we obtain $F^{\downarrow} \approx (F^{\uparrow})^*$ and $|F^{\uparrow}| \approx |F^{\downarrow}| = 1$. The states $|\downarrow\rangle$ and $|\uparrow\rangle$ thus change the phase of the probe field by equal amounts but in opposite directions, and again it is possible to distinguish the two cases via homodyne detection of the output field (if ζ is real, we measure the p-quadrature).

Validity of the approximations

Having computed the steady state cavity field amplitude $\xi^{\uparrow}$ conditioned on the atomic state $|\uparrow\rangle$, we can now check whether assumption (9.1), which evaluates to

$$\frac{2|\zeta|^2}{\gamma} \times \frac{4C(1+D^2)}{(1+D^2+2C)^2 + C^2D^2} \ll 1, \tag{9.9}$$

is consistent. The first factor is the number of photons in the input beam per unit time relative to the average rate of spontaneous emission events for an atom with an average probability of one half to be in the excited state. In the strong coupling limit $C \gg 1$, the second factor is of order $1/C$ independent of whether $D \sim 0$, $D \sim 1$, or $D \sim C$. In the resonant case, $D = 0$, this appears because the possibility of spontaneous emission prevents the cavity field from building up (as for the LSR in Sec. 8.2), while in the nonresonant case, $D \sim C$, it is a consequence of the fact that the driving of the transition between $|\uparrow\rangle$ and $|e\rangle$ is inefficient when the atom-light detuning is large. The second factor is also small if $D \gg C$, but this is uninteresting since the atom does not interact significantly with the field in that limit and $F^{\uparrow} \approx F^{\downarrow} \approx -1$. When $C \gg 1$, the condition thus simplifies to $2|\zeta|^2/(\gamma C) = \kappa|\zeta|^2/g^2 \ll 1$, which is, in fact, the same as the weak probe condition $\sqrt{\kappa}|\zeta|/g \sim \epsilon^{1/2}$. In summary, we thus require $C \gg 1$ and $\kappa|\zeta|^2/g^2 \ll 1$ in order to obtain the desired effect and in order to make the above treatment valid. If the probe field amplitude is too high, we may, for instance, run into the absorptive bistable regime, which is, of course, undesirable in the present context.

It has been a long standing goal to achieve the single atom strong coupling regime $C \gg 1$ experimentally, and several groups working with single atoms in cavities have now succeeded [111, 117, 143, 144, 145, 146]. In these experiments, a typical high value of C is $C \sim 100$. In addition, there are a number of alternative systems, which allow strong coupling between electromagnetic radiation and two-level systems. Strong coupling has, for instance, been achieved for circuit QED systems [147, 148], quantum dots [149, 150], and nitrogen-vacancy centers in diamond [151].

9.2 Two-qubit parity measurement

In the following, we consider two qubits, and we hence change notation from g, κ, γ, Δ, C, D, and F^i to g_q, κ_q, γ_q, Δ_q, C_q, D_q, and F_q^{iq}, where $q = 1, 2$ refers to qubit 1 or to qubit 2.

Qualitative description

To perform a two-qubit parity measurement, we propose to use the setup shown in Fig. 9.2. Let us first consider the case of a resonant light-atom interaction. For the odd parity subspace, the interaction with cavity 1 and cavity 2 altogether changes the phase of the probe field in the loop by π, and we may choose the phase shift imposed by the phase shifter such that all other phase shifts in the loop add up to zero. There is then destructive interference between light fields having traveled a different number of round trips in the loop, and the field in the loop is almost extinguished. This improves the robustness with respect to loss because the total number of photons lost per unit time is proportional to the intensity. The destructive interference also decreases the field amplitudes inside the qubit cavities, which reduces the rate of spontaneous emission events and further decreases the decoherence rate. At the same time, the sensitivity of the parity measurement is not decreased. This happens because the interference in the loop is constructive for the even subspace. The phase of the output field from the loop hence differs by π for the two subspaces.

For the nonresonant case, cavity 1 and cavity 2 change the phase of the probe field by equal amounts but in opposite directions if the state of the qubits belongs to the odd subspace and the parameters for the two cavities are identical. We can hence obtain destructive interference in the loop if the sum of all other phase shifts within the loop add up to π. For the even subspace cavity 1 and cavity 2 change the phase of the light field in the same direction. For an appropriate choice of detuning, the phase shift is plus or minus $\pi/2$ at both cavities, and constructive interference occurs in the loop.

We note that the roles of the odd and the even parity subspaces can be exchanged by adding a phase shift of π within the loop, but in the following we focus on protecting the odd subspace. We do so because the output field from the loop is not exactly the same for the two even parity states because spontaneous emission is possible for $|\uparrow\uparrow\rangle$ but not for $|\downarrow\downarrow\rangle$. While this makes the analysis more complicated, it will not have any significant effects since the corrections are of second order in $1/C$.

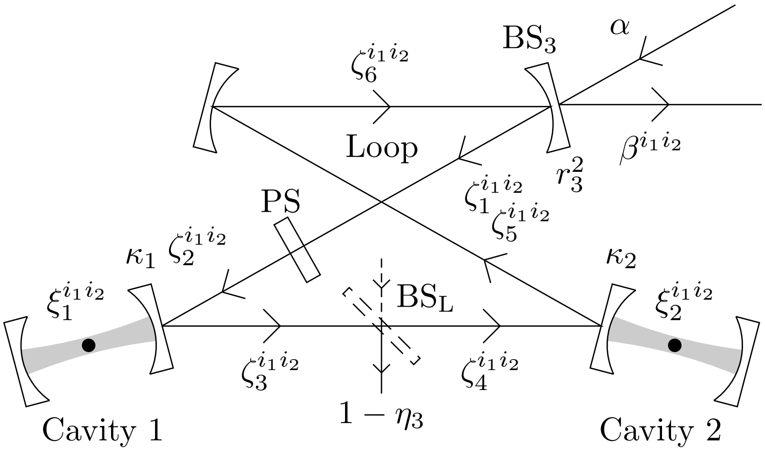

Figure 9.2: Proposed setup to perform a parity measurement on two qubits, each encoded in two ground state levels of a single atom in a cavity. The input field α is in a continuous coherent state, and the output field $\beta^{i_1 i_2}$ is observed with a homodyne detector. The Greek letters label the field at different positions as explained in the text, $r_3^2 = 1 - t_3^2$ is the reflectivity of the input beam splitter BS$_3$ of the loop, the phase shifter (PS) imposes the phase factor $P = e^{i\psi}$ on the light field, and $1 - \eta_3$ is the reflectivity of the fictitious beam splitter BS$_\text{L}$, which is included to account for losses between cavity 1 and cavity 2.

Quantitative description

Since the loop is constructed of optical components, which transform coherent states into coherent states, we can proceed as in the previous section and write the state of the atoms, the two cavity modes, and the modes inside the loop as

$$\rho(t) = \sum_{i_1}\sum_{j_1}\sum_{i_2}\sum_{j_2} c_{i_1 j_1 i_2 j_2}(t) \bigotimes_{k=1}^{N} |\zeta_k^{i_1 i_2}(t)\sqrt{dt_k}\rangle\langle\zeta_k^{j_1 j_2}(t)\sqrt{dt_k}| \\ \bigotimes_{q=1}^{2} |\xi_q^{i_1 i_2}(t)\rangle\langle\xi_q^{j_1 j_2}(t)| \otimes |i_1\rangle\langle j_1| \otimes |i_2\rangle\langle j_2|, \quad (9.10)$$

where $i_q \in \{\downarrow, \uparrow\}$ and $j_q \in \{\downarrow, \uparrow\}$ specify the state of the atom in cavity $q \in \{1, 2\}$ and $c_{i_1 j_1 i_2 j_2}(t)$ are time-dependent coefficients. We have divided the field inside the loop into N time-localized modes of temporal widths dt_k and conditional amplitudes $\zeta_k^{i_1 i_2}(t)$, $k = 1, 2, \ldots, N$, normalized such that $|\zeta_k^{i_1 i_2}(t)|^2 dt_k$ is the expectation value of the number of photons in the kth mode conditioned on the atoms being in the state $|i_1 i_2\rangle$. $\xi_q^{i_1 i_2}(t)$ is the conditional amplitude of the field in cavity q, normalized such that $|\xi_q^{i_1 i_2}(t)|^2$ is the conditional expectation value of the number of photons in cavity

q. The time-dependence of the coefficients $c_{i_1j_1i_2j_2}(t)$, which is discussed in more detail in Sec. 9.3, arises solely from the homodyne detection of the output field and from light field losses. Note that the conditional field amplitudes $\xi_q^{i_1i_2}(t)$ and $\zeta_k^{i_1i_2}(t)$ are not affected by the homodyne detection of the output field from the loop.

When the conditional amplitudes have reached steady state, it is sufficient to use 6 modes to describe the field in the loop, and inspection of Fig. 9.2 gives

$$\zeta_1^{i_1i_2} = t_3\alpha + ir_3\zeta_6^{i_1i_2}, \qquad \zeta_2^{i_1i_2} = P\zeta_1^{i_1i_2}, \qquad \zeta_3^{i_1i_2} = F_1^{i_1}\zeta_2^{i_1i_2}, \tag{9.11a}$$

$$\zeta_4^{i_1i_2} = \sqrt{\eta_3}\zeta_3^{i_1i_2}, \qquad \zeta_5^{i_1i_2} = F_2^{i_2}\zeta_4^{i_1i_2}, \qquad \zeta_6^{i_1i_2} = i\zeta_5^{i_1i_2}, \tag{9.11b}$$

$$\beta^{i_1i_2} = t_3\zeta_6^{i_1i_2} + ir_3\alpha. \tag{9.11c}$$

From these relations we derive

$$\zeta_2^{i_1i_2} = \frac{Pt_3}{1 + r_3PF_1^{i_1}F_2^{i_2}\sqrt{\eta_3}}\alpha, \tag{9.12}$$

$$\beta^{i_1i_2} = i\frac{r_3 + PF_1^{i_1}F_2^{i_2}\sqrt{\eta_3}}{1 + r_3PF_1^{i_1}F_2^{i_2}\sqrt{\eta_3}}\alpha. \tag{9.13}$$

If the atom and cavity parameters are the same for qubit 1 and qubit 2, it follows that $\beta^{i_1i_2} = \beta^{i_2i_1}$, i.e., the conditional amplitude of the output field is exactly the same for the two two-qubit states with odd parity. This is a very important property of the system since it ensures that a superposition of odd parity states can not be destroyed by applying any kind of measurements to the output field, and, in particular, inefficient detection does not give rise to decoherence within the odd subspace.

With the chosen phase convention, BS$_3$ and the upper left mirror in Fig. 9.2 altogether change the phase of the probe field in the loop by π. In the case of a resonant light-atom interaction $D_q = 0$, we should thus choose $P = -1$ to obtain destructive interference in the loop for the odd subspace. Since $F_q^{\downarrow} = -1$ and $F_q^{\uparrow} \to 1$ for $C_q \to \infty$, we find $\beta^{\downarrow\downarrow} = -i\alpha$, $\beta^{\uparrow\downarrow} = \beta^{\downarrow\uparrow} \to i\alpha$, and $\beta^{\uparrow\uparrow} \to -i\alpha$ for $C_q \to \infty$ and $\eta_3 = 1$. As stated above, the phases of the output field from the loop hence differ by π for the two subspaces, which is the optimal situation for a parity measurement. Note that this result is independent of the precise value of the cooperativity parameters for the two qubits as long as they are large compared to unity. Note also that $\zeta_2^{\uparrow\downarrow} = \zeta_2^{\downarrow\uparrow}$ is close to zero when r_3^2 is close to one.

In the nonresonant case $D_q \sim C_q \gg 1$, we choose $P = 1$ to obtain destructive interference in the loop for the odd subspace. Since $F_q^{\uparrow} \approx (F_q^{\downarrow})^*$ for large C_q, we find $\beta^{\uparrow\downarrow} = \beta^{\downarrow\uparrow}$ and $\beta^{\uparrow\uparrow} = -(\beta^{\downarrow\downarrow})^*$ if $\alpha = \alpha^*$ and the atom and cavity parameters are identical for the two qubits. A parity measurement can hence be achieved by detecting the p-quadrature of the output field. If the atom and cavity parameters are not identical, we still have

$\beta^{\uparrow\downarrow} = -(\beta^{\downarrow\uparrow})^*$ and $\beta^{\uparrow\uparrow} = -(\beta^{\downarrow\downarrow})^*$, which is sufficient to facilitate a parity measurement, but detection inefficiency now leads to decoherence within the odd subspace if $\beta^{\downarrow\uparrow} \neq \beta^{\uparrow\downarrow}$.

The condition (9.1) evaluates to

$$\frac{2|\alpha|^2}{\gamma_1} \times \frac{4C_1(1+D_1^2)}{(1+D_1^2+2C_1)^2+C_1^2D_1^2} \times \frac{t_3^2}{|1+r_3PF_1^{\uparrow}F_2^{i_2}\sqrt{\eta_3}|^2} \ll 1, \tag{9.14a}$$

$$\frac{2|\alpha|^2}{\gamma_2} \times \frac{4C_2(1+D_2^2)}{(1+D_2^2+2C_2)^2+C_2^2D_2^2} \times \frac{\eta_3 t_3^2|F_i^{i_1}|^2}{|1+r_3PF_1^{i_1}F_2^{\uparrow}\sqrt{\eta_3}|^2} \ll 1, \tag{9.14b}$$

for cavity 1 and cavity 2, respectively. Note that t_3, r_3, η_3, P, $F_1^{i_1}$, and $F_2^{i_2}$ all have a norm, which is smaller than or equal to one, and the third factor in the two inequalities is hence of order unity or smaller unless r_3, η_3, and $-PF_1^{\uparrow}F_2^{i_2}$ or $-PF_1^{i_1}F_2^{\uparrow}$ are all close to plus one, which corresponds to the situation of perfect constructive interference in the loop.

Symmetry properties of the output field during the transient

Let us briefly consider some properties of the conditional field amplitudes if they are not necessarily in steady state. We denote the amplitude of the field in the loop just before cavity 1 by $\zeta_2^{i_1i_2}(t)$ and the amplitude of the field in the loop just after cavity 2 by $\zeta_5^{i_1i_2}(t)$. When the probe field is turned on at time 0, we know that $\zeta_2^{i_1i_2}(t)$ is zero for $t<0$, but $\zeta_2^{i_1i_2}(t)$ may vary in a complicated way for $t \geq 0$. We can then use Eqs. (9.5) and (9.6) to derive

$$\begin{aligned}\zeta_5^{i_1i_2}(t+T_{12}) = {} & \sqrt{\eta_3}\zeta_2^{i_1i_2}(t) - \sqrt{\eta_3}\kappa_1\int_0^t e^{-K_1^{i_1}(t-t')}\zeta_2^{i_1i_2}(t')dt' \\ & - \sqrt{\eta_3}\kappa_2\int_0^t e^{-K_2^{i_2}(t-t')}\zeta_2^{i_1i_2}(t')dt' \\ & + \sqrt{\eta_3}\kappa_1\kappa_2\int_0^t\int_0^{t'} e^{-K_2^{i_2}(t-t')}e^{-K_1^{i_1}(t'-t'')}\zeta_2^{i_1i_2}(t'')dt''dt',\end{aligned} \tag{9.15}$$

where T_{12} is the light traveling time from cavity 1 to cavity 2 and

$$K_q^{i_q} \equiv \frac{\kappa_q}{2}\left(1+\frac{2C_q\delta_{i_q\uparrow}}{1+D_q^2} - i\frac{2D_qC_q}{1+D_q^2}\left(\delta_{i_q\uparrow}-1/2\right)\right). \tag{9.16}$$

If the atom and cavity parameters are the same for the two qubits, we have $\kappa_1 = \kappa_2$, $K_1^{\downarrow} = K_2^{\downarrow}$, and $K_1^{\uparrow} = K_2^{\uparrow}$. Interchange of i_1 and i_2 thus transforms $K_1^{i_1}$ into $K_1^{i_2} = K_2^{i_2}$ and $K_2^{i_2}$ into $K_2^{i_1} = K_1^{i_1}$. It then follows from (9.15) that $\zeta_5^{i_1i_2}(t)$ is invariant under interchange of i_1 and i_2 if $\zeta_2^{i_1i_2}(t)$ is invariant. We note, however, that $\zeta_2^{i_1i_2}(t)$ is invariant if $\zeta_5^{i_1i_2}(t)$ is invariant because $\zeta_2^{i_1i_2}(t)$ is a linear combination of $\alpha(t-T_{31})$ and $\zeta_5^{i_1i_2}(t-T_{21})$, where T_{31} (T_{21}) is the light traveling time from BS$_3$ (cavity 2) to cavity 1. Since the initial condition is invariant, we conclude that $\zeta_5^{i_1i_2}(t) = \zeta_5^{i_2i_1}(t)$. The output field from the loop is a linear combination of $\alpha(t)$ and $\zeta_5^{i_1i_2}(t-T_{23})$, where T_{23} is the light traveling time from cavity 2 to BS_3, and consequently we have $\beta^{i_1i_2}(t) = \beta^{i_2i_1}(t)$. For identical atom and cavity parameters for the two qubits, we hence conclude that the conditional output field amplitude is the same for the two states within the odd subspace at all times, even if the probe field is time-dependent, and it is hence impossible to distinguish the two states by detecting the output field.

We next remove the assumption of identical atom and cavity parameters for the two qubits and consider the nonresonant case $D_q \sim C_q \gg 1$. To lowest order in C_q^{-1}, we have $K_q^{\downarrow} = (K_q^{\uparrow})^*$, and for $\alpha(t) = \alpha(t)^*$ and $P = P^*$, it follows from (9.15) and the fact that $\zeta_2^{i_1i_2}(t)$ is a linear combination of $\alpha(t-T_{31})$ and $\zeta_5^{i_1i_2}(t-T_{21})$ with real coefficients that $\zeta_5^{i_1i_2}(t) = (\zeta_5^{i_2i_1}(t))^*$. The relations $\beta^{\uparrow\downarrow}(t) = -(\beta^{\downarrow\uparrow}(t))^*$ and $\beta^{\uparrow\uparrow}(t) = -(\beta^{\downarrow\downarrow}(t))^*$ are hence valid at all times even if the probe field is time-dependent. As a consequence, for $\alpha(t) = \alpha(t)^*$, we can not distinguish the two states in the odd subspace or distinguish the two states in the even subspace by measuring the p-quadrature of the output field.

9.3 Purity decay in the odd and even parity subspaces

The back action of the continuous homodyne detection of the output field from the loop gradually projects the state of the atoms onto either the even or the odd parity subspace. The projection occurs through the time evolution of the coefficients $c_{i_1j_1i_2j_2}(t)$ in Eq. (9.10). In the ideal case of no light field losses and infinite cooperativity parameters for the two qubits, the measurement is a QND measurement, and it is unable to distinguish states within the odd subspace and to distinguish states within the even subspace. A main indication of the quality of the measurement is thus the rate at which a state within the odd subspace or a state within the even subspace decoheres compared to the duration of the measurement, i.e., the time required to distinguish odd parity states from even parity states, and we evaluate this parameter in the following.

Measurement time

First, we need to know for how long time one should measure in order to project the initial state of the atoms onto the even or the odd parity subspace. If a continuous coherent state with constant amplitude β is detected with a homodyne detector, it follows from (8.11) with $\kappa = 0$ and the definition of dy_{s} above Eq. (8.13) that the contribution to the integrated photocurrent from t to $t + dt$ is given by $dy_{\mathrm{s}} = -ie^{-i\phi}\beta dt + ie^{i\phi}\beta^* dt + dW_{\mathrm{s}}$. The average of dy_{s} over the noise dW_{s} is hence $\langle\langle dy_{\mathrm{s}}\rangle\rangle = -ie^{-i\theta}\beta dt + ie^{i\theta}\beta^* dt$, and the standard deviation is $\sqrt{dt}$.

The measurement time t_{m} required to distinguish two coherent states with amplitudes β_1 and β_2 may be defined as the time for which the absolute value of the difference in the mean value of $dy_{\mathrm{s},1} = -ie^{-i\phi}\beta_1 dt + ie^{i\phi}\beta_1^* dt + dW_{\mathrm{s}}$ and $dy_{\mathrm{s},2} = -ie^{-i\phi}\beta_2 dt + ie^{i\phi}\beta_2^* dt + dW_{\mathrm{s}}$ integrated from 0 to t_{m}

$$\left|\int_0^{t_{\mathrm{m}}} \langle\langle dy_{\mathrm{s},1}\rangle\rangle - \int_0^{t_{\mathrm{m}}} \langle\langle dy_{\mathrm{s},2}\rangle\rangle\right| = | - ie^{-i\phi}\beta_1 t_{\mathrm{m}} + ie^{i\phi}\beta_1^* t_{\mathrm{m}} + ie^{-i\phi}\beta_2 t_{\mathrm{m}} \\ - ie^{i\phi}\beta_2^* t_{\mathrm{m}}| \quad (9.17)$$

equals the sum of the standard deviations of $\int_0^{t_{\mathrm{m}}} dy_{\mathrm{s},1}$ and $\int_0^{t_{\mathrm{m}}} dy_{\mathrm{s},2}$, which is $2\sqrt{t_{\mathrm{m}}}$. With this definition,

$$t_{\mathrm{m}} = (\mathrm{Re}(-ie^{-i\phi}(\beta_1 - \beta_2)))^{-2}. \quad (9.18)$$

The rate of gain of information due to the homodyne detection, which we define as t_{m}^{-1}, is thus the square of the projection of $\beta_1 - \beta_2$ onto an axis in the complex plane determined by the measured quadrature. For our setup, the measurement time is given by

$$t_{\mathrm{m}} = \max((\mathrm{Re}(-ie^{-i\phi}(\beta^{\downarrow\uparrow} - \beta^{\downarrow\downarrow})))^{-2}, (\mathrm{Re}(-ie^{-i\phi}(\beta^{\downarrow\uparrow} - \beta^{\uparrow\uparrow})))^{-2}, \\ (\mathrm{Re}(-ie^{-i\phi}(\beta^{\uparrow\downarrow} - \beta^{\downarrow\downarrow})))^{-2},)\,\mathrm{Re}(-ie^{-i\phi}(\beta^{\uparrow\downarrow} - \beta^{\uparrow\uparrow})))^{-2}). \quad (9.19)$$

Odd parity subspace

If the atoms are initially in a state of odd parity, the state of the system at time t is given by Eq. (9.10) with the additional requirements $i_1 \neq i_2$ and $j_1 \neq j_2$. The entanglement between the atoms and the light within the cavities and the loop reduces the purity during the measurement of the atomic state obtained by tracing out the light field modes, but this purity is regained when the probe field is turned off and the fields decay to the vacuum state. While the rate of nonregainable loss of purity may be slightly different during the initial and final transients, we do not expect anything dramatic to happen since the transient dynamics does not break the symmetry, which ensures that the odd parity states are indistinguishable in the output field. For a total measurement time t_{m}, which is long compared to the transients, we may thus concentrate on the rate of loss of purity in steady state. (This is a matter of $|\alpha|^2$ being sufficiently small since the duration of the transients does not depend on α, while t_{m}^{-1} is proportional to $|\alpha|^2$.)

It follows from (9.4) that spontaneous emission from the two atoms changes the coefficients according to

$$(dc_{\uparrow\downarrow\downarrow\uparrow}(t))_{\mathcal{L}} = -\frac{\kappa_1 C_1}{1+D_1^2}|\xi_1^{\uparrow\downarrow}|^2 c_{\uparrow\downarrow\downarrow\uparrow}(t)dt - \frac{\kappa_2 C_2}{1+D_2^2}|\xi_2^{\downarrow\uparrow}|^2 c_{\uparrow\downarrow\downarrow\uparrow}(t)dt, \tag{9.20a}$$

$$(dc_{\downarrow\uparrow\uparrow\downarrow}(t))_{\mathcal{L}} = -\frac{\kappa_1 C_1}{1+D_1^2}|\xi_1^{\uparrow\downarrow}|^2 c_{\downarrow\uparrow\uparrow\downarrow}(t)dt - \frac{\kappa_2 C_2}{1+D_2^2}|\xi_2^{\downarrow\uparrow}|^2 c_{\downarrow\uparrow\uparrow\downarrow}(t)dt, \tag{9.20b}$$

$$(dc_{\uparrow\uparrow\downarrow\downarrow}(t))_{\mathcal{L}} = (dc_{\downarrow\downarrow\uparrow\uparrow}(t))_{\mathcal{L}} = 0, \tag{9.20c}$$

in the time interval from t to $t+dt$. In addition, the coefficients change when we trace out the field that is lost between cavity 1 and cavity 2. The conditional state of the field lost at BS_L between t and $t+dt$ is $|\sqrt{1-\eta_3}\zeta_3^{i_1 i_2}\sqrt{dt}\rangle\langle\sqrt{1-\eta_3}\zeta_3^{j_1 j_2}\sqrt{dt}|$, and the trace operation hence transforms the coefficients as

$$c_{\uparrow\downarrow\downarrow\uparrow}(t) \to \langle\sqrt{1-\eta_3}\zeta_3^{\downarrow\uparrow}\sqrt{dt}|\sqrt{1-\eta_3}\zeta_3^{\uparrow\downarrow}\sqrt{dt}\rangle c_{\uparrow\downarrow\downarrow\uparrow}(t), \tag{9.21a}$$

$$c_{\downarrow\uparrow\uparrow\downarrow}(t) \to \langle\sqrt{1-\eta_3}\zeta_3^{\uparrow\downarrow}\sqrt{dt}|\sqrt{1-\eta_3}\zeta_3^{\downarrow\uparrow}\sqrt{dt}\rangle c_{\downarrow\uparrow\uparrow\downarrow}(t), \tag{9.21b}$$

while $c_{\downarrow\downarrow\uparrow\uparrow}(t)$ and $c_{\uparrow\uparrow\downarrow\downarrow}(t)$ are unchanged. Homodyne detection of the p-quadrature of the output field leaves the state unaffected if $\text{Im}(\beta^{\uparrow\downarrow}) = \text{Im}(\beta^{\downarrow\uparrow})$. If $\beta^{\uparrow\downarrow} = \beta^{\downarrow\uparrow}$, it does not even lead to decoherence if the output field is simply traced out, and this is why we do not consider detection inefficiency here.

Collecting the changes during the whole measurement from 0 to t_m and neglecting transients, the final purity of the atomic state after the measurement evaluates to

$$\begin{aligned}\text{Tr}(\rho_\text{at}(t\to\infty)^2) \approx\ & c_{\uparrow\uparrow\downarrow\downarrow}(0)^2 + c_{\downarrow\downarrow\uparrow\uparrow}(0)^2 + 2|c_{\uparrow\downarrow\downarrow\uparrow}(0)|^2 \\ & \times \exp\left(-\left(\nu_{\text{odd},1}^{(\text{SE})} + \nu_{\text{odd},2}^{(\text{SE})} + \nu_{\text{odd}}^{(\text{L})}\right)t_\text{m}\right),\end{aligned} \tag{9.22}$$

where $\rho_\text{at}(t)$ is the density operator representing the state of the atoms obtained by tracing out the light fields,

$$\nu_{\text{odd},q}^{(\text{SE})} = 2C_q\kappa_q(\delta_{1q}|\xi_1^{\uparrow\downarrow}|^2 + \delta_{2q}|\xi_2^{\downarrow\uparrow}|^2)/(1+D_q^2) \tag{9.23}$$

is the rate of spontaneous emission events when atom q is in the state $|\uparrow\rangle$, and

$$\nu_\text{odd}^{(\text{L})} = (1-\eta_3)|\zeta_3^{\uparrow\downarrow} - \zeta_3^{\downarrow\uparrow}|^2 \tag{9.24}$$

is the rate at which it would be possible to distinguish the two states within the odd subspace if the light lost between cavity 1 and cavity 2 was detected. Additional photon losses in cavity 1 and cavity 2 could be taken into account by including extra decay terms $\kappa_{\text{L},q}(2\hat{a}\rho(t)\hat{a}^\dagger - \hat{a}^\dagger\hat{a}\rho(t) - \rho(t)\hat{a}^\dagger\hat{a})/2$, $q=1,2$, in the SME and adding the terms $-\kappa_{\text{L},q}|\xi_q^{\uparrow\downarrow} - \xi_q^{\downarrow\uparrow}|^2 t_\text{m}$, $q=1,2$, to the exponent in (9.22), where $\kappa_{\text{L},q}$ is the contribution to the cavity decay rate of cavity q from additional photon loss.

Even parity subspace

If $\mathrm{Im}(\beta^{\downarrow\downarrow}) = \mathrm{Im}(\beta^{\uparrow\uparrow})$, the final purity of a state restricted to the even subspace is likewise

$$\begin{aligned}\mathrm{Tr}(\rho_{\mathrm{at}}(t\to\infty)^2) \approx\ & c_{\uparrow\uparrow\uparrow\uparrow}(0)^2 + c_{\downarrow\downarrow\downarrow\downarrow}(0)^2 + 2|c_{\uparrow\downarrow\uparrow\downarrow}(0)|^2 \\ & \times \exp\left(-\left(\nu^{(\mathrm{SE})}_{\mathrm{even},1} + \nu^{(\mathrm{SE})}_{\mathrm{even},2} + \nu^{(\mathrm{L})}_{\mathrm{even}}\right) t_{\mathrm{m}}\right), \end{aligned} \tag{9.25}$$

where

$$\nu^{(\mathrm{SE})}_{\mathrm{even},q} = 2C_q\kappa_q|\xi_q^{\uparrow\uparrow}|^2/(1+D_q^2) \tag{9.26}$$

and

$$\nu^{(\mathrm{L})}_{\mathrm{even}} = (1-\eta_3)|\zeta_3^{\uparrow\uparrow} - \zeta_3^{\downarrow\downarrow}|^2. \tag{9.27}$$

For $\mathrm{Im}(\beta^{\downarrow\downarrow}) \neq \mathrm{Im}(\beta^{\uparrow\uparrow})$, the two-qubit state is projected onto either $|\downarrow\downarrow\rangle$ or $|\uparrow\uparrow\rangle$ at a rate, which is of order $|\,\mathrm{Im}(\beta^{\downarrow\downarrow}) - \mathrm{Im}(\beta^{\uparrow\uparrow})|^2 \sim C^{-2}$, and we need to multiply $|c_{\uparrow\uparrow\uparrow\uparrow}(0)|^2$, $|c_{\downarrow\downarrow\downarrow\downarrow}(0)|^2$, and $|c_{\uparrow\downarrow\uparrow\downarrow}(0)|^2$ by the square of the accumulated weight factors arising due to the measurement.

9.4 Nonresonant light-atom coupling

In the following, we compare the performance of the setup in Fig. 9.2 with $r_3 \neq 0$ and an open loop setup with $r_3 = 0$. We first consider a nonresonant light-atom interaction with $D \sim C$ and $C \gg 1$, assuming $D_1 = D_2 \equiv D$ and $C_1 = C_2 \equiv C$. In this case, the primary effect of the light-atom interaction is a phase shift of the light field, and we apply the approximations $F_1^{\uparrow} = F_2^{\uparrow} \approx -(D+iC)/(D-iC) \equiv F$ and $F_1^{\downarrow} = F_2^{\downarrow} \approx F^*$. Combining Eqs. (9.7), (9.11), (9.12), (9.13), (9.19), (9.23), (9.24), (9.26), and (9.27), we then derive

$$t_{\mathrm{m}}^{-1} = \frac{\eta_3(1-r_3^2)^2(1-\sqrt{\eta_3}r_3)^2(1-\mathrm{Re}(F^2))^2|\alpha|^2}{(1+\sqrt{\eta_3}r_3)^2(1+2\sqrt{\eta_3}r_3\,\mathrm{Re}(F^2)+\eta_3r_3^2)^2}, \tag{9.28a}$$

$$\nu^{(\mathrm{SE})}_{\mathrm{odd},1}t_{\mathrm{m}} = \frac{8C(1+2\sqrt{\eta_3}r_3\,\mathrm{Re}(F^2)+\eta_3r_3^2)^2}{\eta_3(C^2+D^2)(1-r_3^2)(1-\sqrt{\eta_3}r_3)^2(1-\mathrm{Re}(F^2))^2}, \tag{9.28b}$$

$$\nu^{(\mathrm{SE})}_{\mathrm{even},1}t_{\mathrm{m}} = \frac{8C(1+\sqrt{\eta_3}r_3)^2(1+2\sqrt{\eta_3}r_3\,\mathrm{Re}(F^2)+\eta_3r_3^2)}{\eta_3(C^2+D^2)(1-r_3^2)(1-\sqrt{\eta_3}r_3)^2(1-\mathrm{Re}(F^2))^2}, \tag{9.28c}$$

$$\nu^{(\mathrm{L})}_{\mathrm{odd}}t_{\mathrm{m}} = \frac{4\,\mathrm{Im}(F)^2(1-\eta_3)(1+2\sqrt{\eta_3}r_3\,\mathrm{Re}(F^2)+\eta_3r_3^2)^2}{\eta_3(1-\mathrm{Re}(F^2))^2(1-r_3^2)(1-\sqrt{\eta_3}r_3)^2}, \tag{9.28d}$$

$$\nu^{(\mathrm{L})}_{\mathrm{even}}t_{\mathrm{m}} = \frac{4\,\mathrm{Im}(F)^2(1-\eta_3)(1+\sqrt{\eta_3}r_3)^2}{\eta_3(1-\mathrm{Re}(F^2))^2(1-r_3^2)}. \tag{9.28e}$$

The latter four quantities are plotted in Fig. 9.3, and we note that $\nu^{(\mathrm{SE})}_{\mathrm{odd},2} = \eta_3\nu^{(\mathrm{SE})}_{\mathrm{odd},1}$ and $\nu^{(\mathrm{SE})}_{\mathrm{even},2} = \eta_3\nu^{(\mathrm{SE})}_{\mathrm{even},1}$.

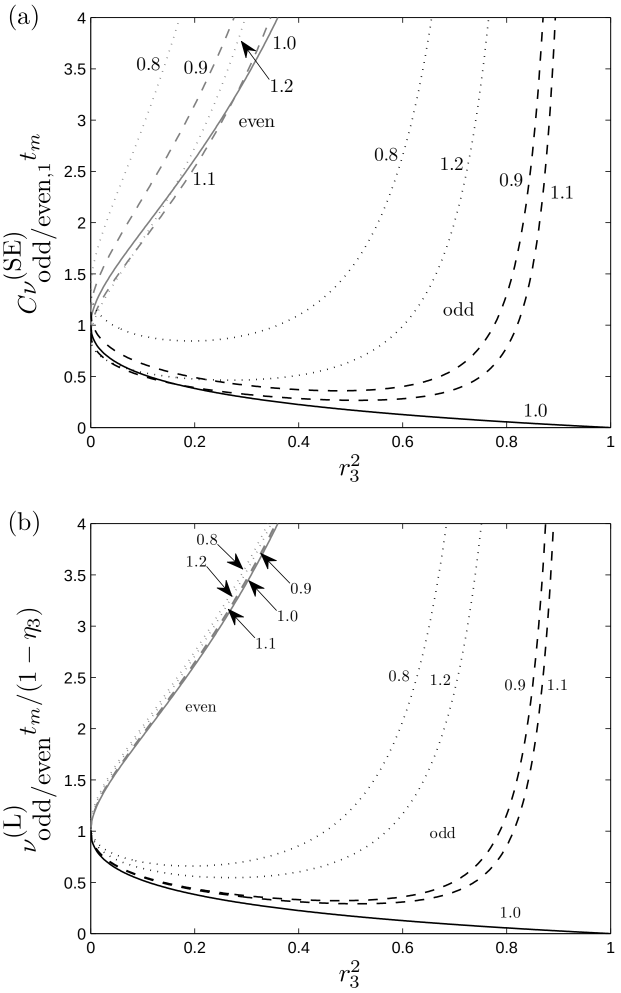

Figure 9.3: (a) Rate of spontaneous emission events relative to the rate of gain of information due to the measurement in units of C^{-1} and (b) rate of decoherence within the even and odd subspaces due to light field losses between cavity 1 and cavity 2 relative to the measurement rate in units of $1-\eta_3$ for a nonresonant light-atom interaction. Both graphs are for $\eta_3 \to 1$ and the different curves correspond to $D/C = 0.8$, 0.9, 1.0, 1.1, and 1.2 as indicated. The curves in the upper left region (gray) are for the even subspace and the lower curves (black) are for the odd subspace (the curves coincide for $r_3^2 = 0$).

The figure shows that it is possible to reduce both the rate of spontaneous emission events and the rate of decoherence due to other light field losses in the odd subspace relative to the rate of gain of information due to the measurement by choosing a nonzero value of r_3, but only if D/C is sufficiently close to plus or minus one, which corresponds to the situation of constructive interference in the loop for the even subspace. Note that $\nu^{(\mathrm{SE})}_{\mathrm{odd},q}$ and $\nu^{(\mathrm{L})}_{\mathrm{odd}}$ depend on r_3 in the same way, and for a given value of $D/C \in [-\sqrt{3}, -1/\sqrt{3}] \cup [1/\sqrt{3}, \sqrt{3}]$ and $\eta_3 = 1$, the optimal choice of beam splitter reflectivity is

$$r_{3,\mathrm{opt}} = \frac{\sqrt{3 - 3\,\mathrm{Re}(F^2)^2} - 2 - \mathrm{Re}(F^2)}{1 + 2\,\mathrm{Re}(F^2)}. \tag{9.29}$$

Outside this interval, it is optimal to choose $r_3 = 0$.

As far as light field losses between cavity 1 and cavity 2 are concerned, the smallest losses occur for $|D|/C = 1$, i.e., for $|\Delta_q| = g_q^2/\kappa_q$, and Fig. 9.3(a) suggests that this is also a good choice to reduce the total number of spontaneous emission events (the optimal value of $|D|/C$ with respect to loss due to spontaneous emission varies from $\sqrt{2}$ for $\sqrt{\eta_3} r_3 = 0$ to 1 for $\sqrt{\eta_3} r_3 = 1$). For $|D|/C \to 1$, we find $r_{3,\mathrm{opt}} \to 1$, but since $\sqrt{\eta_3} P F_1^{\uparrow} F_2^{\uparrow} = -1$ for the even subspace, one should remember the conditions in (9.14). Note also that if $\eta_3 < 1$ or C is not infinite, the curves go to infinity for $r_3 \to 1$. This happens because $t_{\mathrm{m}} \to \infty$, which in turn is a consequence of the fact that it is only possible to couple light into the structure for $r_3 = 1$ if there is perfect constructive interference within the loop and no loss, and the output field amplitude is hence $i\alpha$ for all states of the qubits if this is not the case. In conclusion, a reasonable strategy is to choose the light-atom detuning such that $|D|/C = 1$ and then compute the optimal value of r_3 from Eqs. (9.28) if the relative photon loss $1 - \eta_3$ in the loop is large enough to ensure that the inequalities in (9.14) are fulfilled. Otherwise, one has to optimize r_3 under the constraints in (9.14).

9.5 Resonant light-atom coupling

For a resonant light-atom coupling $D = 0$ and identical atom and cavity parameters, $F_1^{\uparrow} = F_2^{\uparrow} = -(1 - 2C)/(1 + 2C) \equiv G$ and $F_1^{\downarrow} = F_2^{\downarrow} = -1$. In this case,

$$t_{\mathrm{m}}^{-1} = \frac{\eta_3 G^2 (1 + G)^2 (1 - r_3^2)^2 |\alpha|^2}{(1 + \sqrt{\eta_3} r_3 G)^2 (1 - \sqrt{\eta_3} r_3 G^2)^2}, \tag{9.30a}$$

$$\nu^{(\mathrm{SE})}_{\mathrm{odd},1} t_{\mathrm{m}} = \frac{8C (1 - \sqrt{\eta_3} r_3 G^2)^2}{(1 + 2C)^2 \eta_3 G^2 (1 + G)^2 (1 - r_3^2)}, \tag{9.30b}$$

$$\nu^{(\mathrm{SE})}_{\mathrm{even},1} t_{\mathrm{m}} = \frac{8C (1 + \sqrt{\eta_3} r_3 G)^2}{(1 + 2C)^2 \eta_3 G^2 (1 + G)^2 (1 - r_3^2)}, \tag{9.30c}$$

$$\nu_{\mathrm{odd}}^{(\mathrm{L})} t_{\mathrm{m}} = \frac{(1-\eta_3)(1-\sqrt{\eta_3} r_3 G^2)^2}{\eta_3 G^2 (1-r_3^2)}, \tag{9.30d}$$

$$\nu_{\mathrm{even}}^{(\mathrm{L})} t_{\mathrm{m}} = \frac{(1-\eta_3)(1-\eta_3 r_3^2 G^2)^2}{\eta_3 G^2 (1-r_3^2)(1-\sqrt{\eta_3} r_3)^2}, \tag{9.30e}$$

while $\nu_{\mathrm{odd},2}^{(\mathrm{SE})} = \eta_3 \nu_{\mathrm{odd},1}^{(\mathrm{SE})}$ and $\nu_{\mathrm{even},2}^{(\mathrm{SE})} = \eta_3 G^2 \nu_{\mathrm{even},1}^{(\mathrm{SE})}$. These results are illustrated for $\eta_3 \to 1$ in Fig. 9.4, which shows that the total decoherence in the odd subspace also in this case can be reduced by choosing a nonzero value of r_3. For given values of C and η_3, the minimum appears at $r_{3,\mathrm{opt}} = \sqrt{\eta_3} G^2$, but again one should keep the constraints in (9.14) in mind.

Assuming $D = C$ and $C \to \infty$ for the nonresonant case and $C \to \infty$ for the resonant case, we observe that the expressions for t_{m} are the same, and the two possibilities are thus equally efficient in distinguishing the even and the odd subspaces. We also note that $\zeta_1^{i_1 i_2}$ is the same for the resonant and the nonresonant coupling, leading to the same values for the rate of decoherence due to light field losses in the loop. The rates of spontaneous emission events are also the same except for a factor of two, which arises from the details of the light-atom interaction: for cavities containing an atom in the state $|\uparrow\rangle$, the number of photons in the cavity is a factor of $1/(2C^2)$ smaller in the resonant case compared to the nonresonant case, but the fraction of photons lost per round trip is a factor of C^2 larger. Finally, the significance of additional photon losses in cavity 1 and cavity 2 is the same for resonant and nonresonant coupling because $|\xi_q^{\uparrow\downarrow} - \xi_q^{\downarrow\uparrow}|$ assumes the same value for resonant and nonresonant coupling and $|\xi_q^{\uparrow\uparrow} - \xi_q^{\downarrow\downarrow}|$ assumes the same value for resonant and nonresonant coupling. Except for a factor of two for the rate of spontaneous emission events, the performance is thus the same for a resonant and a nonresonant light-atom interaction in the ideal limit.

Figures 9.3 and 9.4 show that the total number of spontaneous emission events is of order C^{-1}, while the contribution to the exponents in (9.22) and (9.25) from light field losses between cavity 1 and cavity 2 is of order $(1-\eta_3)$. The relative importance of the two effects is hence determined by $C(1-\eta_3)$, and high performance is obtained for high cooperativity parameters and low levels of light field losses. Equations (9.28) and (9.30) show that the performance is independent of the intensity of the input field as long as the inequalities in (9.14) are fulfilled. This appears because both the rate of gain of information due to the measurement and the photon loss rates scale linearly with $|\alpha|^2$.

9.6 Conclusion

In conclusion, we have proposed and analyzed the performance of a method to improve an earlier proposed scheme to measure the parity of two qubits,

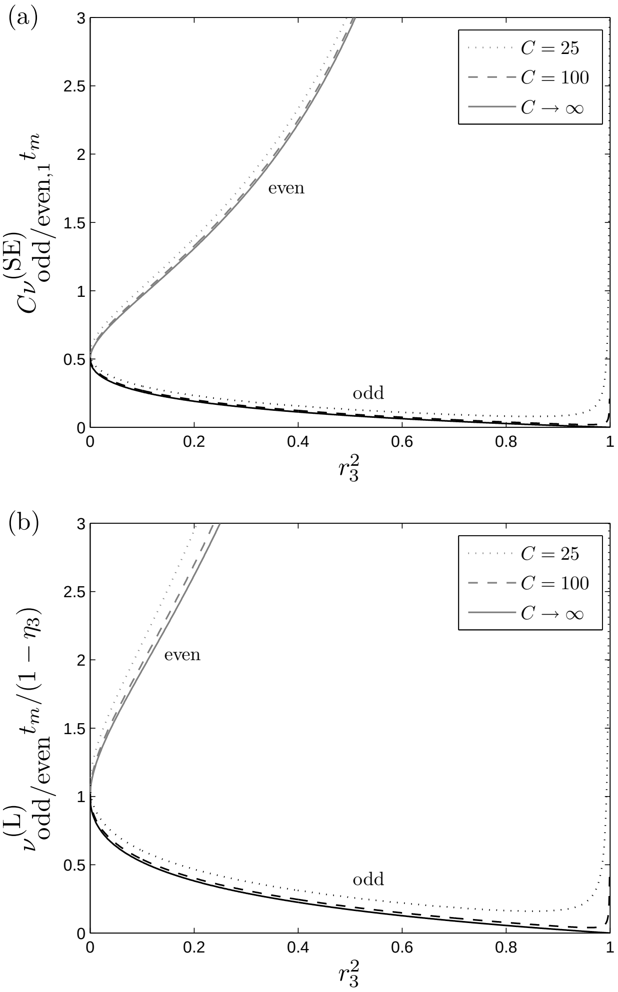

Figure 9.4: (a) Rate of spontaneous emission events relative to the measurement rate in units of C^{-1} and (b) rate of decoherence within the even and odd subspaces due to light field losses between cavity 1 and cavity 2 relative to the measurement rate in units of $1-\eta_3$ for a resonant light-atom interaction and $\eta_3 \to 1$. The solid, dashed, and dotted curves correspond to different values of the cooperativity parameter as shown in the legend. The curves to the upper left (gray) are for the even subspace and the lower curves (black) are for the odd subspace (the curves coincide for $r_3^2 = 0$).

each encoded in two ground state levels of a single atom in a cavity. The measurement relies on the phase shift imposed conditionally on a continuous beam of light, which interacts sequentially with the two qubits, and we have found that the rate of decoherence within the odd parity subspace due to spontaneous emission and light field losses can be decreased by allowing the probe field to interact several times with the two qubits before it is detected. This decrease happens at the expense of an increased decoherence rate within the even parity subspace. We have also proposed and analyzed the possibility to use a nonresonant light-atom interaction rather than a resonant light-atom interaction for the parity measurement, and we have found that the performance is similar for the two cases if the light-atom detuning is chosen as $|\Delta| = g^2/\kappa$, where g is the light-atom coupling strength and κ is the decay rate of light in the cavity. For the resonant interaction, however, the phase shifts imposed on the probe field by the qubits are insensitive to the precise values of the parameters, which is a significant advantage experimentally.

One possible application of the proposed measurement is to prepare two qubits in an entangled odd parity state with higher purity. Improvements can also be obtained in quantum error correction if the qubit state is encoded in the odd subspace and errors are corrected continuously in time such that the even subspace is practically avoided. In case of the three-qubit bit-flip code, for instance, one would use the states $|{\downarrow\uparrow\downarrow}\rangle$ and $|{\uparrow\downarrow\uparrow}\rangle$ as code space. The parity measurements on qubits 1 and 2 and on qubits 2 and 3 could be done either by switching between the two measurements or by using two different polarizations of the light field, one of which interacts with the qubit state $|{\uparrow}\rangle$ and the other with the qubit state $|{\downarrow}\rangle$. Polarizing beam splitters could then be used to guide the polarization components into the desired cavities.

Chapter 10

Quantum state engineering with high finesse optical cavities

In the present chapter, we investigate how one can use the interaction between a light field and an atom in a cavity to transform the state of the light field in various ways. The interaction is the same as in the previous chapter, but we now consider pulses of light and apply a measurement to the atom after the interaction has taken place, and we assume a resonant light-atom interaction $\Delta = 0$ throughout. The idea of using interactions with an atom in a cavity to transform the state of a light field has been utilized in several papers. In [139], it has been shown how one can achieve a controlled phase flip gate between two single-photon pulses by bouncing the two polarization components of the pulses off a cavity or a mirror in a certain order and applying unitary transformations to the atom in between. It has also been proposed to use the interaction between a coherent state and an atom in a cavity followed by a measurement of the state of the atom to generate a Schrödinger cat state of the light field [152]. Another possibility is to use a weak field to control whether the atom is in the state $|\downarrow\rangle$ or $|\uparrow\rangle$, which paves the way to construct a low-energy optical switch because the reflection and transmission properties of the cavity change dramatically depending on the state of the atom [153]. An atom in a cavity in the strong coupling regime can also transform a random stream of photons into a correlated beam of photon pairs [154, 155]. In the present chapter, we propose a setup consisting of an array of cavities, which allows preparation of entangled photon number correlated states, detection of photon loss, and photon number state resolved detection.

The proposed setup is able to project an arbitrary two-mode input state, for instance a product of two single-mode coherent states, onto the subspace S_2 spanned by the state vectors $|n\rangle|n\rangle$, $n = 0, 1, 2, \ldots$, where $|n\rangle$ is a photon number state. The projection is conditioned on a specific outcome of a measurement applied to each of the atoms in the array of cavities and is hence probabilistic. The success probability can, however, be high since it is the square of the norm of the projection of the input state onto S_2. We are, for instance, certain to obtain the desired measurement outcome if the input state already lies in S_2. In other words, the setup may be regarded as a filter [156], which conditionally removes all the undesired components from the input state, while leaving the desired component unaltered. Except for states consisting of a single term $|n\rangle|n\rangle$, the states in S_2 are entangled states of a traveling light field and a useful resource for quantum communication. Possible applications include teleportation [12] and entanglement swapping [157]. As far as the latter is concerned, one can, e.g., produce two two-mode photon number correlated states at different locations, send one mode from the first state to Alice and one mode from the second state to Bob, combine the remaining two modes on a beam splitter, and measure the total number of photons in these modes to produce an entangled state of the modes sent to Alice and Bob [158]. The proposed setup is easily generalized to preparation of M-mode photon number correlated states. In this case, we first project modes 1 and 2 on S_2, modes 3 and 4 on S_2, etc, and then modes 2 and 3 on S_2, modes 4 and 5 on S_2, etc. It can hence also be used for distribution of entanglement in a network with several parties.

The possibility to project an arbitrary two-mode input state onto S_2 also provides a method to detect photon loss. The main idea is that photon loss transforms states in S_2 into states that lie in the orthogonal complement of S_2 unless the same number of photons are lost from both modes. After preparing a state in S_2, we can thus test the state at a later time by sending the state through the proposed setup a second time, and we can thereby purify the state. The purification method can also be used in a communication scenario if we start from an M-mode photon number correlated state and send at least two modes to each party. In addition, one could imagine various ways to increase the entanglement concentration by application of conditional measurements even if no losses occur. A number of proposals exist for producing more entangled states from two-mode squeezed vacuum states, see for instance [159, 160, 161], and we note that two-mode squeezed vacuum states are particular examples of states in S_2.

With a small modification, our setup can also be used for nondestructive detection of photon number states. Photon number state resolved detection is very useful within quantum computing and quantum communication. Examples include conditional preparation of quantum states of light as we have seen in the first part of the thesis, quantum computing with linear optics and measurements [15], security in quantum cryptography [162], interferometry [163], and characterization of quantum light sources [164]. Existing technologies for photon counting [134, 135, 165, 166, 167, 168, 169, 170, 171, 172, 173] such as avalanche photodiodes, cryogenic devices, and quantum dots are typically only able to distinguish photon number states with low photon numbers. Most of them destroy the photon number state in the detection process and some of them do not work for optical photons. An advantage of our proposal for quantum nondemolition photon number state detection is the ability to detect photon number states with high photon numbers with arbitrary resolution. Our scheme is based on successively testing whether the photon number of the observed state is a multiple of integers chosen at will and the required resources scale moderately with the mean and width of the initial photon number distribution of the measured state. In particular, it is possible to achieve a very precise photon number measurement even for high photon numbers by testing only a few factors if the approximate number of photons is known. We also note that our scheme acts on traveling light fields rather than cavity fields as in [134, 172, 173].

In Sec. 10.1, we explain how the conditional projection onto S_2 can be achieved in the ideal limit of infinitely high single atom cooperativity parameters and infinitely long input pulses. In Sec. 10.2, we investigate the possibility to use the setup to detect losses, and in Sec. 10.3, we show that a modified version of the setup can act as a nondestructive photon number state resolving detector. In Sec. 10.4, we consider the significance of a finite input pulse length and obtain a simple analytical expression for the optimal choice of input mode function for coherent state input fields. Nonideal behavior due to a finite single atom cooperativity parameter is discussed in Sec. 10.5. The chapter is based on [XII][1].

10.1 Photon number correlated states

Our aim is to build a setup, which is able to conditionally project any two-mode input state onto the subspace S_2 spanned by the state vectors $|n\rangle|n\rangle$ with $n = 0, 1, 2, \ldots$. To do so, we use two basic ingredients. The first is the possibility to use an interaction with an atom in a cavity followed by a measurement applied to the atom to measure whether the number of photons in a light pulse is even or odd. In the previous chapter, we found that under ideal conditions, the phase of the input field is unchanged if the atom is in the state $|\uparrow\rangle$, whereas a single-photon phase shift of π is imposed if the atom is in the state $|\downarrow\rangle$. If the initial state of the light pulse is $\sum_n c_n|n\rangle$ and the initial state of the atom is $(|\uparrow\rangle + |\downarrow\rangle)/\sqrt{2}$, we thus have the state $\sum_n c_n(|n\rangle|\uparrow\rangle + (-1)^n|n\rangle|\downarrow\rangle)/\sqrt{2}$ after the interaction of the light pulse with the atom. Measuring the state of the atom in the basis $|\pm\rangle = (|\uparrow\rangle \pm |\downarrow\rangle)/\sqrt{2}$, the final state of the light field takes the form $\sum_n(1/2 \pm (-1)^n/2)c_n|n\rangle$, i.e., we project the state of the input field onto the subspace spanned by all even (odd) photon number states if we measure $|+\rangle$ ($|-\rangle$). In the particular case of a coherent state input field, the output field is a Schrödinger cat

---

[1] Copyright (2010) by the American Physical Society.

state [152]. The second ingredient is the Hong-Ou-Mandel interference effect [174] generalized to input pulses containing an arbitrary number of photons. According to the Hong-Ou-Mandel, two identical single photons interfering at a 50:50 beam splitter always leave the beam splitter in the same output port. More generally, if two identical photon number states interfere at a 50:50 beam splitter, then the number of photons in both of the two output modes is even.

The basic idea of our setup is as follows. We start with two single-mode light fields in some state $\sum_n \sum_m c_{nm}|n\rangle|m\rangle$ and allow these to interfere at a 50:50 beam splitter. We then conditionally project both of the resulting modes on the subspace of all even photon number states, and finally, we apply the inverse of the first beam splitter operation to the two modes by use of a second beam splitter. In the following, we refer to the setup applying this set of operations as one unit. Due to the Hong-Ou-Mandel effect, terms of the form $|n\rangle|n\rangle$ are not affected by the operations. On the other hand, most other terms of the input state are removed due to the conditional measurements, for instance all terms with $n+m$ odd. There are, however, exceptions since all combinations of terms, which can be written on the form $U^\dagger|2n\rangle|2m\rangle$, where U is the unitary transformation corresponding to the first beam splitter, $n = 0, 1, 2, \ldots$, and $m = 0, 1, 2, \ldots$, are accepted. To remove the remaining undesired terms, we suggest to alternately apply opposite phase shift operations to the two modes and repeat the above set of transformations. Terms of the form $|n\rangle|n\rangle$ are again not affected, but the phase of all other terms are changed by the phase shift operations. For an appropriate choice of phase shifts the projection onto S_2 is achieved after infinitely many repetitions. For input states with a moderate number of photons, however, a very small number of units suffice in practice as we shall see below. The first part of the required setup is shown in Fig. 10.1.

To turn the above explanation into a quantitative description, we denote the field annihilation operators of the two input modes by $\hat{a}$ and $\hat{b}$, respectively, and define the beam splitter operator as

$$U = \exp\left(\frac{\pi}{4}\left(\hat{a}^\dagger\hat{b} - \hat{a}\hat{b}^\dagger\right)\right), \tag{10.1}$$

the two-mode projection operator onto even photon number states as

$$P = \sum_{n=0}^{\infty}\sum_{m=0}^{\infty} |2n\rangle\langle 2n| \otimes |2m\rangle\langle 2m|, \tag{10.2}$$

and the two-mode phase shift operator as

$$U_\phi = \exp\left(i\phi\left(\hat{a}^\dagger\hat{a} - \hat{b}^\dagger\hat{b}\right)\right). \tag{10.3}$$

The total conditional transformation corresponding to one unit of the setup is thus given by the operator $U^\dagger P U$, and the transformation corresponding

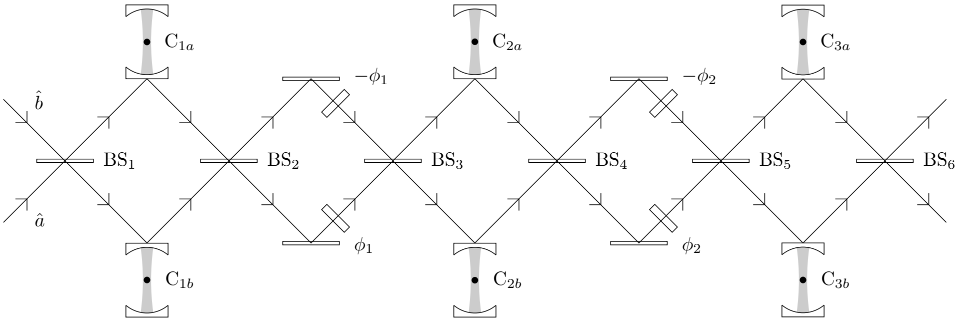

Figure 10.1: The first three units of the proposed setup to conditionally project an arbitrary two-mode input state onto the subspace S_2. The phase shifters between the units change the phase of the two modes by $\pm\phi_1$, $\pm\phi_2$, $\ldots$. All the atoms are prepared in the state $|+\rangle = (|\uparrow\rangle + |\downarrow\rangle)/\sqrt{2}$ before the interaction with the field, and the desired projection occurs conditioned on measuring all atoms in the state $|+\rangle$ after the interaction.

to $N+1$ units with phase shifts in between is represented by the operator

$$\hat{O}_N = U^\dagger PUU_{\phi_N}U^\dagger PU \ldots U_{\phi_2}U^\dagger PUU_{\phi_1}U^\dagger PU \tag{10.4}$$

$$= U^\dagger PU \prod_{i=1}^{N} \cos(\phi_i(\hat{a}^\dagger\hat{a} - \hat{b}^\dagger\hat{b})), \tag{10.5}$$

where $U^\dagger PU$ commutes with the product of cosines in the last line. For $N \to \infty$, the product of cosines vanishes for all terms of the input state with $n \neq m$ if, e.g., all the phases ϕ_i are chosen as the same irrational number times π. For $n = m$, on the other hand, the product of cosines is unity and $U^\dagger PU|n\rangle|n\rangle = |n\rangle|n\rangle$. We note that even though we here apply the two-mode operators one after the other to the input state corresponding to successive interactions of the light pulses with the different components of the setup, the result is exactly the same if the input pulses are longer than the distance between the components such that different parts of the pulses interact with different components at the same time. The only important point is that the state of the atoms is not measured before the interaction with the light field is completed. The proposed setup may thus be very compact even though the pulses are required to be long.

Optimization of the phases

A natural question is how one should optimally choose the angles ϕ_i to approximately achieve the projection with a small number of units. To this end, we define the fidelity of the projection

$$F_N = \frac{|\langle\psi_N|\psi_\infty\rangle|^2}{\langle\psi_N|\psi_N\rangle\langle\psi_\infty|\psi_\infty\rangle} = \frac{\langle\psi_\infty|\psi_\infty\rangle}{\langle\psi_N|\psi_N\rangle} \tag{10.6}$$

as the overlap between the (unnormalized) output state $|\psi_N\rangle = \hat{O}_N|\psi_{\text{in}}\rangle$ after $N+1$ units and the (unnormalized) projection $|\psi_\infty\rangle$ of the input state $|\psi_{\text{in}}\rangle$ onto S_2. The last equality in (10.6) follows from the fact that $|\psi_N\rangle = |\psi_\infty\rangle + |\psi_\perp\rangle$, where $|\psi_\perp\rangle$ lies in the orthogonal complement of S_2. Maximizing F_N for a given $|\psi_{\text{in}}\rangle = \sum_n\sum_m c_{nm}|n\rangle|m\rangle$ thus corresponds to minimizing

$$\langle\psi_N|\psi_N\rangle = \sum_{n=0}^{\infty}\sum_{m=0}^{\infty} c_{nm}\prod_{i=1}^{N}\cos^2(\phi_i(n-m))\langle\psi_{\text{in}}|U^\dagger PU|n\rangle|m\rangle, \tag{10.7}$$

i.e., we would like to find the optimal solution of

$$\begin{aligned}\frac{\partial\langle\psi_N|\psi_N\rangle}{\partial\phi_j} = &-\sum_{n=0}^{\infty}\sum_{m=0}^{\infty} c_{nm}\sin(2\phi_j(n-m))(n-m)\\ &\times\prod_{\substack{i=1\\ i\neq j}}^{N}\cos^2(\phi_i(n-m))\langle\psi_{\text{in}}|U^\dagger PU|n\rangle|m\rangle = 0.\end{aligned} \tag{10.8}$$

A set of solutions valid for any input state can be obtained by requiring $\sin(2\phi_j(n-m))\prod_{i\neq j}\cos^2(\phi_i(n-m)) = 0$ for all even values of $n-m$ (note that $U^\dagger PU|n\rangle|m\rangle = 0$ for $n+m$ odd). One can show that the optimal solution within this set is $\phi_j = 2^{-j}\times\pi/2$. It is interesting to note that choosing one of the phases to be $2^{-j}\times\pi/2$ removes all terms with $n-m = 2^j\times(\pm1,\pm3,\pm5,\ldots)$ from the input state according to (10.5). When the phases are chosen as $\phi_j = 2^{-j}\times\pi/2$, it follows that $|\psi_N\rangle$ only contains terms with $n-m = q2^{(N+1)}$, $q = 0,\pm1,\pm2,\ldots$, which may be a useful property in practical applications of the scheme. Even though this is not necessarily optimal with respect to maximizing F_N for a particular choice of input state, we thus use the phases $\phi_j = 2^{-j}\times\pi/2$ in the following, except for one important case: if the input state fulfils the symmetry relations $c_{nm} = c_{mn}$, it turns out that the operator $U^\dagger PU$ by itself removes all terms with $n-m = \pm2,\pm6,\pm10,\ldots$, i.e., we can choose the phases as $\phi_j = 2^{-j}\times\pi/4$, and $|\psi_N\rangle$ only contains terms with $n-m = q2^{(N+2)}$, $q = 0,\pm1,\pm2,\ldots$. For $N=2$, for instance, only terms with $n-m = 0,\pm16,\pm32,\ldots$ contribute to the output state.

In Fig. 10.2, we have chosen the input state to be a product of two single-mode coherent states with amplitude α and plotted the fidelity (10.6) as a function of $|\alpha|^2$ for different numbers of units of the setup. Even for $|\alpha|^2$ as large as 10, the fidelity is still as high as 0.9961 for $N=2$, and the required number of units is thus quite small in practice. The figure also shows the success probability

$$P_N = \langle\psi_N|\psi_N\rangle \tag{10.9}$$

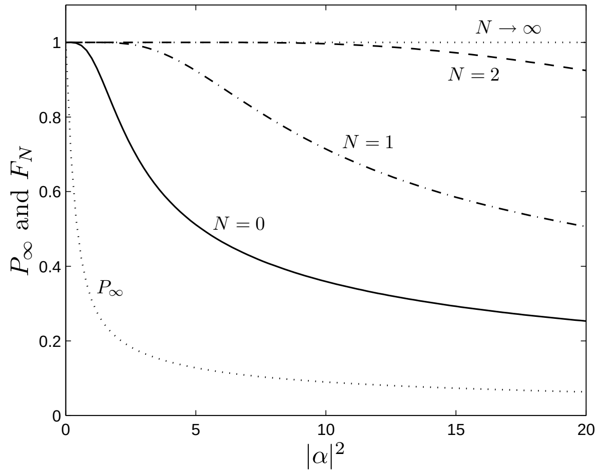

Figure 10.2: Fidelity F_N (see Eq. (10.6)) as a function of the expectation value of the number of photons in one of the input modes for $|\psi_{\text{in}}\rangle = |\alpha\rangle|\alpha\rangle$ and setups with one, two, three, and infinitely many units. The phases are chosen as $\phi_j = 2^{-j} \times \pi/4$. The dotted line labeled P_∞ is the probability in the limit of infinitely many units to actually obtain the required measurement outcome, i.e., all atoms in $(|\uparrow\rangle + |\downarrow\rangle)/\sqrt{2}$ after the interaction with the field.

for $N \to \infty$. For $|\alpha|^2 = 10$, for instance, one should repeat the experiment about 11 times on average before the desired measurement outcome is observed.

10.2 Filtering out losses

In addition to the interest in generating entangled states, the correlations in photon number between the two modes of states in S_2 facilitate an interesting possibility to detect photon loss. This can be done simply by projecting the state of the two modes onto S_2 a second time. If photon loss has occurred, the state is most likely orthogonal to S_2, in which case we obtain a measurement outcome, which is not the one we require in order to accept the projection as successful. On the other hand, if photon loss has not occurred, we are sure to get the desired measurement outcome. We note that loss of a single photon can always be detected by this method, and the state can thus be conditionally recovered with almost perfect fidelity if the loss is sufficiently small. We can improve the ability to detect losses even further at the cost of a reduced success probability if we use an M-mode photon number correlated state, in which case all losses of up to $M-1$ photons can be detected. If we use more modes, we can also distribute the modes to distant parties, while still checking for loss, provided we send at least two

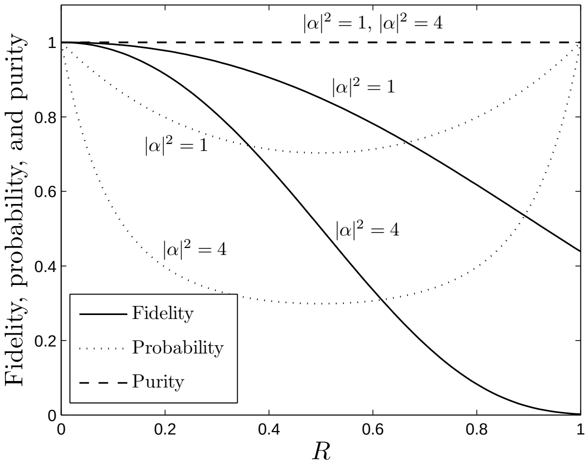

Figure 10.3: Projecting the input state $|\psi_{\text{in}}\rangle = |\alpha\rangle|\alpha\rangle$ onto S_2 followed by a fractional loss R in both modes and a second projection onto S_2, the figure shows the fidelity between the states obtained after the first and the second projection onto S_2, the probability that the second projection is successful given that the first is successful, and the purity of the state after the second projection for two different values of $|\alpha|^2$.

modes to each party.

Let us first consider the two-mode case. We start from the input state $|\psi_{\text{in}}\rangle = |\alpha\rangle|\alpha\rangle$ and use the proposed setup to project it onto the subspace S_2. We then use two fictitious beam splitters with reflectivity R to model a fractional loss in both modes. After tracing out the reflected field, we finally use the proposed setup once more to project the state onto S_2. In Fig. 10.3, we plot the fidelity between the state obtained after the first projection onto S_2 and the state obtained after the second projection onto S_2, the probability that the second projection is successful given that the first is successful, and the purity of the state after the second projection. The second projection is seen to recover the state obtained after the first projection with a fidelity close to unity even for losses of a few percent. This is the case because the main contribution to the fidelity decrease for small R is a simultaneous loss of one photon from both modes. It is also interesting to note that the final state is actually pure for all values of R, which is a consequence of the particular choice of input state. Finally, we note that a single unit is sufficient to detect loss of a single photon, and for small R we thus only need to use one unit for the second projection in practice.

Let us also consider a four-mode input state $|\psi_{\text{in}}\rangle = |\alpha\rangle|\alpha\rangle|\alpha\rangle|\alpha\rangle$. We use the proposed setup three times to project this state onto the subspace S_4 spanned by the state vectors $|n\rangle|n\rangle|n\rangle|n\rangle$, $n = 0, 1, 2, \ldots$. We then imagine a fractional loss of R to take place in all modes. If two of the modes are

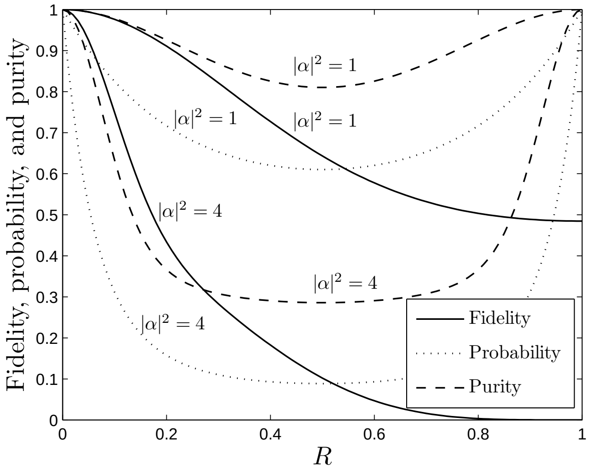

Figure 10.4: Projecting the input state $|\psi_{\text{in}}\rangle = |\alpha\rangle|\alpha\rangle|\alpha\rangle|\alpha\rangle$ onto S_4 followed by a fractional loss R in all four modes and a projection of modes 1 and 2 onto S_2 and of modes 3 and 4 onto S_2, the figure shows the fidelity between the state obtained after the projection onto S_4 and the state obtained after the projections onto S_2, the probability that both projections onto S_2 are successful given that the projection onto S_4 is successful, and the purity of the state after the projections onto S_2 for two different values of $|\alpha|^2$.

on their way to Alice and the two other modes are on their way to Bob, we can only try to recover the original projection by projecting the former two modes onto S_2 and the latter two modes onto S_2. The results are shown in Fig. 10.4, and again the curves showing the fidelity and the purity are seen to be very flat and close to unity for small losses.

10.3 Photon number state detector

The setup in Fig. 10.1 can also be used as a device for photon number resolving measurements as described in the following. We assume that the input state is a product of an unknown n-photon number state in the lower input beam and a vacuum state in the upper input beam. As before, all atoms are initially prepared in the state $|+\rangle$ and are measured in the $|\pm\rangle$ basis after the interaction with the field. If n is even, the result of the measurement of the state of the atoms in cavities C_{1a} and C_{1b} is either $|++\rangle$ or $|--\rangle$, and if n is odd it is either $|-+\rangle$ or $|+-\rangle$. To handle both cases at the same time, we denote $|++\rangle$ and $|-+\rangle$ by $|B_+\rangle$ and $|--\rangle$ and $|+-\rangle$ by $|B_-\rangle$ in the following. A measurement of $|B_+\rangle$ ($|B_-\rangle$) thus projects the state of the mode with annihilation operator $\hat{b}$ onto the subspace of even (odd) photon number states. We also define the operators $\hat{A} = (\hat{a}^\dagger - \hat{b}^\dagger)/\sqrt{2}$

and $\hat{B} = (\hat{a}^\dagger + \hat{b}^\dagger)/\sqrt{2}$, such that $\hat{a}^\dagger|0\rangle \to \hat{A}|0\rangle$ and $\hat{b}^\dagger|0\rangle \to \hat{B}|0\rangle$ at beam splitters BS$_1$, BS$_3$, BS$_5$, …, and $\hat{A}|0\rangle \to \hat{a}^\dagger|0\rangle$ and $\hat{B}|0\rangle \to \hat{b}^\dagger|0\rangle$ at beam splitters BS$_2$, BS$_4$, BS$_6$, ….

The beam splitter BS$_1$ transforms the input state $|n\rangle|0\rangle = \frac{1}{\sqrt{n!}}(\hat{a}^\dagger)^n|0\rangle|0\rangle$ into $\frac{1}{\sqrt{n!}}\left(\frac{\hat{a}^\dagger - \hat{b}^\dagger}{\sqrt{2}}\right)^n|0\rangle|0\rangle$. This state interacts with the atoms in cavities C$_{1a}$ and C$_{1b}$, and the state of the light field after the measurement of the state of the atoms can be written as $|b_\pm\rangle \equiv \frac{1}{\sqrt{2n!}}\left(\left(\frac{\hat{a}^\dagger - \hat{b}^\dagger}{\sqrt{2}}\right)^n \pm \left(\frac{\hat{a}^\dagger + \hat{b}^\dagger}{\sqrt{2}}\right)^n\right)|0\rangle|0\rangle = \frac{1}{\sqrt{2n!}}(\hat{A}^n \pm \hat{B}^n)|0\rangle|0\rangle$, where $|b_+\rangle$ ($|b_-\rangle$) is the state corresponding to the measurement result $|B_+\rangle$ ($|B_-\rangle$). After BS$_2$, the state is given by $\frac{1}{\sqrt{2n!}}((\hat{a}^\dagger)^n \pm (\hat{b}^\dagger)^n)|0\rangle|0\rangle$, and the phase shifters transform this state into $\frac{1}{\sqrt{2n!}}(e^{i\phi_1 n}(\hat{a}^\dagger)^n \pm e^{-i\phi_1 n}(\hat{b}^\dagger)^n)|0\rangle|0\rangle$. Finally, BS$_3$ transforms the state into $\frac{1}{\sqrt{2n!}}(e^{i\phi_1 n}\hat{A}^n \pm e^{-i\phi_1 n}\hat{B}^n)|0\rangle|0\rangle = \frac{1}{2}(e^{i\phi_1 n} \pm e^{-i\phi_1 n})|b_+\rangle + \frac{1}{2}(e^{i\phi_1 n} \mp e^{-i\phi_1 n})|b_-\rangle$. The result of measuring the state of the atoms in cavities C$_{2a}$ and C$_{2b}$ is hence the same (i.e., $|B_\pm\rangle$) as the result of measuring the state of the atoms in cavities C$_{1a}$ and C$_{1b}$ with probability $p_+(\phi_1) = \cos^2(\phi_1 n)$ and opposite (i.e., $|B_\mp\rangle$) with probability $p_-(\phi_1) = \sin^2(\phi_1 n)$. Since the state is again projected onto one of the two states $|b_\pm\rangle$ we can repeat exactly the same calculations for all the following units of the setup and conclude that we obtain the same (opposite) measurement result for the $(i+1)$th unit as for the ith unit with probability $p_+(\phi_i)$ ($p_-(\phi_i)$).

If it is known that $n < \pi/\phi$ for some choice of ϕ, one can estimate n by choosing $\phi_1 = \phi_2 = \ldots = \phi_N = \phi$ and measuring how often the measurement result for unit $i+1$ is the same as the measurement result for unit i. Alternatively, one can measure whether n is a multiple of some positive integer $n_0 \in \mathbb{N}$ by choosing the phases as $\phi_i = 2^{i-1}\pi/n_0$, $i = 1, 2, \ldots, N$, and measuring whether the same measurement result is obtained for all $N+1$ units. The probability that this happens

$$p(n) = \prod_{i=1}^{N} p_+(\phi_i) = \prod_{i=0}^{N-1} \cos^2\left(\frac{2^i\pi}{n_0}n\right) \tag{10.10}$$

is unity for all photon numbers that are multiples of n_0, but for all other values of n it approaches zero for large N. To quantify our ability to determine whether n is a multiple of n_0, we define

$$q \equiv 1 - \max_{n \neq 0, n_0, 2n_0, \ldots} p(n), \tag{10.11}$$

which is the smallest possible value of the probability that we do not obtain the same measurement result for all the units if n is not a multiple of n_0. For $n_0 = 3$, for instance, we obtain $q = 93.75\%$ ($q = 99.61\%$) for $N + 1 = 3$ ($N + 1 = 5$), for $n_0 = 4$, we achieve $q = 100\%$ already for $N + 1 = 3$, and for $n_0 = 5$, we find $q = 93.75\%$ ($q = 99.61\%$) for $N+1 = 3$ ($N+1 = 5$). We

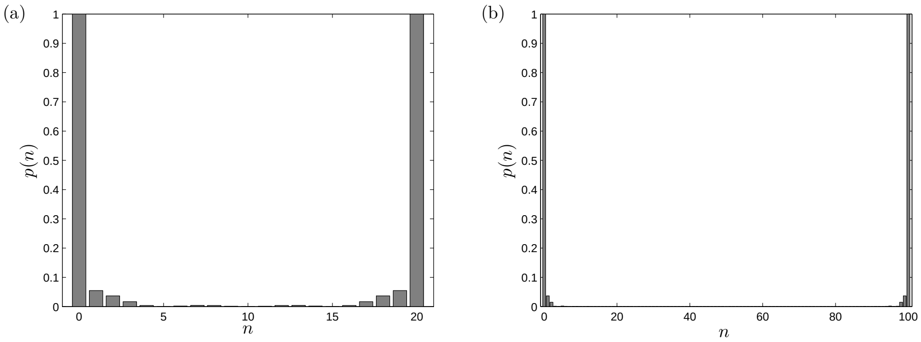

Figure 10.5: (a) Probability $p(n)$ to obtain the same measurement result for all units as a function of n for $n_0 = 20$ and $N + 1 = 5$ resulting in $q = 94.49\%$. We note that $q = 99.66\%$ for $N+1 = 7$. (b) $p(n)$ for $n_0 = 100$ and $N + 1 = 8$ resulting in $q = 96.33\%$. For $N + 1 = 10$, we obtain $q = 99.95\%$.

have shown $p(n)$ for $n_0 = 20$ and $n_0 = 100$ in Fig. 10.5, and we observe that even for these high values of n_0, a rather small number of units is sufficient to obtain high values of q.

Since an integer can be uniquely decomposed into a product of primes, it is sufficient to check whether n is a multiple of any primes or any powers of primes to uniquely determine the value of n. If n is known to be smaller than or equal to some positive integer $n_{\max}$, $n_{\max}$ is also an upper bound for the number of required checks. To obtain a reliable result, we need $q > 1 - 1/n_{\max}$ for all tests. Numerical calculations suggest that this is the case if $N = 2\log_2(n_{\max})$, which leads to a total number of units of order $2n_{\max}\log_2(n_{\max})$. The resources required thus scale moderately with $n_{\max}$.

We note that the setup has a built-in possibility to detect photon loss because the parity of the total number of photons in the two modes is measured each time the state of a pair of atoms belonging to the same unit is measured. If the parity suddenly changes, we know that at least one photon has been lost.

Nondestructive photon number state detection

The measurement scheme described above randomly transforms the input state $|n\rangle|0\rangle$ into one of the two $N00N$ states $(|n\rangle|0\rangle \pm |0\rangle|n\rangle)/\sqrt{2}$, and we may thus also regard the proposal as a $N00N$ state generator. With a modification of the setup, it is possible to measure n without changing the state of the input field. The idea is to allow the light field to interact twice with the same unit before the state of the atoms is measured, or equivalently to use the setup in Fig. 10.6 as the basic building block, where the atoms in cavities C_{1a} and C_{2a} are initially prepared in an entangled

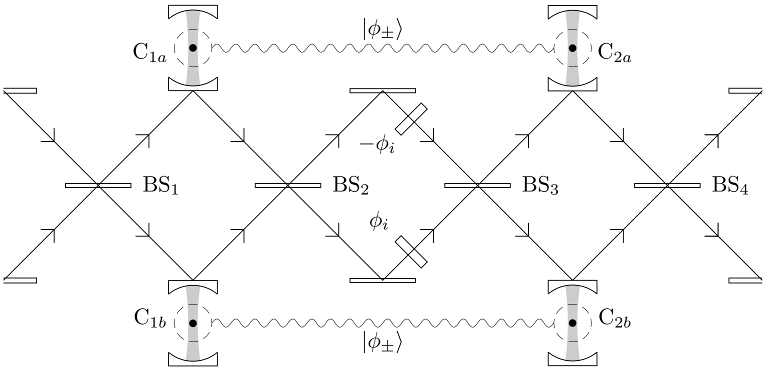

Figure 10.6: Basic building block of the nondestructive photon number resolving detection scheme. The dashed circles and the wavy lines indicate the entanglement between the atoms in cavities C$_{1a}$ and C$_{2a}$ and between the atoms in cavities C$_{1b}$ and C$_{2b}$.

state $|\phi_+\rangle \equiv (|\uparrow\uparrow\rangle + |\downarrow\downarrow\rangle)/\sqrt{2}$, and the atoms in cavities C$_{1b}$ and C$_{2b}$ are also prepared in the state $|\phi_+\rangle$. This can, for instance, be achieved via the parity measurement scheme discussed in Chap. 9. Analyzing the setup (see [XII] for details), we find that the block transforms the input state $|n\rangle|0\rangle|\phi_+\rangle|\phi_+\rangle$ into $|n\rangle|0\rangle(\cos(\phi_i n)|\phi_+\rangle|\phi_+\rangle + i\sin(\phi_i n)|\phi_-\rangle|\phi_-\rangle)$, where $|\phi_-\rangle \equiv (|\uparrow\uparrow\rangle - |\downarrow\downarrow\rangle)/\sqrt{2}$. The state of the light field is thus decoupled from the state of the atoms, but we can still retrieve the same information as before by measuring the state of the atoms because the probability to measure $|\phi_+\rangle|\phi_+\rangle$ is $\cos^2(\phi_i n)$ and the probability to measure $|\phi_-\rangle|\phi_-\rangle$ is $\sin^2(\phi_i n)$. Since $|\phi_+\rangle = (|++\rangle + |--\rangle)/\sqrt{2}$ and $|\phi_-\rangle = (|+-\rangle + |-+\rangle)/\sqrt{2}$, the two states can be distinguished by measuring the atoms in the $|\pm\rangle$ basis. We note that the only valid measurement results are $|\phi_+\rangle|\phi_+\rangle$ and $|\phi_-\rangle|\phi_-\rangle$. A measurement of $|\phi_-\rangle|\phi_+\rangle$ or $|\phi_+\rangle|\phi_-\rangle$ signifies a loss between the two pairs of cavities.

10.4 Optimal input mode function

So far, we have considered the ideal limit of infinitely long pulses and an infinitely strong coupling. In this section, we use the model from Sec. 9.1 to quantify how long the pulses need to be and to derive a simple analytical expression for the optimal choice of the shape of the pulses when the pulses are restricted to a finite time interval. In the following, we concentrate on a single cavity as in Fig. 9.1(a) and assume that the input field to this cavity is in a continuous coherent state $|\{\alpha_{\text{in}}(t)\}\rangle$ (defined in (2.19)) with mode function $f_{\text{in}}(t) = \alpha_{\text{in}}(t)/\alpha$, where $|\alpha|^2 = \int |\alpha_{\text{in}}(t)|^2 dt$ is the expectation value of the total number of photons in the input pulse. Denoting the conditional amplitude of the cavity field by $\xi^i(t)$, $i = \downarrow, \uparrow$, and the conditional amplitude of the output field from the cavity by $\alpha^i_{\text{out}}(t)$, it follows from (9.5) and (9.6) that

$$\frac{d\xi^i(t)}{dt} = -\left(1 + 2C\delta_{i\uparrow}\right)\frac{\kappa}{2}\xi^i(t) + \sqrt{\kappa}\alpha_{\text{in}}(t), \tag{10.12}$$

$$\alpha^i_{\text{out}}(t) = \alpha_{\text{in}}(t) - \sqrt{\kappa}\xi^i(t). \tag{10.13}$$

Solving (10.12), we find $\alpha^i_{\text{out}}(t) = \alpha f^i_{\text{out}}(t)$ with

$$f^i_{\text{out}}(t) = f_{\text{in}}(t) - \kappa \int_{-\infty}^{t} e^{-(1+2C\delta_{i\uparrow})\kappa(t-t')/2} f_{\text{in}}(t')dt'. \tag{10.14}$$

Note that $f^i_{\text{out}}(t)$ is not necessarily normalized due to the possibility of spontaneous emission. The ideal situation is $f^{\uparrow}_{\text{out}}(t) = f_{\text{in}}(t)$ and $f^{\downarrow}_{\text{out}}(t) = -f_{\text{in}}(t)$, and we would thus like the norm of

$$E_i \equiv 1 + (-1)^{\delta_{i\uparrow}} \int_{-\infty}^{\infty} f^*_{\text{in}}(t) f^i_{\text{out}}(t)dt \tag{10.15}$$

to be as small as possible.

For $i = \uparrow$ and $C \gg 1$, the exponential function in (10.14) is practically zero unless $\kappa(t-t') \ll 1$, and as long as $f_{\text{in}}(t)$ changes slowly on the timescale $(C\kappa)^{-1}$, we can take $f_{\text{in}}(t)$ outside the integral to obtain $f^{\uparrow}_{\text{out}}(t) = (1-2/(1+2C))f_{\text{in}}(t)$ and $E_\uparrow = 2/(1+2C) \approx C^{-1}$. As this result is independent of $f_{\text{in}}(t)$, a natural criterion for the optimal choice of input mode function is to minimize

$$|E_\downarrow| = \left| 2 - \kappa \int_{-\infty}^{\infty}\int_{-\infty}^{t} e^{-\kappa(t-t')/2} f^*_{\text{in}}(t) f_{\text{in}}(t')dt'dt \right| \tag{10.16}$$

under the constraint $\int_{-\infty}^{\infty} |f_{\text{in}}(t)|^2 dt = 1$. We also restrict $f_{\text{in}}(t)$ to be zero everywhere outside the time interval $[-T/2, T/2]$. Since we would like the double integral to be as close to 2 as possible, we should choose a time-independent phase of $f_{\text{in}}(t)$, and we may then as well assume $f^*_{\text{in}}(t) = f_{\text{in}}(t)$. Performing the variational calculation, we find that the optimal solution is

$$f_{\text{in}}(t) = \left\{ \begin{array}{cl} A\cos(\omega_0 t) & \text{for } t \in [-T/2, T/2] \\ 0 & \text{otherwise} \end{array} \right. , \tag{10.17}$$

where A and ω_0 are determined by the relations

$$A = \left(\frac{2}{T + \sin(\omega_0 T)/\omega_0}\right)^{1/2}, \qquad \frac{2\omega_0}{\kappa}\tan\left(\frac{\omega_0 T}{2}\right) = 1, \tag{10.18}$$

and $\omega_0 T \in [0, \pi[$.

This solution gives

$$E_\downarrow = \frac{8\omega_0^2}{\kappa^2 + 4\omega_0^2} = 2\cos^2\left(\frac{\omega_0 T}{2}\right). \tag{10.19}$$

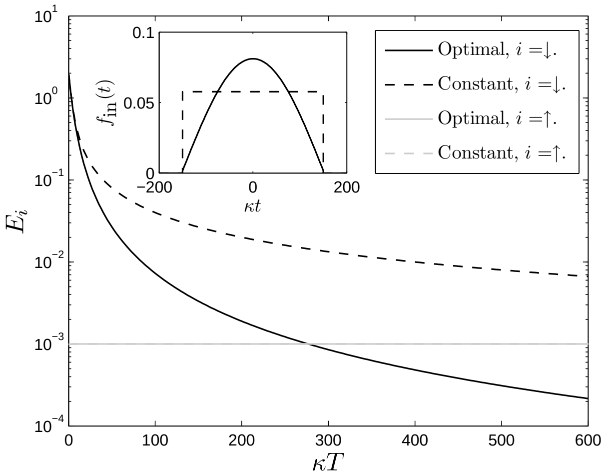

Figure 10.7: Deviation E_i of $\int f_{\mathrm{in}}^*(t) f_{\mathrm{out}}^i(t) dt$ from the ideal value as a function of the pulse length. The single atom cooperativity parameter is assumed to be $C = 10^3$. Solid lines are for the optimal input mode function given in (10.17), and dashed lines are for an input mode function, which is constant in the interval $t \in [-T/2, T/2]$ and zero otherwise. The inset illustrates these functions for $\kappa T = 300$. For $i = \uparrow$, the shape of the output field is almost the same as the shape of the input field as long as $\kappa T \gg C^{-1}$, but the norm of the field amplitude is slightly decreased due to spontaneous emission from the atom such that $E_\uparrow \approx C^{-1}$. This result is independent of the actual shape of the input mode function, and the solid and dashed lines for $E_\uparrow$ are hence indistinguishable in the figure. The results for $E_\downarrow$ are independent of C because the light field does not interact with the atom in this case. Nonzero values of $E_\downarrow$ only occur due to distortion of the shape of the mode function. For $\kappa T \gg 2\pi$, $E_\downarrow \approx 8\pi^2/(\kappa T)^2$ for the optimal input mode function and $E_\downarrow \approx 4/(\kappa T)$ for the constant input mode function.

For fixed κ, ω_0 is a decreasing function of T, and for $\kappa T \gg 2\pi$, $\omega_0 \approx \pi/T$ and $E_\downarrow \approx 8\pi^2/(\kappa T)^2$. Distortion of the input mode function can thus be avoided by choosing a sufficiently long input pulse. This may be understood by considering the Fourier transform of the input mode function. For a very short pulse the frequency distribution is very broad and only a small part of the field is actually on resonance with the cavity, i.e., most of the field is reflected without entering into the cavity. For a very long pulse, on the other hand, the frequency distribution is very narrow and centered at the resonance frequency of the cavity. E_i is plotted in Fig. 10.7 as a function of T, both for the optimal input mode function and an input mode function, which is constant in the interval $[-T/2, T/2]$. The optimal input mode function is seen to provide a significant improvement. In fact, for the constant input mode function $E_\downarrow = 4(1 - \exp(-\kappa T/2))/(\kappa T)$, and hence $E_\downarrow$ scales only as $(\kappa T)^{-1}$ for large κT.

10.5 Finite single atom cooperativity parameter

To investigate the significance of a finite cooperativity parameter, we would like to determine how a single unit of the setup in Fig. 10.1 transforms the state of the field when we use the full multimode description. For this purpose, it is simpler to work in frequency space, and we thus Fourier transform the solution of (10.12) and (10.13) to obtain

$$\xi^j(\omega) = \frac{\sqrt{\kappa}}{(1+2C\delta_{j\uparrow})\kappa/2 - i\omega}\alpha_{\text{in}}(\omega), \tag{10.20}$$

$$\alpha^j_{\text{out}}(\omega) = K_j(\omega)\alpha_{\text{in}}(\omega), \tag{10.21}$$

where

$$K_j(\omega) \equiv -\frac{(1-2C\delta_{j\uparrow})\kappa/2 + i\omega}{(1+2C\delta_{j\uparrow})\kappa/2 - i\omega}. \tag{10.22}$$

Assume now that the density operator representing the state of the two input beams to the unit may be written on the form

$$\rho_{\text{in}} = \sum_n \sum_m c_{nm} |\{\alpha_n(\omega)\}\rangle\langle\{\alpha_m(\omega)\}| \otimes |\{\beta_n(\omega)\}\rangle\langle\{\beta_m(\omega)\}|, \tag{10.23}$$

where n and m are summed over the same set of numbers and $|\{\alpha_n(\omega)\}\rangle$ and $|\{\beta_n(\omega)\}\rangle$ are continuous coherent states in frequency space, i.e.,

$$|\{\alpha_n(\omega)\}\rangle = \exp\left(\int \alpha_n(\omega)\hat{a}^\dagger(\omega)d\omega - \int \alpha_n^*(\omega)\hat{a}(\omega)d\omega\right)|0\rangle \tag{10.24}$$

and similarly for $|\{\beta_n(\omega)\}\rangle$. After the first 50:50 beam splitter, the input state is transformed into

$$\rho' = \sum_n \sum_m c_{nm} \left|\left\{(\alpha_n(\omega)+\beta_n(\omega))/\sqrt{2}\right\}\right\rangle \left\langle\left\{(\alpha_m(\omega)+\beta_m(\omega))/\sqrt{2}\right\}\right| \\ \otimes \left|\left\{(\beta_n(\omega)-\alpha_n(\omega))/\sqrt{2}\right\}\right\rangle \left\langle\left\{(\beta_m(\omega)-\alpha_m(\omega))/\sqrt{2}\right\}\right|, \tag{10.25}$$

and this is the input state to the two cavities. The initial state of the two atoms is

$$\rho_{\text{at}} = \frac{1}{4} \sum_{i\in\{\downarrow,\uparrow\}} \sum_{j\in\{\downarrow,\uparrow\}} \sum_{p\in\{\downarrow,\uparrow\}} \sum_{q\in\{\downarrow,\uparrow\}} |i\rangle\langle p| \otimes |j\rangle\langle q|. \tag{10.26}$$

We thus need to know how the interaction with one of the cavities transforms a term like $c_{nm}|\alpha_{\text{in},n}(\omega)\rangle\langle\alpha_{\text{in},m}(\omega)| \otimes |i\rangle\langle p|$. We can obtain this transformation by combining Eqs. (9.4), (10.20), and (10.21). Altogether, we find that $c_{nm}|\alpha_{\text{in},n}(\omega)\rangle\langle\alpha_{\text{in},m}(\omega)| \otimes |i\rangle\langle p|$ is transformed into $d_{ip}[\alpha_{\text{in},n}(\omega), \alpha_{\text{in},m}(\omega)]c_{nm}$ $|K_i(\omega)\alpha_{\text{in},n}(\omega)\rangle\langle K_p(\omega)\alpha_{\text{in},m}(\omega)| \otimes |i\rangle\langle p|$, where

$$d_{ip}[\alpha_{\text{in},n}(\omega), \alpha_{\text{in},m}(\omega)] = \exp\Bigg(-\int_{-\infty}^{\infty} \frac{C\kappa^2}{(1+2C)^2(\kappa/2)^2+\omega^2} \\ \times \left(|\alpha_{\text{in},n}(\omega)|^2\delta_{i\uparrow} + |\alpha_{\text{in},m}(\omega)|^2\delta_{p\uparrow} - 2\alpha_{\text{in},n}(\omega)\alpha^*_{\text{in},m}(\omega)\delta_{i\uparrow}\delta_{p\uparrow}\right) d\omega\Bigg). \tag{10.27}$$

After projecting both atoms onto $(|\uparrow\rangle + |\downarrow\rangle)/\sqrt{2}$ and taking the final 50:50 beam splitter into account, we obtain the output state after one unit

$$\begin{aligned}
\rho_{\text{out}} = &\sum_n \sum_m \sum_{i\in\{\downarrow,\uparrow\}} \sum_{j\in\{\downarrow,\uparrow\}} \sum_{p\in\{\downarrow,\uparrow\}} \sum_{q\in\{\downarrow,\uparrow\}} \frac{1}{16} c_{nm} \\
&\quad \times d_{ip}[(\alpha_n(\omega) + \beta_n(\omega))/\sqrt{2}, (\alpha_m(\omega) + \beta_m(\omega))/\sqrt{2}] \\
&\quad \times d_{jq}[(\beta_n(\omega) - \alpha_n(\omega))/\sqrt{2}, (\beta_m(\omega) - \alpha_m(\omega))/\sqrt{2}] \\
&\times \left| \left\{ \frac{1}{2}(K_i(\omega) + K_j(\omega))\alpha_n(\omega) + \frac{1}{2}(K_i(\omega) - K_j(\omega))\beta_n(\omega) \right\} \right\rangle \\
&\left\langle \left\{ \frac{1}{2}(K_p(\omega) + K_q(\omega))\alpha_m(\omega) + \frac{1}{2}(K_p(\omega) - K_q(\omega))\beta_m(\omega) \right\} \right| \\
&\otimes \left| \left\{ \frac{1}{2}(K_i(\omega) + K_j(\omega))\beta_n(\omega) + \frac{1}{2}(K_i(\omega) - K_j(\omega))\alpha_n(\omega) \right\} \right\rangle \\
&\left\langle \left\{ \frac{1}{2}(K_p(\omega) + K_q(\omega))\beta_m(\omega) + \frac{1}{2}(K_p(\omega) - K_q(\omega))\alpha_m(\omega) \right\} \right| . \qquad (10.28)
\end{aligned}$$

A subsequent phase shifter is easily taken into account by multiplying the coherent state amplitudes by the appropriate phase factors. We note that the result has the same form as the input state (10.23) if we collect n, i, and j into one index and m, p, and q into another index. We can thus apply the transformation repeatedly to obtain the output state after $N + 1$ units of the setup.

If we assume $\alpha_n(\omega)$ and $\beta_m(\omega)$ to have the same shape for all n and m, the output field simplifies to a two-mode state for $\kappa T \gg 1$ as expected. This may be seen as follows. When T is much larger than κ^{-1}, the width of the distribution $\alpha_n(\omega)$ in frequency space is much smaller than κ. For the relevant frequencies we thus have $\omega \ll \kappa/2$, and in this case the right hand side of (10.22) reduces to $-(1 - 2C\delta_{j\uparrow})/(1 + 2C\delta_{j\uparrow})$, i.e., $K_j(\omega)$ is independent of frequency, and the amplitudes of all the continuous coherent states of the output density operator are proportional to $\alpha_n(\omega)$.

In Fig. 10.8, we have used (10.28) in the limit $\kappa T \gg 1$ to compute the fidelity (10.6) as a function of the single atom cooperativity parameter for $\rho_{\text{in}} = |\alpha\rangle\langle\alpha| \otimes |\alpha\rangle\langle\alpha|$. The ideal values for $C \to \infty$ are also shown, and the deviations are seen to be very small for C larger than about 10^3. As mentioned in the previous chapter, current experiments have demonstrated single atom cooperativity parameters on the order of 10^2, and high fidelities can also be achieved for this value. When C is finite, there is a relative photon loss of $1 - \int |f_{\text{out}}^{\uparrow}(t)|^2 dt \approx 2/C$ due to spontaneous emission each time the field interacts with a cavity containing an atom in the state $|\uparrow\rangle$. We note, however, that the setup is partially robust against such losses because the next unit of the setup removes all components of the state for which a single photon has been lost.

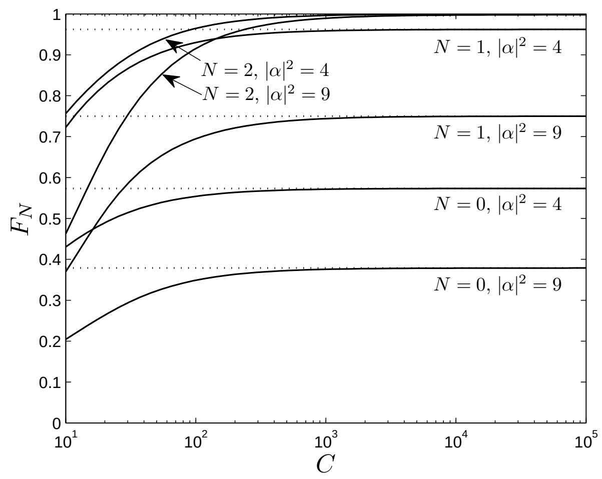

Figure 10.8: Fidelity F_N as defined in (10.6) as a function of the single atom cooperativity parameter C for different values of the expectation value of the number of photons in one of the input modes and different numbers of units of the setup, assuming $\kappa T \gg 1$ and $\rho_{\text{in}} = |\alpha\rangle\langle\alpha| \otimes |\alpha\rangle\langle\alpha|$. The dotted lines are the asymptotes for $C \to \infty$.

10.6 Conclusion

In conclusion, we have investigated the possibility to transform the state of light fields by allowing the light fields to interact with single atoms in cavities in the strong coupling limit and subsequently detecting the state of the atoms. Specifically, we have proposed a method to project an arbitrary two mode input state onto the subspace spanned by the state vectors $|n\rangle|n\rangle$, $n = 0, 1, 2, \ldots$, and we have shown that the proposed setup can also be used for checking whether photon loss has occurred. The setup facilitates generation and distribution of multimode entangled states in networks. We have also shown that atoms in cavities can be used for nondestructive photon number resolving detection and for preparation of $N00N$ states. Finally, we have computed the optimal shape of the mode function of the light field modes, and we have investigated the significance of a finite single atom cooperativity parameter.

Chapter 11

Feedback control, model reduction, and unsupervised manifold learning

As we saw in Chap. 8, the time evolution of the state of a continuously monitored quantum system is governed by a stochastic differential equation, but it is typically a very slow process to integrate this equation numerically due to the large dimensionality of the relevant Hilbert space. This is, in particular, a problem if we would like to control the system dynamics through state dependent measurement based feedback (such as in Eq. (8.18)) since, in that case, one needs to track the state of the system in real time in order to calculate the appropriate feedback (for instance, the value of $\langle\hat{x}\rangle$ in Eq. (8.18)). One way to get around the problem, is to feed back the measured signal (for instance, the measured photocurrent) directly [175, 176], but we have more freedom in the construction of feedback schemes if we can use the measured signal to compute the current value of various state dependent quantities that we would like to include in the feedback terms. Due to the intrinsic robustness of feedback, small inaccuracies in the calculations can be tolerated. In the present chapter, we consider the possibility to derive simplified approximate models of the dynamics of quantum systems as a tool to speedup state estimation in feedback schemes. Quantum feedback control has several applications such as cooling [177], deterministic atomic spin squeezing [178], quantum error correction [140, 141], and deterministic state preparation [54, 179, 180], and general methods to speedup state estimation are hence very useful.

The model reduction method presented below builds on the observation that the dynamics of quantum systems typically explores only a tiny portion of the degrees of freedom in the full Hilbert space and on the possibility to use numerical methods to learn the structure of the dynamics from example trajectories. The most straightforward approach in this direction is to restrict the system dynamics to the affine linear subspace of low dimension, which leads to the smallest error when a series of states obtained from an example trajectory in the full space is projected onto the subspace. This technique has turned out to be very successful when applied to the case of phase bistable dynamics of a single probed two-level atom in a cavity [128, 133], while the results for absorptive bistability are less satisfactory [133]. The latter case involves more complicated dynamics due to the lack of symmetry between the two semistable regions. In the present work, we consider the more flexible case of restricting the dynamics to a nonlinear low-dimensional manifold embedded in the full space, and for the case of absorptive bistability, we demonstrate that the obtained simplified models of the dynamics are sufficiently accurate to be utilized in a feedback scheme.

Other methods to achieve model reduction include derivation of connections between expectation values of different operators by fitting [133], and to approximate the dynamics of nearly Gaussian systems by a Gaussian description [181, 182]. We emphasize that the method used in the present chapter is generally applicable and does not require any specific knowledge about the behavior of the system.

In Sec. 11.1, we explain how we compute the low-dimensional manifold, which captures most of the dynamics, and in Sec. 11.2, we show how we obtain reduced models by projecting the dynamics onto this manifold. In Secs. 11.3 and 11.4, we apply the general method to the case of absorptive bistability for a single, probed atom in a cavity to test the ability of the reduced models to reproduce the actual dynamics, and we demonstrate that the predictions of the reduced models can be used to keep the system within one of the semistable regions in a feedback scheme. The chapter is based on [IX][1], and further background material can be found in [133].

11.1 Unsupervised manifold learning

We first need to identify a suitable manifold in the space of density operators onto which we can project the dynamics. Several manifold learning strategies have already been investigated in the literature [183, 184], and here we use the method of local tangent space alignment (LTSA) [185]. LTSA belongs to the class of unsupervised manifold learning strategies, which means that, apart from the initial data set and the dimension of the sought manifold, we do not need to supply additional structural information to run the algorithm. An advantage of LTSA is the fact that it optimizes the choice of low-dimensional space in local areas, and it is hence well-suited to describe systems with more than one semistable region. LTSA defines the manifold in terms of single points, but in order to perform the projection, we need a differentiable function, which relates the coordinates of all points in the low-

---

[1] Copyright (2009) by IOP Publishing Ltd and Deutsche Physikalische Gesellschaft.

dimensional space to the coordinates of the same points in the full space. We solve this problem by fitting a function to the points obtained from LTSA.

In brief, the input to the LTSA algorithm is a set of N vectors $x^{(i)}$, $i = 1, 2, \ldots, N$, which are assumed to be sampled with noise from an unknown d-dimensional (nonlinear) manifold embedded in an m-dimensional space, where $m > d$, and the objective is to identify the underlying d-dimensional manifold. For a linear manifold this is done by computing the d-dimensional affine subspace, which minimizes the sum of the square of the errors between the original vectors and the projection of the vectors onto the affine subspace. To tackle the more general case, the LTSA procedure aligns local linear structures into a global nonlinear manifold, where the local structures are the affine subspaces obtained by applying the above procedure to subsets of the N points. The ith subset is chosen as the ith point and the $k-1$ nearest neighbors of the ith point, where k is a number fulfilling $d \ll k \ll N$. (Ideally, the outcome is practically independent of k as long as $d \ll k \ll N$ is fulfilled, and this is why we do not count k as an additional input.) The output of the algorithm is the coordinates $\tau^{(i)}$ of the points in the d-dimensional space and an approximate map from the d-dimensional space to the full m-dimensional space, from which it is possible to compute corrected coordinates $\tilde{x}^{(i)}$ of the points in the m-dimensional space. The map is, however, only valid in small regions around each $\tau^{(i)}$, and it is not differentiable everywhere because it consists of local linear spaces glued together.

In our case, we start from a set of density matrices sampled from the time evolution of the state of the system obtained when we integrate the full SME. These density matrices of size $L \times L$ are transformed into column vectors $x^{(i)}$ in $\mathbb{R}^m$, where $m = L^2$, by concatenating the real part of the columns of the upper right triangular part including the diagonal followed by the concatenation of the imaginary part of the columns of the upper right triangular part excluding the diagonal, i.e.,

$$x^{(i)}_{n(n+1)/2} = \rho^{(i)}_{nn}, \tag{11.1a}$$

$$x^{(i)}_{m(m-1)/2+n} = \mathrm{Re}(\rho^{(i)}_{nm}), \tag{11.1b}$$

$$x^{(i)}_{N(N+1)/2+(m-1)(m-2)/2+n} = \mathrm{Im}(\rho^{(i)}_{nm}), \tag{11.1c}$$

where $n = 1, 2, \ldots, N$ in (11.1a) and $n = 1, 2, \ldots, m-1$ and $m = 2, 3, \ldots, N$ in (11.1b) and (11.1c). This construction method ensures that every vector x in the m-dimensional space corresponds to a Hermitian matrix. Furthermore, the LTSA algorithm ensures that the new points in the m-dimensional space are correctly normalized. There is, however, no guarantee that the constructed points correspond to positive semi-definite matrices, and here we rely on the ability of the time evolution equation to keep the state of the system within the physically acceptable region. Depending on the purpose of the reduced model, it is not necessarily optimal to minimize the projection error with respect to the dot product $(x^{(i)})^T x^{(j)}$, and one could, for instance, consider to multiply the density matrix elements with different weight factors in a given basis as noted in [133].

Having obtained a set of points $\tau^{(i)}$ in the low-dimensional space and the corresponding coordinates $\tilde{x}^{(i)}$ in the full space from the LTSA algorithm, we next construct a map from the low-dimensional space to the full space via fitting. We need to compute one fit for each of the m coordinates in the full space, and to make this procedure practical, we use the same fitting model for all the coordinates and choose this model to be linear in the fitting parameters, i.e., we assume a map of form $x = cf(\tau)$, where x is a vector in the m-dimensional space, c is an $m \times r$ matrix of fitting parameters, where r is the number of elements in $f(\tau)$, and $f(\tau)$ is an $r \times 1$ vector, whose elements $f_j(\tau)$ are arbitrary differentiable functions of the coordinates $\tau = (\tau_1, \tau_2, \dots, \tau_d)^T$ in the d-dimensional space. To ensure that x is correctly normalized for all τ, we choose $f_1(\tau) = 1$ and minimize $\sum_i (\tilde{x}^{(i)} - cf(\tau^{(i)}))^T (\tilde{x}^{(i)} - cf(\tau^{(i)}))$ under the r constraints $v^T c = (1, 0, \dots, 0)$, where v is an $m \times 1$ vector, whose ith entry is one if $i = n(n+1)/2$ for some $n \in \{1, 2, \dots, N\}$ and zero otherwise (i.e., $v^T x = \mathrm{Tr}(\rho)$, where ρ is the density matrix corresponding to the vector x). The result is

$$c = \tilde{c} + \frac{1}{\sqrt{m}} v((1, 0, \dots, 0) - v^T \tilde{c}), \tag{11.2}$$

where $\tilde{c} = ((z^T z)^{-1} z^T y)^T$ is the standard linear least squares result without constraints and the matrices z and y have elements $z_{ij} = f_j(\tau^{(i)})$ and $y_{ij} = \tilde{x}_j^{(i)}$.

11.2 Projection onto the low-dimensional manifold

The result of the last section is a relation of form

$$\rho(\tau) = \sum_j c_j f_j(\tau_1, \tau_2, \dots, \tau_d), \tag{11.3}$$

where c_j is the matrix obtained by applying the inverse of (11.1) to the jth column of c. To project the considered SME onto the manifold defined by (11.3), we follow the derivation in [133]. We would like to interpret $d\rho$ as a vector, but $d\rho$ only transforms as a vector if $(dW_\mathrm{s})^2 = 0$, i.e., if we use Stratonovich calculus, and we thus rewrite the SME into Stratonovich form $d\rho = \underline{A}[\rho]dt + B[\rho] \circ dW_\mathrm{s}$. Starting from a point $\rho(\tau)$ on the manifold, we then project $d\rho$ onto the tangent space of the manifold at that point, which is spanned by the d vectors $\partial\rho(\tau)/\partial\tau_i$. Using the dot product $\langle \rho_A, \rho_B \rangle \equiv$

$\mathrm{Tr}(\rho_A \rho_B)$, we obtain

$$d\rho(\tau) = \sum_i \sum_j (g^{-1})_{ij} \,\mathrm{Tr}\left(\underline{A}[\rho(\tau)] \frac{\partial \rho(\tau)}{\partial \tau_j} \right) \frac{\partial \rho(\tau)}{\partial \tau_i} dt$$
$$+ \sum_i \sum_j (g^{-1})_{ij} \,\mathrm{Tr}\left(B[\rho(\tau)] \frac{\partial \rho(\tau)}{\partial \tau_j} \right) \frac{\partial \rho(\tau)}{\partial \tau_i} \circ dW_{\mathrm{s}}, \quad (11.4)$$

where $g = g(\tau)$ is the metric tensor with elements

$$g_{ij} = \mathrm{Tr}\left(\frac{\partial \rho}{\partial \tau_i} \frac{\partial \rho}{\partial \tau_j} \right) = \sum_p \sum_q \frac{\partial f_p}{\partial \tau_i} \mathrm{Tr}(c_p c_q) \frac{\partial f_q}{\partial \tau_j} \quad (11.5)$$

and we have written f_p for $f_p(\tau)$. Combining this relation with

$$d\rho(\tau) = \sum_i \frac{\partial \rho(\tau)}{\partial \tau_i} \circ d\tau_i, \quad (11.6)$$

we obtain a stochastic differential equation for the time evolution of τ_i

$$d\tau_i = \sum_j (g^{-1})_{ij} \,\mathrm{Tr}\left(\underline{A}[\rho(\tau)] \frac{\partial \rho(\tau)}{\partial \tau_j} \right) dt$$
$$+ \sum_j (g^{-1})_{ij} \,\mathrm{Tr}\left(B[\rho(\tau)] \frac{\partial \rho(\tau)}{\partial \tau_j} \right) \circ dW_{\mathrm{s}}, \quad (11.7)$$

which we can finally convert to an Itô equation of form

$$d\tau_i = a_i[\tau] dt + b_i[\tau] dW_{\mathrm{s}}. \quad (11.8)$$

For a given choice of system, we can now approximately predict the time evolution of the density operator from (11.3) by integrating the simple low-dimensional equation (11.8) for $d\tau_i$.

11.3 Test of the model reduction method

To test the ability of the reduced models to predict the correct time evolution, we apply it to the bistable system considered in Sec. 8.2. Concretely, we apply the LTSA algorithm to the points (11.1) obtained from the value of the density matrix at times $t = 501\ \gamma_\perp^{-1}$, $t = 502\ \gamma_\perp^{-1}$, …, $t = 2500\ \gamma_\perp^{-1}$ for the trajectory used to compute the results shown in Fig. 8.2, and we choose $k = 60$ as in [133]. As fitting models, we choose various low-dimensional polynomials. A calculation shows that $\hat{a}_i[\tau]$ and $\hat{b}_i[\tau]$ in Eq. (11.8) evaluate to

$$\begin{aligned}
a_i[\tau] = {} & \frac{1}{2} v_1^T f b_i[\tau] + \sum_j (g^{-1})_{ij} \left(\frac{\partial f^T}{\partial \tau_j} M_H f + v_2^T f \frac{\partial f^T}{\partial \tau_j} M_g f \right) \\
& + \frac{1}{2} \sum_j \sum_k (g^{-1})_{ij} \bigg(\frac{\partial^2 f^T}{\partial \tau_k \partial \tau_j} M_1 f + \frac{\partial f^T}{\partial \tau_j} M_1 \frac{\partial f}{\partial \tau_k} - v_1^T \frac{\partial f}{\partial \tau_k} \frac{\partial f^T}{\partial \tau_j} M_g f \\
& - v_1^T f \frac{\partial^2 f^T}{\partial \tau_k \partial \tau_j} M_g f \bigg) b_k[\tau] - \frac{1}{2} \sum_j \sum_k \sum_q (g^{-1})_{ij} \bigg(\frac{\partial^2 f^T}{\partial \tau_k \partial \tau_j} M_g \frac{\partial f}{\partial \tau_q} \\
& + \frac{\partial f^T}{\partial \tau_j} M_g \frac{\partial^2 f}{\partial \tau_k \partial \tau_q} \bigg) b_k[\tau] b_q[\tau]
\end{aligned} \tag{11.9}$$

and

$$b_i[\tau] = \sum_j (g^{-1})_{ij} \left(\frac{\partial f^T}{\partial \tau_j} M_1 f - v_1^T f \frac{\partial f^T}{\partial \tau_j} M_g f \right), \tag{11.10}$$

where the vectors v_1 and v_2 have elements

$$(v_1)_j = -i\sqrt{\kappa}\,\mathrm{Tr}\left(\left(\hat{a}^\dagger e^{i\phi} - \hat{a} e^{-i\phi} \right) c_j \right), \tag{11.11a}$$

$$(v_2)_j = \kappa\,\mathrm{Re}\left(\mathrm{Tr}\left(\left(\hat{a}^\dagger e^{i\phi} - \hat{a} e^{-i\phi} \right) \hat{a} e^{-i\phi} c_j \right) \right), \tag{11.11b}$$

the matrices M_g, M_H, and M_1 have elements

$$(M_g)_{ij} = \mathrm{Tr}(c_i c_j), \tag{11.12a}$$

$$(M_H)_{ij} = 2\,\mathrm{Re}(\mathrm{Tr}(M c_j c_i)) + 2\gamma\,\mathrm{Tr}(\hat{\sigma} c_j \hat{\sigma}^\dagger c_i), \tag{11.12b}$$

$$(M_1)_{ij} = -i\sqrt{\kappa}\,\mathrm{Tr}((c_j \hat{a}^\dagger e^{i\phi} + \hat{a} e^{-i\phi} c_j) c_i), \tag{11.12c}$$

and $M \equiv -iH/\hbar - i(\omega_\mathrm{C} - \omega_\mathrm{L})\hat{a}^\dagger \hat{a} + \sqrt{\kappa}(\beta \hat{a}^\dagger - \beta^* \hat{a}) - \frac{\kappa}{2}\hat{a}^\dagger \hat{a} + \frac{\kappa}{2}\hat{a}^2 e^{-2i\phi} - \gamma \hat{\sigma}^\dagger \hat{\sigma}$.

Since we would like to use the reduced models to predict the state of the system in a feedback scheme, we should check the performance of the reduced models by generating a realistic photocurrent using the full SME and then use that photocurrent to integrate the reduced models, i.e., in each time step

$$dW_{\mathrm{s,reduced}} = \langle \hat{A} + \hat{A}^\dagger \rangle_{\mathrm{full}} dt - \langle \hat{A} + \hat{A}^\dagger \rangle_{\mathrm{reduced}} dt + dW_{\mathrm{s,full}} \tag{11.13}$$

according to (8.11), where $dW_{\mathrm{s,full}}$ is simulated by a random number generator. Results of this procedure are provided in Fig. 11.1. We have plotted $\langle \hat{x} \rangle$ because this is the quantity we need to predict in the feedback scheme considered in the next section. For the case of homodyne detection of the p-quadrature we have used a weighted linear least squares method to compute $\tilde{c}$ in (11.2) to reduce the effect of outliers. The precise initial state of the reduced models is not important because the observed value of the photocurrent quickly drags the reduced model to the correct state, and we have thus chosen $\tau = (0, 0, \ldots, 0)^T$ (the average of $\tau^{(i)}$) for simplicity. In case of instability, we have reset the reduced model to $\tau = (0, 0, \ldots, 0)^T$ whenever the program returned a non-determined value of τ.

The figure shows that simple low-dimensional models are able to provide accurate predictions for the value of $\langle \hat{x} \rangle$ for the case of homodyne detection of the x-quadrature. For homodyne detection of the p-quadrature, the two-dimensional model obtained by using a second order polynomial as fitting model is observed to largely reproduce the time evolution of $\langle \hat{x} \rangle$, but the details differ. In particular, the reduced model does not reproduce the highest values of $\langle \hat{x} \rangle$. To improve the agreement between the full model and the reduced model, one could try to increase the order of the fitting polynomial or use a higher-dimensional model. For a fourth order polynomial in two dimensions, the reduced model is able to reach the highest values of $\langle \hat{x} \rangle$ and the value of $\langle \hat{x} \rangle$ in the LSR is also more accurate, but the model is seen to predict false jumps to the LSR, which is undesirable in a feedback scheme. False jumps are not observed in the figure for the four-dimensional model with a second order polynomial as fitting model, and we thus use this model in the following sections to predict the state of the system. For homodyne detection of the x-quadrature, we also use the four-dimensional model with a second order polynomial as fitting model.

We obtain very accurate results for the case of homodyne detection of the x-quadrature because we use the actual photocurrent obtained from the full SME to drive the reduced models. This means that the back action of the measurement on the system is large whenever the value of $\langle \hat{x} \rangle$ predicted from the reduced model differs significantly from the value obtained from the full SME (as is apparent from (11.13) with $\hat{A} \equiv -ie^{-i\phi}(\beta - \sqrt{\kappa}\hat{a})$). It is, in fact, a much harder test of the performance of the reduced models to check whether they are able to predict the value of quantities that are not related in a simple way to the observed quadrature such as the value of $\langle \hat{x} \rangle$ for homodyne detection of the p-quadrature. The above results thus indicate that the low-dimensional models actually capture most of the dynamics of the system. As expected, we also find that the reduced models for homodyne detection of the p-quadrature provide more accurate results for $\langle \hat{p} \rangle$ than for $\langle \hat{x} \rangle$.

11.4 Application to feedback control

We next add the feedback term (8.18) to the SME to see if we can use the predictions of the reduced models to keep the state of the system within one of the semistable regions. As before, we use the full SME to simulate the measured photocurrent, but we use the reduced model to predict the value of $\langle \hat{x} \rangle$ in (8.18). In a theoretical treatment, we thus need to integrate the full model alongside of the reduced model.

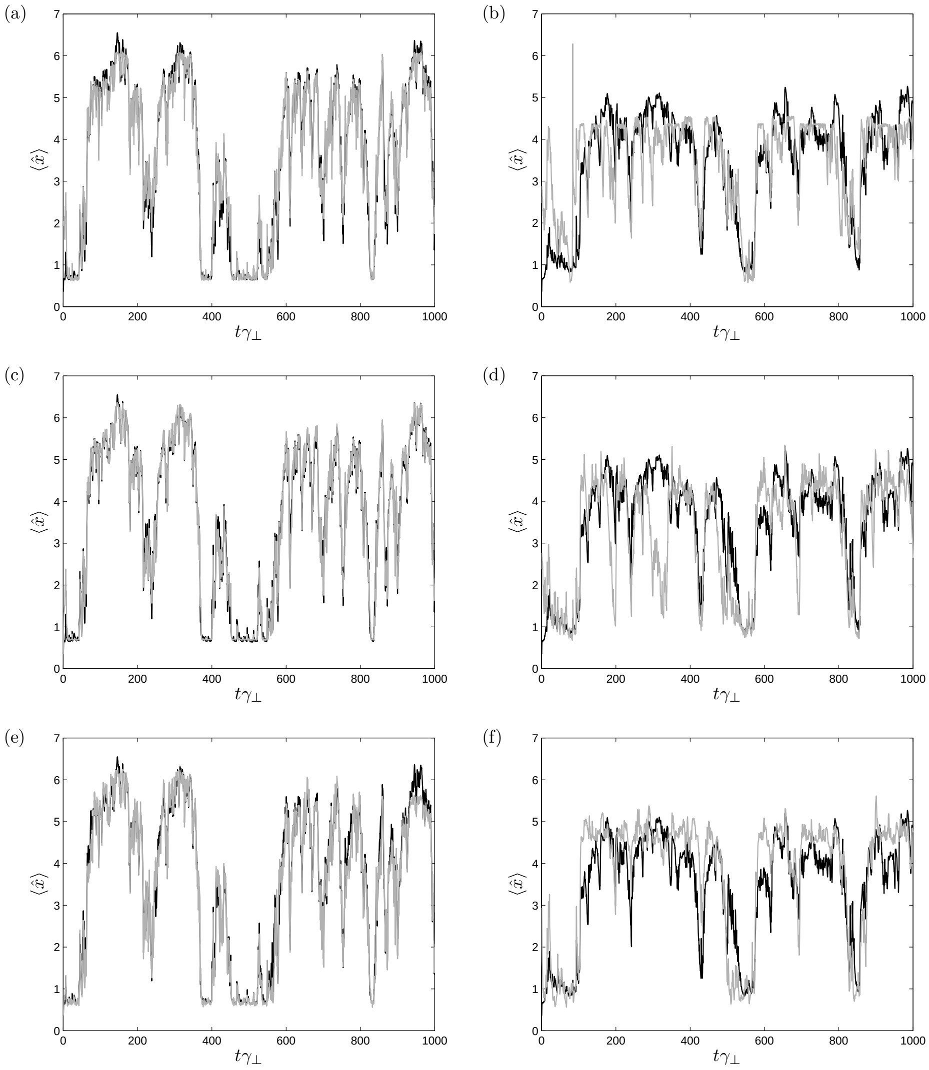

Figure 11.1: Time evolution of $\langle \hat{x} \rangle$ obtained from the full SME (black) and from various reduced models (gray) assuming the same photocurrent. For (a) and (b) the fitting model is a second order polynomial in two dimensions, i.e., $f(\tau) = (1, \tau_1, \tau_2, \tau_1^2, \tau_1\tau_2, \tau_2^2)^T$, for (c) and (d) it is a fourth order polynomial in two dimensions, and for (e) and (f) it is a second order polynomial in four dimensions. The left figures are for homodyne detection of the x-quadrature, and the right figures are for homodyne detection of the p-quadrature.

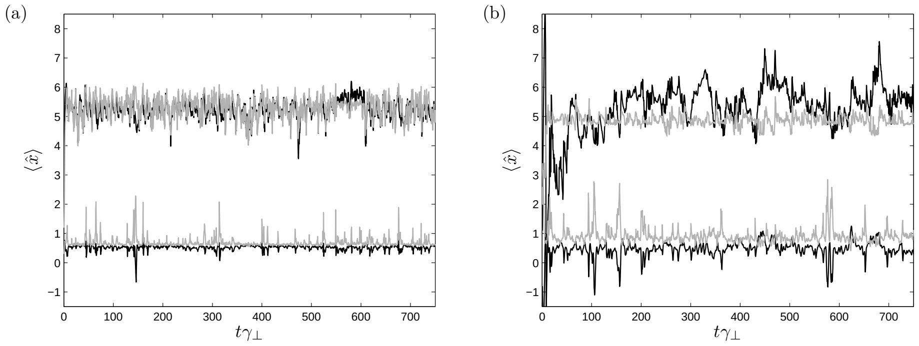

Figure 11.2: Time evolution of $\langle \hat{x} \rangle$ obtained from the full SME (black) and from the reduced model (gray) for (a) homodyne detection of the x-quadrature and (b) homodyne detection of the p-quadrature for the same noise realization as in Fig. 11.1, but with the feedback term in (8.18) included. In (a), $x_0 = 5.37$ and $s_\mathrm{p} = 0.53$ for the upper curves and $x_0 = 0.57$ and $s_\mathrm{p} = 0.71$ for the lower curves, and in (b), $x_0 = 4.95$ and $s_\mathrm{p} = 0.53$ for the upper curves and $x_0 = 0.71$ and $s_\mathrm{p} = 0.71$ for the lower curves (i.e., the same parameters as in Fig. 8.4).

Example trajectories are shown in Fig. 11.2. Comparing these trajectories to those in Fig. 11.1, it is apparent that the feedback term affects the time evolution, and that the system stays close to the USR or the LSR for the considered values of x_0. For the USR, $\langle \hat{x} \rangle$ is seen to fluctuate with a relatively large amplitude, which reflects the fact that the USR is relatively broad as observed in Fig. 8.2. For the LSR, $\langle \hat{x} \rangle$ is roughly constant except for sudden spikes. By choosing a value of x_0, which is slightly below the average value of $\langle \hat{x} \rangle$ predicted by the reduced model, we can ensure that the feedback term almost always acts to decrease $\langle \hat{x} \rangle$. This keeps the full model away from the transition region, and as seen in the figure the spikes tend to point towards negative values of $\langle \hat{x} \rangle$ rather than towards larger positive values of $\langle \hat{x} \rangle$ as observed for higher values of x_0.

For the case of homodyne detection of the p-quadrature, we note that the predictions of the reduced model for $x_0 = 4.95$ fluctuate less than the results obtained from the full SME, while the fluctuations of the full and the reduced model are approximately the same for the case of homodyne detection of the x-quadrature. This is because we use the reduced model to evaluate the error $e(t)$, which means that the feedback term always acts to reduce $e(t)$ for the low-dimensional model. For the full model, on the other hand, $e(t)$ may have the opposite sign, in which case the full model is pushed away from x_0. The resulting change in the photocurrent drives the reduced model in the same direction as the full model, but this latter mechanism is more efficient in the case of homodyne detection of the x-quadrature than for homodyne detection of the p-quadrature.

The used values of the strength $s_{\rm p}$ of the feedback have been chosen to be sufficiently large to affect the dynamics, but sufficiently small to avoid instabilities. Discrepancies between the full model and the reduced model lead to a feedback of noise into the system, so even though a large value of s_p may reduce the variance of $e(t)$ for the low-dimensional model, we observe that the predictions for $\langle\hat{x}\rangle$ obtained from the full model fluctuate over a range that is broader than the distance between the USR and the LSR if s_p is chosen too large. The effects of the added noise can be inferred by comparing Figs. 8.4 and 11.2 (which are computed for different noise realizations). The fluctuations of the trajectories in Fig. 11.2 are seen to be comparable to or larger than for the trajectories in Fig. 8.4. For homodyne detection of the x-quadrature, the standard deviation $\sigma_{\rm s}(\langle\hat{x}\rangle_{\rm full})$ of $\langle\hat{x}\rangle_{\rm full}$ ($\langle\hat{x}\rangle$ obtained from the full model) for the points in the time interval from $t = 100\ \gamma_\perp^{-1}$ to $t = 750\ \gamma_\perp^{-1}$ changes from 0.28 to 0.33 for the upper curves and from 0.09 to 0.09 for the lower curves when we use the reduced model rather than the full model to compute the feedback. For homodyne detection of the p-quadrature, $\sigma_{\rm s}(\langle\hat{x}\rangle_{\rm full})$ changes from 0.16 to 0.56 for the upper curves and from 0.10 to 0.27 for the lower curves.

Integral feedback

The power spectrum of the time evolution of $\langle\hat{x}\rangle$ predicted by the full model and the power spectrum of the difference between the predictions of the reduced model and the full model for the case of homodyne detection of the p-quadrature show that the relative error of the reduced model in predicting $\langle\hat{x}\rangle$ is smaller at low frequencies. This appears because the reduced model is able to predict quantum jumps of the system but does not capture the details of the dynamics in the semistable regions, and it suggests that it might be an advantage to mainly feed back the low frequency behavior, which can be achieved by adding an integral term to the controller

$$d\rho_{\rm fb}(t) = \left(s_{\rm p}e(t) + s_{\rm i}\int_0^t \exp\left(-\zeta(t-t')\right)e(t')dt'\right)[\hat{a}-\hat{a}^\dagger,\rho(t)]\gamma_\perp dt, \tag{11.14}$$

where $s_{\rm i}$ and ζ are constants. We find, however, that even though the standard deviation of the difference between the predictions of the full model and the reduced model relative to the standard deviation of the predictions of the full model tends to decrease when we use integral feedback, the standard deviation of the results obtained from the full model are typically increased because the integral term is less efficient in keeping $\langle\hat{x}\rangle$ close to the desired value. For the examples shown in Fig. 11.3, for instance, we find that $\sigma_{\rm s}(\langle\hat{x}\rangle_{\rm full}-\langle\hat{x}\rangle_{\rm reduced})/\sigma_{\rm s}(\langle\hat{x}\rangle_{\rm full})$ for the time interval from $t = 100\ \gamma_\perp^{-1}$ to $t = 750\ \gamma_\perp^{-1}$ for the USR is reduced from 0.71 to 0.46 for homodyne detection of the x-quadrature and from 1.01 to 0.82 for homodyne detection of the p-quadrature compared to the results in Fig. 11.2. $\sigma_{\rm s}(\langle\hat{x}\rangle_{\rm full})$,

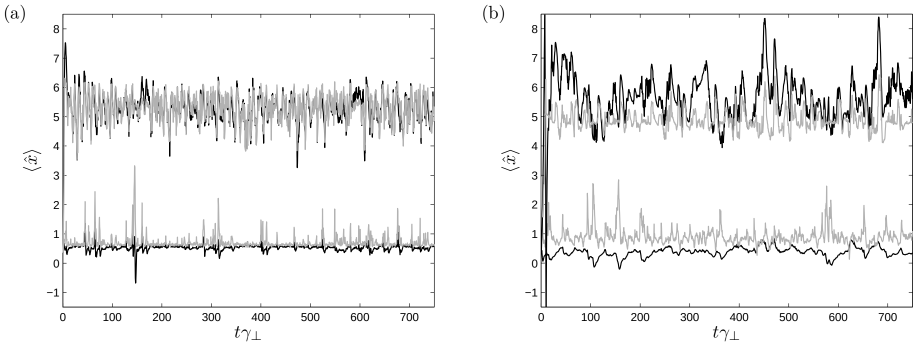

Figure 11.3: Time evolution of $\langle\hat{x}\rangle$ obtained from the full SME (black) and from the reduced model (gray) for (a) homodyne detection of the x-quadrature and (b) homodyne detection of the p-quadrature for the same noise realization as in Fig. 11.1, but with the feedback term in (11.14) included. The parameters are $s_\mathrm{p} = 0$, $s_\mathrm{i} = 0.51\ \gamma_\perp$, and $\zeta = 2\pi \times 0.1\ \gamma_\perp$ in (a) and $s_\mathrm{p} = 0$, $s_\mathrm{i} = 0.15\ \gamma_\perp$, and $\zeta = 2\pi \times 0.02\ \gamma_\perp$ in (b), while the values of x_0 are the same as in Fig. 11.2.

on the other hand, is increased from 0.33 to 0.46 for homodyne detection of the x-quadrature and from 0.56 to 0.70 for homodyne detection of the p-quadrature. For the LSR, the fluctuations of $\langle\hat{x}\rangle_\mathrm{full} - \langle\hat{x}\rangle_\mathrm{reduced}$ relative to the fluctuations of $\langle\hat{x}\rangle_\mathrm{full}$ also decrease, and for homodyne detection of the p-quadrature there is a decrease in $\sigma_\mathrm{s}(\langle\hat{x}\rangle_\mathrm{full})$ compared to Fig. 11.2(b).

11.5 Conclusion

We have shown that it is possible to derive simple low-dimensional models for the dynamics of a single atom interacting with a cavity field mode in the absorptive bistable regime, and we have demonstrated that the models can be used in a feedback scheme, which is able to hold the system within one of the semistable regions. This is an important result because it is unrealistic to integrate the full stochastic master equation in real time.

The suggested feedback scheme relies on predictions of the expectation value of the x-quadrature of the cavity field, and we have considered both the case of homodyne detection of the x-quadrature of the output field from the cavity and homodyne detection of the p-quadrature. The former case is relatively easy to handle because the estimated quantity is directly related to the observed quantity. For homodyne detection of the p-quadrature, on the other hand, the expectation value of the x-quadrature has to be inferred from the precise dynamics of the p-quadrature, and the reduced model has to do significantly more work. It is thus promising for the method that we also obtain reasonable results in this case.

There are many degrees of freedom in the modeling procedure, for instance the sampling of the points used to compute the low-dimensional manifold, the choice of transformation between density operators and vectors in the m-dimensional space, and the choice of fitting model. This leaves possibilities to optimize the reduced model depending on the purpose of the model, and it would be useful to develop general guidelines for the optimization. In a feedback scheme, one should concentrate on optimizing the ability of the reduced model to predict the quantity that determines the feedback since errors in this quantity lead to a feedback of noise into the system, which limits the performance of the feedback.

Chapter 12

Conditional preparation of collective atomic spin states

Having explored various properties of the dynamics of a single atom in a cavity, we now turn to probing of atomic ensembles in cavities. As in Chaps. 9 and 10, we consider atoms with two ground state levels, which we treat as a spin-1/2 system. Denoting the spin vector operator of the ith atom by $\hat{\mathbf{j}}_i$, we define the collective spin vector $\hat{\mathbf{J}} = (\hat{J}_x, \hat{J}_y, \hat{J}_z)$ by $\hat{\mathbf{J}} = \sum_i \hat{\mathbf{j}}_i$. In [VIII], we show how probing can be used for conditionally preparing a state, which is a superposition of two states with very different values of $\langle \hat{J}_z \rangle$, and we investigate the possibility to use CW squeezed light rather than a continuous coherent state to probe the state of the atoms.

In the present chapter, we contribute to the very active research field of preparation of squeezed spin states. The typical starting point is the coherent spin state $((|{\downarrow}\rangle + |{\uparrow}\rangle)/\sqrt{2})^{N_{\mathrm{at}}}$ with all N_{at} atoms in the spin up state with respect to the x-axis. Such a state can be prepared experimentally by pumping the atoms to the spin down state (with respect to the z-axis) and then applying a radio frequency $\pi/2$-pulse between the two ground state levels. When the number of atoms is sufficiently large and we are not too far away from the above coherent spin state, we can treat the x-component of the spin classically, $\hat{J}_x \approx \langle \hat{J}_x \rangle$. The spin commutator relation $[\hat{J}_y, \hat{J}_z] = i\hbar \hat{J}_x$ then turns into the canonical commutator $[\hat{x}_{\mathrm{at}}, \hat{p}_{\mathrm{at}}] = i$ between the scaled spin components $\hat{x}_{\mathrm{at}} = \hat{J}_y/(\hbar\langle \hat{J}_x \rangle)^{1/2}$ and $\hat{p}_{\mathrm{at}} = \hat{J}_z/(\hbar\langle \hat{J}_x \rangle)^{1/2}$. The coherent spin state has $\mathrm{var}(\hat{x}_{\mathrm{at}}) = \mathrm{var}(\hat{p}_{\mathrm{at}}) = 1/2$, which fulfils Heisenberg's uncertainty relation with an equality sign, and in analogy to light fields, we can obtain a squeezed spin state by reducing the variance of $\hat{p}_{\mathrm{at}}$ at the expense of an increased variance of $\hat{x}_{\mathrm{at}}$. More generally, the criterion for spin squeezing may be defined as $\mathrm{var}(\hat{J}_\perp)/(\hbar|\langle \hat{\mathbf{J}} \rangle|) < 1/2$ [186], where $\hat{J}_\perp$ is the spin vector component orthogonal to $\langle \hat{\mathbf{J}} \rangle$, which has the smallest variance. One also often considers the metrologically relevant squeezing parameter $\xi \equiv (N_{\mathrm{at}}\,\mathrm{var}(\hat{J}_\perp))^{1/2}/|\langle \hat{\mathbf{J}} \rangle|$. This parameter is relevant, because squeezed spin states, besides their fundamental interest, have practical applications within precision measurements of, for instance, frequencies [14] and weak magnetic fields [187], and in this connection ξ quantifies the improvements one can obtain by using a squeezed spin state with $\xi < 1$ rather than, for instance, a coherent spin state with $\xi = 1$ in the measurement process [186] (see also [188] for a different measure and [189] for a related discussion of polarization squeezing of light).

Reduction in the variance of $\hat{J}_z$ can be obtained via probing. The probing may consist in a QND measurement, in which the atoms interact with an off-resonant probe, which is subsequently detected [190, 191]. Specifically, we here consider Faraday rotation, where the light-atom interaction rotates the polarization direction of a linearly polarized probe field by an amount, which is proportional to $\hat{J}_z$, and the rotation angle is measured in a polarization rotation measurement, which is closely related to balanced homodyne detection. We note that such procedures lead to conditional squeezing because we need to know the measurement outcome to reduce the variance of $\hat{J}_z$, but unconditional squeezing can be obtained by combining the measurement with feedback [178].

Conditional measurements have recently been utilized to demonstrate metrologically relevant spin squeezing of 3.4 dB [192] and 3.0 dB [193] in atomic ensembles. Squeezed spin states can also be produced by applying a Hamiltonian, which is nonlinear in the atomic spin operators as proposed in [194]. The challenge is to construct such Hamiltonians. A common strategy in this direction is to use coherent feedback, where an output from the system is fed back into the system without being measured. Such a scheme has been demonstrated very recently in [195], where 5.6 dB of metrologically relevant, unconditional squeezing has been achieved. Interactions between atoms in a Bose-Einstein condensate provide another method to obtain spin squeezing [196] and 3.8 dB of metrologically relevant spin squeezing in Bose-Einstein condensates has been observed recently in [197]. Spin squeezing via transfer of a squeezed state of light to atoms is also a possibility [198].

The experiments involving interactions between light and atomic ensembles are particularly interesting because such interactions are extremely useful within quantum information processing and communication. Some of the goals achieved so far include entanglement of distant atomic ensembles [199, 200], quantum memory [68], and teleportation [13]. Numerous theoretical papers have been written within the field, of which [201, 202, 203] are particularly relevant for our purposes. Our contribution is an investigation of the performance of conditional spin squeezing in a cavity relative to single-pass spin squeezing, where the probe field interacts only once with the atoms as in [202]. The above mentioned papers exploit the fact that a Gaussian description can be applied, and it is then sufficient to consider the time evolution of the vector of mean values and the covariance matrix, which is a significant simplification. Although we shall mainly be concerned with the Gaussian limit below, we start from the SME, which allows us to derive generally applicable analytical results for the dynamics in the limit, where spontaneous emission is negligible. We also consider the dynamics, when spontaneous emission is included. As argued in [203], it is still possible to approximately describe the system dynamics within the Gaussian description in this case, and below we provide an alternative way to derive the time evolution equations, which emerge from the approach in [201, 202, 203].

The chapter, which is based on publication [VII][1], is structured as follows. In Sec. 12.1, we provide more details on the setup and solve the relevant SME for spin squeezing in a cavity, neglecting spontaneous emission. In Sec. 12.2, we evaluate the variances and mean values of the collective atomic spin operators and the quadrature operators of the cavity field as a function of time in the Gaussian limit to determine the rate of squeezing. Effects of losses due to spontaneous emission are considered in Sec. 12.3.

12.1 Faraday rotation and atomic spin squeezing in a cavity

The considered experimental setup is illustrated in Fig. 12.1. We decompose the cavity field into right and left circularly polarized light with annihilation operators $\hat{a}_\pm = (\mp\hat{a}_x + i\hat{a}_y)/\sqrt{2}$, where $\hat{a}_x$ ($\hat{a}_y$) is the annihilation operator of the cavity field linearly polarized in the x-direction (y-direction). The field represented by $\hat{a}_+$ ($\hat{a}_-$) couples the ground state level $|g_{-,i}\rangle$ ($|g_{+,i}\rangle$) of the ith atom, $i = 1, 2, \ldots, N_{\mathrm{at}}$, off-resonantly to the excited level $|e_{+,i}\rangle$ ($|e_{-,i}\rangle$) as shown in the inset, and we do not consider spontaneous emission in this section. Due to the large detuning, the excited states never become significantly populated, but the interaction changes the phase of the light field by an amount, which is proportional to the number of atoms in the state $|g_-\rangle$ ($|g_+\rangle$). The relative phase shift between the two circularly polarized components is thus proportional to the difference in population of the two ground state levels and hence to $\hat{J}_z$. In the basis of linearly x- and y-polarized light, this relative phase shift translates into a (small) rotation of the polarization direction. Starting from a large amplitude coherent state linearly polarized in the x-direction, the rotation displaces the y-polarized field away from the vacuum state in phase space. If the amplitude of the probe field is real, the resulting amplitude of the y-polarized field is also real, and it is thus possible to indirectly measure $\hat{J}_z$ by measuring the x-quadrature of the y-polarized field leaking out of the cavity. This is accomplished via the polarization rotation measurement, which is effectively a balanced homodyne detection with the x-polarized field acting as the local oscillator.

---

[1] Copyright (2008) by the American Physical Society.

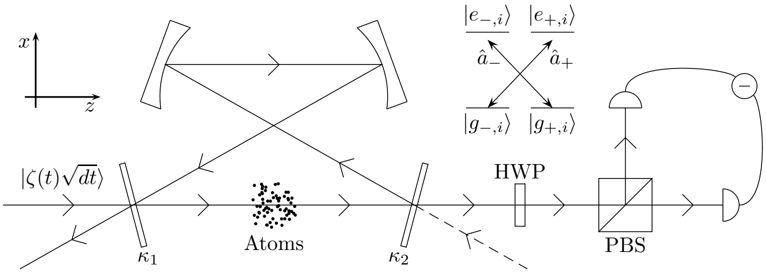

Figure 12.1: Experimental setup for probing the z-component $\hat{J}_z$ of the collective spin vector of an atomic ensemble in a cavity with a continuous wave light field. A laser beam on resonance with the cavity, propagating in the positive z-direction, linearly polarized in the x-direction, and with large amplitude $\zeta(t)$, enters the cavity from the left. The interaction between the light and the atoms rotates the polarization vector of the light field by an amount, which is proportional to $\hat{J}_z$. The angle of rotation is measured by performing a polarization rotation measurement of the light leaking out of the cavity. The HWP transforms the field operators $\hat{b}_x$ and $\hat{b}_y$ of x- and y-polarized light hitting the HWP into $(\hat{b}_x+\hat{b}_y)/\sqrt{2}$ and $(\hat{b}_x-\hat{b}_y)/\sqrt{2}$, and these polarization components are subsequently separated by the PBS. The measurement outcome is the difference in photocurrent between the two photodetectors. The level structure of the ith atom and the interaction with the cavity field are illustrated in the inset, where $\hat{a}_\pm$ are the annihilation operators of right and left circularly polarized light in the cavity.

Stochastic master equation

Turning to a quantitative description, we can represent the light-atom interaction in a frame rotating with the angular frequency of the relevant cavity resonance (which is also the angular frequency of the probe light) by the Hamiltonian

$$H = \hbar g \sum_{i=1}^{N_{\mathrm{at}}} \Big(\hat{a}_+ |e_{+,i}\rangle\langle g_{-,i}| + \hat{a}_+^\dagger |g_{-,i}\rangle\langle e_{+,i}| + \hat{a}_- |e_{-,i}\rangle\langle g_{+,i}| \\ + \hat{a}_-^\dagger |g_{+,i}\rangle\langle e_{-,i}| \Big) + \hbar\Delta \sum_{i=1}^{N_{\mathrm{at}}} \left(|e_{+,i}\rangle\langle e_{+,i}| + |e_{-,i}\rangle\langle e_{-,i}| \right). \quad (12.1)$$

For simplicity, we assume that the mode function of the cavity modes is constant within a volume V_{mode} and zero otherwise such that $\hbar g = -\mathbf{d}_{ge} \cdot \mathbf{e}_\pm \sqrt{\hbar\omega_{\mathrm{C}}/(2\epsilon_0 V_{\mathrm{mode}})}$ (see Sec. 8.2) for all the atoms, where $\mathbf{e}_\pm = (\mp\mathbf{e}_x - i\mathbf{e}_y)/\sqrt{2}$ [204] are the unit vectors determining the polarization direction ($\mathbf{e}_x$ and $\mathbf{e}_y$ are unit vectors in the x-direction and in the y-direction, respectively).

For sufficiently large detuning, $g^2|\langle\hat{a}_\pm\rangle|^2/\Delta^2 \ll 1$, we can eliminate the excited states adiabatically to obtain the effective Hamiltonian

$$H = -\frac{\hbar g^2}{\Delta}\sum_{i=1}^{N_{\mathrm{at}}}\left(\hat{a}_+^\dagger\hat{a}_+|g_{-,i}\rangle\langle g_{-,i}| + \hat{a}_-^\dagger\hat{a}_-|g_{+,i}\rangle\langle g_{+,i}|\right) \tag{12.2a}$$

$$= -\frac{\hbar g^2}{\Delta}\frac{N_{\mathrm{at}}}{2}(\hat{a}_x^\dagger\hat{a}_x + \hat{a}_y^\dagger\hat{a}_y) - i\frac{\hbar g^2}{\Delta}\left(\hat{a}_x^\dagger\hat{a}_y - \hat{a}_y^\dagger\hat{a}_x\right)\frac{\hat{J}_z}{\hbar}, \tag{12.2b}$$

where we have used the relation $\sum_i |g_{\pm,i}\rangle\langle g_{\pm,i}| = N_{\mathrm{at}}/2 \pm \hat{J}_z/\hbar$ to obtain the last expression. The first term in (12.2b) gives rise to a common phase shift of the x- and y-polarized light fields and can be compensated by introducing an additional phase shift in the cavity, for instance by adjusting the length of the cavity. We thus ignore this term in the following.

Assuming an only infinitesimal change of the atomic quantum state on the timescale of the round trip time τ of light in the cavity and a high finesse cavity $\kappa\tau \ll 1$, where κ is the total cavity decay rate, we can refer back to Chap. 8 to derive the linear SME

$$\begin{aligned} d\rho(t) = {} & -\frac{i}{\hbar}\left[H,\rho(t)\right]dt + \sqrt{\kappa_1}\zeta(t)[\hat{a}_x^\dagger,\rho(t)]dt - \sqrt{\kappa_1}\zeta^*(t)[\hat{a}_x,\rho(t)]dt \\ & + \sqrt{\eta_{\mathrm{d}}\kappa_2}\left(\hat{a}_y\rho(t) + \rho(t)\hat{a}_y^\dagger\right)dy_{\mathrm{s}} + \mathcal{D}[\sqrt{\kappa}\hat{a}_y]\rho(t)dt + \mathcal{D}[\sqrt{\kappa}\hat{a}_x]\rho(t)dt \end{aligned} \tag{12.3}$$

for the setup in Fig. 12.1. Here, the density operator $\rho(t)$ represents the state of the atoms and the x- and y-polarized cavity fields,

$$\mathcal{D}[\hat{O}]\rho(t) \equiv \hat{O}\rho(t)\hat{O}^\dagger - (\hat{O}^\dagger\hat{O}\rho(t) + \rho(t)\hat{O}^\dagger\hat{O})/2, \tag{12.4}$$

κ_1 (κ_2) is the contribution to $\kappa = \kappa_1 + \kappa_2 + \kappa_{\mathrm{L}}$ from transmission through the lower left (right) cavity mirror in Fig. 12.1, κ_{L} is the contribution to the cavity decay rate from intracavity losses, $\zeta(t)$ is the amplitude of the incoming probe beam, and η_{d} is the efficiency of the photodetectors.

Solution of the linear stochastic master equation

Since the Hamiltonian (12.2b) commutes with $\hat{\boldsymbol{J}}^2$, we can restrict ourselves to the basis consisting of the states with total spin quantum number $J = N_{\mathrm{at}}/2$ if the initial state is a coherent spin state. We thus consider the states $\hat{J}_z|n\rangle = \hbar n|n\rangle$ with $n = -N_{\mathrm{at}}/2, -N_{\mathrm{at}}/2+1, \ldots, N_{\mathrm{at}}/2$, and write the density matrix as

$$\rho(t) = \sum_n\sum_m \rho_{nm}(t)|n\rangle\langle m|, \tag{12.5}$$

where $\rho_{nm}(t)$ are operators on the space of the x- and y-polarized cavity field modes.[2] Substituting (12.5) into (12.3) leads to the $(N_{\mathrm{at}}+1)^2$ independent

---

[2] The general case of all simultaneous eigenstates of $\hat{\boldsymbol{J}}^2$ and $\hat{J}_z$ is handled simply by including more terms on the right hand side of (12.5).

equations

$$\begin{aligned} d\rho_{nm}(t) = & -\frac{g^2}{\Delta} n(\hat{a}_x^\dagger \hat{a}_y - \hat{a}_y^\dagger \hat{a}_x)\rho_{nm}(t)dt + \frac{g^2}{\Delta} m\rho_{nm}(t)(\hat{a}_x^\dagger \hat{a}_y - \hat{a}_y^\dagger \hat{a}_x)dt \\ & + \sqrt{\kappa_1}\zeta(t)[\hat{a}_x^\dagger, \rho_{nm}(t)]dt - \sqrt{\kappa_1}\zeta^*(t)[\hat{a}_x, \rho_{nm}(t)]dt + \mathcal{D}[\sqrt{\kappa}\hat{a}_x]\rho_{nm}(t)dt \\ & + \mathcal{D}[\sqrt{\kappa}\hat{a}_y]\rho_{nm}(t)dt + \sqrt{\eta_{\mathrm{d}}\kappa_2}(\hat{a}_y\rho_{nm}(t) + \rho_{nm}(t)\hat{a}_y^\dagger)dy_{\mathrm{s}}. \end{aligned} \tag{12.6}$$

When the cavity fields are in the vacuum state at time $t = 0$, we can write the solution as

$$\rho_{nm}(t) = C_{nm}(t)|\xi_n(t)\rangle_x\langle\xi_m(t)| \otimes |\alpha_n(t)\rangle_y\langle\alpha_m(t)|, \tag{12.7}$$

where $|\xi_n(t)\rangle$ and $|\alpha_n(t)\rangle$ are coherent states of the x- and y-polarized cavity fields, respectively, with amplitudes fulfilling

$$\frac{d\xi_n(t)}{dt} = -\frac{\kappa}{2}\xi_n(t) - n\frac{g^2}{\Delta}\alpha_n(t) + \sqrt{\kappa_1}\zeta(t), \tag{12.8a}$$

$$\frac{d\alpha_n(t)}{dt} = -\frac{\kappa}{2}\alpha_n(t) + n\frac{g^2}{\Delta}\xi_n(t). \tag{12.8b}$$

For $\zeta(t) = \zeta^*(t)$, we thus have

$$\xi_n(t) = \sqrt{\kappa_1}\int_0^t e^{-\frac{\kappa}{2}(t-t')}\cos\left(\frac{ng^2}{\Delta}(t-t')\right)\zeta(t')dt', \tag{12.9a}$$

$$\alpha_n(t) = \sqrt{\kappa_1}\int_0^t e^{-\frac{\kappa}{2}(t-t')}\sin\left(\frac{ng^2}{\Delta}(t-t')\right)\zeta(t')dt', \tag{12.9b}$$

which simplify to

$$\xi_n(t) = \sqrt{\kappa_1}\int_0^t e^{-\frac{\kappa}{2}(t-t')}\zeta(t')dt' = \langle\hat{a}_x\rangle, \tag{12.10a}$$

$$\alpha_n(t) = \frac{ng^2}{\Delta}\sqrt{\kappa_1}\int_0^t (t-t')e^{-\frac{\kappa}{2}(t-t')}\zeta(t')dt' \equiv n\alpha(t), \tag{12.10b}$$

for a small polarization rotation angle, i.e., $2ng^2/(\kappa\Delta) \ll 1$. Under these conditions the coefficients $C_{nm}(t)$ in (12.7) fulfil

$$\frac{dC_{nm}(t)}{C_{nm}(t)} = \sqrt{\eta_{\mathrm{d}}\kappa_2}(n+m)\alpha(t)dy_{\mathrm{s}} - \frac{\kappa}{2}(n-m)^2\alpha(t)^2dt \tag{12.11}$$

with solution

$$\begin{aligned} C_{nm}(t) = C_{nm}(0)\exp\biggl(& -\frac{\kappa}{2}(n-m)^2\int_0^t \alpha(t')^2dt' \\ & + \sqrt{\eta_{\mathrm{d}}\kappa_2}(n+m)\int_0^t \alpha(t')dy_{\mathrm{s}}' - \frac{\eta_{\mathrm{d}}\kappa_2}{2}(n+m)^2\int_0^t \alpha(t')^2dt'\biggr). \end{aligned} \tag{12.12}$$

As in Chap. 9, we observe that the coherent state amplitudes $\xi_n(t)$ and $\alpha_n(t)$ evolve deterministically, while the coefficients $C_{nm}(t)$ depend on the measurement results. For the special case of a pump field with constant amplitude ζ for $t > 0$, $\langle \hat{a}_x(t) \rangle$ and $\alpha(t)$ decay at a rate $\kappa/2$ towards their respective steady state values

$$\langle \hat{a}_x \rangle = \frac{2\sqrt{\kappa_1}\zeta}{\kappa} \quad \text{and} \quad \alpha = \frac{2g^2}{\kappa\Delta}\langle \hat{a}_x \rangle. \tag{12.13}$$

We obtain the probability distribution

$$P_S = \sum_n \frac{C_{nn}(0)}{\sqrt{8\pi\eta_{\mathrm{d}}\kappa_2 \int_0^t \alpha(t')^2 dt'}} \exp\left(-\frac{(S - 4n\eta_{\mathrm{d}}\kappa_2 \int_0^t \alpha(t')^2 dt')^2}{8\eta_{\mathrm{d}}\kappa_2 \int_0^t \alpha(t')^2 dt'} \right) \tag{12.14}$$

for the stochastic variable $S \equiv 2\sqrt{\eta_{\mathrm{d}}\kappa_2}\int_0^t \alpha(t') dy_{\mathrm{s}}'$ from (8.15) by integrating over all realizations of the measurement records that lead to the same value of S at time t. We note that P_S is a sum of $N_{\mathrm{at}}+1$ Gaussians with mean values $4n\eta_{\mathrm{d}}\kappa_2 \int_0^t \alpha(t')^2 dt'$ and standard deviation $(4\eta_{\mathrm{d}}\kappa_2 \int_0^t \alpha(t')^2 dt')^{1/2}$. The Gaussians corresponding to neighboring values of n thus begin to separate when $\eta_{\mathrm{d}}\kappa_2 \int_0^t \alpha(t')^2 dt' \sim (\eta_{\mathrm{d}}\kappa_2 \int_0^t \alpha(t')^2 dt')^{1/2}$. As far as spin squeezing is concerned, we are interested in probing times much shorter than this, but for illustrative purposes we show the gradual projection onto eigenstates of $\hat{J}_z$ for $N_{\mathrm{at}} = 4$ in Fig. 12.2.

12.2 Time evolution of expectation values in the Gaussian limit

Having obtained the state of the atoms and the x- and y-polarized cavity fields as a function of time, we can now evaluate mean values and variances of the atomic spin operators and the field quadrature operators $\hat{x}_{\mathrm{ph}} = (\hat{a}_y + \hat{a}_y^\dagger)/\sqrt{2}$ and $\hat{p}_{\mathrm{ph}} = -i(\hat{a}_y - \hat{a}_y^\dagger)/\sqrt{2}$ of the y-polarized cavity field. We assume in the following that $N_{\mathrm{at}} \gg 1$, and the initial state of the atoms is taken to be a coherent spin state with $\langle \hat{\mathbf{J}} \rangle$ pointing in the x-direction. As mentioned above, this is a typical experimental situation, and it allows us to simplify the obtained expressions considerably. In order to stay within the parameter regime, where the Gaussian approximation is valid, it is also required that the total measurement time is very short compared to the time it takes to collapse the state of the atoms onto a single eigenstate of $\hat{J}_z$ due to the measurement. More precisely, we assume that $4\eta_{\mathrm{d}}\kappa_2 \int_0^t \alpha(t')^2 dt'$ is of order N_{at}^{-1} or smaller, while $2\sqrt{\eta_{\mathrm{d}}\kappa_2}\int_0^t \alpha(t') d\hat{y}_{\mathrm{s}}'$ is of order $N_{\mathrm{at}}^{-1/2}$ or smaller. We note that the results derived below can also be obtained by assuming right from the start that the state of the atoms and the y-polarized cavity field is represented by a Gaussian Wigner function of the quadrature variables

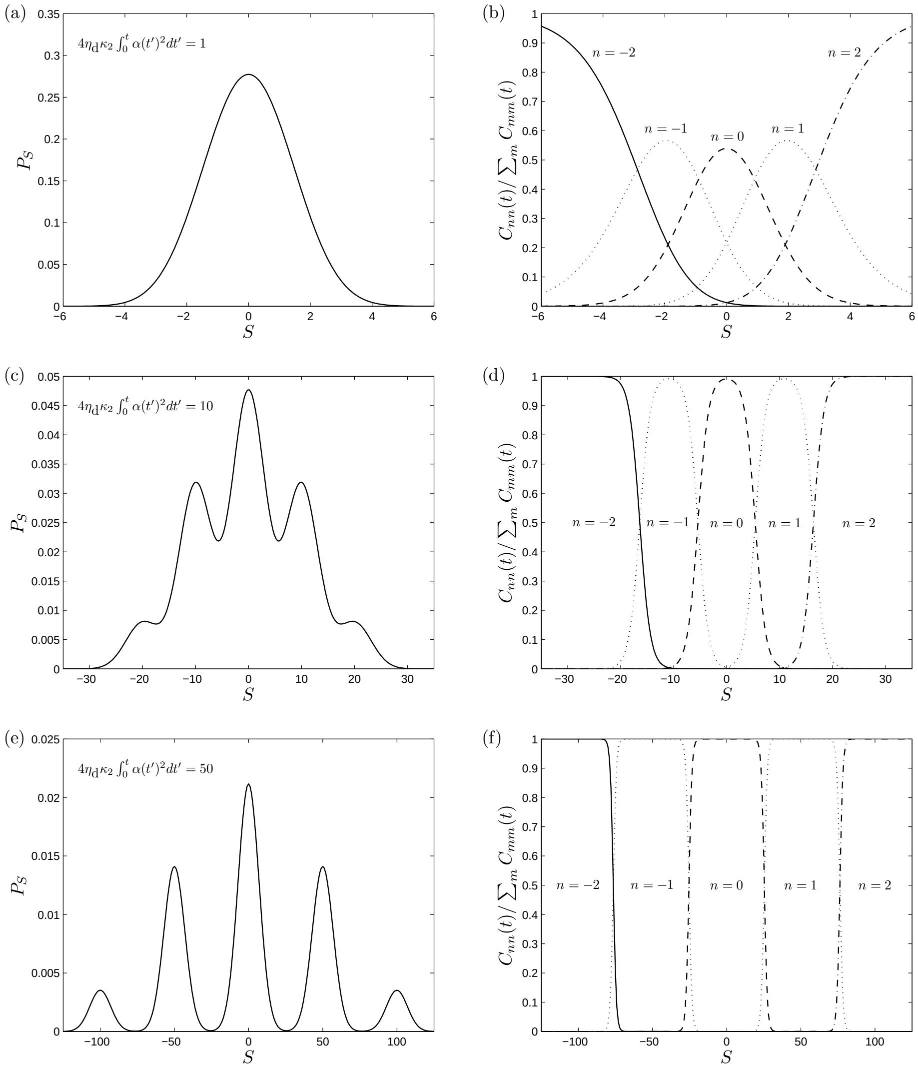

Figure 12.2: Measurement induced collapse onto eigenstates of $\hat{J}_z$. The left plots show the probability density P_S to measure a given value of $S \equiv 2\sqrt{\eta_d\kappa_2}\int_0^t \alpha(t')dy'_s$, and the right plots show the fidelity between $\rho(t)$ and the $\hat{J}_z$ eigenstates $|n\rangle$ after tracing out the cavity fields. $N_{at} = 4$, $C_{00}(0) = 3/8$, $C_{11}(0) = C_{-1-1}(0) = 1/4$, and $C_{22}(0) = C_{-2-2}(0) = 1/16$. The dimensionless, effective probing time $4\eta_d\kappa_2\int_0^t \alpha(t')^2 dt'$ is 1 for the upper plots, 10 for the middle plots, and 50 for the lower plots. The left plots show how the Gaussians in (12.14) gradually separate into distinct peaks because the separation between the Gaussians increases faster than the width of the Gaussians, and the right plots show how the fidelity with a given $|n\rangle$ evolves into a function, which is unity for an interval of values of S and zero otherwise.

x_{at}, p_{at}, x_{ph}, and p_{ph}. One can then derive time evolution equations for the covariance matrix and the vector of mean values by rewriting the SME into an equation for the Wigner function. See [VII] for details.

Variances

First, we would like to determine whether the atomic spin is indeed squeezed, and we thus trace out the cavity fields and compute the variance of $\hat{J}_z/\hbar$,

$$\mathrm{var}\left(\hat{J}_z/\hbar\right) = \frac{\sum_n n^2 C_{nn}(t)}{\sum_n C_{nn}(t)} - \left(\frac{\sum_n n C_{nn}(t)}{\sum_n C_{nn}(t)}\right)^2 . \tag{12.15}$$

For a coherent spin state with $\langle \hat{\mathbf{J}} \rangle$ pointing in the x-direction, we have

$$\begin{aligned} C_{nm}(0) &= \frac{1}{2^{N_{\mathrm{at}}}} \sqrt{\frac{N_{\mathrm{at}}!}{(N_{\mathrm{at}}/2+n)!(N_{\mathrm{at}}/2-n)!}} \sqrt{\frac{N_{\mathrm{at}}!}{(N_{\mathrm{at}}/2+m)!(N_{\mathrm{at}}/2-m)!}} \\ &\approx \sqrt{\frac{2}{\pi N_{\mathrm{at}}}} \exp\left(-\frac{n^2+m^2}{N_{\mathrm{at}}}\right), \end{aligned} \tag{12.16}$$

and combining (12.12), (12.15), and (12.16), we find

$$\frac{\mathrm{var}\left(\hat{J}_z/\hbar\right)}{N_{\mathrm{at}}/2} = \frac{1}{2}\left(1 + N_{\mathrm{at}}\eta_{\mathrm{d}}\kappa_2 \int_0^t \alpha(t')^2 dt'\right)^{-1} . \tag{12.17}$$

Remarkably, this result does not depend on the measurement readout and is thus deterministic. To lowest order in $N_{\mathrm{at}}^{-1/2}$, the expectation value of the spin vector still points in the x-direction and has magnitude $\hbar N_{\mathrm{at}}/2$. The decrease of the right hand side of (12.17) below 1/2 thus shows that the atomic spin is squeezed for probing times larger than zero if $\eta_{\mathrm{d}} > 0$. If we average over all possible measurement outcomes by setting $\eta_{\mathrm{d}} = 0$, however, we do not obtain squeezing.

Applying $C_{n\pm1n\mp1}(0) = C_{nn}(0)(1 - 2/N_{\mathrm{at}} + O(N_{\mathrm{at}}^{-2}))$, we also find

$$\frac{\mathrm{var}\left(\hat{J}_y/\hbar\right)}{N_{\mathrm{at}}/2} = \frac{1}{2}\left(1 + N_{\mathrm{at}}\kappa \int_0^t \alpha(t')^2 dt' + N_{\mathrm{at}}\alpha(t)^2\right) . \tag{12.18}$$

Since $\kappa \geq \eta_{\mathrm{d}}\kappa_2$, the product of (12.17) and (12.18) is larger than or equal to 1/4, as required by Heisenberg's uncertainty relation. Equality is only obtained for $\alpha(t) = 0$ and $\kappa = \eta_{\mathrm{d}}\kappa_2$, where the first equation is fulfilled if the y-polarized cavity field is in the vacuum state at the final time t, and the second equation is fulfilled if all the y-polarized light is detected. For the setup in Fig. 12.1, we need to take the limit $\kappa_1 \to 0$ for fixed $\sqrt{\kappa_1}\zeta(t)$ and assume $\eta_{\mathrm{d}} = 1$ and $\kappa_{\mathrm{L}} = 0$ to achieve $\kappa = \eta_{\mathrm{d}}\kappa_2$. Alternatively, one can choose $\kappa_2 = 0$ and detect the reflected light from the cavity rather than the transmitted light, which would correspond to the transformation $\kappa_1 \to \kappa_1$, $\kappa_2 \to \kappa_1$, and $\kappa = \kappa_1 + \kappa_2 + \kappa_\mathrm{L} \to \kappa = \kappa_1 + \kappa_\mathrm{L}$ in Eq. (12.3).

It follows from

$$\mathrm{var}(\hat{x}_\mathrm{ph}) = \frac{1}{2} \frac{1 + N_\mathrm{at}\alpha(t)^2 + N_\mathrm{at}\eta_\mathrm{d}\kappa_2 \int_0^t \alpha(t')^2 dt'}{1 + N_\mathrm{at}\eta_\mathrm{d}\kappa_2 \int_0^t \alpha(t')^2 dt'} \tag{12.19}$$

and

$$\mathrm{var}(\hat{p}_\mathrm{ph}) = 1/2 \tag{12.20}$$

that the cavity field is not squeezed, but the uncertainty in $\hat{x}_\mathrm{ph}$ generally decreases with probing time if $\alpha(t)$ is kept at a constant value. The Heisenberg limit is only achieved exactly at times, where the cavity field is in the vacuum state.

Comparison with single-pass squeezing

For the special case, where $\Phi(t) \equiv |\zeta(t)|^2$ is zero for $t < 0$ and assumes the constant value Φ for $t > 0$, we have $\langle \hat{a}_x(t) \rangle = \sqrt{4\kappa_1\Phi/\kappa^2}(1 - \exp(-\kappa t/2))$, and

$$\frac{\mathrm{var}\left(\hat{J}_z/\hbar\right)}{N_\mathrm{at}/2} = \frac{1}{2}\left(1 + N_\mathrm{at}\frac{4\kappa_1\Phi}{\kappa^2}\frac{4g^4}{\kappa^2\Delta^2}\frac{\eta_\mathrm{d}\kappa_2}{\kappa}\kappa\tilde{t}\right)^{-1}, \tag{12.21}$$

where

$$\tilde{t} \equiv t - \frac{11}{2\kappa} + \frac{2\kappa t + 8}{\kappa}e^{-\kappa t/2} - \frac{\kappa^2 t^2 + 6\kappa t + 10}{4\kappa}e^{-\kappa t}. \tag{12.22}$$

This is to be compared to the corresponding expression

$$\left(\frac{\mathrm{var}(\hat{J}_z/\hbar)}{N_\mathrm{at}/2}\right)_\mathrm{SP} = \frac{1}{2}\left(1 + N_\mathrm{at}\Phi\frac{g^4\tau^2}{\Delta^2}\eta_\mathrm{d}t\right)^{-1} \tag{12.23}$$

for single-pass squeezing derived in [202]. Apart from what effectively amounts to a small reduction of the probing time, appearing because it takes a short while to build up the cavity field, the effect of the cavity is to increase the coefficient multiplying t (henceforth denoted the squeezing rate R) by a factor of $Q = 16\kappa_1\kappa_2/(\kappa^4\tau^2)$.

In the single-pass case each segment of temporal width τ of the probe beam interacts only once with the atoms, and $\langle \hat{a}_x \rangle = \sqrt{\Phi\tau}$ for all times $t > 0$. Assuming a classical x-polarized field with a real amplitude, the time evolution operator corresponding to the second term of the Hamiltonian (12.2b) is

$$U = \exp\left(\frac{g^2}{\Delta}\langle \hat{a}_x \rangle \left(\hat{a}_y^\dagger - \hat{a}_y\right)\frac{\hat{J}_z}{\hbar}\tau\right), \tag{12.24}$$

and the light-atom interaction thus transforms the y-polarized mode from the vacuum state $|0\rangle$ into the coherent state $U|0\rangle = |n(g^2\tau/\Delta)\sqrt{\Phi\tau}\rangle$, where, for simplicity, we assume that the state of the atoms is $|n\rangle$. The number of y-polarized photons observed per unit time is thus $n^2(g^4\tau^2/\Delta^2)\Phi\eta_\mathrm{d}$. If the cavity is included, on the other hand, the number of y-polarized photons observed per unit time is the product of the number of y-polarized photons in the cavity $|\alpha_n|^2$, the rate κ_2 with which the photons leave the cavity through the cavity output mirror in Fig. 12.1, and the detector efficiency η_d, and the result, $n^2(4g^4/(\kappa^2\Delta^2))(4\kappa_1\Phi/\kappa^2)\eta_\mathrm{d}\kappa_2$, is larger than in the single-pass case by precisely the factor Q.

To understand this increase in the number of detected y-polarized photons, Q may be divided into the three factors, κ_2/κ, $4\kappa_1/(\kappa^2\tau)$, and $4/(\kappa\tau)$, where the first appears because the effective detector efficiency is $\eta_\mathrm{d}\kappa_2/\kappa$ for squeezing in a cavity and η_d for single-pass squeezing, the second factor appears due to the increase in the number of photons in the x-polarized mode, as can be seen from the increase in the production rate of y-polarized photons, when the flux of x-polarized photons in the case of single-pass squeezing is increased from Φ to $4\kappa_1\Phi/(\kappa^2\tau)$, and the third factor appears because photons are present in the y-polarized mode in the cavity, as can be seen by comparing the number of produced y-polarized photons when U acts on $|\alpha_n\rangle$ and when U acts on $|0\rangle$ (in the former case the number of y-polarized photons is increased by $|\alpha_n + ng^2\tau\langle\hat{a}_x\rangle/\Delta|^2 - |\alpha_n|^2 \approx 4n^2g^4\tau\langle\hat{a}_x\rangle^2/(\kappa\Delta^2)$ and in the latter case it is increased by $n^2g^4\tau^2\langle\hat{a}_x\rangle^2/\Delta^2$).

Mean values

The mean values

$$\langle\hat{J}_z/\hbar\rangle = \frac{\sqrt{\eta_\mathrm{d}\kappa_2}\int_0^t \alpha(t')dy'_\mathrm{s}}{2/N_\mathrm{at} + 2\eta_\mathrm{d}\kappa_2\int_0^t \alpha(t')^2dt'} \tag{12.25}$$

and $\langle\hat{x}_\mathrm{ph}\rangle = \sqrt{2}\alpha(t)\langle\hat{J}_z/\hbar\rangle$ both depend on the measurement outcome, while $\langle\hat{J}_y/\hbar\rangle = \langle\hat{p}_\mathrm{ph}\rangle = 0$. The final value of $\langle\hat{J}_z/\hbar\rangle$ thus changes from realization to realization. As mentioned above, one can, however, use a feedback loop to continuously rotate the spin vector towards $\langle\hat{J}_z/\hbar\rangle = 0$ and thereby obtain unconditional squeezing [178].

12.3 Inclusion of loss due to spontaneous emission

If the atoms are allowed to decay by spontaneous emission, there will be a loss of atomic coherence as well as a decay of the mean spin. To include spontaneous emission in the analysis, we write the SME for the complete setup as

$$\begin{aligned} d\rho(t) = \mathcal{L}\rho(t)dt + \sqrt{\kappa_1}\zeta(t)[\hat{a}_x^\dagger, \rho(t)]dt - \sqrt{\kappa_1}\zeta^*(t)[\hat{a}_x, \rho(t)]dt \\ + \sqrt{\eta_{\mathrm{d}}\kappa_2}\left(\hat{a}_y - \langle\hat{a}_y\rangle\right)\rho(t)dW_{\mathrm{s}} + \sqrt{\eta_{\mathrm{d}}\kappa_2}\rho(t)\left(\hat{a}_y^\dagger - \langle\hat{a}_y^\dagger\rangle\right)dW_{\mathrm{s}} \\ + \mathcal{D}[\sqrt{\kappa}\hat{a}_x]\rho(t)dt + \mathcal{D}[\sqrt{\kappa}\hat{a}_y]\rho(t)dt, \end{aligned} \tag{12.26}$$

where[3]

$$\begin{aligned} \mathcal{L}\rho(t) = -\frac{i}{\hbar}[H, \rho(t)] + \gamma\sum_{i=1}^{N_{\mathrm{at}}}\bigg(\frac{2}{3}\mathcal{D}[|g_{-,i}\rangle\langle e_{+,i}|]\rho(t) + \frac{1}{3}\mathcal{D}[|g_{+,i}\rangle\langle e_{+,i}|]\rho(t) \\ + \frac{2}{3}\mathcal{D}[|g_{+,i}\rangle\langle e_{-,i}|]\rho(t) + \frac{1}{3}\mathcal{D}[|g_{-,i}\rangle\langle e_{-,i}|]\rho(t)\bigg) \end{aligned} \tag{12.27}$$

and H is given by (12.1). After adiabatic elimination of the excited states of the atoms, (12.27) turns into

$$\begin{aligned} \mathcal{L}\rho(t) = -\frac{g^2\Delta}{\Delta^2 + \frac{\gamma^2}{4}}\left[\left(\hat{a}_x^\dagger\hat{a}_y - \hat{a}_y^\dagger\hat{a}_x\right)\frac{\hat{J}_z}{\hbar}, \rho(t)\right] \\ + \frac{\gamma}{2}\frac{g^2}{\Delta^2 + \frac{\gamma^2}{4}}\Bigg(- \hat{a}_-^\dagger\hat{a}_-\left(\frac{N_{\mathrm{at}}}{2} + \frac{\hat{J}_z}{\hbar}\right)\rho(t) - \rho(t)\left(\frac{N_{\mathrm{at}}}{2} + \frac{\hat{J}_z}{\hbar}\right)\hat{a}_-^\dagger\hat{a}_- \\ - \hat{a}_+^\dagger\hat{a}_+\left(\frac{N_{\mathrm{at}}}{2} - \frac{\hat{J}_z}{\hbar}\right)\rho(t) - \rho(t)\left(\frac{N_{\mathrm{at}}}{2} - \frac{\hat{J}_z}{\hbar}\right)\hat{a}_+^\dagger\hat{a}_+\Bigg) + \frac{\gamma}{2}\frac{g^2}{\Delta^2 + \frac{\gamma^2}{4}} \\ \times\sum_{i=1}^{N_{\mathrm{at}}}\bigg(\frac{4}{3}\hat{a}_-|g_{+,i}\rangle\langle g_{+,i}|\rho(t)|g_{+,i}\rangle\langle g_{+,i}|\hat{a}_-^\dagger + \frac{4}{3}\hat{a}_+|g_{-,i}\rangle\langle g_{-,i}|\rho(t)|g_{-,i}\rangle\langle g_{-,i}|\hat{a}_+^\dagger \\ + \frac{2}{3}\hat{a}_-|g_{-,i}\rangle\langle g_{+,i}|\rho(t)|g_{+,i}\rangle\langle g_{-,i}|\hat{a}_-^\dagger + \frac{2}{3}\hat{a}_+|g_{+,i}\rangle\langle g_{-,i}|\rho(t)|g_{-,i}\rangle\langle g_{+,i}|\hat{a}_+^\dagger\bigg), \end{aligned} \tag{12.28}$$

where we assume $g^2|\langle\hat{a}_\pm\rangle|^2/(\Delta^2 + (\gamma/2)^2) \ll 1$ and omit the term in the Hamiltonian, which gives rise to a common phase shift of the light modes.

Ricatti equation

We next use the SME and the relation $d\langle\hat{O}(t)\rangle/dt = \mathrm{Tr}(\hat{O}d\rho(t)/dt)$, where $\hat{O}$ is some operator, to derive time evolution equations for $\langle\hat{J}_x(t)\rangle$, $\langle\hat{a}_x(t)\rangle$, and the covariances of $\hat{x}_{\mathrm{at}} = \hat{J}_y/(\hbar\langle\hat{J}_x(t)\rangle)^{1/2}$, $\hat{p}_{\mathrm{at}} = \hat{J}_z/(\hbar\langle\hat{J}_x(t)\rangle)^{1/2}$, $\hat{x}_{\mathrm{ph}} =$

---

[3] The factors of 1/3 and 2/3 arise from Clebsch-Gordan coefficients if we assume that the total angular momentum (i.e., the sum of the total angular momentum of the electron and the spin of the nucleus) is 1/2 for the states $|g_\pm\rangle$ and for the states $|e_\pm\rangle$. Other ratios of the decay rates could be relevant, but these factors are not particularly important here, and we thus stick to the above values for simplicity.

$(\hat{a}_y + \hat{a}_y^\dagger)/\sqrt{2}$, and $\hat{p}_{\text{ph}} = -i(\hat{a}_y - \hat{a}_y^\dagger)/\sqrt{2}$. The latter can be expressed conveniently as a time evolution equation for the covariance matrix V (defined below Eq. (2.22)) with $\hat{y}$ defined as $\hat{y} = (\hat{x}_{\text{at}}, \hat{p}_{\text{at}}, \hat{x}_{\text{ph}}, \hat{p}_{\text{ph}})^T$. As in the previous section, we take the initial state of the atoms to be a coherent spin state with $\langle \hat{\mathbf{J}} \rangle$ pointing in the x-direction, we treat the x-polarized cavity field and the x-component of the collective atomic spin vector classically, and we assume that typical values of $\hat{a}_y$ are small compared to typical values of $\hat{a}_x$ and that typical values of $\hat{J}_y$ and of $\hat{J}_z$ are small compared to typical values of $\hat{J}_x$. We also assume that the probing time t is very small compared to the time it takes to project the atomic state onto an eigenstate of $\hat{J}_z$ due to the measurement and small compared to the time it takes $\langle \hat{J}_x(t) \rangle$ to decay significantly.

We first derive

$$\frac{1}{\hbar}\frac{d\langle \hat{J}_x(t)\rangle}{dt} = -\langle \hat{a}_x(t)\rangle^2 \frac{\gamma}{2}\frac{g^2}{\Delta^2+\gamma^2/4}\frac{\langle \hat{J}_x(t)\rangle}{\hbar}, \tag{12.29}$$

and hence

$$\langle \hat{J}_x(t)\rangle = \frac{\hbar N_{\text{at}}}{2}\exp\left(-\int_0^t \eta(t')dt'\right), \tag{12.30}$$

where

$$\eta(t) \equiv \langle \hat{a}_x(t)\rangle^2 \frac{\gamma}{2}\frac{g^2}{\Delta^2+\gamma^2/4} \tag{12.31}$$

is the (time-dependent) decay rate of the atomic spin. Likewise, we find

$$\frac{d\langle \hat{a}_x(t)\rangle}{dt} = -\frac{\kappa+\epsilon}{2}\langle \hat{a}_x(t)\rangle + \sqrt{\kappa_1}\Phi, \tag{12.32}$$

where

$$\epsilon \equiv N_{\text{at}}\frac{\gamma}{2}\frac{g^2}{\Delta^2+\gamma^2/4} \tag{12.33}$$

is the photon absorption rate, which increases the total cavity decay rate from κ to $\kappa+\epsilon$.

Computing the time derivative of the first and second order moments of $\hat{J}_y$, $\hat{J}_z$, $\hat{x}_{\text{ph}}$, and $\hat{p}_{\text{ph}}$, we find that, apart from third order moments appearing in the stochastic terms of the equations for the time derivative of the second order moments, these expressions contain only first and second order moments. Since the state of the atoms and the light field is nearly Gaussian under the above conditions [203], we approximate the third order moments by a sum over products of first and second order moments to obtain a closed set of equations. We also approximate the covariance matrix elements V_{12}, V_{13}, V_{24}, and V_{34} by zero, because these elements are zero if spontaneous emission is neglected, and because the rest of the covariance matrix elements only couple to V_{12}, V_{13}, V_{24}, and V_{34} through terms that are proportional to the small factor $(\gamma/2)g^2/(\Delta^2+\gamma^2/4)$.

Within these approximations, we find after a very long calculation that the time evolution of the covariance matrix is given by the Ricatti equation

$$\frac{dV}{dt} = G - DV - VE - VFV \tag{12.34}$$

with

$$G = \begin{bmatrix} \hbar N_{\mathrm{at}}\eta(t)/\langle \hat{J}_x(t)\rangle & 0 & 0 & 0 \\ 0 & 2\hbar N_{\mathrm{at}}\eta(t)/(3\langle \hat{J}_x(t)\rangle) & 0 & 0 \\ 0 & 0 & \kappa+\epsilon-\eta_{\mathrm{d}}\kappa_2 & 0 \\ 0 & 0 & 0 & \kappa+\epsilon \end{bmatrix}, \tag{12.35}$$

$$D = E^T = \begin{bmatrix} \eta(t)/2 & 0 & 0 & -\tilde{g}(t) \\ 0 & \eta(t)/6 & 0 & 0 \\ 0 & -\tilde{g}(t) & (\kappa+\epsilon)/2-\eta_{\mathrm{d}}\kappa_2 & 0 \\ 0 & 0 & 0 & (\kappa+\epsilon)/2 \end{bmatrix}, \tag{12.36}$$

and

$$F = \begin{bmatrix} 0 & 0 & 0 & 0 \\ 0 & 0 & 0 & 0 \\ 0 & 0 & \eta_{\mathrm{d}}\kappa_2 & 0 \\ 0 & 0 & 0 & 0 \end{bmatrix}, \tag{12.37}$$

where we have introduced the effective light-atom coupling strength

$$\tilde{g}(t) = \frac{2\Delta g^2}{\Delta^2 + (\gamma/2)^2}\sqrt{\frac{\langle \hat{J}_x(t)\rangle}{\hbar}}\frac{\langle \hat{a}_x(t)\rangle}{\sqrt{2}}, \tag{12.38}$$

in terms of which the Hamiltonian giving rise to the first term on the right hand side of (12.28) reads $H = \hbar\tilde{g}(t)\hat{p}_{\mathrm{at}}\hat{p}_{\mathrm{ph}}$. Apart from a factor of 1/3 in the matrix elements D_{22} and E_{22} and a factor of 2/3 in the matrix element G_{22}, which appear as a direct consequence of the factors of 1/3 and 2/3 in Eq. (12.27), this is exactly what is obtained by generalizing the Gaussian treatment of spontaneous decay in [201, 202, 203] to spin squeezing in a cavity. We have thus found an alternative way to derive this result.

Numerical results

Integrating the Ricatti equation numerically, we obtain the lower curves in Fig. 12.3, where $\Delta p_{\mathrm{at}} \equiv (\mathrm{var}(\hat{p}_{\mathrm{at}}))^{1/2}$. For the chosen parameters $\tilde{g}(\kappa^{-1} \ll t \ll \eta(t \gg \kappa^{-1})^{-1})\tau = 2\times 10^{-3}$, $\kappa\tau = 6\times 10^{-3}$, and $\Phi\tau = 3\times 10^{4}$, and the requirements of a dilute atomic gas, a high finesse cavity, and a strong local oscillator are fulfilled. The values $\langle \hat{J}_x(0)\rangle/\hbar = 5\times 10^{11} \gg 1$ and $\langle \hat{a}_x(t \gg \kappa^{-1})\rangle = 4.6\times 10^{3} \gg 1$ justify the classical treatment of these quantities, and $t = 1$ ms fulfils $t \ll (4\eta_{\mathrm{d}}\kappa_2\alpha(t \gg \kappa^{-1})^2)^{-1} = 2.7\times 10^{4}$ s and $t \ll \eta(t \gg \kappa^{-1})^{-1} = 0.13$ s. Furthermore, $g^2|\langle \hat{a}_\pm\rangle|^2/(\Delta^2+(\gamma/2)^2) \approx$

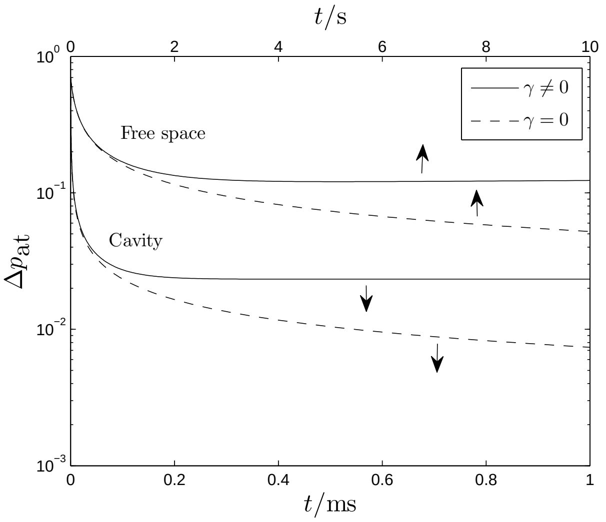

Figure 12.3: Standard deviation of p_{at} as a function of time with atomic decay included (solid curves) and excluded (dashed curves). The upper and lower curves represent squeezing of the same atomic system in free space and in a cavity, respectively (note the different timescales). The chosen parameters are (see [202]): $N_{\mathrm{at}} = 10^{12}$, $\Phi = 10^{14}\ \mathrm{s}^{-1}$, $\tau = 3 \times 10^{-10}$ s, $\Delta = 2\pi \times 10$ GHz, $g = 2\pi \times 1.5$ kHz, $\gamma = 2\pi \times 4.9$ MHz, $\eta_{\mathrm{d}} = 1$, $\kappa_{\mathrm{L}} = 0$, and $\kappa = \kappa_1 = 2\pi \times 3$ MHz (we assume the alternative case, where it is the reflected light that is detected).

$g^2\langle\hat{a}_x\rangle^2/(2\Delta^2) = 2 \times 10^{-7} \ll 1$ justifies the adiabatic elimination. The figure shows that the uncertainty in p_{at} does not decrease indefinitely when atomic decay is included, but begins to rise at a certain point if the probing is continued. For the given example, the minimum value of the uncertainty $(\Delta p_{\mathrm{at}})_{\mathrm{min}} = 0.0233$ is obtained after a probing time of $t = 0.47$ ms. We note that $\kappa^{-1} = 53$ ns for the chosen parameters, and the transient is hence not visible on the timescale of the figure.

For comparison, we also show the results obtained by integrating the corresponding equation

$$\left(\frac{d\,\mathrm{var}(\hat{p}_{\mathrm{at}})}{dt}\right)_{\mathrm{SP}} = -2N_{\mathrm{at}}\Phi\frac{g^4\tau^2}{\Delta^2}\eta_{\mathrm{d}}\,\mathrm{var}(\hat{p}_{\mathrm{at}})^2e^{-\eta t} - \frac{1}{3}\eta\,\mathrm{var}(\hat{p}_{\mathrm{at}}) + \frac{2}{3}\eta e^{\eta t} \tag{12.39}$$

for single-pass squeezing [202] in Fig. 12.3 (η is still the decay rate of the atomic spin, but it is now time-independent). The squeezing is seen to occur on a significantly slower timescale, and we note that $Q = 5 \times 10^5$ for the chosen parameters. The attained minimum value of the uncertainty $(\Delta p_{\mathrm{at}})_{\mathrm{min}} = 0.121$, obtained for $t = 5.1$ s, is also significantly higher. This value is in accordance with the value 0.118 obtained from the approximate relation

$$(\Delta p_{\rm at})_{\rm min} = \left(\frac{\eta}{3R}\right)^{1/4} = \left(\frac{\eta\Delta^2}{3N_{\rm at}\Phi g^4\tau^2\eta_{\rm d}}\right)^{1/4} \tag{12.40}$$

derived in [202] for $\Delta^2+(\gamma/2)^2 \approx \Delta^2$ (we have included an additional factor of 2/3 to take the factors 1/3 and 2/3 in Eq. (12.27) into account).

Since we found in Sec. 12.2 that the main effect of the cavity is to increase the squeezing rate R by a factor of Q, and since it follows from (12.31) that η is a factor of $4\kappa_1/((\kappa+\epsilon)^2\tau)$ larger for squeezing in a cavity than for single-pass squeezing, we expect that $(\Delta p_{\rm at})_{\rm min}$ is approximately decreased by a factor of $((\kappa+\epsilon)^2\tau/(4\kappa_2))^{1/4}$ if the atoms are enclosed in a cavity. This leads to the predicted value $(\Delta p_{\rm at})_{\rm min} = 0.0230$ for squeezing in a cavity, which is close to the value $(\Delta p_{\rm at})_{\rm min} = 0.0233$ observed in Fig. 12.3. When a cavity is included in the setup, η/R is inversely proportional to the collective cooperativity parameter $N_{\rm at}2g^2/(\kappa\gamma)$, which is hence, not surprisingly, the quantity determining whether we achieve a significant amount of squeezing before decay has degraded the state too much. Since $(\Delta p_{\rm at})_{\rm min}$ is proportional to $N_{\rm at}^{-1/4}$, we could also regard the squeezing enhancement factor as a multiplicative factor on $N_{\rm at}$ and thereby use the cavity to achieve measurement induced squeezing of a smaller number of atoms. For $N_{\rm at} = 10^{12}\times(\kappa+\epsilon)^2\tau/(4\kappa_2) = 1.4\times10^9$ we thus find a minimum standard deviation of 0.121 after a probing time of 7 ms. Finally, we note that $\tilde{g}(t)$, $\eta(t)$, and ϵ are all unchanged if Φ, $N_{\rm at}$, and the transverse area A of the cavity mode are all scaled by a common factor.

12.4 Conclusion

In conclusion, we have studied spin squeezing in an atomic ensemble by detection of the Faraday rotation of the polarization of a light beam, which interacts with the atoms prior to detection. We have been particularly concerned with the differences between spin squeezing in a cavity and single-pass spin squeezing, and we have found that the cavity increases the rate R of squeezing by a factor of $16\kappa_1\kappa_2/((\kappa+\epsilon)^4\tau^2)$, which is roughly the square of the finesse of the cavity. This appears because both the x-polarized photons and the generated y-polarized photons on average interact approximately $1/((\kappa+\epsilon)\tau)$ times with the ensemble, before they escape out of the cavity. At the same time, the rate of spontaneous emission events is increased, but only by a factor of $4\kappa_1/((\kappa+\epsilon)^2\tau)$, which is roughly the finesse of the cavity. This appears because the spontaneously emitted photons escape out of the side of the cavity, and we thus only obtain an enhancement due to the larger flux of x-polarized photons inside the cavity. Spontaneous emission is the main cause of decay of the mean value of the length of the spin vector, and the decay rate η of the atomic spin is also increased by a factor of $4\kappa_1/((\kappa+\epsilon)^2\tau)$. The randomization of the spin of the individual atoms due to spontaneous emission means that the degree of squeezing attains a minimum value after a certain probing time. For single-pass squeezing, the minimum value of $\mathrm{var}(\hat{J}_\perp)/(\hbar|\langle\hat{\mathbf{J}}\rangle|)$ is approximately $(\eta/(3R))^{1/2}$, and we thus expect the minimum value of $\mathrm{var}(\hat{J}_\perp)/(\hbar|\langle\hat{\mathbf{J}}\rangle|)$ to be reduced by approximately a factor of $((\kappa+\epsilon)^2\tau/(4\kappa_2))^{1/2}$ if a cavity is included in the setup, which is consistent with the obtained numerical results. Altogether, the cavity thus improves the performance.

Chapter 13

Conclusion

In conclusion, we have investigated a number of different ways to prepare various quantum states of light and atoms with applications within quantum computing, quantum cryptography, quantum communication, and precision measurements. First, we have analyzed various light state preparation protocols, which rely on conditional measurements applied to the output field from an OPO. Conditional measurements provide a powerful and easy way to transform Gaussian states into non-Gaussian states, and single-photon states, two-photon states, and Schrödinger cat states have already been produced experimentally by this method. We have used a multimode description to calculate the optimal mode function for n-photon state generation from a continuous wave OPO. We have also presented a model describing the multimode structure of light emitted from an OPO pumped with a time-dependent pump field, and we have used this model to analyze under which conditions it is possible to use time gating to produce quantum states of light at a specific time with a probability smaller than unity rather than producing quantum states at random times. In addition, we have proposed a protocol to generate large amplitude Schrödinger cat states. The projects on single-photon state generation and time gating have been carried out in connection with the experiments presented in [31] and [67], and our ideas for two-photon state generation from a continuous wave OPO and for Schrödinger cat state generation have been used in a new proposal, which has led to the experimental demonstration of the largest Schrödinger cat states of traveling light ever reported at the time of the experiment [86]. An advantage of the considered protocols is the fact that high fidelity states can be obtained even if the efficiency of the trigger channel is low. In those cases, where the successful generation of the state is heralded by more than about two trigger detection events, the high fidelity limit is, however, only obtained under conditions, where the probability of success is very low, and in practice, this limits the variety of states that can be produced by conditional measurements with inefficient on/off detectors. Improvements of current detectors and invention of new detectors could overcome this limitation.

An interesting alternative to conditional on/off detections is to allow the light field to interact with an atom in a cavity in the strong coupling limit and subsequently apply a measurement to the atom. This procedure allows generation of interesting quantum states of light, for instance Schrödinger cat states, from coherent states [152]. In the thesis, we have shown how one can use the interaction to construct a device, which is able to compare the number of photons in two modes, and we have pointed out a number of useful applications of this device, including state preparation and photon number state resolved detection. The proposed state preparation protocols are probabilistic, but the success probabilities are significantly higher than those for photon subtraction via conditional detection with an on/off detector because the setup acts as a filter, which conditionally selects the desired component of the input state. A large number of different transformations of states of light can be obtained by combining linear optics with measurements of the state of atoms in cavities in the strong coupling regime, and it could be interesting to investigate the possibilities further. One could, for instance, think of constructing quantum communication schemes, which explicitly utilize the specific properties of the photon number correlated states that can be produced by the proposed device. Experimentally, it is so far possible to trap an atom in a cavity in the strong coupling regime, to prepare the atom in the desired initial state, and to read out the state of the atom with high fidelity.

We have also proposed to use the Rydberg blockade mechanism and cooperative spontaneous emission from an atomic ensemble to generate quantum states of light. The method is deterministic and facilitates generation of a large number of different multimode states. At present, the Rydberg blockade mechanism has been observed experimentally, and gates between two atoms have been demonstrated. With further experimental progress, both application of high finesse cavities and application of Rydberg blockade and cooperative spontaneous emission seem to be very promising candidates for quantum state engineering devices. As a further direction of research, we are currently investigating the possibility to demonstrate properties of topological states prepared in atomic ensembles by use of the Rydberg blockade mechanism. Topological states possess nonlocal entanglement and open new possibilities for quantum computing [205]. Methods have been proposed to generate and manipulate topological states of atoms in optical lattices, including minimum instances of the resonating valence-bond state and the Laughlin state [206]. Such states can also be generated in atomic ensembles, but there are some differences because the states are now encoded in qubits, for which the two possible states are the presence and absence of an atom in a given internal single-atom state rather than two different internal states of a single atom, and because the easily applicable transformations are different.

Concerning preparation of atomic states, we have investigated probing of single atoms in cavities and atomic ensembles in cavities. Specifically, we have proposed a method to improve a protocol to measure the parity of two qubits, each consisting of a single atom in a cavity, and we have compared the performance of squeezing of one component of the collective spin vector of an atomic ensemble in a cavity to the performance of single-pass spin squeezing. The parity measurement can be used for preparing two qubits in an entangled state and for continuous quantum error correction codes [142], and spin squeezing can be used for improving precision measurements [14]. For the considered light-atom interactions, we have found that the density operator representing the state of the atoms and the light fields has a simple structure, in which the light fields can be described in terms of a few coherent state amplitudes (if we neglect spontaneous emission in the case of spin squeezing), and this observation has allowed us to derive a number of analytical results. In [VIII], we take this a step further and show that a description, which combines Wigner functions and density operators, is efficient to describe probing with a continuous squeezed state under otherwise similar conditions. There are several other ways to manipulate the state of atoms. Transformations involving more than one atom can, for instance, be obtained via the Rydberg blockade mechanism, via controlled collisions of atoms in optical lattices, and via transitions between combinations of electronic and vibrational states of ions in an ion trap. A particularly interesting feature of probing is the possibility to generate entanglement between distant atoms, which is relevant in quantum communication.

In addition to the state preparation protocols, we have presented a numerical method to obtain a simplified model of the dynamics of a probed quantum system, which can be used to estimate the current state of the system in a feedback loop. To test the model, we use the complete stochastic master equation to simulate a realistic series of measurement outcomes, and we then use this series and the simplified model to compute an approximation to the time evolution of the state of the system, which can be compared to the exact time evolution. It could be interesting also to investigate to what extent it is possible to use the simplified model to predict the time evolution of the system in theoretical investigations, where we use the simplified model to simulate the measurement outcomes to avoid integrating the full stochastic master equation.

Let us finally comment on some general aspects of the presented work. In quantum optics, there is a close connection between theory and experiment. For the presented work, for instance, photon number state generation, time gating, Schrödinger cat state generation, and spin squeezing have been realized experimentally. To accommodate this trend, our analyses generally include relevant experimental sources of error such as light field losses and detection efficiencies below unity, and we generally work with density operators or Wigner functions rather than state vectors. The Wigner function approach used in Chaps. 3-5 is very convenient for including such losses. Furthermore, for most of the investigated state preparation protocols, we study the performance of the protocols, for instance the fidelity and success probability, as a function of the experimental parameters rather than just considering some idealized limit, in which the desired state is produced with perfect fidelity. Another point to note is that we generally use a multimode model to describe the state of light beams rather than a simplified single-mode model. We intend hereby to make our models more realistic and hopefully more accessible for experimental investigations.

Danish and English summary

Dansk resume

Fælder, der kan fastholde et enkelt atom, og studier af lys på niveau af enkelte fotoner er i dag en eksperimentel realitet. Sådanne systemer beskrives ved hjælp af kvantemekanik, og de har en række interessante egenskaber, som blandt andet åbner muligheder for at bygge meget hurtige computere, at udføre ekstremt præcise målinger og at frembringe tilfældige tal. I afhandlingen undersøges det, hvordan målinger påvirker dynamikken af kvantesystemer, og hvordan målinger kan anvendes til at fremstille kvantesystemer i bestemte tilstande. Effektive metoder til at manipulere tilstanden af kvantesystemer er en væsentlig forudsætning for praktiske og videnskabelige anvendelser af systemerne.

English summary

Traps, which can trap a single atom, and studies of light at the level of single photons are today an experimental reality. Such systems are described by means of quantum mechanics, and they have a number of interesting properties which, among other things, open up possibilities for building very fast computers, for performing extremely precise measurements, and for generating random numbers. In the thesis, it is investigated how measurements affect the dynamics of quantum systems and how measurements can be used for preparing quantum systems in particular states. Effective methods to manipulate the state of quantum systems are an important precondition for practical and scientific applications of the systems.

List of abbreviations

APD: avalanche photo diode
BS: beam splitter
CW: continuous wave
FSR: free spectral range
FWHM: full width at half maximum
GHZ: Greenberger-Horne-Zeilinger
HWP: half wave plate
LHS: left hand side
LO: local oscillator
LSR: lower stable region
LTSA: local tangent space alignment
OPO: optical parametric oscillator
PBS: polarizing beam splitter
PDC: parametric down conversion
PS: phase shifter
QED: quantum electrodynamics
QND: quantum nondemolition
RHS: right hand side
SME: stochastic master equation
SP: single-pass
USR: upper stable region
WP: wave plate

Bibliography

[1] M. A. Nielsen and I. L. Chuang, *Quantum Computation and Quantum Information*, Cambridge University Press (2000).

[2] D. Deutsch and R. Jozsa, Proc. R. Soc. Lond. A **439**, 553 (1992).

[3] P. W. Shor, Proceedings of the 35th Annual Symposium on Foundations of Computer Science, Santa Fe, NM, USA, Nov. 20-22, 1994, pp. 124-134.

[4] L. Grover, Proceedings of the 28th Annual ACM Symposium on the Theory of Computing (STOC), May 1996, pp. 212-219.

[5] A. W. Harrow, A. Hassidim, and S. Lloyd, Phys. Rev. Lett. **103**, 150502 (2009).

[6] R. P. Feynman, International Journal of Theoretical Physics **21**, 467 (1982).

[7] S. Gulde, M. Riebe, G. P. T. Lancaster, C. Becher, J. Eschner, H. Häffner, F. Schmidt-Kaler, I. L. Chuang, and R. Blatt, Nature (London) **421**, 48 (2003).

[8] R. Blatt and D. Wineland, Nature (London) **453**, 1008 (2008).

[9] B. P. Lanyon, J. D. Whitfield, G. G. Gillett, M. E. Goggin, M. P. Almeida, I. Kassal, J. D. Biamonte, M. Mohseni, B. J. Powell, M. Barbieri, A. Aspuru-Guzik, and A. G. White, Nature Chem. **2**, 106 (2010).

[10] C. H. Bennett and G. Brassard, Proceedings of the IEEE International Conference on Computers, Systems and Signal Processing, Bangalore, India, December 1984, pp. 175-179.

[11] D. Stucki, N. Gisin, O. Guinnard, G. Ribordy, and H. Zbinden, New J. Phys. **4**, 41 (2002).

[12] C. H. Bennett, G. Brassard, C. Crépeau, R. Jozsa, A. Peres, and W. K. Wootters, Phys. Rev. Lett. **70**, 1895 (1993).

[13] J. F. Sherson, H. Krauter, R. K. Olsson, B. Julsgaard, K. Hammerer, I. Cirac, and E. S. Polzik, Nature (London) **443**, 557 (2006).

[14] A. Louchet-Chauvet, J. Appel, J. J. Renema, D. Oblak, and E. S. Polzik, arXiv:0912.3895.

[15] E. Knill, R. Laflamme, and G. J. Milburn, Nature (London) **409**, 46 (2001).

[16] P. Kok, W. J. Munro, K. Nemoto, T. C. Ralph, J. P. Dowling, and G. J. Milburn, Rev. Mod. Phys. **79**, 135 (2007).

[17] D. J. Griffiths, *Introduction to Electrodynamics*, Prentice-Hall, 3rd edition (1999).

[18] D. A. Steck, *Quantum and Atom Optics*, available online at `http://steck.us/teaching` (2006).

[19] K. J. Blow, R. Loudon, S. J. D. Phoenix, and T. J. Shepherd, Phys. Rev. A **42**, 4102 (1990).

[20] P. W. Milonni and J. H. Eberly, *Lasers*, Wiley (1988).

[21] R. Loudon, *The Quantum Theory of Light*, Oxford Science Publications, 3rd edition (2000).

[22] D. F. Walls and G. J. Milburn, *Quantum Optics*, Springer-Verlag Berlin Heidelberg, 1st edition (1994).

[23] J. J. Sakurai, *Modern Quantum Mechanics*, Addison Wesley Longman, revised edition (1994).

[24] M. G. A. Paris, Phys. Lett. A **217**, 78 (1996).

[25] R. A. Campos, B. E. A. Saleh, and M. C. Teich, Phys. Rev. A **40**, 1371 (1989).

[26] C. W. Gardiner, *Quantum Noise*, Springer-Verlag Berlin Heidelberg (1991).

[27] P. P. Rohde and T. C. Ralph, J. Mod. Opt. **53**, 1589 (2006).

[28] L. A. Jiang, E. A. Dauler, and J. T. Chang, Phys. Rev. A **75**, 062325 (2007).

[29] A. I. Lvovsky and M. G. Raymer, Rev. Mod. Phys. **81**, 299 (2009).

[30] J. S. Neergaard-Nielsen, B. M. Nielsen, C. Hettich, K. Mølmer, and E. S. Polzik, Phys. Rev. Lett. **97**, 083604 (2006).

[31] J. S. Neergaard-Nielsen, B. M. Nielsen, H. Takahashi, A. I. Vistnes, and E. S. Polzik, Opt. Express **15**, 7940 (2007).

[32] M. J. Collett and C. W. Gardiner, Phys. Rev. A **30**, 1386 (1984).

[33] M. J. Collett and R. Loudon, J. Opt. Soc. Am. B **4**, 1525 (1987).

[34] P. D. Drummond and M. D. Reid, Phys. Rev. A **41**, 3930 (1990).

[35] H. H. Adamyan and G. Yu. Kryuchkyan, Phys. Rev. A **74**, 023810 (2006).

[36] K. Wakui, H. Takahashi, A. Furusawa, and M. Sasaki, Opt. Express **15**, 3568 (2007).

[37] R. S. Bennink and R. W. Boyd, Phys. Rev. A **66**, 053815 (2002).

[38] W. Wasilewski, A. I. Lvovsky, K. Banaszek, and C. Radzewicz, Phys. Rev. A **73**, 063819 (2006).

[39] T. Opatrný, N. Korolkova, and G. Leuchs, Phys. Rev. A **66**, 053813 (2002).

[40] P. D. Drummond, K. J. McNeil, and D. F. Walls, Opt. Acta **28**, 211 (1981).

[41] M. D. Reid and P. D. Drummond, Phys. Rev. A **40**, 4493 (1989).

[42] Y. J. Lu and Z. Y. Ou, Phys. Rev. A **62**, 033804 (2000).

[43] N. M. VanMeter, P. Lougovski, D. B. Uskov, K. Kieling, J. Eisert, and J. P. Dowling, Phys. Rev. A **76**, 063808 (2007).

[44] A. N. Boto, P. Kok, D. S. Abrams, S. L. Braunstein, C. P. Williams, and J. P. Dowling, Phys. Rev. Lett. **85**, 2733 (2000).

[45] C. Santori, D. Fattal, J. Vučković, G. S. Solomon, and Y. Yamamoto, Nature (London) **419**, 594 (2002).

[46] M. Keller, B. Lange, K. Hayasaka, W. Lange, and H. Walther, Nature (London) **431**, 1075 (2004).

[47] M. Hijlkema, B. Weber, H. P. Specht, S. C. Webster, A. Kuhn, and G. Rempe, Nature Phys. **3**, 253 (2007).

[48] S. Chen, Y.-A. Chen, T. Strassel, Z.-S. Yuan, B. Zhao, J. Schmiedmayer, and J.-W. Pan, Phys. Rev. Lett. **97**, 173004 (2006).

[49] L. H. Pedersen and K. Mølmer, Phys. Rev. A **79**, 012320 (2009).

[50] B. Lounis and M. Orrit, Rep. Prog. Phys. **68**, 1129 (2005).

[51] A. I. Lvovsky, H. Hansen, T. Aichele, O. Benson, J. Mlynek, and S. Schiller, Phys. Rev. Lett. **87**, 050402 (2001).

[52] S. Lloyd and S. L. Braunstein, Phys. Rev. Lett. **82**, 1784 (1999).

[53] S. D. Bartlett, B. C. Sanders, S. L. Braunstein, and K. Nemoto, Phys. Rev. Lett. **88**, 097904 (2002).

[54] JM Geremia, Phys. Rev. Lett. **97**, 073601 (2006).

[55] T. Tyc and N. Korolkova, New J. Phys. **10**, 023041 (2008).

[56] H. Kang and Y. Zhu, Phys. Rev. Lett. **91**, 093601 (2003).

[57] C. K. Hong and L. Mandel, Phys. Rev. Lett. **56**, 58 (1986).

[58] T. B. Pittman, B. C. Jacobs, and J. D. Franson, Opt. Commun. **246**, 545 (2004).

[59] S. R. Huisman, N. Jain, S. A. Babichev, F. Vewinger, A. N. Zhang, S. H. Youn, and A. I. Lvovsky, Opt. Lett. **34**, 2739 (2009).

[60] N. Jain, S. R. Huisman, E. Bimbard, and A. I. Lvovsky, arXiv:0912.1552.

[61] A. Ourjoumtsev, R. Tualle-Brouri, and P. Grangier, Phys. Rev. Lett. **96**, 213601 (2006).

[62] J. Wenger, R. Tualle-Brouri, and P. Grangier, Phys. Rev. Lett. **92**, 153601 (2004).

[63] A. Ourjoumtsev, R. Tualle-Brouri, J. Laurat, and P. Grangier, Science **312**, 83 (2006).

[64] M. Sasaki and S. Suzuki, Phys. Rev. A **73**, 043807 (2006).

[65] K. Mølmer, Phys. Rev. A **73**, 063804 (2006).

[66] W. H. Louisell, *Quantum Statistical Proporties of Radiation*, Wiley New York (1973).

[67] B. M. Nielsen, J. S. Neergaard-Nielsen, and E. S. Polzik, Opt. Lett. **34**, 3872 (2009).

[68] B. Julsgaard, J. Sherson, J. I. Cirac, J. Fiurášek, and E. S. Polzik, Nature (London) **432**, 482 (2004).

[69] R. Tualle-Brouri, A. Ourjoumtsev, A. Dantan, P. Grangier, M. Wubs, and A. S. Sørensen, Phys. Rev A **80**, 013806 (2009).

[70] Z. Y. Ou, Quantum Semiclass. Opt. **9**, 599 (1997).

[71] T. C. Ralph, A. Gilchrist, G. J. Milburn, W. J. Munro, and S. Glancy, Phys. Rev. A **68**, 042319 (2003).

[72] A. P. Lund, T. C. Ralph, and H. L. Haselgrove, Phys. Rev. Lett. **100**, 030503 (2008).

[73] J. P. Dowling, Contemp. Phys. **49**, 125 (2008).

[74] M. W. Mitchell, J. S. Lundeen, and A. M. Steinberg, Nature (London) **429**, 161 (2004).

[75] M. Rådmark, M. Żukowski, and M. Bourennane, Phys. Rev. Lett. **103**, 150501 (2009).

[76] M. Dakna, T. Anhut, T. Opatrný, L. Knöll, and D.-G. Welsch, Phys. Rev. A **55**, 3184 (1997).

[77] A. M. Brańczyk and T. C. Ralph, Phys. Rev. A **78**, 052304 (2008).

[78] H. Jeong, Phys. Rev. A **78**, 042101 (2008).

[79] A. P. Lund, H. Jeong, T. C. Ralph, and M. S. Kim, Phys. Rev. A **70**, 020101(R) (2004).

[80] A. Ourjoumtsev, H. Jeong, R. Tualle-Brouri, and P. Grangier, Nature (London) **448**, 784 (2007).

[81] T. Gerrits, S. Glancy, T. S. Clement, B. Calkins, A. E. Lita, A. J. Miller, A. L. Migdall, S. W. Nam, R. P. Mirin, and E. Knill, arXiv:1004.2727.

[82] M. Takeoka and M. Sasaki, Phys. Rev. A **75**, 064302 (2007).

[83] G. Masada, T. Suzudo, Y. Satoh, H. Ishizuki, T. Taira, and A. Furusawa, arXiv:0912.4076.

[84] M. Takeoka, H. Takahashi, and M. Sasaki, Phys. Rev. A **77**, 062315 (2008).

[85] M. Sasaki, M. Takeoka, and H. Takahashi, Phys. Rev. A **77**, 063840 (2008).

[86] H. Takahashi, K. Wakui, S. Suzuki, M. Takeoka, K. Hayasaka, A. Furusawa, and M. Sasaki, Phys. Rev. Lett. **101**, 233605 (2008).

[87] J. S. Neergaard-Nielsen, M. Takeuchi, K. Wakui, H. Takahashi, K. Hayasaka, M. Takeoka, and M. Sasaki, arXiv:1002.3211.

[88] M. Saffman, T. G. Walker, and K. Mølmer, arXiv:0909.4777.

[89] E. Brion, K. Mølmer, and M. Saffman, Phys. Rev. Lett. **99**, 260501 (2007).

[90] E. Brion, L. H. Pedersen, M. Saffman, and K. Mølmer, Phys. Rev. Lett. **100**, 110506 (2008).

[91] M. Saffman and T. G. Walker, Phys. Rev. A **66**, 065403 (2002).

[92] D. Porras and J. I. Cirac, Phys. Rev. A **78**, 053816 (2008).

[93] D. N. Matsukevich, T. Chanelière, S. D. Jenkins, S.-Y. Lan, T. A. B. Kennedy, and A. Kuzmich, Phys. Rev. Lett. **97**, 013601 (2006).

[94] R. Heidemann, U. Raitzsch, V. Bendkowsky, B. Butscher, R. Löw, L. Santos, and T. Pfau, Phys. Rev. Lett. **99**, 163601 (2007).

[95] L. Isenhower, E. Urban, X. L. Zhang, A. T. Gill, T. Henage, T. A. Johnson, T. G. Walker, and M. Saffman, Phys. Rev. Lett. **104**, 010503 (2010).

[96] T. Wilk, A. Gaëtan, C. Evellin, J. Wolters, Y. Miroshnychenko, P. Grangier, and A. Browaeys, Phys. Rev. Lett. **104**, 010502 (2010).

[97] D. Jaksch, J. I. Cirac, P. Zoller, S. L. Rolston, R. Côté, and M. D. Lukin, Phys. Rev. Lett. **85**, 2208 (2000).

[98] M. D. Lukin, M. Fleischhauer, R. Cote, L. M. Duan, D. Jaksch, J. I. Cirac, and P. Zoller, Phys. Rev. Lett. **87**, 037901 (2001).

[99] D. Porras and J. I. Cirac, arxiv:0704.0641.

[100] G. Tabia and B.-G. Englert, arXiv:0910.5375.

[101] M. A. Nielsen, Reports on Mathematical Physics **57**, 147 (2006).

[102] R. Raussendorf and H. J. Briegel, Phys. Rev. Lett. **86**, 5188 (2001).

[103] L.-M. Duan, M. D. Lukin, J. I. Cirac, and P. Zoller, Nature (London) **414**, 413 (2001).

[104] A. Kuzmich, W. P. Bowen, A. D. Boozer, A. Boca, C. W. Chou, L.-M. Duan, and H. J. Kimble, Nature (London) **423**, 731 (2003).

[105] A. Gaëtan, Y. Miroshnychenko, T. Wilk, A. Chotia, M. Viteau, D. Comparat, P. Pillet, A. Browaeys, and P. Grangier, Nature Phys. **5**, 115 (2009).

[106] E. Urban, T. A. Johnson, T. Henage, L. Isenhower, D. D. Yavuz, T. G. Walker, and M. Saffman, Nature Phys. **5**, 110 (2009).

[107] N. H. Lindner and T. Rudolph, Phys. Rev. Lett. **103**, 113602 (2009).

[108] M. Saffman and K. Mølmer, Phys. Rev. A **78**, 012336 (2008).

[109] T. Pfau, private communication.

[110] S. E. Economou, N. Lindner, and T. Rudolph, arXiv:1003.2410.

[111] J. A. Sauer, K. M. Fortier, M. S. Chang, C. D. Hamley, and M. S. Chapman, Phys. Rev. A **69**, 051804(R) (2004).

[112] K. M. Fortier, S. Y. Kim, M. J. Gibbons, P. Ahmadi, and M. S. Chapman, Phys. Rev. Lett. **98**, 233601 (2007).

[113] F. Brennecke, T. Donner, S. Ritter, T. Bourdel, M. Köhl, and T. Esslinger, Nature (London) **450**, 268 (2007).

[114] Y. Colombe, T. Steinmetz, G. Dubois, F. Linke, D. Hunger, and J. Reichel, Nature (London) **450**, 272 (2007).

[115] A. Öttl, S. Ritter, M. Köhl, and T. Esslinger, Phys. Rev. Lett. **95**, 090404 (2005).

[116] M. Trupke, J. Goldwin, B. Darquié, G. Dutier, S. Eriksson, J. Ashmore, and E. A. Hinds, Phys. Rev. Lett. **99**, 063601 (2007).

[117] R. Gehr, J. Volz, G. Dubois, T. Steinmetz, Y. Colombe, B. L. Lev, R. Long, J. Estève, and J. Reichel, arXiv:1002.4424.

[118] L. Bouten, R. van Handel, and M. James, SIAM J. Control Optim. **46**, 2199 (2007).

[119] J. Gough and M. R. James, Commun. Math. Phys. **287**, 1109 (2009).

[120] L. Bouten and A. Silberfarb, Commun. Math. Phys. **283**, 491 (2008).

[121] L. Bouten, R. van Handel, and A. Silberfarb, J. Funct. Anal. **254**, 3123 (2008).

[122] H. M. Wiseman and G. J. Milburn, Phys. Rev. A **47**, 642 (1993).

[123] K. Jacobs and D. Steck, Contemp. Phys. **47**, 279 (2006).

[124] P. E. Kloeden and E. Platen, *Numerical Solution of Stochastic Differential Equations*, Springer-Verlag Berlin Heidelberg (1992).

[125] M. A. Armen and H. Mabuchi, Phys. Rev. A **73**, 063801 (2006).

[126] S. Ya. Kilin and T. B. Krinitskaya, J. Opt. Soc. Am. B **8**, 2289 (1991).

[127] H. Mabuchi and H. M. Wiseman, Phys. Rev. Lett. **81**, 4620 (1998).

[128] R. van Handel and H. Mabuchi, J. Opt. B: Quantum Semiclass. Opt. **7**, 226 (2005).

[129] C. M. Savage and H. J. Carmichael, IEEE J. Quantum Elect. **24**, 1495 (1988).

[130] D. E. Grant and H. J. Kimble, Opt. Lett. **7**, 353 (1982).

[131] G. Rempe, R. J. Thompson, R. J. Brecha, W. D. Lee, and H. J. Kimble, Phys. Rev. Lett. **67**, 1727 (1991).

[132] M. Armen, A. Miller, and H. Mabuchi, Phys. Rev. Lett. **103**, 173601, (2009).

[133] A. S. Hopkins, *Reduced Order Models for Open Quantum Systems*, PhD thesis, California Institute of Technology (2008).

[134] C. Guerlin, J. Bernu, S. Deléglise, C. Sayrin, S. Gleyzes, S. Kuhr, M. Brune, J.-M. Raimond, and S. Haroche, Nature (London) **448**, 889 (2007).

[135] N. Imoto, H. A. Haus, and Y. Yamamoto, Phys. Rev. A **32**, 2287 (1985).

[136] C. M. Caves, K. S. Thorne, R. W. P. Drever, V. D. Sandberg, and M. Zimmermann, Rev. Mod. Phys. **52**, 341 (1980).

[137] S. Massar and E. S. Polzik, Phys. Rev. Lett. **91**, 060401 (2003).

[138] J. Kerckhoff, L. Bouten, A. Silberfarb, and H. Mabuchi, Phys. Rev. A **79**, 024305, (2009).

[139] L.-M. Duan and H. J. Kimble, Phys. Rev. Lett. **92**, 127902 (2004).

[140] C. Ahn, A. C. Doherty, and A. J. Landahl, Phys. Rev. A **65**, 042301 (2002).

[141] M. Sarovar, C. Ahn, K. Jacobs, and G. J. Milburn, Phys. Rev. A **69**, 052324 (2004).

[142] J. Kerckhoff, H. I. Nurdin, D. S. Pavlichin, and H. Mabuchi, arXiv:0907.0236.

[143] H. J. Kimble, Phys. Scr. **T76**, 127 (1998).

[144] A. Boca, R. Miller, K. M. Birnbaum, A. D. Boozer, J. McKeever, and H. J. Kimble, Phys. Rev. Lett. **93**, 233603 (2004).

[145] T. Puppe, I. Schuster, A. Grothe, A. Kubanek, K. Murr, P. W. H. Pinkse, and G. Rempe, Phys. Rev. Lett. **99**, 013002 (2007).

[146] M. Khudaverdyan, W. Alt, I. Dotsenko, T. Kampschulte, K. Lenhard, A. Rauschenbeutel, S. Reick, K. Schörner, A. Widera, and D. Meschede, New J. Phys. **10**, 073023 (2008).

[147] I. Chiorescu, P. Bertet, K. Semba, Y. Nakamura, C. J. P. M. Harmans, and J. E. Mooij, Nature (London) **431**, 159 (2004).

[148] A. Wallraff, D. I. Schuster, A. Blais, L. Frunzio, R.-S. Huang, J. Majer, S. Kumar, S. M. Girvin, and R. J. Schoelkopf, Nature (London) **431**, 162 (2004).

[149] J. P. Reithmaier, G. Sęk, A. Löffler, C. Hofmann, S. Kuhn, S. Reitzenstein, L. V. Keldysh, V. D. Kulakovskii, T. L. Reinecke, and A. Forchel, Nature (London) **432**, 197 (2004).

[150] T. Yoshie, A. Scherer, J. Hendrickson, G. Khitrova, H. M. Gibbs, G. Rupper, C. Ell, O. B. Shchekin, and D. G. Deppe, Nature (London) **432**, 200 (2004).

[151] Y.-S. Park, A. K. Cook, and H. Wang, Nano Letters **6**, 2075 (2006).

[152] B. Wang and L.-M. Duan, Phys. Rev. A **72**, 022320 (2005).

[153] H. Mabuchi, Phys. Rev. A **80**, 045802 (2009).

[154] I. Schuster, A. Kubanek, A. Fuhrmanek, T. Puppe, P. W. H. Pinkse, K. Murr, and G. Rempe, Nature Phys. **4**, 382 (2008).

[155] A. Kubanek, A. Ourjoumtsev, I. Schuster, M. Koch, P. W. H. Pinkse, K. Murr, and G. Rempe, Phys. Rev. Lett. **101**, 203602 (2008).

[156] R. Okamoto, J. L. O'Brien, H. F. Hofmann, T. Nagata, K. Sasaki, and S. Takeuchi, Science **323**, 483 (2009).

[157] X. Jia, X. Su, Q. Pan, J. Gao, C. Xie, and K. Peng, Phys. Rev. Lett. **93**, 250503 (2004).

[158] C. A. Muschik, E. S. Polzik, and J. I. Cirac, arXiv:0806.3448.

[159] L.-M. Duan, G. Giedke, J. I. Cirac, and P. Zoller, Phys. Rev. Lett **84**, 4002 (2000).

[160] D. Menzies and N. Korolkova, Phys. Rev. A **74**, 042315 (2006).

[161] A. Ourjoumtsev, A. Dantan, R. Tualle-Brouri, and P. Grangier, Phys. Rev. Lett. **98**, 030502 (2007).

[162] W.-Y. Hwang, Phys. Rev. Lett. **91**, 057901 (2003).

[163] K. Edamatsu, R. Shimizu, and T. Itoh, Phys. Rev. Lett. **89**, 213601 (2002).

[164] D. Achilles, C. Silberhorn, and I. A. Walmsley, Phys. Rev. Lett. **97**, 043602 (2006).

[165] J. Kim, S. Takeuchi, S. Yamamoto, and H. H. Hogue, Appl. Phys. Lett. **74**, 902 (1999).

[166] K. Banaszek and I. A. Walmsley, Optics Lett. **28**, 52 (2003).

[167] A. J. Miller, S. W. Nam, J. M. Martinis, and A. V. Sergienko, Appl. Phys. Lett. **83**, 791 (2003).

[168] D. Achilles, C. Silberhorn, C. Sliwa, K. Banaszek, I. A. Walmsley, M. J. Fitch, B. C. Jacobs, T. B. Pittman, and J. D. Franson, J. Mod. Opt. **51**, 1499 (2004).

[169] B. E. Kardynał, S. S. Hees, A. J. Shields, C. Nicoll, I. Farrer, and D. A. Ritchie, Appl. Phys. Lett. **90**, 181114 (2007).

[170] E. J. Gansen, M. A. Rowe, M. B. Greene, D. Rosenberg, T. E. Harvey, M. Y. Su, R. H. Hadfield, S. W. Nam, and R. P. Mirin, Nature Photon. **1**, 585 (2007).

[171] B. E. Kardynał, Z. L. Yuan, and A. J. Shields, Nature Photon. **2**, 425 (2008).

[172] M. J. Holland, D. F. Walls, and P. Zoller, Phys. Rev. Lett. **67**, 1716 (1991).

[173] J. Larson and M. Abdel-Aty, Phys. Rev. A **80**, 053609 (2009).

[174] C. K. Hong, Z. Y. Ou, and L. Mandel, Phys. Rev. Lett. **59**, 2044 (1987).

[175] H. M. Wiseman and G. J. Milburn, Phys. Rev. Lett. **70**, 548 (1993).

[176] H. M. Wiseman and G. J. Milburn, Phys. Rev. A **49**, 1350 (1994).

[177] A. Naik, O. Buu, M. D. LaHaye, A. D. Armour, A. A. Clerk, M. P. Blencowe, and K. C. Schwab, Nature (London) **443**, 193 (2006).

[178] L. K. Thomsen, S. Mancini, and H. M. Wiseman, Phys. Rev. A **65**, 061801(R) (2002).

[179] M. Yanagisawa, Phys. Rev. Lett. **97**, 190201 (2006).

[180] A. Negretti, U. V. Poulsen, and K. Mølmer, Phys. Rev. Lett. **99**, 223601 (2007).

[181] D. A. Steck, K. Jacobs, H. Mabuchi, T. Bhattacharya, and S. Habib, Phys. Rev. Lett. **92**, 223004 (2004).

[182] D. A. Steck, K. Jacobs, H. Mabuchi, S. Habib, and T. Bhattacharya, Phys. Rev. A **74**, 012322 (2006).

[183] L. K. Saul and S. T. Roweis, Journal of Machine Learning Research **4**, 119 (2003).

[184] T. Lin and H. Zha, IEEE T. Pattern Anal. **30**, 796 (2008).

[185] Z. Zhang and H. Zha, SIAM J. Sci. Comput. **26**, 313 (2004).

[186] D. J. Wineland, J. J. Bollinger, W. M. Itano, F. L. Moore, and D. J. Heinzen, Phys. Rev. A **46**, R6797 (1992).

[187] V. Petersen, *Gaussian Description of Squeezed Light and Magnetometry*, PhD thesis, University of Aarhus (2006).

[188] J. Combes and H. M. Wiseman, J. Opt. B: Quantum Semiclass. Opt. **7**, 14 (2005).

[189] A. Luis and N. Korolkova, Phys. Rev. A **74**, 043817 (2006).

[190] A. Kuzmich, N. P. Bigelow, and L. Mandel, Europhys. Lett. **42**, 481 (1998).

[191] A. Kuzmich, L. Mandel, and N. P. Bigelow, Phys. Rev. Lett. **85**, 1594 (2000).

[192] J. Appel, P. J. Windpassinger, D. Oblak, U. B. Hoff, N. Kjærgaard, and E. S. Polzik, Proc. Nat. Acad. Sci. **106**, 10960 (2009).

[193] M. H. Schleier-Smith, I. D. Leroux, and V. Vuletić, Phys. Rev. Lett. **104**, 073604 (2010).

[194] M. Kitagawa and M. Ueda, Phys. Rev. A **47**, 5138 (1993).

[195] I. D. Leroux, M. H. Schleier-Smith, and V. Vuletić, Phys. Rev. Lett. **104**, 073602 (2010).

[196] A. Sørensen, L.-M. Duan, J. I. Cirac, and P. Zoller, Nature (London) **409**, 63 (2001).

[197] J. Estève, C. Gross, A. Weller, S. Giovanazzi, and M. K. Oberthaler, Nature (London) **455**, 1216 (2008).

[198] J. Hald, J. L. Sørensen, C. Schori, and E. S. Polzik, Phys. Rev. Lett. **83**, 1319 (1999).

[199] L.-M. Duan, J. I. Cirac, P. Zoller, and E. S. Polzik, Phys. Rev. Lett. **85**, 5643 (2000).

[200] B. Julsgaard, A. Kozhekin, and E. S. Polzik, Nature (London) **413**, 400 (2001).

[201] K. Hammerer, K. Mølmer, E. S. Polzik, and J. I. Cirac, Phys. Rev. A **70**, 044304 (2004).

[202] L. B. Madsen and K. Mølmer, Phys. Rev. A **70**, 052324 (2004).

[203] J. Sherson and K. Mølmer, Phys. Rev. A **71**, 033813 (2005).

[204] B. Julsgaard, *Entanglement and Quantum Interactions with Macroscopic Gas Samples*, PhD thesis, University of Aarhus (2003).

[205] C. Nayak, S. H. Simon, A. Stern, M. Freedman, and S. D. Sarma, Rev. Mod. Phys. **80**, 1083 (2008).

[206] B. Paredes and I. Bloch, Phys. Rev. A **77**, 023603 (2008).